Metallic Magnets without Inversion Symmetry and Antiferromagnetic Quantum Critical Points

Inaugural-Dissertation

zur

Erlangung des Doktorgrades

der Mathematisch-Naturwissenschaftlichen Fakultät

der Universität zu Köln

vorgelegt von

Inga Anita Fischer

aus Göttingen

Köln 2006

Berichterstatter:	Prof. Dr. A. Rosch
	Prof. Dr. E. Müller-Hartmann
Tag der mündlichen Prüfung:	30. Juni 2006

Contents

0. Introduction

The Fermi liquid description of metals is of paramount importance to the quantum theory of solids. First formulated by Landau in the 1950's, the theory predicts that at very low temperatures a system of strongly interacting electrons can be described by weakly interacting electron-like "quasiparticles". Although these quasiparticles are in fact complex many-body approximations, they have many properties in common with electrons: the quasiparticles have the same quantum numbers as electrons and the quasiparticle energy spectrum is in one-to-one correspondence with the energy spectrum of a free Fermi gas.

Starting in the early eighties, more and more materials have emerged whose experimentally observed behaviour is inconsistent with Fermi liquid phenomenology. Most notably, exponents characterizing the temperature-dependence of thermodynamic and transport quantities can deviate from those predicted by Fermi liquid theory. This "Non-Fermi liquid behaviour" encompasses a wide range of physical phenomena, many of which are subject of current theoretical and experimental interest. For example, collective excitations of the electronic quasiparticles can dominate the low-energy behaviour of a system in the vicinity of a quantum critical point. In this case, the Fermi liquid paradigm in fact does not fail, since electronic quasiparticles are still present in the system. In other cases, however, the quasiparticle concept breaks down completely and the elementary excitations of the system are no longer of an electronic nature at all. Examples are one-dimensional metals (Luttinger liquids), where separate spin and charge degrees of freedom exist, and the fractional Quantum Hall effect, where the elementary excitations can be shown to have fractional charge.

This thesis focusses on two classes of systems that exhibit non-Fermi liquid behaviour in experiments. In the first part of the thesis we investigated aspects of chiral ferromagnets. In these ferromagnetic materials, the absence of inversion symmetry and the subsequent appearance of spin-orbit coupling gives rise to a helical modulation of the ferromagnetically ordered state. A much-studied example for this class of systems is MnSi, in which the temperature dependence of the resistivity has an exponent of 1.5 in a large section of the phase diagram. Moreover, recent neutron scattering experiments uncovered the existence of a peculiar kind of partial order in a region of the phase diagram adjacent to the ordered state of MnSi. So far, no theoretical explanation has been found for either the non-Fermi liquid behaviour or the partial order.

In the second part of the thesis, we study aspects of quantum critical points in antiferromagnetic metals. There are many antiferromagnetic heavy-fermion systems that can be tuned into a regime where they exhibit non-Fermi liquid exponents in the temperature dependence of thermodynamic quantities such as the specific heat capacity; this behaviour could be due to a quantum critical point. Unfortunately, an extension of the Ginzburg-Landau-Wilson theory of order-parameter fluctuations to a position- and *time*-dependent order parameter for quantum critical points fails to model the experimental data of many of these systems

– a theoretical description of the observed non-Fermi liquid behaviour in such systems is an ongoing challenge.

Thesis outline

The first chapter of the first part of this thesis constitutes an introduction to MnSi: an overview of experiments as well as the current status of the theoretical description of the system is given.

In the second chapter we study the motion of electrons in a helical state by calculating the generic band-structure of electrons in the magnetically ordered state of a metal without inversion symmetry. We found that even in the case of weak spin-orbit interaction, as realized in MnSi, the answer to this question is surprisingly complex: the interplay of two weak spin-orbit effects of similar strength leads to a pronounced restructuring of the Fermi surface. For a large portion of the Fermi surface the electron motion parallel to the helix turns out to be almost completely frozen. Signatures of this effect can be expected to show up in measurements of the anomalous Hall effect.

In the third chapter we focus on the partially ordered state of MnSi, with the underlying premise that this partially ordered state is indeed a thermodynamically distinct phase. We therefore investigated an extended Ginzburg-Landau theory for chiral ferromagnets which includes momentum-dependent interaction terms. In a certain parameter regime, we established the emergence of crystalline phases that are reminiscent of the so-called blue phases in liquid crystals. We discuss the relevance of our results to the phase diagram of MnSi. This concludes the first part of the thesis.

The second part starts with an introduction to quantum critical points with a particular emphasis on the Hertz-Millis-Moriya theory of order parameter fluctuations, its shortcomings and possible alternatives. We also give a very brief overview of the experimental status.

Many recent experiments on quantum critical points focus on field-induced quantum critical behavior. A magnetic field applied to a three-dimensional antiferromagnetic metal can destroy the long-range order and thereby induce a quantum critical point. In Chapter 5, we investigated theoretically the quantum critical behavior of clean antiferromagnetic metals subject to a static, spatially uniform external magnetic field. The external field does not only suppress (or induce in some systems) antiferromagnetism but also influences the dynamics of the order parameter by inducing spin precession. We investigated how the interplay of precession and damping determines the specific heat, magnetization, magnetocaloric effect, susceptibility and scattering rates. We found that the susceptibility $\chi = \partial M/\partial B$ is the thermodynamic quantity which shows the most significant change upon approaching the quantum critical point and which gives experimental access to the (dangerously irrelevant) spin-spin interactions.

The subject of the last chapter of the thesis is the quantum critical behaviour of two-dimensional antiferromagnetic metals. Going beyond an order parameter theory, we investigated the interaction of the electronic degrees of freedom with their collective fluctuations by means of a functional Renormalization Group calculation. Preliminary results indicate a behaviour of the system that is incompatible with the Hertz-Millis picture.

Part I.

Metallic Magnets without Inversion Symmetry: MnSi

1. Introduction

The transition-metal compound MnSi has been known for more than 35 years to exhibit a helical modulation of the ferromagnetic order in its ordered phase, due to weak spin-orbit (SO) coupling. This has been predicted theoretically [1], and verified in numerous experiments [2, 3].

1.1. Experimental observations

Experimentally, MnSi is one of the best-studied metals. Its crystal structure is $P2_13$ (T^4), with a lattice parameter $a = 4.558$Å. Until recently, it seemed to be a textbook example for Fermi liquid theory with a well-established magnetic phase diagram. At ambient pressure, MnSi orders around 29 K with a helical modulation of the magnetization. It exhibits an average moment of up to $0.4\mu_B$ Mn atom, where μ_B is the Bohr magneton. Small external magnetic fields of about 0.12 T reorient the helix parallel to the field, and magnetic fields above 0.62 T destroy the helical order: the system becomes ferromagnetic [4].

While the physics of the ordered phase has been well understood for almost 25 years, the interest in MnSi was recently renewed [5, 6, 7] after it was discovered [5] that moderate pressures p suppress the long range helical order and drive the system for $p > p_c \approx 14.6$ kbar into a novel state (see Fig. 1.1). In this state, the system is characterized by an anomalous resistivity, $\rho \sim T^{3/2}$, which is incompatible with Fermi liquid theory. This behaviour is observed over almost three decades [5] in temperature T and over a huge pressure range [6]. Lattice constants remain essentially unchanged throughout the pressure change.

Novel metallic phases have been postulated for a number of systems, notably in high-temperature superconductors and heavy fermion compounds. In most of these cases, the existence of such phases is highly controversial, for various reasons: fine-tuning of the experimental conditions is often necessary, the crystal structures contain defects, and characteristic energy scales are of similar magnitude and cannot be separated properly. In MnSi, however, the region of the phase diagram where anomalous resistivity behaviour is observed is so large that fine-tuning is unnecessary. Moreover, MnSi can be produced at high purity and high crystal perfection with a mean free path of 5000Å and a residual resisitivity of $0.17\mu\Omega$. Finally, the three most relevant energy and length scales are well separated: first, there is itinerant ferromagnetism on length scales of a few lattice constants, second, weak spin-orbit interaction induces the helical modulation of the ferromagnetic order with a pitch of 170Å at ambient pressure, and third, spin-orbit coupling terms of higher order lock the direction of the helix to $\boldsymbol{q}_0 = \langle 111 \rangle$. The typical size of magnetic domains in the ordered state is 10^4Å. The resistivity data on MnSi has therefore been taken as evidence for the existence of a genuine non-Fermi liquid phase.

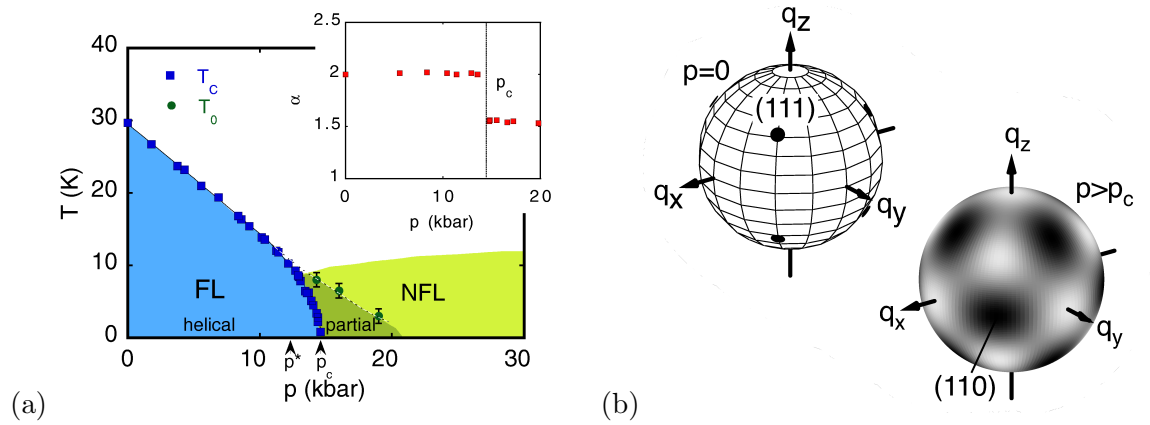

Figure 1.1.: (a) Temperature T versus pressure p phase diagram of MnSi. In the partially ordered phase, the exponent describing the temperature dependence of the electrical resistivity, α, changes apruptly from 2 to 1.5. The non-Fermi liquid phase extens at least up to 30 kbar and down to temperatures of 20 mK. The transition described by T_c changes from second order to first order as T_c drops below ~ 12 K. Taken from [8](b) Distribution of the magnetic scattering intensity for helical magnetic order observed at ambient pressure (left sphere) and for the partial magnetic order observed for $p > p_c$ (right sphere). Taken from [7].

Recent neutron scattering results [7] for $p > p_c$ give tantalizing hints as to the origin of this non-Fermi liquid phase: they suggest that while true long-range order is lost in this phase, a peculiar partial helical order survives on intermediate time and length scales.

In the ordered phase, elastic neutron scattering experiments confirm the existence of long-range helical ordering of the magnetization: at ambient pressure, resolution-limited Bragg peaks are observed at $\boldsymbol{q}_0 = \langle 111 \rangle$ and $|\boldsymbol{q}_0| = 0.037\text{Å}^{-1}$, corresponding to the helix wave vector.

In the vicinity of the ordered phase but still within the non-Fermi liquid phase there is a region where neutron scattering shows signs of static magnetic order (see Fig. 1.1), although bulk properties suggest the loss of long-range order at p_c. More precisely, the scattering intensity is now peaked on the surface of a sphere with a radius equal to the helical wave vector $|\boldsymbol{q}_0| = 0.043\text{Å}^{-1}$: scans radial to that sphere show resolution-limited peaks, whereas tangential scans show a broad angular spread of the signal. There is almost no signal left in the $\langle 111 \rangle$-directions, the intensity is now peaked around $\langle 110 \rangle$ instead. The integrated scattering intensity over that sphere is comparable in magnitude to the scattering intensity at ambient pressure. This signal is lost above a crossover temperature T_0.

Recent experiments in magnetic fields further corroborate the existence of this partially ordered state, see Fig. 1.2: When tuning from the partially ordered state through the helical phase into the ferromagnetic phase with a magnetic field, a hysteresis loop for the intensity of the Bragg peak at $q_0 = 0.04\text{Å}^{-1}$ can be observed. The intensity reaches its peak in the helical phase, but goes down as the field is lowered once again, indicating that the helical order is partially destroyed. Even for zero magnetic field, however, the intensity does not go back down to zero; *some* kind of order remains.

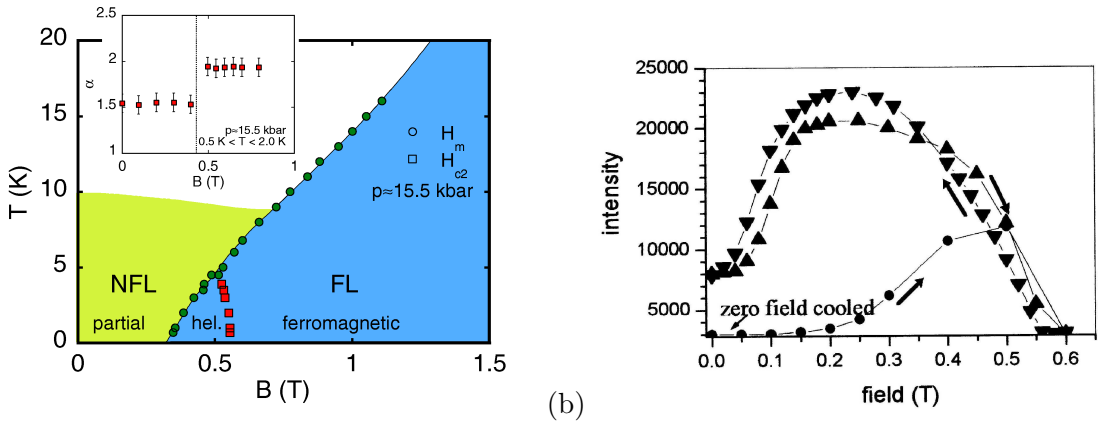

(a) (b)

Figure 1.2.: (a) Temperature T versus magnetic field B phase diagram of MnSi for a pressure $p = 15.50\,\mathrm{kbar}$ about 1 kbar above the critical pressure. The magnetic state changes from partially ordered to long-range helical order at H_m and becomes ferromagnetically ordered above H_{c2}. Taken from [8]. (b) Field dependence of the intensity of the Bragg peak at $q_0 = 0.04\text{Å}^{-1}$ on a small angle scattering instrument. For high fields, helical order is destroyed and ferromagnetic order is induced. Taken from [9].

NMR-measurements complement this picture: recent data [10] support the existence of static or slowly fluctuating magnetism well above the critical pressure p_c. These results are particularly interesting because NMR measurements probe much longer time scales than neutron scattering experiments.

What are other signatures of (i) the first order transition between the helical and the NFL phase (ii) the crossover line T_0 e.g. in thermodynamic and transport quantities? There is a sharp drop in the residual electrical resistivity at T_c, but no signatures are seen at T_0. The a.c. susceptibility is equally unaffected at T_0.

There are a large number of materials with the same crystal structure as MnSi, e.g. FeSi and CoSi. Although FeSi is a narrow-gap semiconductor and CoSi is a diamagnetic semimetal, the doped material $Fe_xCo_{1-x}Si$ is a metal with helical spin structure in the concentration range $0.2 < x < 0.95$. The pitch of the helix in $Fe_xCo_{1-x}Si$ is even larger than in MnSi (e.g. 295Å and 430Å for x=0.8 and 0.9 respectively). In a recent publication [11], the helical spin order in $Fe_{0.5}Co_{0.5}Si$ has been observed in real space by means of Lorentz transmission electron microscopy. The images reveal a surprising number of helical magnetic defects in the form of dislocations and domains with diffuse boundaries, which were not strongly pinned by atomic defects and could be reoriented with an external magnetic field.

Finally, anomalous behaviour of the resistivity at low temperatures is observed in a number of ferromagnets, notably $ZrZn_2$ [12], UGe_2 [13], UCoAl [14], CoS_2 [15] as well as Ni_3Al and YNi_3 [16]. At very low temperatures, these materials exhibit a temperature dependence of the resistivity of the form $\rho \sim a + bT^{\alpha}$, with α well below 2. Moreover, this behaviour is not always restricted to very low temperatures and a rather narrow pressure range [16], as one would expect if a quantum critical point is at the origin of the anomalous exponents. Therefore, there is a distinct possibility that the non-Fermi liquid behaviour observed in

MnSi is not due to its lack of inversion symmetry and helical twist at all. On the other hand, the ubiquitousness of non-Fermi liquid behaviour near ferromagnetic instabilities has led to speculation whether the ferromagnetic phase of some of the materials listed above is not in fact a long pitch spiral phase instead.

1.2. Theory

Little is known from the theoretical side either on the nature of the partially ordered state or on the non-Fermi liquid behaviour observed. A number of scenarios have been proposed to explain the neutron scattering data; among these are the formation of metastable droplets [6], slowly meandering spirals or multi-domain states where the direction of the spiral varies strongly from one domain to the next [7]. Belitz, Kirkpatrick and Rosch considered a theory for the Goldstone modes in the ordered phase of a helical magnet [17, 18, 19]. The scattering of the electrons off these Goldstone modes could then be of relevance to the non-Fermi liquid behaviour seen in MnSi if the partially ordered state consists of domains that are large enough for the electrons to interact with the Goldstone modes before they can scatter off domain walls. This scattering mechanism, however, leads to a $T^{5/2}$-dependence of the resistivity, which means that it is an unlikely candidate to explain the non-Fermi liquid behaviour found in MnSi.

There are two theoretical predictions for the transition between the partially ordered and the isotropic phase, i.e. the T_0-line: Schmalian and Turlakov [20] interpret the T_0-line as the continuation of the (2nd order) phase boundary between the helical and the disordered phase; Tewari *et al.* have proposed a liquid-gas transition model to be relevant for the T_0-line in the phase diagram of MnSi [21].

Recent, more general work of relevance to MnSi includes the investigation of quantum phase transitions of itinerant helimagnets by Vojta and Sknepnek [22], and finally, Belitz et al. have proposed to explain the change of the transition line T_c from second order to first order behaviour to a tricritical point [23].

2. Electrons in the Ordered Phase

In the following we calculate the band structure of electrons within the magnetically ordered phase of a chiral ferromagnet and discuss its experimental consequences. In a first step, we neglect all spin-orbit effects besides the Dzyaloshinsky-Moriya interaction and show that in this case, the mini-bands, which formally arise in the reduced Brillouin zone of the helical phase, can be avoided by a specific choice of reference frame. In a second step, we take the leading spin-orbit corrections in the band-structure into account, which then drastically modify this picture: not only do minibands develop in a region of the Fermi surface, but this region is comparatively large and the minibands are exponentially flat. We discuss several experimental consequences of our results as well as the feedback of this peculiar shape of the Fermi surface on Goldstone modes in the ordered phase. Most of the work presented in this chapter has been published in [24].

2.1. Band structure from coupling of the electrons to the helix

A Ginzburg-Landau theory of magnetic systems like MnSi which lack an inversion symmetry was investigated as early as 1980 by Nakanishi *et al.* and Bak and Høgh [2]. The cubic metal MnSi is characterized by the space group $P2_13$ whose point group T consists only of cyclic permutations of $\hat{\boldsymbol{x}}$, $\hat{\boldsymbol{y}}$ and $\hat{\boldsymbol{z}}$, of rotations by π around the coordinate axes and of combinations thereof. (The transformations contained in $P2_13$ as well as the irreducible representation of the corresponding point group are given in Appendix A.2.) Spin orbit coupling is very weak in this system and the strength of spin-orbit coupling defined below can therefore be used as a small parameter. Spin-orbit coupling manifests itself in a Ginzburg-Landau expansion of the order parameter in the form of the Dzyaloshinsky-Moriya interaction

$$q_0 \int \boldsymbol{\Phi}(\boldsymbol{x}) \cdot (\boldsymbol{\nabla} \times \boldsymbol{\Phi}(\boldsymbol{x})), \tag{2.1}$$

where $\boldsymbol{\Phi}$ is the magnetization of the system, and the prefactor q_0 is of the order of the spin-orbit coupling strength. The term (2.1) arises in the absence of inversion symmetries in linear order of spin orbit coupling; for a more detailed motivation of (2.1) see Chapter A of the appendix. As (2.1) is linear in momentum, a ground state with a finite wave vector is energetically favourable. In this case, an arbitrary small q_0 destabilizes the ferromagnetic state, twisting it into a helix of the form

$$\begin{aligned} \boldsymbol{\Phi}(\boldsymbol{x}) &= \Phi_0(\hat{\boldsymbol{n}}_1 \cos \boldsymbol{q}_0\boldsymbol{x} + \hat{\boldsymbol{n}}_2 \sin \boldsymbol{q}_0\boldsymbol{x}) \\ &= \frac{\Phi_0}{2}\left[(\hat{\boldsymbol{n}}_1 - i\hat{\boldsymbol{n}}_2)e^{i\boldsymbol{q}_0\boldsymbol{x}} + (\hat{\boldsymbol{n}}_1 + i\hat{\boldsymbol{n}}_2)e^{-i\boldsymbol{q}_0\boldsymbol{x}}\right] \end{aligned} \tag{2.2}$$

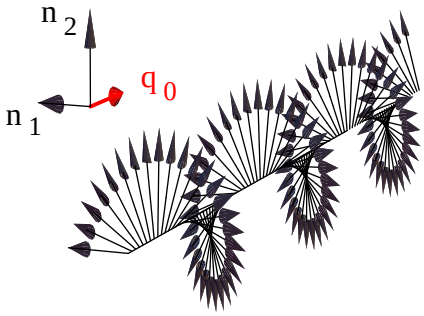

Figure 2.1.: Helical modulation of the magnetization. The direction of the magnetization twists around the $\boldsymbol{q}_0$-axis, planes of constant magnetization are perpendicular to $\boldsymbol{q}_0$.

where $\hat{\boldsymbol{n}}_1 \perp \hat{\boldsymbol{n}}_2 \perp \boldsymbol{q}_0$ are three perpendicular vectors and $|\boldsymbol{q}_0| = q_0$. A more thorough discussion of the Ginzburg-Landau theory of a chiral ferromagnet will be presented in the following chapter. Since relativistic effects are weak, the pitch $2\pi/q_0$ of the helix should in general be large: it is 175Å in the case of MnSi and even larger (> 300 Å) in the case of the isostructural compound $\mathrm{Fe}_x\mathrm{Co}_{1-x}\mathrm{Si}$. The dimensionless constant $\delta_{\mathrm{DM}} = q_0/k_F$, where k_F is a typical Fermi momentum, is therefore at most of the order of a few percent. The energy gain due to the formation of the helix is of order δ_{DM}^2, as can be seen from Eq. (2.1): when the helix solution (2.2) is inserted into (2.1), both the prefactor and the helix wavevector contribute a factor of δ_{DM}. Higher order corrections of order δ_{DM}^4 can be shown to lock the direction of the helix to the $\langle 111\rangle$ direction if q_0 is negative, which is the case for MnSi, or to the $\langle 100\rangle$ direction for positive q_0 [2]. While these terms are important for the Goldstone modes in the system [17], they can be neglected for the following discussion.

The large pitch of the helix implies a large unit-cell in the ordered phase with more than 300 atoms which makes a band-structure calculation from first principles difficult. So far, only non-relativistic calculations [25, 26] exist; those assume a ferromagnetic state and neglect the helical modulation. The results are rather complex with several bands crossing the Fermi energy, which is consistent with de Haas-van Alphen experiments [26] in large magnetic fields. We will not try to model these details: for example, we will not keep track of multiple bands. Instead, we want to capture the main qualitative features in the band-structure, and we therefore consider the following simple non-interacting one-band Hamiltonian

$$H_0 = \sum_{\boldsymbol{k},\alpha\alpha'} \epsilon_{\boldsymbol{k}}^{\alpha\alpha'} c_{\boldsymbol{k}\alpha}^\dagger c_{\boldsymbol{k}\alpha'} + 2\int d^3x\, \boldsymbol{\Phi}(\boldsymbol{x})\boldsymbol{S}(\boldsymbol{x}) \tag{2.3}$$

where $\boldsymbol{S}(\boldsymbol{x}) = \sum e^{i(\boldsymbol{k}-\boldsymbol{k}')\boldsymbol{x}} c_{\boldsymbol{k}\alpha}^\dagger\, \boldsymbol{\sigma}_{\alpha\alpha'}/2\, c_{\boldsymbol{k}'\alpha'}$ is the spin of the conduction electrons and $\boldsymbol{\Phi}(\boldsymbol{x})$ is defined in Eq. (2.2). Note that (2.3) is already strongly simplified: in real systems $\epsilon_{\boldsymbol{k}}^{\alpha\alpha'}$ can depend on the magnetization and interband couplings may be relevant for a quantitative description, but we will neglect these aspects in the following calculation.

In a first step, we disperse with spin-orbit effects in the band-structure, assuming that $\epsilon_{\boldsymbol{k}}^{\alpha\alpha'} = \epsilon_{\boldsymbol{k}}^0 \delta_{\alpha\alpha'}$. While we will show below that this approximation turns out to be unjustified, it will serve as a starting point for the full calculation.

The coupling of the electrons to the helical ordered state $\mathbf{\Phi}$, i.e. the second term of (2.3), formally leads to a coupling of electrons with different wave vectors, since

$$2\int d^3x\, \mathbf{\Phi}(\boldsymbol{x})\boldsymbol{S}(\boldsymbol{x}) = \Phi_0 \int d^3x \sum e^{i(\boldsymbol{k}-\boldsymbol{k}')\boldsymbol{x}} \left(c^\dagger_{\boldsymbol{k}\uparrow}\, e^{-\mathrm{i}\boldsymbol{q}_0\boldsymbol{x}}\, c_{\boldsymbol{k}'\downarrow} + c^\dagger_{\boldsymbol{k}\downarrow}\, e^{\mathrm{i}\boldsymbol{q}_0\boldsymbol{x}}\, c_{\boldsymbol{k}'\uparrow} \right). \tag{2.4}$$

However, for the case of a spin-rotation invariant band-structure, a residual symmetry leads to a very simple band-structure. In the magnetically ordered state, the helical modulation breaks spontaneously both the spin-rotation invariance and the translational invariance along $\boldsymbol{q}_0$. Nonetheless, the product of a translation by a lattice vector $\boldsymbol{x}$ and a rotation of spins around the $\boldsymbol{q}_0$ axis by an angle $-\boldsymbol{q}_0\boldsymbol{x}$

$$\tilde{T}_{\boldsymbol{x}} = e^{i\boldsymbol{x}\boldsymbol{P}} e^{-i\boldsymbol{q}_0\boldsymbol{x}\int d^3x'\,(\boldsymbol{S}(\boldsymbol{x}')\boldsymbol{q}_0)/q_0} \tag{2.5}$$

is still a symmetry of the Hamiltonian, where $\boldsymbol{P}$ is the generator of translations. As a consequence, instead of many minibands (in a reduced Brillouin zone of width q_0) just two bands form like in the ferromagnetic state. This can be seen by going to a frame of reference rotating with the helix, i.e. by applying the unitary transformation U with

$$U = e^{\mathrm{i}\int d^3x\, q_0 z\, S_z(\boldsymbol{x})} = e^{\frac{\mathrm{i}}{2}\int d^3x\, q_0 z\, c^\dagger_\alpha(x)\sigma^z_{\alpha\alpha'}c_{\alpha'}(x)}, \tag{2.6}$$

where we assumed $\hat{\boldsymbol{z}} \| \boldsymbol{q}_0$ for notational simplicity, so that the electrons are transformed as

$$c_{\boldsymbol{k},\sigma} \to U^+ c_{\boldsymbol{k},\sigma} U = \int d^3x\, e^{\mathrm{i}\,\boldsymbol{k}\boldsymbol{x}} \left(e^{-\mathrm{i}\, q_0 z \frac{\sigma^z}{2}} \right)_{\sigma\sigma'} c_{\sigma'}(\boldsymbol{x}) = c_{(\boldsymbol{k}-\sigma\boldsymbol{q}_0/2),\sigma}. \tag{2.7}$$

In this coordinate system, $\Phi(x) = \Phi_0\hat{\boldsymbol{x}}$ is a constant vector pointing into the $\hat{\boldsymbol{x}}$ direction and the Hamiltonian (2.3) takes the form

$$H_0 = \sum_{\boldsymbol{k}} \left(c^\dagger_{\boldsymbol{k},\uparrow}\, c^\dagger_{\boldsymbol{k},\downarrow} \right) \begin{pmatrix} \epsilon^0_{\boldsymbol{k}+\frac{\boldsymbol{q}_0}{2}} & \Phi_0 \\ \Phi_0 & \epsilon^0_{\boldsymbol{k}-\frac{\boldsymbol{q}_0}{2}} \end{pmatrix} \begin{pmatrix} c_{\boldsymbol{k},\uparrow} \\ c_{\boldsymbol{k},\downarrow} \end{pmatrix} \tag{2.8}$$

and the 2×2 matrix can now easily be diagonalized to calculate the dispersion:

$$E_\pm(\boldsymbol{k}) \;=\; \frac{\epsilon^0_{\boldsymbol{k}+\frac{\boldsymbol{q}_0}{2}} + \epsilon^0_{\boldsymbol{k}-\frac{\boldsymbol{q}_0}{2}}}{2} \pm \sqrt{\frac{\left(\epsilon^0_{\boldsymbol{k}+\frac{\boldsymbol{q}_0}{2}} - \epsilon^0_{\boldsymbol{k}-\frac{\boldsymbol{q}_0}{2}}\right)^2}{4} + \Phi_0^2} \approx \epsilon^0_{\boldsymbol{k}} \pm \Phi_0 \pm \frac{(\boldsymbol{v}_{\boldsymbol{k}}\boldsymbol{q}_0)^2}{8|\Phi_0|} \tag{2.9}$$

where we used that q_0 is small. In this rotated frame, one obtains the Fermi surface of a ferromagnetic state: the two bands are essentially separated by $2\Phi_0$, with a slight deformation in the $\boldsymbol{q}_0$ direction caused by the last term of (2.9). As emphasized above, no minibands form. The eigenstates $d_{\boldsymbol{k},\pm}$ in which $H_0 = \sum_{i=\pm} E_i(\boldsymbol{k}) d^\dagger_{\boldsymbol{k}i} d_{\boldsymbol{k}i}$ is diagonal are given by $d_{\boldsymbol{k},\pm} = \pm 1/\sqrt{2}(c_{\boldsymbol{k},\uparrow} \pm c_{\boldsymbol{k},\downarrow})$ to lowest order in spin-orbit coupling. The main results of this chapter have been published in [24].

2.2. Form of the spin-orbit coupling term in the bandstructure

We want to derive the most simple form that spin-orbit coupling can take in the bandstructure of the electrons while respecting the crystal symmetry. The crystal lattice of MnSi is invariant under transformations of the space group $P2_13$ (T^4). The lack of inversion symmetry of this crystal lattice is a necessary prerequisite for spin-orbit coupling in the bandstructure: in the presence of inversion symmetry,

$$E^{\uparrow}_{\boldsymbol{k}} \overset{\mathrm{T-reversal}}{=} E^{\downarrow}_{-\boldsymbol{k}} \overset{\mathrm{inversion}}{=} E^{\downarrow}_{\boldsymbol{k}}, \tag{2.10}$$

and spin-orbit coupling terms are absent. In general, spin-orbit coupling is included in the Hamiltonian via a term of the form

$$H_{soc} \propto \boldsymbol{\sigma} \cdot (\boldsymbol{k} \times \boldsymbol{E}), \tag{2.11}$$

where $\boldsymbol{E}$ is the electric field induced by the crystal potential. This term is of relativistic origin; its prefactor is small.

Let us treat spin-orbit coupling as a perturbation and consider how crystal symmetry restricts the form of the spin-orbit coupling correction of *first order* in δ to the Hamiltonian at a general point $\boldsymbol{k}$ in the Brillouin zone without band degeneracy and for one specific band, neglecting interband mixing.

What kind of spin-orbit corrections in the band structure of the electrons are compatible with the symmetry group? The general ansatz for spin-orbit coupling terms in the Hamiltonian is

$$H_{soc} = \boldsymbol{g}_{\boldsymbol{k}} \cdot \boldsymbol{\sigma}, \tag{2.12}$$

where $\boldsymbol{g}_{\boldsymbol{k}} = (g^x_{\boldsymbol{k}}, g^y_{\boldsymbol{k}}, g^z_{\boldsymbol{k}})$. The possible form of $\boldsymbol{g}_{\boldsymbol{k}}$ in (2.11) is restricted by the requirement that the representation of the space group of the crystal according to which H_{soc} transforms has to contain the identity representation. A list of the irreducible representations of T (i.e. the point group of $P2_13$) is given in Appendix A.3. The irreducible representation according to which $\boldsymbol{\sigma}$ transforms has to be F, since T has only one three dimensional irreducible representation. As a consequence, $\boldsymbol{g}_{\boldsymbol{k}}$ has to transform according to F as well. When $\boldsymbol{g}_{\boldsymbol{k}}$ is expanded in momenta, the lowest order term is simply

$$\boldsymbol{g}_{\boldsymbol{k}} = \boldsymbol{k}, \tag{2.13}$$

since k_x, k_y, k_z are basis functions for F in $\boldsymbol{k}$-space (see [27], erratum).

2.3. Electron band structure and the Fermi surface

Spin-orbit coupling terms in the band structure occur to first order in spin-orbit coupling and therefore to the same order in spin-orbit coupling as the Dzyaloshinskii-Moriya interaction – it is a priori not clear why they should be neglected. As discussed in section 2.1, we therefore set $\epsilon^{\alpha\alpha'}_{\boldsymbol{k}} = \epsilon^0_{\boldsymbol{k}}\delta_{\alpha\alpha'} + \sum g^i_{\boldsymbol{k}}\sigma^i_{\alpha\alpha'}$ where $\boldsymbol{g}_{\boldsymbol{k}} \propto \boldsymbol{k}$. As $\boldsymbol{g}_{\boldsymbol{k}}$ arises to first order in the spin-orbit

coupling, typical matrix elements are of order $\delta_B \epsilon_F$, where ϵ_F is the Fermi energy and the dimensionless constant δ_B has the same order of magnitude as δ_{DM}

$$\delta_B \sim \delta_{\mathrm{DM}} = q_0/k_F \sim \delta \tag{2.14}$$

and is therefore small, i.e. of the order of a few percent in MnSi. We will continue to use δ_B as well as δ_{DM} to make the origin of different contributions to the Hamiltonian of the system more apparent. The full Hamiltonian H is given by

$$H = H_0 + H_{SO} = H_0 + \sum_{\boldsymbol{k}} g^i_{\boldsymbol{k}} \sigma^i_{\alpha\alpha'} c^\dagger_{\boldsymbol{k}\alpha} c_{\boldsymbol{k}\alpha'} \tag{2.15}$$

with H_0 from (2.3). Throughout the rest of this chapter we will set the $\hat{\boldsymbol{z}}$-axis parallel to the helix wave vector $\boldsymbol{q}_0$.

To extract the main effect of H_{SO} on the band structure discussed in section 2.1, a sequence of transformations will be performed on H:

(1) Even though spin-orbit coupling terms break the residual symmetry (2.5) in real systems, it is convenient to transform H_{SO} first to the rotating frame, where

$$H_{SO} \approx \sum_{\boldsymbol{k}} \begin{pmatrix} c^\dagger_{\boldsymbol{k}-\boldsymbol{q}_0/2,\uparrow} \\ c^\dagger_{\boldsymbol{k}+\boldsymbol{q}_0/2,\downarrow} \end{pmatrix}^T \begin{pmatrix} g^z_{\boldsymbol{k}} & g^x_{\boldsymbol{k}} - i g^y_{\boldsymbol{k}} \\ g^x_{\boldsymbol{k}} + i g^y_{\boldsymbol{k}} & -g^z_{\boldsymbol{k}} \end{pmatrix} \begin{pmatrix} c_{\boldsymbol{k}-\boldsymbol{q}_0/2,\uparrow} \\ c_{\boldsymbol{k}+\boldsymbol{q}_0/2,\downarrow} \end{pmatrix}, \tag{2.16}$$

and then to the eigenstates $d_{\boldsymbol{k},\pm}$ corresponding to the energies $E_\pm(\boldsymbol{k})$ in Eq. (2.9) ,

$$H_{SO} \approx \frac{1}{2} \sum_{\boldsymbol{k}} \begin{pmatrix} d^\dagger_{\boldsymbol{k}-\boldsymbol{q}_0/2,+} - d^\dagger_{\boldsymbol{k}-\boldsymbol{q}_0/2,-} \\ d^\dagger_{\boldsymbol{k}+\boldsymbol{q}_0/2,+} + d^\dagger_{\boldsymbol{k}+\boldsymbol{q}_0/2,-} \end{pmatrix}^T \begin{pmatrix} g^z_{\boldsymbol{k}} & g^x_{\boldsymbol{k}} - i g^y_{\boldsymbol{k}} \\ g^x_{\boldsymbol{k}} + i g^y_{\boldsymbol{k}} & -g^z_{\boldsymbol{k}} \end{pmatrix} \begin{pmatrix} d_{\boldsymbol{k}-\boldsymbol{q}_0/2,+} - d_{\boldsymbol{k}-\boldsymbol{q}_0/2,-} \\ d_{\boldsymbol{k}+\boldsymbol{q}_0/2,+} + d_{\boldsymbol{k}+\boldsymbol{q}_0/2,-} \end{pmatrix}. \tag{2.17}$$

In this basis, H_0 is diagonal, and all off-diagonal matrix elements are at least of order δ_B and therefore small.

(2) H_{SO} induces transitions from $\boldsymbol{k}$ to $\boldsymbol{k} + \boldsymbol{q}_0$ and leads to the formation of mini-bands in the new Brillouin zone of width q_0. As the + and − band of H_0 are separated by $\Phi_0 \ll q_0$, transitions between these bands in the presence of H_{SO} can be neglected, and H can be separated into two contributions H^+_{SO} and H^-_{SO}:

$$H^-_{SO} = \sum E_-(\boldsymbol{k}) d^\dagger_{\boldsymbol{k}-} d_{\boldsymbol{k}-} - \left(\sum d^\dagger_{\boldsymbol{k}-\boldsymbol{q}_0/2,-} \frac{g^x_{\boldsymbol{k}} - i g^y_{\boldsymbol{k}}}{2} d_{\boldsymbol{k}+\boldsymbol{q}_0/2,-} + h.c. \right) \tag{2.18}$$

$$H^+_{SO} = \sum E_+(\boldsymbol{k}) d^\dagger_{\boldsymbol{k}+} d_{\boldsymbol{k}+} + \sum d^\dagger_{\boldsymbol{k}-\boldsymbol{q}_0/2,+} \frac{g^x_{\boldsymbol{k}} - i g^y_{\boldsymbol{k}}}{2} d_{\boldsymbol{k}+\boldsymbol{q}_0/2,+} + h.c. \tag{2.19}$$

The contributions due to g^z only lead to a minor deformation of the bands and can therefore be absorbed in $E_\pm$. We will restrict the following discussion to H^-_{SO}; analogous contributions can be expected from H^+_{SO} as well. Although the second term of H^-_{SO} is linear in spin-orbit coupling, it is not always small compared to the first term: for regions on the Fermi surface

where $E_-(\boldsymbol{k}) - E_-(\boldsymbol{k}+\boldsymbol{q}_0)$ is very small, it is the second term that dominates and gives rise to non-negligible corrections to the band-structure.

(3) To take a closer look at the region where $E_-(\boldsymbol{k}) - E_-(\boldsymbol{k}+\boldsymbol{q}_0) \ll 1$, where the main effects from spin-orbit coupling terms in the band structure can be expected to arise, we expand $E_-(\boldsymbol{k})$ around planes in momentum space where the Fermi velocity $\partial_{\boldsymbol{k}} E_-(\boldsymbol{k})$ is perpendicular to Q_0 and account for the band structure in the magnetic Brillouin zone of width q_0 in the $\hat{\boldsymbol{z}}$-direction by introducing new momentum coordinates $(\kappa_\perp, \kappa_z, n)$, where n is an integer (the band index) and $-q_0/2 < \kappa_z < q_0/2$ is a momentum in the reduced Brillouin zone. By construction, $k_z = k_0^z + \kappa_z + nq_0$ and $\partial_{\boldsymbol{k}} E_-(\kappa_\perp, k_z^0)\boldsymbol{q}_0 = 0$. In this region,

$$E_-(\kappa_\perp, \kappa_z, n) \approx E_-(\kappa_\perp) + (\kappa_z + nq_0)^2/(2m_{\kappa_\perp}) \tag{2.20}$$

$$g^x_{\boldsymbol{k}} - ig^y_{\boldsymbol{k}} \approx const. \tag{2.21}$$

where $m_{\kappa_\perp}$ is a measure of the curvature of the Fermi surface. For fixed $\kappa_\perp$ and k_z the Hamiltonian (2.18) takes the form

$$H_{SO}^{\kappa_\perp,\kappa_z} \approx \epsilon_F \sum_n c_1\delta_B(d^\dagger_{n+1}d_n + d^\dagger_n d_{n+1}) + c_2\delta^2_{\mathrm{DM}}(n - \frac{\kappa_z}{q_0})^2 d^\dagger_n d_n + c_3 \tag{2.22}$$

where $c_1 = |g^x_{k_\perp,k_z^0} - \mathrm{i}g^y_{k_\perp,k_z^0}|/(2\delta_B\epsilon_F)$, $c_2 = k_F^2/(2m_{\kappa_\perp}\epsilon_F)$ and $c_3 = E_-(\kappa_\perp, k_z^0)/\epsilon_F$ are constants of order 1. The special case where c_1 vanishes at some points on the Fermi surface, i.e. where $|\boldsymbol{g}_{\boldsymbol{k}} \times \boldsymbol{q}_0| = 0$, will be discussed below. For finite c_1, interband coupling takes the form of a tight binding Hamiltionian. The band-structure (2.9) was due to the second term in Eq. (2.22), which contributes only to order $\delta^2_{DM} \sim \delta^2_B$. The first term, which originates from $g^x_{\boldsymbol{k}} - \mathrm{i}g^y_{\boldsymbol{k}}$, is linear in spin-orbit coupling and can therefore be expected to strongly modify (2.9). The qualitative aspects of the spectrum of the Hamiltonian (2.22) can now already be read off by comparing Eq. (2.22) to the Hamiltonian of a harmonic oscillator.

(4) For a more detailed analysis of the spectrum of (2.22) it is convenient to Fourier transform it from band-index space n to the conjugate variable ξ. Setting

$$d_n = \sum e^{-\mathrm{i}n\xi} d_\xi, \quad d^\dagger_n = \sum e^{\mathrm{i}n\xi} d^\dagger_\xi, \tag{2.23}$$

the Hamiltonian (2.22) reads (in first quantized notation)

$$H_{SO}^{\kappa_\perp,\kappa_z} \approx \epsilon_F \left[2c_1\delta_B \cos(\xi) - c_2\delta^2_{DM}\left(\partial_\xi + \mathrm{i}\frac{\kappa_z}{q_0}\right)^2 + c_3 \right]. \tag{2.24}$$

The dependence of (2.24) on κ_z can be absorbed in the boundary condition by a gauge transformation $\Psi \to e^{\mathrm{i}\xi\kappa_z/q_0}\Psi$, so that we finally have

$$H_{SO}^{\kappa_\perp} \approx \epsilon_F \left[2c_1\delta_B \cos(\xi) - c_2\delta^2_{DM}\partial^2_\xi + c_3 \right]. \tag{2.25}$$

The fact that the κ_z-dependence of (2.24) can be eliminated by a gauge transformation also shows that the spectrum of (2.25) is the same as for (2.22) with varying κ_z, or, in other words, that the bandwidth of (2.22) in the $\boldsymbol{q}_0$-direction is the same as the bandwidth of (2.25). (2.25) is now the familiar Hamiltonian of a particle in a periodic potential. Similar models show up in many different problems, see e.g. ref. [28] where eigenfunctions of (2.22) are discussed in detail.

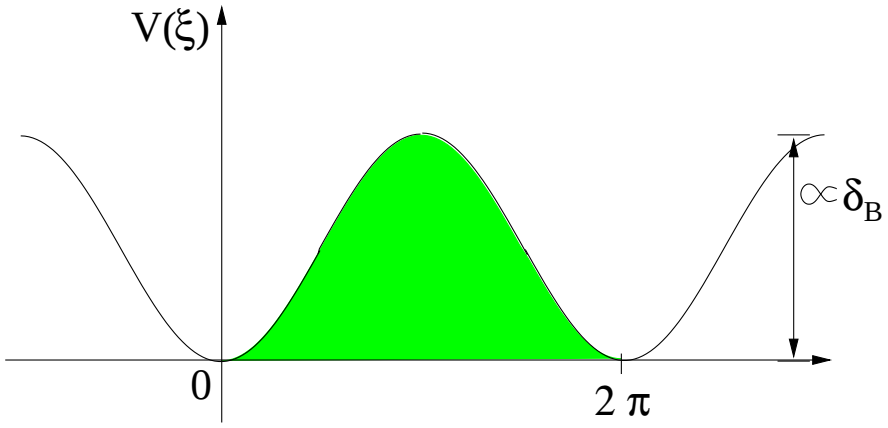

Figure 2.2.: The cosine potential of (2.25). For energies much larger than the peak height, particle motion is not affected by the potential. For very low energies, the particle oscillates around a potential minimum. The instanton energy is equal to the energy needed to cross the barrier, i.e. to the shaded area.

2.3.1. Band structure

Since the cosine potential, i.e. the first term of (2.25), is proportional to δ_B, this term originates from H_{SO} in contrast to the second term which arises as a consequence of the Dzyaloshinsky-Moriya interaction term in the original Hamiltonian. Whether H_{SO} modifies the spectrum (2.9) or not depends on how strong the influence of the cosine potential is, and therefore the spectrum of (2.25) can be easily obtained in two limits.

For energies $E \gg E_0 = \epsilon_F \delta_B$ much higher than the cosine potential, the periodic potential has little influence. The dispersion relation (2.9) is recovered, and the bandgaps at the boundaries of the magnetic Brillouin zone are exponentially small and are therefore irrelevant.

In the other limit $E \ll E_0$, the "particle" sits deep in the minima of the cosine potential. In this limit, the potential can be approximated to great accuracy by a harmonic oscillator potential, and the band-splitting, or rather the level spacing ΔE, can be directly read off from the prefactors of the terms in (2.25): Setting $\varepsilon_F c_2 \delta_{DM}^2 = 1/(2m)$ and $\varepsilon_F c_1 \delta_B = m\omega_0^2/2$, where m is the mass of the harmonic oscillator and ω_0 its frequency,

$$\Delta E = \omega_0 = 2\epsilon_F \delta_{\mathrm{DM}} \sqrt{\delta_B} \sqrt{c_1 c_2} \propto \delta^{3/2}. \tag{2.26}$$

The harmonic oscillator levels are slightly broadened by tunnelling events, when the particle tunnels from one minimum of the cosine potential to the next. This gives a finite bandwidth W, which can be calculated with the help of a WKB approximation or an instanton expansion:

$$W \sim \Delta E \, e^{-S_0}, \tag{2.27}$$

(see [29], chapter 7), where S_0 is the energy of one instanton, i.e. the energy needed by the particle to tunnel from one minimum of the cosine potential to the next,

$$S_0 = \int_0^{2\pi} d\xi \, \sqrt{2mV} = \int_0^{2\pi} d\xi \, \sqrt{\frac{2c_1 \, \delta_B}{c_2 \, \delta_{DM}^2}(\cos\xi + 1)} = 8\sqrt{2} \sqrt{\frac{c_1}{c_2}} \frac{\sqrt{\delta_B}}{\delta_{DM}} \propto \delta^{-1/2}, \tag{2.28}$$

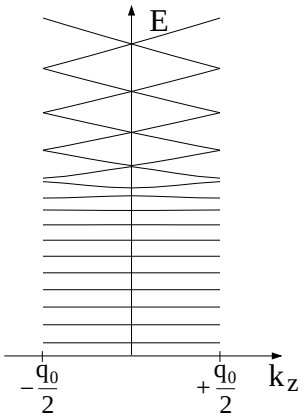

Figure 2.3.: Band structure of the Hamiltonian (2.3) with $\epsilon^0_{\boldsymbol{k}} = k^2/2 - 1/2$, $\Phi_0 = 0.3$, $\boldsymbol{q}_0 = (0, 0, 0.1)$, $\boldsymbol{g}_{\boldsymbol{k}} = 0.1\boldsymbol{k}$, $k_x = 1.26$, $k_y = 0$ which corresponds to $\delta_{\mathrm{DM}} = \delta_B = 0.1$, $c_1 \approx 1.26$, $c_2 \approx 1$. The lowest bands have exponentially small band widths, e.g. $2 \cdot 10^{-10}\epsilon_F$ for the first band, consistent with Eq. (2.29). Only the E_- bands are shown.

and therefore

$$W \sim \Delta E \exp\left[-8\sqrt{\frac{c_1}{c_2}}\frac{\sqrt{\delta}_B}{\delta_{DM}}\right] \sim \delta^{3/2} \exp\left[-c'\frac{1}{\sqrt{\delta}}\right]. \tag{2.29}$$

And finally, the number of bands that are exponentially flat can be estimated by counting the number of bands n_{max} whose energy is smaller than E_0:

$$n_{max} \sim \frac{E_0}{\Delta E} \sim \frac{\sqrt{\delta_B}}{\delta_{DM}} \sim \delta^{-1/2}. \tag{2.30}$$

To sum up, the interplay of the Dzyaloshinsky-Moriya interaction of strength δ_{DM} and spin-orbit coupling in the band-structure parameterized by δ_B, two weak relativistic effects, leads to the formation of exponentially flat bands. In those bands, the motion of the electrons parallel to the wave vector $\boldsymbol{q}_0$ of the helix practically stops. The non-analytic dependence of W and ΔE on δ_B and δ_{DM} shows that this is a non-perturbative effect, which originates from the interplay of resonant backscattering from the helix and crystal field effects. Corrections to the exponent in (2.29) are of the order $(n + 1/2)^2\delta_{DM}/\sqrt{\delta_B}$, where n is the band index.

We have confirmed our analytical results (2.26), (2.29) and (2.30) by comparing to a numerical diagonalization of the Hamiltonian (2.3) shown in Fig. 2.3. Note that the transition from equidistant harmonic oscillator bands to bands with negligible bandgaps, i.e. the transition between the two limiting cases, happens quite abruptly over the distance of roughly two bands.

2.3.2. Shape of the Fermi surface

In which way does the band structure found in the previous section affect the shape of the Fermi surface? Let us consider the Fermi surface in the extended Brillouin zone, where

$\boldsymbol{k} = (\boldsymbol{\kappa}_\perp, k_z)$. For $\varepsilon^0_{\boldsymbol{k}} = \boldsymbol{k}^2/2m$ quadratic in $\boldsymbol{k}$ and for $\delta_B = 0$, there are two ellipsoidal Fermi surfaces, which are given by

$$0 = E_\pm(\boldsymbol{\kappa}_\perp, k_z) - E_F = \frac{\kappa_\perp^2}{2m} + \frac{k_z^2 + (q_0/2)^2}{2m} \pm \sqrt{\left(\frac{q_0\, k_z}{2m}\right)^2 + \Phi_0^2} - E_F, \tag{2.31}$$

where E_F is the Fermi energy. For $\delta_B \neq 0$, the $\kappa_\perp$- and k_z-dependent parts of the energy are still independent of each other, i.e.

$$E(\kappa_\perp, k_z) = \frac{\kappa_\perp^2}{2m} + f(k_z), \tag{2.32}$$

where $f(k_z)$ now describes minibands close to $\partial_{\boldsymbol{k}} E(\boldsymbol{k}) \cdot \boldsymbol{q}_0 = 0$. The $\kappa_\perp$-dependent part of (2.32) serves to shift the Fermi level through the energy levels of H (see Fig. 2.3) and thus transfers the band structure of H to the Fermi surface. The resulting Fermi surface (for one band only) is shown in figure 2.4.

The interplay of the two spin-orbit coupling terms present in the model causes a whole section of the Fermi surface to split up into bands with negligible bandwidth and huge band gaps in between. Electrons from that belt-shaped region of the Fermi surface will stop their motion parallel to $\boldsymbol{q}_0$. The width w of the belt of minibands can be estimated from (2.30) as follows: there are n_{max} minibands of width q_0, and therefore

$$w \sim k_F\, \delta_{DM} \frac{\sqrt{\delta_B}}{\delta_{DM}} = k_F \sqrt{\delta_B}. \tag{2.33}$$

As a result, even for very small δ_B of the order of a few percent, a sizable fraction of the Fermi surface is affected by those ultra-flat bands. It is interesting to note that the belt of minibands perseveres even if δ_B is small compared to δ_{DM}. In the limit $\delta_B \to 0$ and $\delta_{DM} = const.$ the bandgaps do not close, but instead the section of the Fermi surface containing the mini-bands gets smaller until it eventually vanishes. Even when δ_B is small, mini-bands are present in principle, although only in a small region on the Fermi surface.

If $|\boldsymbol{g}_{\boldsymbol{k}} \times \boldsymbol{q}_0| = 0$ at some singular points on the Fermi surface in the vicinity of the region where $\boldsymbol{q}_0$ is parallel to the Fermi surface, the results quoted above are not valid close to those points. In this case, $g^x_{k_\perp, k_z^0} - \mathrm{i} g^y_{k_\perp, k_z^0}$ can be approximately linearized, and the first term in eq. (2.22) has to be replaced by $\epsilon_F \sum_n c_1' \delta_{\mathrm{DM}} \delta_B (d^\dagger_{n+1} d_n + d^\dagger_n d_{n+1})(n - \kappa_z/q_0)$. This term is now of order δ^2 and will generate $\mathcal{O}(\delta_B/\delta_{DM}) \approx 1$ minibands that will cover an area of width $k_F \delta_B$ close to these points.

2.4. Fermi surface: Experimental consequences

The interplay of the two spin-orbit coupling effects in the model leads to the opening of large gaps on a considerable part of the Fermi surface. In this section we want to investigate what characteristic signatures these band gaps show either directly in experiments that probe the Fermi surface or indirectly by affecting e.g. transport coefficients.

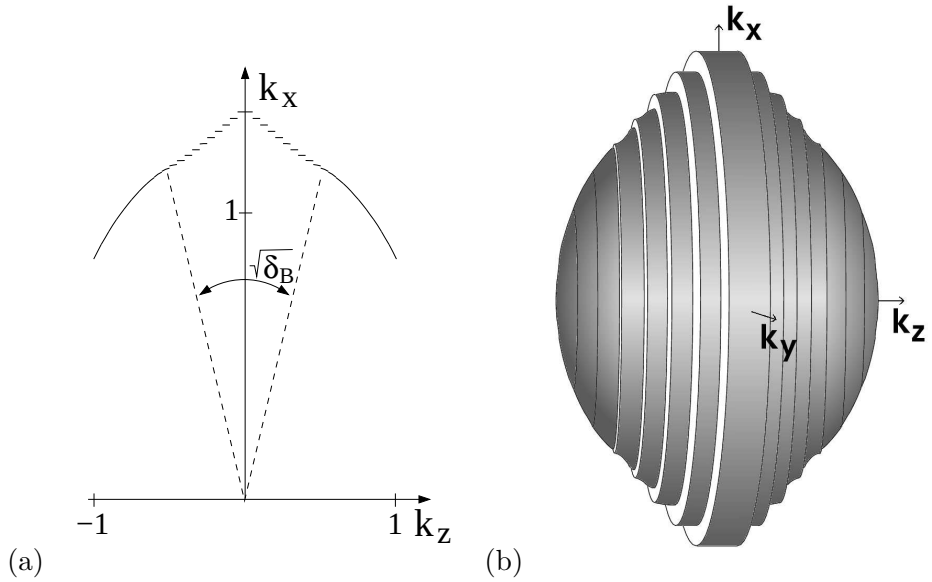

Figure 2.4.: a) Fermi surface of the Hamiltonian (2.3) for $k_y = 0$ in an extended Brillouin zone ($\epsilon^0_{\boldsymbol{k}} = k^2/2 - 1/2$, $\Phi_0 = 0.3$, $\boldsymbol{q}_0 = (0, 0, 0.1)$, $\boldsymbol{g}_{\boldsymbol{k}} = 0.1\boldsymbol{k}$, $k_x = 1.26$, $k_y = 0$ which corresponds to $\delta_{\mathrm{DM}} = \delta_B = 0.1$, $c_1 \approx 1.26$, $c_2 \approx 1$). b) Sketch of the Fermi surface. In a belt of width $\sqrt{\delta_B}$ the mini-bands are completely flat in the direction parallel to the helix.

There are numerous experimental methods available to determine the shape of the Fermi surface of a metal; however, most of them involve the application of external magnetic fields. The experimental difficulty in this case lies in the fact that MnSi cannot be subjected to high magnetic fields since fields larger than 0.62T destroy the helical spin ordering in the metal [4].

2.4.1. De-Haas–van-Alphen Effect

When an external magnetic field B is applied to a metal, the magnetic susceptibility can be shown to depend periodically on $1/B$; this is the De-Haas–van-Alphen effect. The period of the oscillations is proportional to the extremal cross-sectional area of the Fermi surface in a plane normal to the magnetic field and therefore gives direct information on the shape of the Fermi surface.

The De-Haas–van-Alphen effect can be derived theoretically from the semiclassical equations that govern the motion of the electrons in the presence of a uniform magnetic field:

$$\hbar\dot{\boldsymbol{k}} = -e\boldsymbol{B} \times \boldsymbol{k}, \tag{2.34}$$

$$\dot{\boldsymbol{r}} = \boldsymbol{v}(\boldsymbol{k}) = \frac{1}{\hbar}\frac{\partial\epsilon(\boldsymbol{k})}{\partial\boldsymbol{k}}. \tag{2.35}$$

The external magnetic field forces the electrons to move in the plane normal to the external magnetic field, or more specifically, along paths formed by the intersection of the Fermi surface

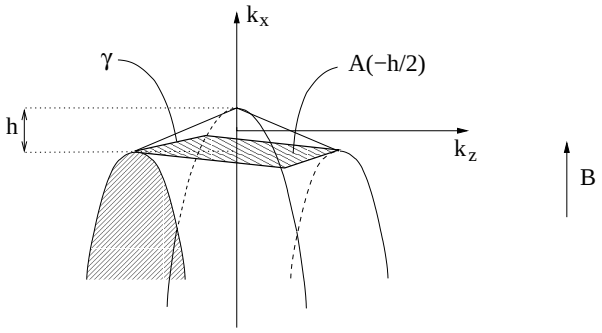

Figure 2.5.: Highest miniband of MnSi: A magnetic field applied along k_x causes electrons to move along γ. The form of the band is simplified as shown.

with planes normal to the external magnetic field. Equation (2.34) can be used in concordance with the Bohr phase-integral formula

$$\oint \boldsymbol{p} \cdot \boldsymbol{d}r = (n + \phi)2\pi\hbar, \tag{2.36}$$

where n is an integer and ϕ is a phase correction, to show that the energies of electrons in a crystal subjected to an external magnetic field aligned along the k_x-direction are given by

$$\epsilon(n, k_x) \approx \hbar\omega_c n + f(k_x), \tag{2.37}$$

which is quite similar to the free electron case. The harmonic oscillator frequency ω_c can be obtained from (2.34):

$$T(\epsilon, k_x) = \frac{2\pi}{\omega_c} = \frac{\hbar^2}{eB} \oint_\gamma \frac{\mathrm{d}\boldsymbol{k}}{\left|\frac{\partial\epsilon(\boldsymbol{k})}{\partial \boldsymbol{k}_\perp}\right|}, \tag{2.38}$$

where γ is given by the intersection of the plane through k_x and normal to $\boldsymbol{B}$ with the Fermi surface.

The oscillatory part of the free energy of the system, from which the oscillations of the magnetic susceptibility can be derived, has the form [30]

$$F_{\text{osc.}} = \frac{2}{\beta} \sum_{\nu=1}^{\infty} (-1)^\nu \frac{1}{8\pi^4} \frac{eB}{c\hbar} \frac{\beta\hbar\omega_c}{\nu^2} \frac{\frac{2\pi^2\nu}{\beta\hbar\omega_c}}{\sinh\left(\frac{2\pi^2\nu}{\beta\hbar\omega_c}\right)} \int_{-\infty}^{\infty} \mathrm{d}k_x \ \cos\left[\nu\left(\frac{c\hbar}{eB}\right) A(k_x)\right], \tag{2.39}$$

where $A(k_x)$ is the area enclosed by the intersection of the Fermi surface with the plane through k_x and normal to $\boldsymbol{B}$.

Turning back to MnSi, each of the energy bands supports electron oscillations and is responsible for a particular frequency in the oscillations. In the following, we evaluate the contribution of the "highest" miniband (i.e. with maximal k_x) only.

Approximating the band structure by two straight lines and taking only the $\nu = 1$-component, the area $A(k_x)$ encircled by the electrons can be evaluated as a function of k_x, see Fig. 2.5.

The oscillating part of the free energy is then approximately given by

$$F \propto \int_{-h/2}^{h/2} \mathrm{d}k_x \ \cos\left(\frac{c\hbar}{eB}A(k_x)\right) = \frac{c\hbar}{eB}\frac{h}{A(-h/2)}\sin\left(\frac{c\hbar}{eB}A(-h/2)\right), \tag{2.40}$$

where the area $A(-h/2)$ can in turn be expressed as a function of the band height h and k_F:

$$A(-h/2) \approx \frac{q_0\sqrt{2k_F}}{3}\sqrt{h} - \mathcal{O}(h^{3/2}). \tag{2.41}$$

The sine of the free energy is zero for

$$\frac{c\hbar}{eB}A(-h/2) = 2\pi n. \tag{2.42}$$

Oscillations of the magnetic susceptibility can only occur upon variation of the magnetic field up to a maximal value

$$B_{\max} = \frac{c\hbar}{2\pi e}A(-h/2) \tag{2.43}$$

i.e. where $n = 1$. Assuming k_F to be equal to the typical Fermi wavevector in a metal, i.e. $k_F \approx 1 \cdot 10^{10} m^{-1}$, and setting $q_0 = 1/150$ Å, the maximal magnetic field is therefore

$$B_{\max} = \sqrt{h}\ 0.0003\ \mathrm{T}\sqrt{\mathrm{m}}. \tag{2.44}$$

For the oscillations to be actually observable, however, the mean free path $l_0 = v_0\tau$ of the electrons has to be such that they can travel a reasonable distance along such a maximal orbit in the first band before they are scattered, i.e. the scattering frequency $1/\tau$ has to be below the cyclotron frequency:

$$\omega_c\tau \ll 2\pi. \tag{2.45}$$

The time $T = 2\pi/\omega_c$ can be calculated from (2.38) where the path γ is given by the intersection of the Fermi surface with the plane normal to $\boldsymbol{B}$ that maximizes the area enclosed by γ. Assuming a velocity of $v_0 = 2 * 10^6$ m/s for the electrons, the required mean free path l of the electrons is (in metres)

$$l_{\mathrm{req}} = v_0 T = \frac{4.4 * 10^{-6}}{B\sqrt{h}}\ \mathrm{T}\sqrt{\mathrm{m}}. \tag{2.46}$$

According to (2.44), B is at most of the order of 0.1 mT; furthermore, the bandheight h is exponentially small, so l can be expected to be of the order of at least centimetres. Therefore, unrealistically clean samples of MnSi would be required for the oscillations to be actually observable.

2.4.2. Impurity scattering

Assuming that electron scattering is only due to impurities, the transport scattering rate $1/\tau_{\boldsymbol{k}}$ near the Fermi surface is given by [30]

$$\frac{1}{\tau_{\boldsymbol{k}'}} = \int \mathrm{d}^3\boldsymbol{k}\, \delta(\epsilon_{\boldsymbol{k}})(1-\cos\phi_{kk'})W_{kk'}, \tag{2.47}$$

where $\phi_{kk'}$ is the angle between $\boldsymbol{v}_{\boldsymbol{k}} = d\epsilon_{\boldsymbol{k}}/d\boldsymbol{k}$ and $\boldsymbol{v}_{\boldsymbol{k}'}$. If s-wave scattering with $W_{kk'} \equiv W = const.$ can be assumed, then the cosine drops out due to $\cos\phi + \cos(\pi-\phi) = 0$, so that

$$\frac{1}{\tau_{\boldsymbol{k}'}} \equiv \frac{1}{\tau} = W\int \mathrm{d}^3\boldsymbol{k}\, \delta(\epsilon_{\boldsymbol{k}}) = W\int \mathrm{d}^3\boldsymbol{k}\, \frac{1}{\left|\frac{\partial\epsilon_{\boldsymbol{k}}}{\partial\boldsymbol{k}}\right|_{\boldsymbol{k}=\boldsymbol{k}_F}}\, \delta(\boldsymbol{k}-\boldsymbol{k}_F). \tag{2.48}$$

As the band gaps open, the contribution $\propto 2\pi k_F\sqrt{\delta_B}$ to $1/\tau$ *in the absence of* H_{SO} gets replaced by $\sum_n 2\pi(k_F + n\, m_{\kappa_\perp}\omega_0/k_F)(\sqrt{\delta_B}/n_{max})$. Therefore, the presence of the minibands on the Fermi surface in a region of size $\sqrt{\delta}_B$ around k_0^z leads to an additional contribution

$$\Delta\left(\frac{1}{\tau}\right) = 2\pi\frac{m_{\kappa_\perp}\omega_0}{k_F}\frac{\sqrt{\delta_B}}{n_{max}}\sum_n n \propto \delta_B\,\delta_{DM}\frac{n_{max}+1}{2} \tag{2.49}$$

to the transport scattering rate, where $n_{max} \propto \sqrt{\delta_B}/\delta_{DM}$. This additional term is of the order of $\delta^{3/2}$ and therefore small.

2.4.3. Conductivity

The electrical conductivity due to impurity scattering is given by (see [31], chapter 13)

$$\sigma_{\alpha\beta} = e^2\int \frac{\mathrm{d}\boldsymbol{k}}{4\pi^3}\,\tau(\epsilon_{\boldsymbol{k}})v_\alpha v_\beta\left(-\frac{\partial f}{\partial\epsilon}\right)_{\epsilon=\epsilon_{\boldsymbol{k}}}, \tag{2.50}$$

where $\boldsymbol{v} = \partial\epsilon_{\boldsymbol{k}}/\partial\boldsymbol{k}$ is the velocity of the quasiparticles, $f(\epsilon_{\mathrm{k}})$ is the Fermi function and $\tau(\epsilon_{\boldsymbol{k}})$ is the (elastic) transport scattering time of the quasiparticles. In a metal, this can be evaluated at $T = 0$ to an accuracy of order $(k_BT/E_F)^2$ as:

$$\begin{aligned}\sigma_{\alpha\beta} &= -e^2\int \frac{\mathrm{d}\boldsymbol{k}}{4\pi^3}\,\tau(\epsilon_{\boldsymbol{k}})v_\alpha v_\beta\,\delta(\epsilon_{\boldsymbol{k}}-E_F)\\ &= -e^2\tau(E_F)\int\limits_{FS}\frac{\mathrm{d}\boldsymbol{k}}{4\pi^3}\,v_\alpha v_\beta,\end{aligned} \tag{2.51}$$

where the momentum integral in the last line is over the Fermi surface. The contribution of the region of size $\sqrt{\delta}_B$ around $k_z = 0$ to the zz-component of the electrical conductivity *in the absence of* H_{SO} from one of the bands $E^\pm$ is given by

$$\begin{aligned}\Delta\sigma_{zz} &= -e^2\tau(E_F)\int\limits_{\mathrm{FS},\,-k_F\frac{\delta_B}{2}<k_z<k_F\frac{\delta_B}{2}}\frac{\mathrm{d}\boldsymbol{k}}{4\pi^3}\,v_zv_z\\ &= -\tau(E_F)\frac{e^2}{2\pi^2}\int\limits_{-k_F\sqrt{\delta_B}/2}^{k_F\sqrt{\delta_B}/2}\mathrm{d}k_z\,\sqrt{{k_F}^2-k_z^2}\,\frac{k_z^2}{m^2}\\ &= \mathcal{O}(\delta_B^{3/2}),\end{aligned} \tag{2.52}$$

where a spherical Fermi surface with radius k_F has been assumed. This contribution is missing when spin-orbit coupling terms in the band structure cause bandgaps to open, since the bands are exponentially flat and the z-component of the Fermi velocity is zero to a very good approximation. Once again, the effect is rather small for small δ_B and difficult to observe.

2.4.4. Anomalous Skin effect

A high-frequency alternating electromagnetic field is able to penetrate into the body of a metallic sample only up to a depth of Δ, the so-called skin depth of the metal. This phenomenon is called the skin effect; the skin depth can be derived from classical electromagnetic theory

$$\Delta = \sqrt{\frac{2}{\sigma\omega\mu\mu_0}}, \tag{2.53}$$

where σ is the conductivity of the metal, ω is the frequency of the external electromagnetic field and $\mu\mu_0$ is the magnetic permeability. In the derivation of (2.53) it is implicitly assumed that the mean free path l_0 is much smaller than Δ. When this assumption is no longer valid, e.g. at high frequencies of the external field and low temperatures of the sample, the simple theory ceases to be applicable, and the so-called anomalous skin effect can be observed.

In the regime of the anomalous skin effect it can be shown that the main contribution to the electric current is given by electrons whose velocity vector forms an angle of l_0/Δ or less with the surface: only those electrons that remain inside the skin depth for most of their mean free path l_0 can pick up energy from the electric field and participate in the absorption and reflection of the electromagnetic wave. In other words, only electrons whose velocity component $v_F^\perp$ perpendicular to the surface is sufficiently large, $v_F^\perp/v_F < \Delta/l_0$, contribute to the screening of electromagnetic waves. Those electrons originate from a narrow, belt-shaped region around the Fermi surface, and therefore the measurable quantities like surface impedance can be related to the geometry of the Fermi surface.

In contrast to the previous experiments, the advantage of this experimental technique regarding the belt of minibands is that it probes only the electrons in the relevant region in momentum space.

The minibands affect the motion of electrons whose velocity component parallel to the direction of the helix is small. One can therefore expect a pronounced modification of the skin depth when orienting the helix either parallel or perpendicular to the surface of the metal. A rotating magnetic field can be used to rotate the helix to the necessary direction, since a small magnetic field of about 0.12 T is sufficient [4, 32] to orient the helix parallel to the field.

If the helix is oriented parallel to the surface, $v_F^\perp$ is not affected by the minibands, see fig. 2.6. As only electrons with $v_F^\perp/v_F < \Delta/l_0$ contribute to σ, the conductivity in eq. (2.53) is reduced by a factor of order Δ/l_0 and therefore the anomalous skin depth $\Delta_a^\parallel$ is estimated to be

$$\Delta_a^\parallel \sim \Delta_0\sqrt{l_0/\Delta_a^\parallel} \sim (\Delta_0^2 l_0)^{1/3}. \tag{2.54}$$

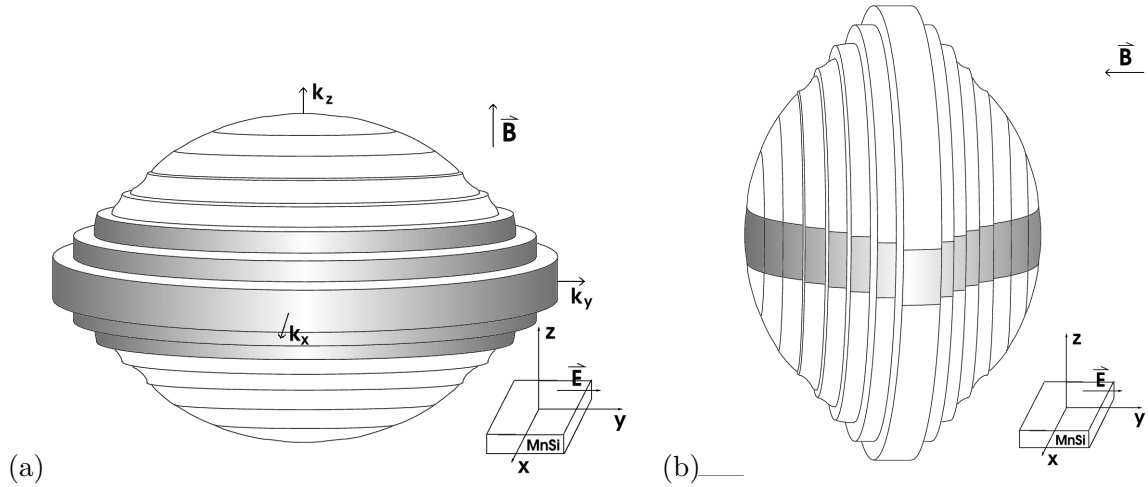

Figure 2.6.: Belt of effective electrons that participate in the anomalous Skin effect (a) for $\boldsymbol{B}$ perpendicular to the crystal surface (b) for $\boldsymbol{B}$ parallel to the crystal surface.

For an orientation of the helix perpendicular to the crystalline surface all electrons in a belt of width $\sqrt{\delta_B}$ move parallel to the surface, therefore the effective surface conductivity will not drop below $\sigma\sqrt{\delta_B}$, which leads to a skin depth of order

$$\Delta_a^{\perp} \sim \Delta_0/\delta_B^{1/4} \tag{2.55}$$

for $\Delta_a^{\parallel}/l_0 \ll \sqrt{\delta_B}$ or $\Delta_0 \ll l_0\delta_B^{3/4}$. By rotating the small external magnetic field one can directly compare the two orientations experimentally,

$$\Delta_a^{\parallel}/\Delta_a^{\perp} \sim \delta_B^{1/4}\left(\frac{l_0}{\Delta_0}\right)^{1/3}. \tag{2.56}$$

While it may be difficult to observe large ratios, a sizable qualitative effect can be expected for $\Delta_0/l_0 \lesssim \delta_B^{3/4}$. MnSi crystals can be grown with exceptionally high quality, ref. [6] reports a residual resistivity $\rho_0 \approx 0.17\,\mu\Omega$cm. For frequencies of for example 20 GHz one obtains $\Delta_0 \approx 1500$Å which is already well below the estimated [6] mean-free path, $l_0 > 5000$Å. While larger frequencies or cleaner samples ($\Delta_0/l_0 \propto \rho_0^{3/2}/\sqrt{\omega}$) may be needed to reach the regime $\Delta_0/l_0 < \delta_B^{3/4}$ where eq. (2.56) is valid, a measurable dependence on the field orientation can nonetheless be expected for the parameters used above. A more quantitative estimate would require a detailed study of the band structure.

2.5. Minibands and Damping

Finally, we want to calculate the effect of the minibands on damping in the ordered phase of MnSi.

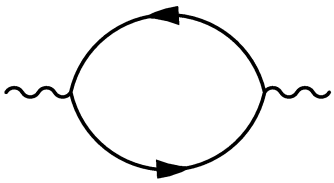

Figure 2.7.: Correction to the bosonic propagator from integrating out the fermions.

Starting point is the action

$$S = \int d^3x\, c^\dagger_\alpha(\boldsymbol{x}) \left(g_0^{-1}\right)_{\alpha\alpha'} c_{\alpha'}(\boldsymbol{x}) + q_0 \boldsymbol{S}(\boldsymbol{x}) \cdot (\nabla \times \boldsymbol{S}(\boldsymbol{x})) + J\boldsymbol{S}(\boldsymbol{x})^2 \tag{2.57}$$

where g_0 is the propagator and $\boldsymbol{S}(\boldsymbol{x}) = \sum e^{\mathrm{i}(\boldsymbol{k}-\boldsymbol{k}')\boldsymbol{x}} c^\dagger_{\boldsymbol{k}\alpha}\sigma_{\alpha\alpha'}/2c_{\boldsymbol{k}\alpha'}$ is the spin of the conduction electrons. The interaction terms can be decoupled by means of a Hubbard Stratonovich field $\boldsymbol{M}$, which leads to an action of the form

$$S = \int \frac{d^3k}{(2\pi)^3}\, \boldsymbol{M}_{\boldsymbol{k}} \frac{G(\boldsymbol{k})^{-1}}{2} \boldsymbol{M}_{-\boldsymbol{k}} + \int \frac{d^3k}{(2\pi)^3}\, \frac{d^3k'}{(2\pi)^3}\, c^\dagger_{\boldsymbol{k}\alpha} \left((g_0^{-1})_{\alpha\alpha'}\delta_{\boldsymbol{k}\boldsymbol{k}'} - \boldsymbol{M}_{\boldsymbol{k}-\boldsymbol{k}'} \frac{\sigma_{\alpha\alpha'}}{2} \right) c_{\boldsymbol{k}'\alpha'}, \tag{2.58}$$

where $(G(\boldsymbol{k}))_{ik} = J\delta_{ik} - q_0 \varepsilon_{ijk}\, k_j$.

Fluctuations of helical Goldstone modes in the ordered phase of MnSi and their effect on the electron resistivity have been discussed extensively in [17]. Our aim here is simply to calculate the effect of the belt of minibands on the dynamics of magnetic fluctuations in the ordered phase.

In order to obtain an effective theory for the fluctuating magnetization $\boldsymbol{\Psi}$ we have to integrate out the electrons in (2.58). This generates infinitely many one-loop diagrams with electrons in the internal and and an even number of bosonic fields in the external lines. This will be discussed in more detail in chapter 5. Of all these diagrams, the polarization bubble shown in Fig. 2.7 will generate corrections to the propagator of $\boldsymbol{\Psi}$, i.e. to the first integral of (2.58).

To evaluate the polarization bubble, we need to diagonalize the electron propagator and evaluate the form of the coupling to the bosonic mode. Let us therefore take a closer look at the second integral in (2.58). In the ordered phase, $\boldsymbol{M} = \boldsymbol{\Phi} + \boldsymbol{\Psi}$, where $\boldsymbol{\Phi}$ is the chiral helix (2.2),

$$\Phi_{\boldsymbol{k}} = \frac{\Phi_0}{2} \left[(\hat{\boldsymbol{n}}_1 - \mathrm{i}\hat{\boldsymbol{n}}_2)(2\pi)^3 \delta(\boldsymbol{k} + \boldsymbol{q}_0) + (\hat{\boldsymbol{n}}_1 + \mathrm{i}\hat{\boldsymbol{n}}_2)(2\pi)^3 \delta(\boldsymbol{k} - \boldsymbol{q}_0) \right]. \tag{2.59}$$

We have already seen in section 2.3 that the term that describes the coupling of the electrons to $\boldsymbol{\Phi}$ is considerably simplified by transforming to a coordinate system that is comoving with the helix, and even in the presence of spin-orbit coupling terms in the band structure of the electrons, the transformation proved to be advantageous. So once again, we transform the fields first to the rotating frame, taking $\boldsymbol{q}_0 \| \hat{\boldsymbol{z}}$:

$$c_\alpha(\boldsymbol{x}) \to \left(e^{-\mathrm{i}q_0 z \frac{\sigma_z}{2}} \right)_{\alpha\alpha'} c_{\alpha'}(\boldsymbol{x}), \quad c^\dagger_\alpha(\boldsymbol{x}) \to c^\dagger_{\alpha'}(\boldsymbol{x}) \left(e^{\mathrm{i}q_0 z \frac{\sigma_z}{2}} \right)_{\alpha'\alpha}, \quad \boldsymbol{\Psi}(\boldsymbol{x}) \to e^{\mathrm{i}q_0 z L_z} \boldsymbol{\Psi}(\boldsymbol{x}), \tag{2.60}$$

and then introduce the eigenstates $E^{\pm}_{\boldsymbol{k}}$ in which H_0 is diagonal. The only term that will be added to $H^{+/-}$ are the terms that couple the electrons to the fluctuating magnetization $\boldsymbol{\Psi}$. Introducing the complex field $\Psi^{\perp} \equiv \Psi^x + \mathrm{i}\Psi^y$, these terms take the form

$$\frac{1}{8}\int \frac{d^3k}{(2\pi)^3}\,\frac{d^3p}{(2\pi)^3}\Big[2\,d^{\dagger}_{\boldsymbol{k}+\boldsymbol{p},+}d_{\boldsymbol{p},+}(\Psi^{\perp}_{\boldsymbol{k}}+\Psi^{\perp\,*}_{\boldsymbol{k}}) - 2\,d^{\dagger}_{\boldsymbol{k}+\boldsymbol{p},-}d_{\boldsymbol{p},-}(\Psi^{\perp}_{\boldsymbol{k}}+\Psi^{\perp\,*}_{\boldsymbol{k}}) + 2d^{\dagger}_{\boldsymbol{k}+\boldsymbol{p},-}d_{\boldsymbol{p},+}(\Psi^{\perp}_{\boldsymbol{k}}-\Psi^{\perp\,*}_{\boldsymbol{k}}) - d^{\dagger}_{\boldsymbol{k}+\boldsymbol{p},+}d_{\boldsymbol{p},-}(\Psi^{\perp}_{\boldsymbol{k}}-\Psi^{\perp\,*}_{\boldsymbol{k}}) - \Psi^{z}_{\boldsymbol{k}}\left(d^{\dagger}_{\boldsymbol{k}+\boldsymbol{p},-}d_{\boldsymbol{p},+}+d^{\dagger}_{\boldsymbol{k}+\boldsymbol{p},+}d_{\boldsymbol{p},-}\right)\Big]. \quad (2.61)$$

The main contribution to the low-energy physics of the order parameter should come from coupling to electrons with the same index $(+/-)$, so we will concentrate on that contribution to the susceptibility $\Pi^{\perp}$ of $\Psi^{\perp}$. Furthermore, we will only calculate the contribution from the $+$-quasiparticles to $\Pi^{\perp}$, since it can be argued that the $-$-quasiparticles give a similar contribution. In the following calculation, we therefore set $d_{\boldsymbol{k},+} \equiv d_{\boldsymbol{k}}$.

As in previous calculations, we introduce momentum coordinates $\boldsymbol{k} = (\boldsymbol{\kappa}_{\perp}, \kappa_z, n)$ in the reduced Brillouin zone, with $k_z = k_z^0 + \kappa_z + nq_0$ and $-q_0/2 < \kappa_z < q_0/2$. For $-n_{max} \le n \le n_{max}$, with n_{max} defined in (2.30), the true energy eigenstates f are related to d by a unitary transformation U:

$$d_{\boldsymbol{\kappa}_{\perp},\kappa_z,n} = \sum_m U^{\dagger}_{nm} f_{\boldsymbol{\kappa}_{\perp},\kappa_z,m}, \qquad d^{\dagger}_{\boldsymbol{\kappa}_{\perp},\kappa_z,n} = \sum_m f^{\dagger}_{\boldsymbol{\kappa}_{\perp},\kappa_z,m} U_{mn}. \quad (2.62)$$

In this notation,

$$\int d^3k\, d^3p\, \Psi^{\perp}_{\boldsymbol{k}}\, d^{\dagger}_{\boldsymbol{k}+\boldsymbol{p}} d_{\boldsymbol{p}} \;\to\; \sum_{n_1,n_2}\int d\boldsymbol{\kappa}_{\perp}\, d\boldsymbol{q}_{\perp} \int_{-q_0/2}^{q_0/2} dq_z d\kappa_z \Psi^{\perp}_{\boldsymbol{\kappa}_{\perp},\kappa_z,n_1}\, d^{\dagger}_{\kappa_{\perp}+q_{\perp},\tilde{\kappa}_z(\kappa_z,q_z),m(n_1,n_2,\kappa_z,q_z)} d_{q_{\perp},q_z,n_2}$$

The diagram that modifies the propagator of the Goldstone modes as the electrons are integrated out is shown in Fig. 2.7. For very small external momenta of $\Pi^{\perp}$, the only coupling which is necessary is for $n_1 = 0$, and since we are only interested in the contributions from the minibands region we can demand that $0 \le n_2 \le n_{max}$. Introducing the energy eigenstates f defined previously, we obtain

$$\int d\boldsymbol{\kappa}_{\perp}\, d\boldsymbol{q}_{\perp} \int_{-q_0/2}^{q_0/2} dq_z d\kappa_z \sum_{n_2,N_1,N_2} \Psi^{\perp}_{\boldsymbol{\kappa}_{\perp},\kappa_z,0}\, U_{N_1,m(0,n_2,\kappa_z,q_z)} U^{\dagger}_{n_2,N_2} f^{\dagger}_{\kappa_{\perp}+q_{\perp},\tilde{\kappa}_z(\kappa_z,q_z),N_1} f_{q_{\perp},q_z,N_2}.$$

Finally, we can separate this into an intraband and an interband contribution by using that for $|\kappa_z + q_z| \le q_0/2$, $m(n_2,\kappa_z,q_z) = n_2$, and $\sum_{n_2} U_{N_1,n_2} U^{\dagger}_{n_2,N_2} = \delta_{N_1,N_2}$:

$$\int d\boldsymbol{\kappa}_{\perp}\, d\boldsymbol{q}_{\perp} \int_{-q_0/2}^{q_0/2} dq_z d\kappa_z \sum_{N_1,N_2} \Psi^{\perp}_{\boldsymbol{\kappa}_{\perp},\kappa_z,0} f^{\dagger}_{\kappa_{\perp}+q_{\perp},\tilde{\kappa}_z,N_1} f_{q_{\perp},q_z,N_2}$$
$$\left(\delta_{N_1,N_2}\Theta\left(\frac{q_0}{2} - |\kappa_z+q_z|\right) + A^{+}_{N_1,N_2}\Theta\left(\frac{q_0}{2} - (\kappa_z+q_z)\right) + A^{-}_{N_1,N_2}\Theta\left(\frac{q_0}{2} + \kappa_z + q_z\right)\right),$$

where

$$A^{+}_{N_1,N_2} = \sum_n U_{N_1,n+1} U^{\dagger}_{n,N_2}, \tag{2.63}$$

$$A^{-}_{N_1,N_2} = \sum_n U_{N_1,n-1} U^{\dagger}_{n,N_2}. \tag{2.64}$$

The diagram to be evaluated (at $T = 0$) is the polarization bubble

$$\Pi^{\perp}(q_\perp, q_z, \omega) = \frac{1}{16\pi} \frac{1}{(2\pi)^3} \sum_{N_1,N_2} \int d\boldsymbol{\kappa}_\perp \int_{q_0/2}^{q_0/2} d\kappa_z \left(\delta_{N_1,N_2} \Theta\left(\frac{q_0}{2} - (\kappa_z + q_z) \right) + A^{+}_{N_1,N_2} A^{-}_{N_2,N_1} \Theta\left(\kappa_z + q_z - \frac{q_0}{2} \right) \right) \frac{n_F(\xi^{N_1}_{k_\perp}) - n_F(\xi^{N_2}_{k_\perp + q_\perp})}{\xi^{N_2}_{k_\perp + q_\perp} - \xi^{N_1}_{k_\perp} + \omega}, \tag{2.65}$$

where $\xi^{N}_{k_\perp} = \frac{\kappa_\perp^2}{2m} + N\omega_0 - E_F$, with ω_0 from (2.26). For higher bands, c_1 (and as a consequence ω_0 as well) can no longer be taken to be constant but depends on $\kappa_\perp$; this dependence will be neglected. Furthermore, the bands are taken to be absolutely flat in this calculation.

A detailed evaluation of (2.65) can be found in Appendix A.4:

$$\operatorname{Re} \Pi^{\perp}(q_\perp, q_z, 0) = \frac{1}{8} \frac{1}{(2\pi)^3} \, m \, q_0 \, n_{max} \tag{2.66}$$

$$\operatorname{Im} \Pi^{\perp}(q_\perp, q_z, \omega) \sim \frac{\omega}{q_\perp} \, q_0 \, n_{max}. \tag{2.67}$$

The contribution of electrons from the miniband region to the susceptibility is now completely independent of $\boldsymbol{q}$, at least as long as the momentum dependence of ω_0 is neglected, and the dynamics induced by these electrons is proportional to the inverse of the momentum component $q_\perp$ instead of q. This comes as no surprise: in that area the Fermi surface is essentially two-dimensional, and the damping of magnons induced by coupling to the electrons is $\propto \omega/q$ for either two-dimensional or three-dimensional metals. For $\boldsymbol{q}_\perp \to 0$, damping is enhanced compared to the case of a spherical Fermi surface.

2.6. Discussion

We have found that two small relativistic effects of spin-orbit coupling in a crystal without inversion symmetry, the Dzyaloshinsky-Moriya interaction and the splitting of the Fermi surface for opposite spin, conspire to produce exponentially flat minibands in a magnetic metal. These minibands occur on a belt-shaped region of the Fermi surface where the helical wave vector $\boldsymbol{q}_0$ is parallel to the surface; electrons from the belt can no longer move parallel to $\boldsymbol{q}_0$.

Although the change to the Fermi surface is quite drastic, the minibands are difficult to observe experimentally. For a direct probing of the miniband region by means of a de-Haas–van-Alphen experiment, unrealistically clean samples would be required. The exponentially flat minibands prevent electron motion $\|\boldsymbol{q}_0$, which has to influence transport quantities such as the (residual) resistivity. Unfortunately, since electrons from that belt of width δ only have a velocity component $\|\boldsymbol{q}_0$ of order $v \sim \delta$ in the absence of minibands, where δ is the strength of spin-orbit coupling in the system, the effect can be expected to be of order $\delta^{3/2}$ and is therefore difficult to observe. However, for an experimental technique that only probes the relevant belt-shaped region on the Fermi surface, such as the anomalous skin effect, the opening of the bandgaps can be expected to leave a distinct and observable trace.

Finally, the opening of band-gaps on the Fermi surface can be expected to reduce damping of Goldstone modes for momenta parallel to the helical wave vector.

3. New Phases from a Ginzburg-Landau theory

The work presented in this chapter is motivated by the peculiar signature present in neutron scattering data in the partially ordered state of MnSi. The transition from the helically ordered phase to the partially ordered state is known to be (weakly) first order. Hysteretic behaviour can be observed when a magnetic field is used to tune across T_0 (see introduction). Among the theoretical scenarios proposed for the partially ordered state are multi-domain or emulsion-like configurations or entirely new phases. So far, experimental data cannot rule out either of these scenarios.

We start from the assumption that the partially ordered state of MnSi is indeed a thermodynamically distinct phase and, starting from the Ginzburg-Landau theory, attempt to find new phases for chiral ferromagnets. We first review the construction of a Ginzburg-Landau theory for ferromagnetic metals without inversion symmetry. We then briefly review work done by Schmalian and Turlakov concerning the stability of the helix solution in an approximation of that Ginzburg-Landau theory, and proceed to a detailled local stability analysis of the uniform helix solution in the third section. The results of this analysis motivated us to propose an extended Ginzburg-Landau theory, which exhibits a phase consisting of crystals of double-twist cylinders. This phase, which is the main result of our work, is closely related to blue phase in liquid crystals. We give a detailled presentation of the phase diagram of the extended Ginzburg-Landau theory and its consequences for MnSi in the final section of this chapter.

3.1. Ginzburg-Landau theory and the helix

In thermal equilibrium, the state of any system is the one that minimizes its free energy. In a Ginzburg-Landau theory of chiral ferromagnets, the free energy is given by the volume integral of the free energy density, which is constructed as a local function of the order parameter and its derivatives that respects the fundamental symmetries of the system. This function is expanded in powers of the order parameter, usually just far enough to guarantee thermodynamic stability. A fourth order term, for example, ensures stability against unbounded growth of the amplitude of the order parameter.

A first investigation of Ginzburg-Landau theory of magnetic systems such as the cubic metal MnSi, which lacks inversion symmetry, has been carried out by Nakanishi *et al.* and Bak and Høgh [2]. For a general chiral ferromagnet, the order parameter is the magnetization vector, and the minimal free energy density is given by

$$f(\boldsymbol{r}) = \frac{\delta}{2}(\boldsymbol{M})^2 + \frac{\alpha}{2}\sum(\nabla M_i)^2 + \gamma \boldsymbol{M}\cdot(\nabla\times\boldsymbol{M}) + u(\boldsymbol{M})^4, \tag{3.1}$$

where $\boldsymbol{M} = \boldsymbol{M}(\boldsymbol{r})$ is the position-dependent magnetization. All terms except for the third one, the so-called Dzyaloshinsky-Moriya term, are invariant under separate rotations of the magnetization and the coordinates; the Dzyaloshinsky-Moriya term is invariant under rotations in coordinate space combined with a rotation of the magnetization. This term is a consequence of the spin-orbit interaction present in systems without inversion symmetry, and since spin-orbit coupling is a relativistic effect, γ can be expected to be small.

The free energy density (3.1) is minimized by a magnetization of the form

$$\boldsymbol{M}(\boldsymbol{r}) = \Phi_0(\hat{\boldsymbol{n}}_1 \cos(\boldsymbol{q}_0\boldsymbol{r}) + \hat{\boldsymbol{n}}_2 \sin(\boldsymbol{q}_0\boldsymbol{r})), \tag{3.2}$$

where $\hat{\boldsymbol{n}}_1 \perp \hat{\boldsymbol{n}}_2 \perp \boldsymbol{q}_0$ are three perpendicular vectors (the spiral is right-handed for $\gamma < 0$) and $|\boldsymbol{q}_0| = q_0$. The values of Φ_0 and q_0 can be determined by inserting (3.2) into (3.1):

$$\begin{aligned} f_{\text{helix}}(\boldsymbol{r}) &= \frac{\alpha}{2}\left(q_0 - \frac{\gamma}{\alpha}\right)^2 \Phi_0^2 + \left(\frac{\delta}{2} - \frac{\gamma^2}{2\alpha}\right)\Phi_0^2 + u\Phi_0^4 \\ &= -\frac{1}{4u}\left(\frac{\delta}{2} - \frac{\gamma^2}{2\alpha}\right)^2 \end{aligned} \tag{3.3}$$

where the equilibrium values $q_0 = \gamma/\alpha$ and $\Phi_0^2 = -(\delta/2 - \gamma^2/(2\alpha))/(2u)$, which minimize $f_{\text{helix}}(\boldsymbol{r})$, have been used in to obtain the result in the second line. The helical order breaks down for $\delta > \gamma^2/\alpha$.

The space group of MnSi is $P2_13$ whose point group T contains cyclic permutations of $\hat{\boldsymbol{x}}$,$\hat{\boldsymbol{y}}$ and $\hat{\boldsymbol{z}}$, rotations by π around the coordinate axes and combinations thereof. Additional terms to this order in the Ginzburg-Landau expansion, which are not rotationally invariant but allowed by the space group $P2_13$, are e.g. [2, 18]

$$\begin{aligned} \frac{1}{2}B_2\left[(\partial_x M_x)^2 + (\partial_y M_y)^2 + (\partial_z M_z)^2\right] + B_3\left((\partial_x^2\boldsymbol{M})^2 + (\partial_y^2\boldsymbol{M})^2 + (\partial_z^2\boldsymbol{M})^2\right) \\ + D(M_x^4 + M_y^4 + M_z^4). \end{aligned} \tag{3.4}$$

These terms contribute to the free energy density to fourth order in spin-orbit coupling [18]. They serve to orient the helix in the (111)-direction (and symmetry-equivalent directions) for $B_3 > 0$ and in the (100)-direction for $B_3 < 0$, where the former is the case for MnSi. These terms will not be considered in the stability analysis of the following chapter, since we want our analysis to be applicable to chiral ferromagnets in general.

3.2. Stability of the helix solution

How can the helix solution be destabilized? That this is in principle possible has been shown recently by Schmalian and Turlakov [20], who investigated fluctuations around the helical state of a chiral ferromagnet. We briefly review their results before we proceed to present the results of a more extended stability analysis of (3.1).

3.2.1. Quantum phase transitions of magnetic rotons

Schmalian and Turlakov show [20] that close to $T = 0$, fluctuations can induce a quantum phase transition of magnetic rotons. Starting from an action of the form 3.1, where the components of the fluctuating magnetization $\boldsymbol{M}$ are coupled by the spin-orbit coupling term, they diagonalize the propagator matrix for the magnetization and integrate out the two modes with the highest masses to obtain an effective action for the remaining mode, which has the form

$$S = \frac{1}{2}\int_{\boldsymbol{q}} \left(|\omega|^{2/z} + r_0 + (|\boldsymbol{q}| - 1)^2\right)\phi_{\boldsymbol{q}}\phi_{-\boldsymbol{q}} + \int_{\boldsymbol{q}_1,\boldsymbol{q}_2,\boldsymbol{q}_3} \frac{\lambda_{\boldsymbol{q}_1,\boldsymbol{q}_2,\boldsymbol{q}_3,\boldsymbol{q}_4}}{4}\phi_{\boldsymbol{q}_1}\phi_{\boldsymbol{q}_2}\phi_{\boldsymbol{q}_3}\phi_{\boldsymbol{q}_4}. \tag{3.5}$$

in momentum space. A term for the dynamics of the mode has been added, and momenta, frequencies, the mass and the coupling constant have been rescaled to obtain an action in terms of dimensionless variables.

The momentum dependence of λ for an effective low energy action can then be derived completely analogously to a renormalisation group treatment of interacting fermions [33]. In the low-energy limit, the interaction predominantly couples fluctuations with momenta equal to the helical wave vector: $|\boldsymbol{q}_i| = |\boldsymbol{q}_0|$. Momentum conservation then restricts a momentum dependent interaction $\lambda_{\boldsymbol{q}_1,\boldsymbol{q}_2,\boldsymbol{q}_3,\boldsymbol{q}_4}|_{|\boldsymbol{q}_i|=|\boldsymbol{q}_0|}$ to have two components V and F: either there are two pairs of collinear vectors, in which case $V(\boldsymbol{q}_1 \cdot \boldsymbol{q}_2) \equiv \lambda_{-\boldsymbol{q}_1,\boldsymbol{q}_1,-\boldsymbol{q}_2,\boldsymbol{q}_2}$ only depends on the angle between the vectors, or two pairs of vectors form the same angle each, in which case $F \equiv \lambda_{\boldsymbol{q}_1,\boldsymbol{q}_2,\boldsymbol{q}_3,\boldsymbol{q}_4}|_{\boldsymbol{q}_1\cdot\boldsymbol{q}_2=\boldsymbol{q}_3\cdot\boldsymbol{q}_4}$. In the latter case, λ depends not only on the angle between $\boldsymbol{q}_1$ and $\boldsymbol{q}_2$, but also on the angle between the planes containing $\boldsymbol{q}_1, \boldsymbol{q}_2$ and $\boldsymbol{q}_3, \boldsymbol{q}_4$, respectively. However, V and F renormalize differently: while F does not get any first-order corrections, V flows to infinity for $T \to 0$. In the case of fermions, this corresponds to the BCS-instability: a system of interacting fermions always becomes superconducting for $T \to 0$. At finite temperatures above the superconducting transition temperature, F can dominate V, in which case one obtains a Fermi liquid. Schmalian and Turlakov only consider an interaction of the V-type: they proceed to approximate λ in the low-energy theory by $\lambda \equiv \lambda_{\boldsymbol{q}_1,-\boldsymbol{q}_1,\boldsymbol{q}_2,-\boldsymbol{q}_2} = V((\boldsymbol{q}_1 \cdot \boldsymbol{q}_2)^2)$, presumably assuming that temperatures are sufficiently low for this term to dominate.

The helix solution has the form $\phi_{\text{Helix}}(\boldsymbol{q}) = \phi_0\left[\delta^3(\boldsymbol{q} - \boldsymbol{q}_0) + \delta^3(\boldsymbol{q} + \boldsymbol{q}_0)\right]$ in this effective theory, where $\phi_0^2 = -r_0/(4(\Delta L)^3 V(\boldsymbol{q}_0 \cdot \boldsymbol{q}_0))$ minimizes the free energy density. The energy density takes the value $-3r_0^2/(16V(\boldsymbol{q}_0 \cdot \boldsymbol{q}_0))$ in this phase. With this form of the interaction, a local stability analysis for the helix solution leads to the condition

$$\phi_0^2\,(2V(\boldsymbol{k} \cdot \boldsymbol{q}_0) - V(\boldsymbol{q}_0 \cdot \boldsymbol{q}_0)) > 0 \tag{3.6}$$

for the helix to be stable against fluctuations with a wave vector $\boldsymbol{k}$. With the help of a renormalization group analysis for $\overline{V} \equiv V(\boldsymbol{k} \cdot \boldsymbol{q}_0)$ (for generic directions $\boldsymbol{k}$) and $V_\parallel \equiv V(\boldsymbol{q}_0 \cdot \boldsymbol{q}_0)$, Schmalian and Turlakov then identify two possible scenarios for the transition from the helically ordered to the disordered phase: If $\overline{V}$ dominates, the transition is 2nd order and anisotropies dominate the low-energy physics. As a consequence, the direction of the helix is fixed. If, on the other hand, $V_\parallel \to -\infty$ in the RG-flow, then the transition is a fluctuation induced first-order transition. In this case, the possible directions of the helix are degenerate in the vicinity of the transition, and the mean-field solution is dubbed a magnetic roton.

Schmalian and Turlakov conclude their analysis by predicting a $\sqrt{\omega}$-dependence of the conductivity in the disordered high-temperature phase. To sum up, this analysis only investigates the nature of the phase transition coming from the disordered phase; no predictions about the nature of the partially ordered state are made.

3.2.2. A new phase for magnetic rotons?

The results of [20] allow to interpret the T_0-line as the continuation of the (2nd order) phase boundary between the helical and the disordered phase, but the theory does not make any predictions concerning the first-order transition between the helical phase and the partially ordered phase.

It would be tempting to guess – as we did – $\phi_{\text{Sphere}}(\boldsymbol{q}) = \tilde{\phi}_0\,\delta(|\boldsymbol{q}| - q_0)$ as another mean-field solution to (3.5) with $\lambda_{\boldsymbol{q}_1,\boldsymbol{q}_2,\boldsymbol{q}_3,\boldsymbol{q}_4} = \lambda_{\boldsymbol{q}_1,-\boldsymbol{q}_1,\boldsymbol{q}_2,-\boldsymbol{q}_2}$ as above. This configuration solves the mean-field equation and has an energy density of $-r_0^2/(4V_\perp)$ per length, which has to be compared to the energy density $-3r_0^2/(16V_\parallel)$ per volume of the helix. The appealing property of this solution is that in momentum space, its intensity is uniformly distributed over a sphere, which matches experimental data to a first approximation.

The solution ϕ_{Sphere} is extended in momentum space and therefore has to be localized in real space; it simply means that if such a solution were to occur in a real system, it would have to be in the form of a crystalline structure. However, ϕ_{Sphere} only solves the mean-field equation of the theory (3.5) with $\lambda \equiv \lambda_{\boldsymbol{q}_1,-\boldsymbol{q}_1,\boldsymbol{q}_2,-\boldsymbol{q}_2} = V((\boldsymbol{q}_1\cdot\boldsymbol{q}_2)^2)$. As soon as the interaction develops a component of the form F, for example, ϕ_{Sphere} is simply no longer a solution of the mean-field equations.

3.2.3. Stability analysis of the Ginzburg-Landau expansion

We then asked the question whether the helix solution can be destabilized by additional terms in the Ginzburg-Landau expansion (3.1). This is more general than the analysis done by Schmalian and Turlakov, since their effective action (3.5) with $\lambda_{\boldsymbol{q}_1,\boldsymbol{q}_2,\boldsymbol{q}_3,\boldsymbol{q}_4} \equiv \lambda_{\boldsymbol{q}_1,-\boldsymbol{q}_1,\boldsymbol{q}_2,-\boldsymbol{q}_2}$ is only valid at very low temperatures and close to the phase transition line T_c: two of the three modes of the fluctuating magnetization have been integrated out, and the interaction can take a different form for $T \neq 0$.

Our aim was to find a theory that exhibits a helix solution in some parameter regime, which becomes unstable for a suitable choice of parameters and leaves open the possibility for a second phase, which is thermodynamically distinct from the helical phase. We perform the analysis at finite temperature, assuming that all modes with Matsubara frequencies ω_n, $n \neq 0$, are massive and can be integrated out.

We introduced a field $\boldsymbol{\Phi}$ for fluctuations around the helix by setting

$$\boldsymbol{M}(\boldsymbol{r}) = \Phi_0(\hat{\boldsymbol{n}}_1\cos(\boldsymbol{q}_0\boldsymbol{r}) + \hat{\boldsymbol{n}}_2\sin(\boldsymbol{q}_0\boldsymbol{r})) + \boldsymbol{\Phi}(\boldsymbol{r}), \qquad \hat{\boldsymbol{n}}_1 \perp \hat{\boldsymbol{n}}_2 \perp \hat{\boldsymbol{q}}_0. \tag{3.7}$$

We replaced the interaction term in (3.1), neglecting quantum fluctuations for the moment (no dynamics for $\boldsymbol{\Phi}$), derived the Gaussian theory for $\boldsymbol{\Phi}$ and checked the propagator of $\boldsymbol{\Phi}$ for

interaction	result of stability analysis
$\int_{\boldsymbol{x},\boldsymbol{x}'} \lvert\boldsymbol{M}_{\boldsymbol{x}}\rvert^2 \lvert\boldsymbol{M}_{\boldsymbol{x}'}\rvert^2$	stable
$\int_{\boldsymbol{x},\boldsymbol{x}'} ((\sum_i \nabla M_{i,\boldsymbol{x}})^2 \lvert\boldsymbol{M}_{\boldsymbol{x}'}\rvert^2 + \boldsymbol{x} \leftrightarrow \boldsymbol{x}')$	stable
$\int_{\boldsymbol{x},\boldsymbol{x}'} (\sum_i \nabla M_{i,\boldsymbol{x}})^2 (\sum_j \nabla M_{j,\boldsymbol{x}'})^2$	stable
$\int_{\boldsymbol{x},\boldsymbol{x}'} ((\boldsymbol{M}_{\boldsymbol{x}} \cdot (\nabla \times \boldsymbol{M}_{\boldsymbol{x}})) \lvert\boldsymbol{M}_{\boldsymbol{x}'}\rvert^2 + \boldsymbol{x} \leftrightarrow \boldsymbol{x}')$	stable
$\int_{\boldsymbol{x},\boldsymbol{x}'} (\boldsymbol{M}_{\boldsymbol{x}} \cdot (\nabla \times \boldsymbol{M}_{\boldsymbol{x}}))(\boldsymbol{M}_{\boldsymbol{x}'} \cdot (\nabla \times \boldsymbol{M}_{\boldsymbol{x}'}))$	stable
$\int_{\boldsymbol{x},\boldsymbol{x}'} f(\boldsymbol{x}-\boldsymbol{x}') \lvert\boldsymbol{M}_{\boldsymbol{x}}\rvert^2 \lvert\boldsymbol{M}_{\boldsymbol{x}'}\rvert^2$	stable for f Gaussian
$\int_{\boldsymbol{k},\boldsymbol{k}'} f(\boldsymbol{k}-\boldsymbol{k}')(\boldsymbol{M}_{-\boldsymbol{k}} \cdot \boldsymbol{M}_{\boldsymbol{k}})(\boldsymbol{M}_{\boldsymbol{k}'} \cdot \boldsymbol{M}_{-\boldsymbol{k}'})$	*unstable* for f narrow Gaussian
$\int_{\boldsymbol{k},\boldsymbol{k}',\boldsymbol{q}} g(\boldsymbol{q}) f(\boldsymbol{k}-\boldsymbol{k}')(\boldsymbol{M}_{\boldsymbol{k}} \cdot \boldsymbol{M}_{-\boldsymbol{k}+\boldsymbol{q}})(\boldsymbol{M}_{\boldsymbol{k}'} \cdot \boldsymbol{M}_{-\boldsymbol{k}'-\boldsymbol{q}})$	*unstable* for f (broad) Gaussian, depends only weakly on shape of g; unstable even for $g = 1$.
$\int_{\boldsymbol{x}} \lvert\boldsymbol{M}_{\boldsymbol{x}}\rvert^4$	stable
$\int_{\boldsymbol{x}} (\boldsymbol{M}_{\boldsymbol{x}} \nabla \boldsymbol{M}_{\boldsymbol{x}})^2$	*unstable*

Table 3.1.: Results of the stability analysis for various interaction terms in a Ginzburg-Landau theory for chiral ferromagnets.

negative eigenvalues while varying the interaction strength; the prefactor of the interaction was taken to be negative.

The practical difficulty in deriving an action for fluctuations around a helical phase arises from the fact that a helix solution breaks translational invariance along its direction of propagation $\boldsymbol{q}_0$: $\boldsymbol{\Phi}(\boldsymbol{q})$ is coupled to $\boldsymbol{\Phi}(\boldsymbol{q} + 2\boldsymbol{q}_0)$ in momentum space[1]. This introduces a Brillouin zone of width $2\boldsymbol{q}_0$ and a bandstructure in the propagator of the fluctuations. Since a residual symmetry remains, as discussed in the previous chapter, this difficulty could in principle be avoided by chosing a rotating reference frame. In a rotating reference frame, however, interaction terms would assume a considerably more complicated form. This convinced us to keep the stationary reference frame, in which we diagonalized the propagator for the fluctuations numerically and then looked for negative eigenvalues.

We did not restrict our stability analysis to local terms but also included non-local interactions. In the limit of infinite-range interactions (first block of table 3.1), calculations simplify considerably: the helix solution no longer couples modes of momenta that differ by $2\boldsymbol{q}_0$.

The results are summed up in table 3.1. Above everything else, the stability analysis shows that the helix configuration is surprisingly stable. Among the interaction terms that destabilize a helical magnetization, the third of the long-range interaction terms of Table 3.1 seems to be the least artificial. Setting $g(\boldsymbol{q}) = 1$ and transforming back to real space we obtain an interaction of the form

$$\int_{\boldsymbol{x},\boldsymbol{y}} (\boldsymbol{M}_{\boldsymbol{x}+\boldsymbol{y}} \cdot \boldsymbol{M}_{\boldsymbol{x}})(\boldsymbol{M}_{\boldsymbol{x}-\boldsymbol{y}} \cdot \boldsymbol{M}_{\boldsymbol{x}}) \tilde{f}(y). \tag{3.8}$$

[1] In the first chapter, the interaction term coupled two fermionic fields to one bosonic field; the helix therefore induced transitions between electrons whose wavevectors differed by $\boldsymbol{q}_0$. In this case, the interaction term consists of four bosonic fields. When two of these are replaced by their mean-field value, the wavevectors of the remaining fluctuating fields differ by $2\boldsymbol{q}_0$.

Doing a Taylor expansion of this then leads to a local interaction of the form

$$\int_{\boldsymbol{y}} \tilde{f}(y) \int_{\boldsymbol{x}} |\boldsymbol{M}_{\boldsymbol{x}}|^4 - \left(\int_{\boldsymbol{y}} \sum_i \tilde{f}(y)\, y_i^2 \right) \left(\int_{\boldsymbol{x}} \sum_i (\boldsymbol{M}_{\boldsymbol{x}} \partial_i \boldsymbol{M}_{\boldsymbol{x}})^2 \right), \tag{3.9}$$

and indeed, a *local* term of the form

$$\xi \int_{\boldsymbol{x}} (\boldsymbol{M}_{\boldsymbol{x}} \nabla \boldsymbol{M}_{\boldsymbol{x}})^2 \tag{3.10}$$

also turned out to destabilize the helix for sufficiently negative ξ. The term (3.10) can be rewritten as $(\nabla \boldsymbol{M}^2)^2$, it acts solely on the magnitude of the magnetization, not on its direction. Therefore, it gives no contribution to the free energy if the magnetization takes the helical form (3.2), which has a uniform amplitude. If a term such as (3.10) is present in the Ginzburg-Landau theory, then a sufficiently large negative prefactor ξ will cause the uniform helix solution to be locally unstable in favour of a phase with a magnetization that varies strongly in magnitude. If the free energy is dominated by (3.10), then it is unclear whether there are remnants of helical order in such a new phase at all.

Finally, if a term of the form is included in the Ginzburg-Landau theory with a negative prefactor, then higher order terms have to be included to ensure the stability of mean-field solutions against unbound gradients and an unbound amplitude.

3.3. Blue Phases

A term such as (3.10), which favours amplitude fluctuations of the magnetization, will eventually drive the helical solution (3.2) to local instability. Before that happens, however, an intermediate phase for negative but not overly large ξ can be found, where a peculiar kind of helical order remains. This phase, which is sandwiched between the helical phase and the isotropic phase, can be reached from the helical phase in a first-order phase transition and bears a strong semblance to blue phases in liquid crystals. In the following, we will therefore briefly discuss what is known about blue phases in cholesteric liquid crystals, before examining in detail the corresponding phase in chiral ferromagnets.

3.3.1. Blue Phases in cholesteric liquid crystals

Just as chiral ferromagnets, chiral liquid crystals exhibit helical order in a region of their phase diagram. At the transition out of this helical phase, however, helical order is not completely destroyed. Instead, the liquid crystals enter novel phases, the so-called blue phases (they obtained their name from their visual appearance), which still harbour some kind of helical order.

Blue phases in liquid crystals have been studied extensively, both theoretically and experimentally. In this section, the salient points are mentioned briefly, closely following the review by Wright and Mermin [34]. We will adopt their notation for this subsection. Three different kinds of blue phases, which will be denoted by BPI, BPII and BPIII, have been observed in

chiral liquid crystals. Of these three phases, two can be described theoretically as crystalline states, as will be discussed below. The provenance of BPIII is an unsolved theoretical problem even today.

Starting point for a theoretical description of the blue phases is a Ginzburg-Landau theory for the order parameter, which in the case of (uniaxial) chiral liquid crystals is a director field. This director field is usually represented as a tensor, but in the case of a uniaxial chiral liquid crystal it can be written as

$$\chi_{ij} = \frac{1}{\sqrt{6}}\lambda(3\, n_i n_j - \delta_{ij}), \tag{3.11}$$

where both the director $\boldsymbol{n}(\boldsymbol{r})$ and the overall amplitude $\lambda(\boldsymbol{r})$ are allowed to be position-dependent. In the one-constant approximation, where temperature, length scales, the order parameter and the free-energy density have been rescaled in such a way that the gradient part of the free enery density only depends on the parameter κ and the bulk part only depends on t, the free energy density takes the form (see e.g. [35] for a detailled calculation)

$$\varphi = \varphi_{\text{bulk}} + \varphi_{\text{grad}}, \tag{3.12}$$

$$\varphi_{\text{bulk}} = t\lambda^2 - \lambda^3 + \lambda^4, \tag{3.13}$$

$$\begin{aligned}\varphi_{\text{grad}} = \kappa^2 \Bigg(& (\nabla\lambda)^2 + \frac{1}{4}\lambda^2 + 3\lambda^2 \nabla\cdot[(\boldsymbol{n}\cdot\nabla)\boldsymbol{n} - \boldsymbol{n}(\nabla\cdot\boldsymbol{n})] \\ & + 3\lambda^2 \left\{ (\nabla\cdot\boldsymbol{n})^2 + [\boldsymbol{n}\times(\nabla\times\boldsymbol{n})]^2 + \left(\boldsymbol{n}\cdot\nabla\times\boldsymbol{n} + \frac{1}{2}\right)^2 \right\} \Bigg)\end{aligned} \tag{3.14}$$

$$= \kappa^2 \left[(\nabla\lambda)^2 - \frac{1}{2}\lambda^2 + 3\lambda^2 \left(\nabla_i n_j + \frac{1}{2}\varepsilon_{ijk} n_k \right)^2 \right] \tag{3.15}$$

In the case of a fixed amplitude λ_0, it can be shown that the helical phase with

$$\boldsymbol{n}^{\text{helix}}(\boldsymbol{r}) = \hat{\boldsymbol{x}}\cos(q_0 z) + \hat{\boldsymbol{y}}\sin(q_0 z), \tag{3.16}$$

where $q_0 = 1/2$, gives the unique minimum to the Frank free energy, i.e. the last three terms of (3.14). Since the first and the third term of (3.14) are zero for (3.16) (the first term is zero because the helix has a constant amplitude and the third term constitutes a boundary term), the helix solution minimizes the gradient part of the free energy density if a uniform amplitude is required. More precisely, for the helix solution one obtains $\varphi_{\text{grad}}^{\text{helix}} = -(1/4)\kappa^2\lambda_0^2$, which is however above the lower bound $-(1/2)\kappa^2\lambda_0^2$ for (3.15). It is impossible to find a director field for which this lower bound is reached everywhere in space, i.e. which satisfies

$$\nabla_i n_j + \frac{1}{2}\varepsilon_{ijk} n_k = 0. \tag{3.17}$$

This condition can, however, be fulfilled along lines with a director field of the form (in cylindrical coordinates)

$$\boldsymbol{n}^{\text{dt}}(\boldsymbol{r}) = \hat{\boldsymbol{z}}\cos(qr) - \hat{\boldsymbol{\phi}}\sin(qr), \tag{3.18}$$

for which the gradient energy density is given by

$$\left(\nabla_i (n^{\mathrm{dt}})_j + \frac{1}{2}\varepsilon_{ijk}(n^{\mathrm{dt}})_k\right)^2 = \frac{1}{4} + \left(\frac{\sin qr}{r}\right)^2 - \frac{\sin(2\,qr)}{2\,r}. \tag{3.19}$$

How can the director field (3.18) be visualized? In the helical phase (3.16), the sheets of constant $\boldsymbol{n}$ form planes perpendicular to the axis of the helix. For a director field of the form (3.18), these planes of constant $\boldsymbol{n}$ are wrapped around the axis $r = 0$ and form cylinders of "double-twist" regions – double-twist because the director field twists about two directions instead of one single direction in the case of the helix. For the configuration (3.18), the axis of the cylinder points into the $\boldsymbol{z}$-direction.

The equilibrium value of the double-twist wave vector is $q = 1/2$, which is equal to the wave vector of the helix (3.16) in the helical phase.

As can be seen from (3.19), the gradient free energy grows as r gets larger; one double twist cylinder has to have a finite extension along r in order to be energetically favourable. The maximal extension R, above which the cylinder has a higher energy density than the helix solution (3.16), can be estimated by comparing $\varphi_{\mathrm{grad}}^{\mathrm{helix}}$ to $\varphi_{\mathrm{grad}}^{\mathrm{dt}}$ for the same, fixed amplitude:

$$\varphi_{\mathrm{grad}}^{\mathrm{dt}} - \varphi_{\mathrm{grad}}^{\mathrm{helix}} \propto \int_0^R dr\, r \left[\left(\frac{\sin\frac{r}{2}}{\frac{r}{2}}\right)^2 - 2\,\frac{\sin r}{r}\right], \tag{3.20}$$

where the equilibrium value for the double-twist wave vector, $q = 1/2$, has been inserted. For this difference to be negative, R cannot exceed 3.58, which corresponds to a maximal angle of 102.56° that the director field is allowed to twist outwards. The difference is maximal for $R = 2.331$, i.e. an angle of 66.8°. This should, however, not be taken too literally, since a uniform amplitude λ and a constant wave vector q have been assumed in the calculation. When these conditions are relaxed, the maximum allowed value R_{max} for R can change. Also, R_{max} is influenced by the terms in φ_{bulk} or higher order terms which could be added to φ_{bulk}. A consequence of (3.20) is that the amplitude λ is necessarily nonuniform in a double-twist cylinder phase, and double-twist cylinders can have a lower energy than the helix solution only if the energy gain of (3.19) close to the axis of the cylinder is not offset by the energy cost of a nonuniform amplitude λ.

Necessary conditions for the existence of a single stable double-twist cylinder are therefore (i) that its amplitude vanishes at large distances from the axis and (ii) that the isotropic phase has lower free energy than the helical phase. If these are fulfilled, then there is a region just above the isotropic-helical transition where *single* double-twist cylinders of variable amplitude can become stable, as Hornreich, Kugler and Shtrikman [36] showed.

A stable phase that contains double-twist structures is obviously going to consist of many such cylinders. One possibility is that these are well separated and embedded in the isotropic phase. Such an arrangement is still a possible candidate for BPIII. When cylinders are tightly packed in periodic structures, the amplitude λ only has to drop to zero at isolated points or lines, if at all. Such structures reduce the bulk free-energy cost further and are indeed believed to lie at the heart of BPI and BPII.

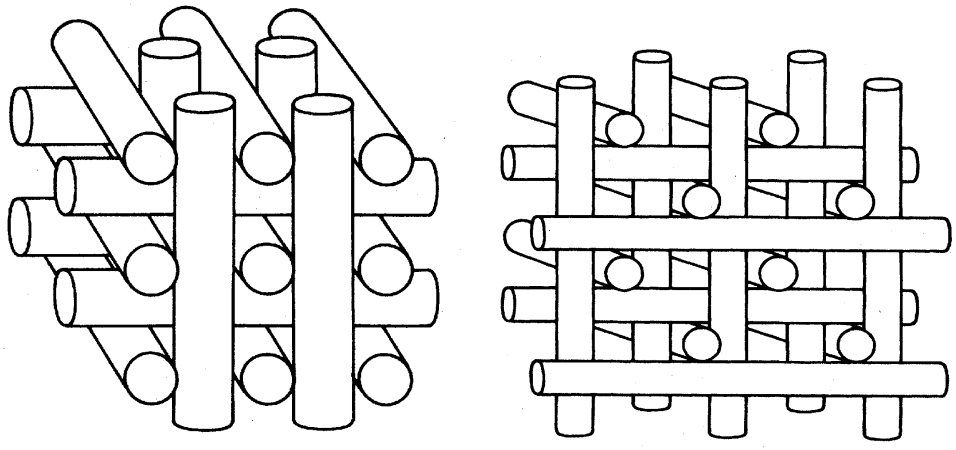

(a) (b)

Figure 3.1.: The arrangement of double-twist cylinders in (a) the O^2- structure and (b) the O^8-structure. In both cases, the director twists out to 45° at the cylinder surfaces. There are other possibilities for realizing an O^8-crystal with double-twist cylinders, see Fig. 3.2. Taken from [34].

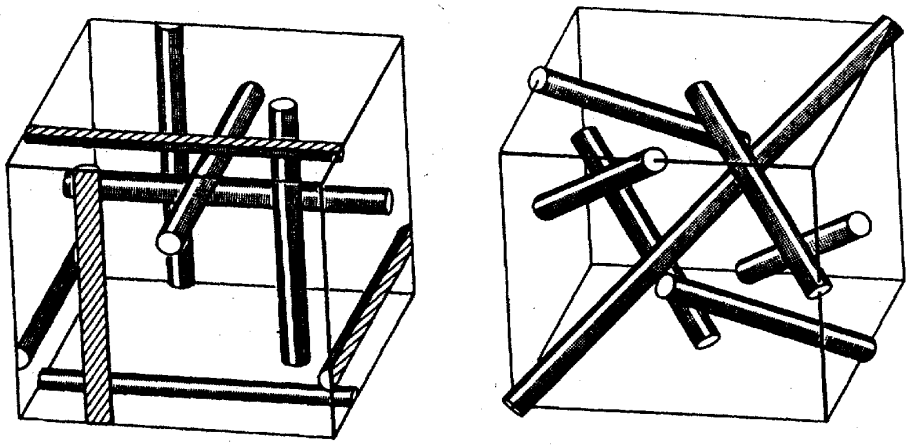

Figure 3.2.: Wigner-Seitz cell for the two ways of realizing O^8 symmetry with director field double-twist cylinders. To make the structure apparent, cylinders are not shown to touch. The director twists out to 45° at the cylinder surface in the O^{8-}-configuration on the left side and out to 54.7° in the O^{8+}-configuration on the right side. Taken from [34].

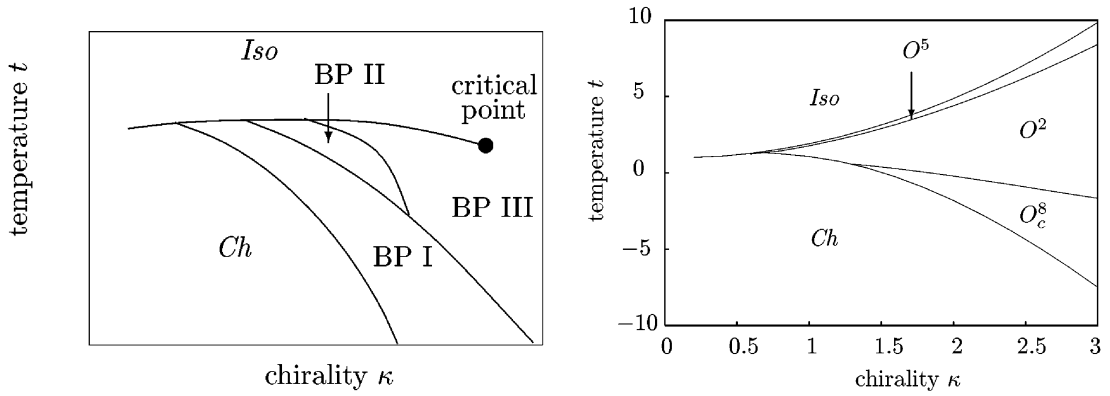

Figure 3.3.: (a) Sketch of the experimental phase diagram of chiral nematic liquid crystals; κ and t are in arbitrary units. (b) Phase diagram calculated form Landau-Ginzburg-de Gennes theory of Grebel et al. Taken from [34].

The possible structures are restricted by two basic requirements: First, the director fields at points where cylinders touch have to be aligned. Second, the director can only turn as much as roughly 100° from the cylinder axis. Two of the three-dimensional crystal structures that meet these requirements, those belonging to the cubic space groups O^8 and O^2, are shown in Fig. 3.1 and Fig. 3.2. In calculations there is a very narrow region where a third structure, O^5, has the lowest free energy, see Fig. 3.3. This structure has however not been found in any real materials.

In order to determine which of these structures are realized, if at all, in liquid crystals, Meiboom, Sammon and Berreman [37] carried out detailed calculations of the intensities of the first few Bragg reflections, which were then compared to the experiments. For O^2- and O^8-symmetric crystals with lattice constants a_1 and a_2, the first Bragg reflexes are situated at (110) and (111), respectively. Calculations based on an analysis of the free energy density (3.12) predict a phase diagram as shown in 3.3. The transitions from helical phase to BPI, BPII, BPIII and finally to the isotropic phase are all first order, with possible exception of the BPIII-to-isotropic transition.

While the theory of BPI and BPII seems to be well established, the origin of BPIII remains, so far, unclear. That some kind of BPIII might be relevant to the partially ordered state of MnSi has first been suggested in [7]; Tewari et al. have tried to establish a closer connection [21], as will be mentioned briefly below. Here, we just give a brief summary of the known experimental facts on BPIII followed by a list of possible theoretical scenarios, both taken from [38]:

- BPIII selectively reflects circularly polarized light but exhibits only one Bragg peak [39] and not the higher order ones that would point to a crystal structure.
- The heat capacity shows a small peak at the transition between BPIII and BPI/II but a much more pronounced peak between BPIII and the isotropic phase. The structure of BPIII therefore seems to be closer to BPII than to the isotropic phase.

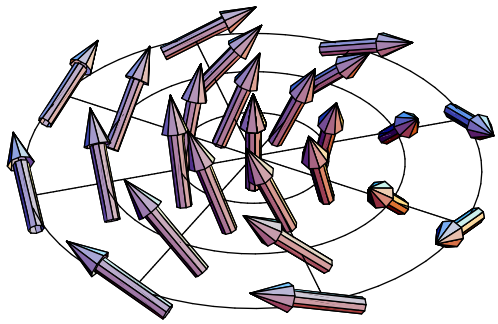

Figure 3.4.: Double-twist structure in a plane perpendicular to the cylinder axis. Sheets of constant magnetization are wrapped around the cylinder axis.

- At high chirality, the transition line between BPIII and the isotropic phase ends at a critical point, similar to a liquid-gas transition.
- Electron microscopy images of freeze-fractured samples of BPIII exhibit a filamentary structure [40].

Theoretical proposals concerning the nature of BPIII that have not yet been ruled out by experiments include [38]

- the *double twist model* of Hornreich et al. [36] which assumes BPIII to be a spaghetti-like tangle of double-twist cylinders, e.g. from melted lattices of double-twist cylinders,
- the *cubic domain model* wich assumes that BPIII retains a locally cubic structure but only over very short correlated regions,
- the *icosahedral model*, i.e. a structure with reciprocal lattice vectors derived from the vertices of a regular icosahedron,
- the *liquid gas transition model*: Lubensky and Stark provide a phenomenological model of the BPIII-isotropic critical point in which $\langle(\nabla \times \boldsymbol{\chi}) \cdot \boldsymbol{\chi}\rangle$ is viewed as the new, pseudoscalar order parameter, where $\boldsymbol{\chi}$ is the order parameter tensor. This model predicts that the isotropic-to-BPIII transition is in the same universality class (3D Ising) as the liquid-gas transition. Tewari *et al.* have argued [21] that this model should be relevant to the T_0-line in the phase diagram of MnSi (see Figs. 1.1 and 1.2).

3.3.2. Chiral Ferromagnets

The free energy density of chiral liquid crystals is quite similar to that of chiral ferromagnets in principle, as can be seen below. Both materials can be tuned into a phase with helical ordering. Because of these similarities, one could be led to assume that the blue phases of liquid crystals also have their counterpart in chiral ferromagnets. However, there are a few obstacles in the case of chiral ferromagnets, as Wright and Mermin have shown [34].

The part bilinear in magnetization of the free energy density (3.1) can be rewritten by setting $\boldsymbol{M} = \lambda\,\hat{\boldsymbol{n}}$, where λ is the amplitude and $\hat{\boldsymbol{n}}$ is the direction of the magnetization $\boldsymbol{M}$:

$$\begin{aligned} f &= \frac{\alpha}{2}\lambda^2\left(\nabla_i n_j + \frac{\gamma}{\alpha}\varepsilon_{ijk}n_k\right)^2 - \frac{\gamma^2}{\alpha}\lambda^2 + \frac{\alpha}{2}(\nabla\lambda)^2 \\ &= \kappa^2\left[(\nabla\lambda)^2 - \frac{\lambda^2}{2} + \lambda^2\left(\nabla_i n_j + \frac{1}{2}\varepsilon_{ijk}n_k\right)^2\right] \end{aligned} \tag{3.21}$$

where we have rescaled the coordinates, $\boldsymbol{x} \to \alpha/(2\gamma)\boldsymbol{x}$, in the second line and set $\kappa^2 = 2\gamma^2/\alpha$ in order to facilitate the comparison with (3.15). When comparing (3.21) to (3.15), we see that the two differ in the relative weights assigned to $(\nabla_i n_j + \frac{1}{2}\varepsilon_{ijk}n_k)^2$, which favours double-twist, and $(\nabla\lambda)^2$, which penalizes amplitude fluctuations. Wright and Mermin [34] argue that this makes amplitude fluctuations just too costly for blue phases to appear in chiral ferromagnets. They demonstrate this by using the identity

$$\begin{aligned} &\kappa_1^2\lambda^2(\nabla_i n_j + \frac{1}{2}\varepsilon_{ijk}n_k)^2 + \kappa_2^2(\nabla\lambda)^2 = \\ &\kappa_1^2\lambda^2\left\{(\nabla\cdot\boldsymbol{n} + \boldsymbol{n}\cdot\nabla\lambda/\lambda)^2 + (\boldsymbol{n}\cdot\nabla\times\boldsymbol{n} + \frac{1}{2})^2 + [\boldsymbol{n}\times(\nabla\times\boldsymbol{n}) + \nabla\lambda - \boldsymbol{n}(\boldsymbol{n}\cdot\nabla)\lambda]^2\right\} \\ &\qquad + \frac{1}{4}\kappa_1^2\lambda^2 + (\kappa_2^2 - \kappa_1^2)(\nabla\lambda)^2 \end{aligned} \tag{3.22}$$

where

$$\begin{array}{ll} \kappa_2^2 = \kappa_1^2 & \text{for a ferromagnet,} \\ \kappa_2^2 = \frac{1}{3}\kappa_1^2 & \text{for a nematic liquid crystal.} \end{array} \tag{3.23}$$

The term in the large curly brackets is the sum of three square and therefore nonnegative terms. All of these vanish in the helical phase for a uniform amplitude λ. While the coefficient of $(\nabla\lambda)^2$ is negative for the chiral liquid crystal, it is exactly zero for the chiral ferromagnet. As a consequence, the helix minimizes the gradient as well as the bulk free energy in the case of the chiral ferromagnet. It should be pointed out, however, that the double-twist cylinders are still locally favourable for the chiral ferromagnet. For crystalline configurations of double-twist cylinders where the amplitude is non-zero everywhere, blue phases might still be possible for a system described by the free energy density given above.

The analysis performed by Wright and Mermin [34] pertains to the free energy density (3.21), but the results do not necessarily have to hold true if higher order terms are taken into account. And indeed, since it is precisely the role of the additional term (3.10) to make amplitude fluctuations less costly, it comes as no surprise that there is a parameter range for ξ where (3.10) can stabilize extended configurations composed of double-twist cylinders, as we will show below.

The free energy density that will be investigated in subsequent sections is of the form

$$f(\boldsymbol{r}) = \frac{\delta}{2}\boldsymbol{M}^2 + \frac{\alpha}{2}\sum(\nabla M_i)^2 + \gamma\boldsymbol{M}\cdot(\nabla\times\boldsymbol{M}) + u\boldsymbol{M}^4 + \xi(\boldsymbol{M}\nabla\boldsymbol{M})^2 + \eta\,h_i(\boldsymbol{M}), \tag{3.24}$$

where $\xi < 0$, $\eta > 0$ and $h_i(\boldsymbol{M})$ is a term containing k powers of $\boldsymbol{M}$ and l derivatives ($k > 4$, $l \geq 2$), which is used to stabilize solutions against an unbounded magnetization

and oscillations thereof. Possible choices are for example $h_1(\boldsymbol{M}) = (\boldsymbol{M}\nabla\boldsymbol{M})^2 \sum(\nabla M_i)^2$, $h_2(\boldsymbol{M}) = (\boldsymbol{M}\nabla\boldsymbol{M})^4$ and $h_3(\boldsymbol{M}) = \boldsymbol{M}^2(\boldsymbol{M}\nabla\boldsymbol{M})^2$.

While the free energy density formally depends on 6 parameters, three of these can be set to one by a suitable rescaling of coordinates, the magnetization and the free energy F: setting $\boldsymbol{r} \to r_0\boldsymbol{r}$, $\boldsymbol{M} \to M_0\boldsymbol{M}$ and $\tilde{f} = f/F_0$, (3.24) reads

$$\begin{aligned}\tilde{f}(\boldsymbol{r}) &= \frac{uM_0^4}{F_0}\Bigg(\frac{\delta}{2uM_0^2}\boldsymbol{M}^2 + \frac{\alpha}{2uM_0^2r_0^2}\sum(\nabla M_i)^2 + \frac{\gamma}{uM_0^2r_0}\boldsymbol{M}\cdot(\nabla\times\boldsymbol{M}) + \boldsymbol{M}^4 \\ &\quad + \frac{\xi}{u\,r_0^2}(\boldsymbol{M}\nabla\boldsymbol{M})^2 + \frac{\eta M_0^{k-4}}{u\,r_0^l}\,h_i(M_0\boldsymbol{M})\Bigg) \\ &= \tilde{\delta}\boldsymbol{M}^2 + \sum(\nabla M_i)^2 + \boldsymbol{M}\cdot(\nabla\times\boldsymbol{M}) + \boldsymbol{M}^4 + \tilde{\xi}(\boldsymbol{M}\nabla\boldsymbol{M})^2 + \tilde{\eta}\,h_i(\boldsymbol{M}),\end{aligned} \tag{3.25}$$

where the following values for the parameters r_0, M_0 and F_0 were chosen so as to set the prefactors of the second, third and fourth term to one,

$$M_0^2 = \frac{2\gamma^2}{u\,\alpha}, \tag{3.26}$$

$$r_0 = \frac{\gamma}{uM_0^2} = \frac{\alpha}{2\gamma}, \tag{3.27}$$

$$F_0 = uM_0^4 = \frac{4\gamma^4}{u\,\alpha^2}, \tag{3.28}$$

and the new parameters

$$\tilde{\delta} = \delta\frac{1}{2uM_0^2} = \delta\frac{\alpha}{4\gamma^2} \tag{3.29}$$

$$\tilde{\xi} = \xi\frac{1}{u\,r_0^2} = \xi\frac{4\gamma^2}{u\,\alpha^2} \tag{3.30}$$

$$\tilde{\eta} = \eta\frac{M_0^{k-4}}{u\,r_0^l} = \eta\frac{1}{u}\left(\frac{2\gamma}{\alpha}\right)^l\left(\frac{2\gamma^2}{u\,\alpha}\right)^{\frac{k-4}{2}} \tag{3.31}$$

have been introduced. This is *not* the parameter region which is to be expected for MnSi. Since the Dzaloshinsky-Moriya term is of relativistic origin, its prefactor should be at least an order of magnitude smaller than the other prefactors, and especially in MnSi, $|\boldsymbol{q}_0| = \gamma/\alpha$ has been experimentally determined to be very small.

The energy density $\tilde{f}_{\text{Helix}}$ of the helical phase of (3.25) has a quadratic dependence on $\tilde{\delta}$,

$$\tilde{f}_{\text{Helix}} = -\frac{1}{4}\left(\frac{1}{4} - \tilde{\delta}\right)^2, \tag{3.32}$$

which places the phase boundary to the isotropic phase at $\tilde{\delta} = 1/4$ in the absence of other phases.

For the free energy density (3.25) we have found stable structures of single double-twist cylinders as well as two-dimensional and three-dimensional crystals of cylinders.

3.3.3. Single Double-Twist Cylinders

As a first step we will explore stable configurations consisting of a single double-twist cylinder at the transition from the helical to the isotropic phase. At this transition, the energy of the helical phase is equal to the energy of the isotropic phase, i.e. exactly zero. If a single double-twist cylinder can already be shown to have negative energy, then we can expect the formation of a whole network of these structures, which will be the subject of the following sections.

We make the following ansatz for the magnetization (in cylindrical coordinates):

$$\boldsymbol{M}^{\mathrm{dt}} = \hat{\boldsymbol{\theta}}\lambda(r)\sin(qr) - \hat{\boldsymbol{z}}\lambda(r)\cos(qr), \tag{3.33}$$

where q is the double twist wave vector and where we allow for a position-dependent amplitude $\lambda(r)$. Inserting this into (3.25) leads to the following expression for the free energy density f_{cyl} of one cylinder (with $\lambda \equiv \lambda(r)$ and $\lambda' \equiv \partial_r\lambda(r)$):

$$f_{\mathrm{cyl}} = \frac{2}{R^2}\int_0^R dr\, r\Bigg(\left((\lambda')^2 + q^2\lambda^2 + \frac{\lambda^2}{r^2}\sin^2(qr)\right) - \left(q\lambda^2 + \lambda^2\frac{\sin(2qr)}{2r}\right) + \tilde{\delta}\lambda^2 \\ + \lambda^4 + \tilde{\xi}\,\lambda^2(\lambda')^2 + \tilde{\eta}\,h_i(\lambda,\lambda')\Bigg) \tag{3.34}$$

with

$$h_1(\lambda) = \lambda^2\left((\lambda')^2 + q^2\lambda^2 + \frac{\lambda^2}{r^2}\sin^2(qr)\right)(\lambda')^2, \tag{3.35}$$

$$h_2(\lambda) = \lambda^4(\lambda')^4, \tag{3.36}$$

$$h_3(\lambda) = \lambda^4(\lambda')^2. \tag{3.37}$$

If λ is taken to be constant, then the minimum value for the double-twist wave vector q is $q = 1/2$ just as in the helix case.

We set $\tilde{\delta} = 1/4$ so that the amplitude of the uniform helix is exactly zero, i.e. the system is at the phase boundary of the helix solution in the absence of other phases. We discretized $\lambda(r)$ in the interval $0 \le r \le R$ and minimized f_{cyl} with respect to R, $\lambda(r)$ and q with the boundary condition that $\lambda(R) = 0$. Results for the stabilizing terms h_1 and h_2 are shown in figures 3.5 and 3.6. The term h_3 does not lead to stable single double-twist cylinders: the amplitude starts oscillating as soon as it drops below a certain level.

Let us go back to (3.24) for a moment and try to estimate for which parameter range of α, γ and u in a real system single double-twist cylinders are most likely to form. As can be seen from the parameters used in figures 3.5 and 3.6 and from their behaviour under rescaling (3.29, 3.30, 3.31), these double-twist cylinders can occur in a parameter region of (3.24) where γ and α are of comparable size (i.e. where q is large, which favours terms with gradients) and u is small, which favours a large amplitude of the magnetization. In this parameter region, only small prefactors ξ and η are required to stabilize double-twist cylinders. As a rule of thumb, a small γ penalizes terms with many gradients, and a large u penalizes terms in the Ginzburg Landau expansion of higher power in the magnetization. Taking these considerations into account, the stabilizing term $h_1(\boldsymbol{M})$ will be used exclusively in the following calculations.

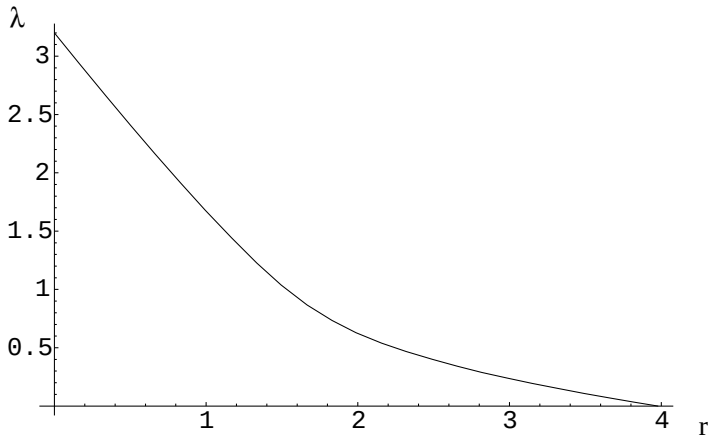

Figure 3.5.: Amplitude function for the stabilizing term h_1 and the following choice of parameters: $\alpha = 1$, $\delta = 0.25$, $\gamma = -1$, $u = 1$, $\xi = -6.5$ and $\eta = 5$. The free energy density takes the value $f_{\mathrm{cyl}} = -0.0043$, and the width of the cylinder and the wave vector are $R = 3.98$ and $q/q_0 = 0.38$, respectively.

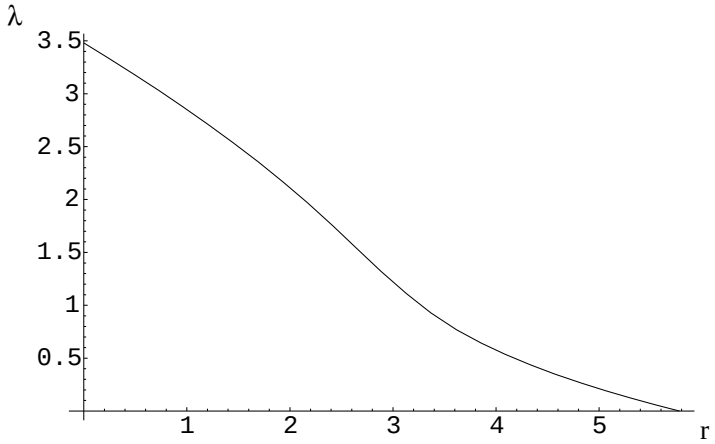

Figure 3.6.: Amplitude function for the stabilizing term h_2 and the following choice of parameters: $\alpha = 1$, $\delta = 0.25$ $\gamma = -1$, $u = 1$, $\xi = -15$ and $\eta = 7500$. The free energy density takes the value $f_{\mathrm{cyl}} = -0.00056$, and the width of the cylinder and the wave vector are $R = 5.78$ and $q/q_0 = 0.78$, respectively.

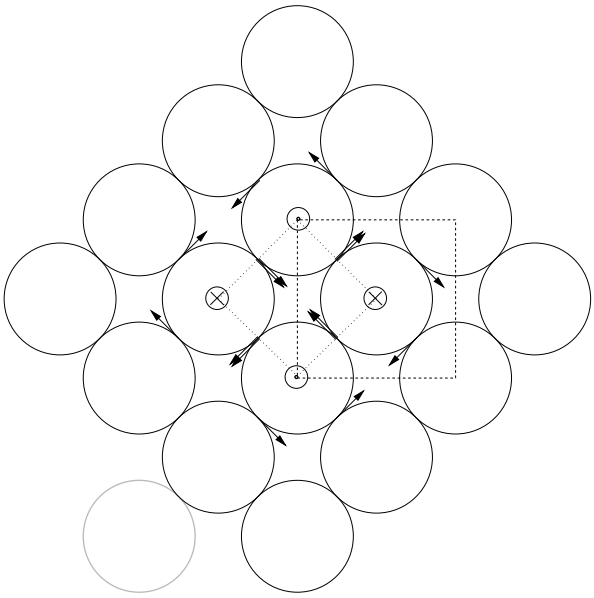

Figure 3.7.: Square lattice of double-twist cylinders. Shown are the magnetization at some of the points where cylinders touch as well as on the cylinder axes, the Wigner-Seitz cell (dashed line) and the area of integration (dotted line) in the arrangement of cylinders used for numerical calculations. The next closest cylinder not included in the numerical calculation is shown in grey.

This analysis could be generalized further by considering a magnetization

$$\boldsymbol{M}^{\mathrm{dt},2} = \hat{\boldsymbol{\theta}}\lambda(r)\sin(\omega(r)) - \hat{\boldsymbol{z}}\lambda(r)\cos(\omega(r)), \tag{3.38}$$

i.e. by allowing not only the amplitude but also the wave-vector to be position-dependent. For chiral liquid crystals, an analysis of this type showed $\omega(r)$ to be approximately linear [36]. We have not carried out such a calculation here, since the analyis of single double-twist cylinders is of limited interest: A phase based on double twist cylinders will necessarily contain a whole network of these structures, arranged so as to fill up space with the favourable double-twist configuration as efficiently as possible. In these configurations, the magnetization only has to drop to zero on lines or at points, if at all. It was important, however, to verify that single cylinders can exist because it justifies the variational ansatz for the amplitude function that we will adopt in the next sections and it gives credence to the assumption that stable double twist regions can exist.

3.3.4. Crystal of Double Twist Cylinders I: Square Lattice

Compared to a director order parameter, the possibilities to form a crystal made up of vector-order parameter double twist cylinders are greatly reduced: it is now vectors and not directors that have to match where two cylinders touch; their orientation matters.

As far as two-dimensional lattices are concerned, the most likely candidate is the square lattice as shown in Fig. 3.7. This kind of structure is also what one would expect locally in the double-twist model for BPIII, see section 3.3.1.

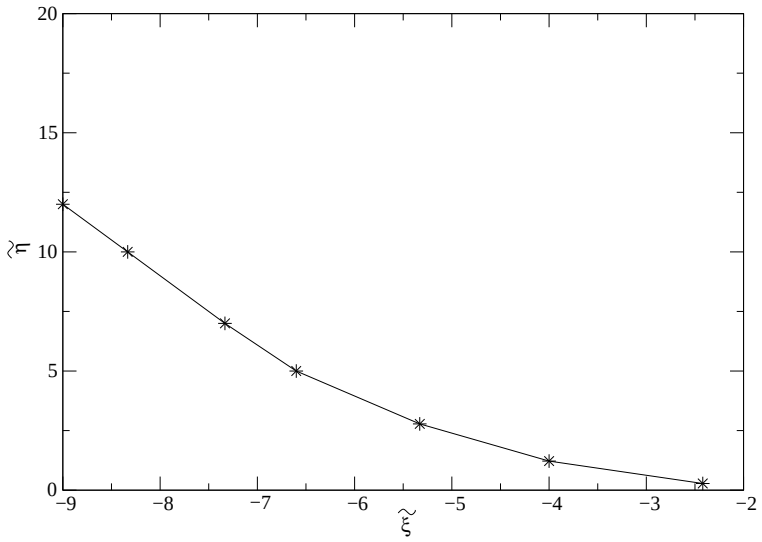

Figure 3.8.: Approximate region of stability of the square lattice of double-twist cylinders in the $\tilde{\xi}$-$\tilde{\eta}$-plane for $\tilde{\delta} = 0.25$. The line shown indicates where the free energy density has a value of -0.003 ± 0.00025. Below that line, the configuration of double twist cylinders is stable for $\tilde{\eta} > 0$.

Since the magnetization of neighbouring cylinders has to match at the point where they touch, the director has to twist out to 90° at the cylinder surface, which means that two neighbouring cylinders touch at distances $R = \pi/(2q)$ from the respective cylinder cores, where q is the double-twist wave vector. The size a of the unit cell is therefore given by $a = 2\sqrt{2}R = \sqrt{2}\pi/q$. This is illustrated in Fig. 3.7.

We calculated the free energy density of a square lattice of double twist cylinders for various values of δ and ξ, using an amplitude function $\lambda(r)$ of the form

$$\lambda(r) = y_0 \cdot (r - r_0)e^{-r/r_1}\Theta(r - r_0). \tag{3.39}$$

This choice is motivated by the fact that this amplitude function is closely mimics the form obtained from minimization for a single double-twist cylinder. Of the four parameters y_0, r_0, r_1 and q, we keep r_0 fixed. We want to ensures that no other cylinders except for those considered in the numerical calculation extend into the (part of the) Wigner-Seitz cell over which we integrate, see Fig. 3.7. To fulfill this requirement, we could have chosen r_0 to be as large as $4R = 2\pi/q$. To facilitate comparison with results from the next section, we set it to $\sqrt{5}\pi/(2q)$ instead. We then minimized the free energy density for the configuration shown in Fig. 3.7 with respect to the parameters y_0, r_1 and q.

As we will see in the next section, the square lattice of double-twist cylinders is not the configuration with the lowest free energy density that can be constructed out of double-twist cylinders. A disadvantage of the square lattice of double-twist cylinders is that the

magnetization in the center of the Wigner-Seitz cell has to drop to zero for symmetry reasons, i.e. the magnetization is zero on lines. This can be avoided by stacking the double-twist cylinders in three-dimensional configurations, which is the topic of the next subsection.

In a first step, we set the parameter $\tilde{\delta}$ equal to 0.25, i.e. at the phase boundary of the helix phase in the absence of other phases. The free energy density (3.25) then only depends on the parameters $\tilde{\xi}$ and $\tilde{\eta}$. We determined the boundaries of the region of stability of the square lattice within the variational ansatz (3.40), the result is shown in Fig. 3.8. This ansatz is likely to underestimate the extent of the stability region at the boundary to the isotropic phase, i.e. for large values of $\tilde{\xi}$ if $\tilde{\eta}$ is fixed.

We then kept $\tilde{\eta}$ fixed and calculated the free energy density for various $\tilde{\delta}$ and $\tilde{\xi}$. The results are presented in table B.1 in Appendix B, where the results for the variational parameters y_0, r_1 and q are given in addition to the value of the free energy density. Within our variational ansatz, the square lattice is not the configuration with the lowest free energy density. A configuration with an even lower value of the free energy density will be presented in section 3.3.5.

Finally, what is the signature of the square lattice of double-twist cylinders that can be expected in neutron scattering experiments? The lowest order Bragg reflexes should occur at wave vectors $2\pi/a = \sqrt{2}q$; higher order reflexes are situated at $2\sqrt{2}\pi/a = 2q$, $4\pi/a = 2\sqrt{2}q$ and so on.

3.3.5. Crystal of Double Twist Cylinders II: Cubic Lattice

There are strong experimental indications (see for example [37]) that the BPI and BPII in liquid crystals consist of O^{8-}- and O^2-crystals of double twist cylinders respectively. Structures for a director order parameter, however, do not automatically lead to admissible structures when the order parameter is a vector. The crystals of double twist cylinders that are the building blocks of BPI and BPII are believed to be realized with order parameter configurations that contain π-disclinations [41, 37, 42], i.e. order parameter configurations where the director field rotates by 180° along a closed path enclosing the topological defect. A π-disclination arises from a configuration of three cylinders as shown on the left hand side of Fig. 3.9. These π-disclinations, which appear to be ubiquitous for liquid crystal blue phases, are too expensive energetically for a vector order parameter: they necessitate the introduction of singular planes across which the directions of the arrows reverse.

Of the cubic lattices considered for double-twist cylinders in liquid crystals, the configuration shown in Fig. 3.1 (b) can be replicated with double twist cylinders that only form right-hand corners, and, as a consequence, is a candidate for a cubic phase of double-twist cylinders in chiral ferromagnets.

The symmetry transformations that leave this structure invariant are cyclic permutations of the axes and a translation by $a/2$ along all axes combined with time reversal (i.e. $\boldsymbol{M} \to -\boldsymbol{M}$).

Where cylinders touch, the magnetization has to form an angle of 45° with the axis of each cylinder, which means that neighbouring cylinders touch at a distance of $R = \pi/(4q)$ from the respective cylinder axes. The size of the unit cell is then $a = 8R = 2\pi/q$.

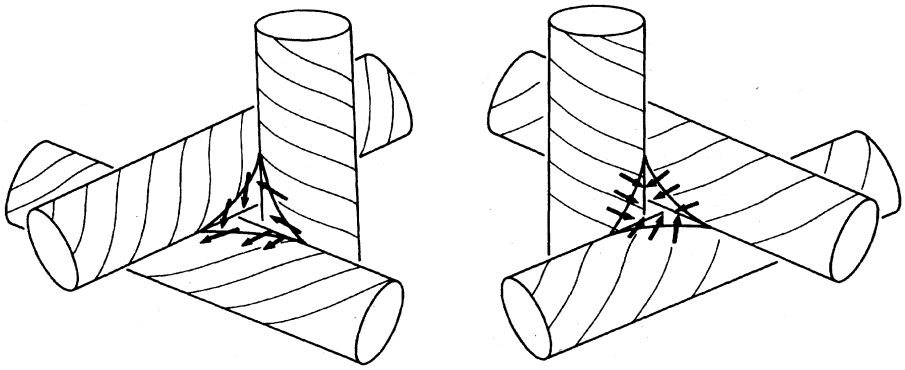

Figure 3.9.: Left hand side: cylinders arranged in such a way that magnetization does not match at all of the three points where the cylinders touch; a π-defect is enclosed by the cylinders. The energy cost of such a configuration is prohibitive for chiral ferromagnets. Right hand side: the magnetization matches at all points where cylinders touch; this configuration can be realized in chiral ferromagnets. Taken from [43].

We checked numerically that in this structure the magnetization only vanishes at the points $a\left(\frac{1}{8},\frac{5}{8},\frac{3}{8}\right)$ and $a\left(\frac{3}{8},\frac{3}{8},\frac{3}{8}\right)$ and symmetry-equivalent points in the unit cell.

As in the case of the square lattice, we used the stabilizing term $h_1(\boldsymbol{M})$ and employed the following ansatz for the amplitude $\lambda(r)$:

$$\lambda(r) = y_0 \cdot (r - r_0)e^{-r/r_1}\Theta(r - r_0). \tag{3.40}$$

We arranged 24 cylinders in a configuration sketched in Fig. 3.10. For each plane, only crossections with radius R of the cylinders whose axis is perpendicular to that plane are shown. We then set $r_0 = \sqrt{5}\pi/2q$ to make certain that no other cylinder further away extends into the central Wigner-Seitz-cell over which we integrate; the extension of the amplitude of one cylinder away from the cylinder axis is now controlled by the parameter r_1 only.

As in the case of the square lattice, we started by determining the region of stability for the cubic lattice of double twist cylinders as a function of $\tilde{\xi}$ and $\tilde{\eta}$ and for $\tilde{\delta} = 0.25$. The result is shown in Fig. 3.11.

Then we set $\tilde{\eta} = 5.375$, 1.0 and 0.05 and calculated the respective free energy densities as a function of $\tilde{\delta}$ and $\tilde{\xi}$. This is more likely to be relevant for experiments, since the parameter $\tilde{\eta}$ is probably less susceptible to changes of temperature and/or pressure than $\tilde{\delta}$ and $\tilde{\eta}$. We determined the phase boundary between the helical phase and the cubic crystal of double-twist cylinders, which are shown in Figs 3.12, 3.13 and 3.14. The results for the free energy density and the values of the variational parameters are given in tables B.2, B.4 and B.6 in Chapter B of the Appendix. Of all the variational parameters, it is most interesting to track the change of q/q_0 as shown in Figs B.2, B.4 and B.6 in Chapter B of the Appendix: this ratio of the double-twist to the helical wave vector is around one as the phase boundary between the helical and the cubic crystal phases is approached but drops significantly close to the boundary to the isotropic phase.

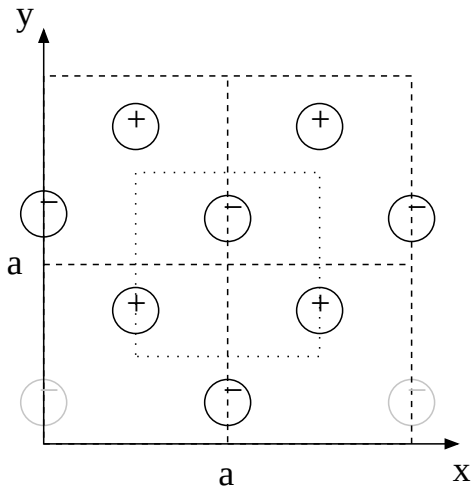

Figure 3.10.: Arrangement of the 24 cylinders. Shown are the crossections of the cylinders with axes parallel to the z-axis. The sign indicates the orientation of the magnetization on the cylinder axis. Because of invariance w.r.t. cyclic rotations of the axes, the corresponding diagrams for the z-x- and the y-z-plane are identical to the one above. We integrate over the area enclosed by the dotted line. The next closest cylinders to this area are shaded in grey.

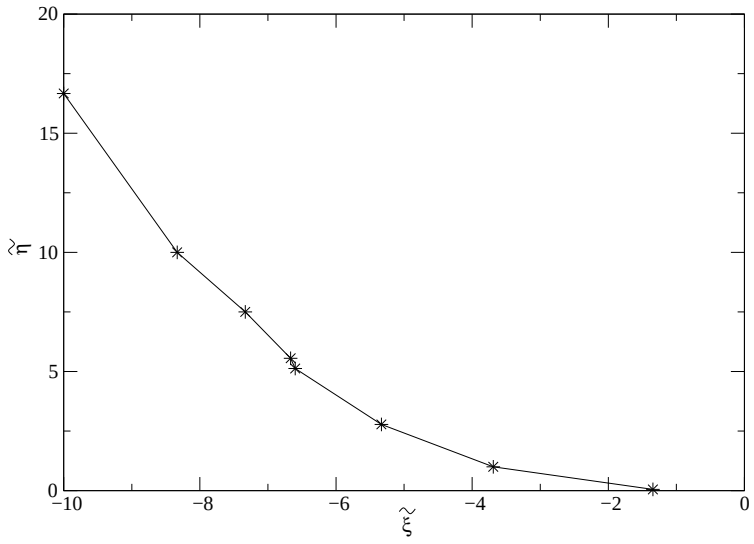

Figure 3.11.: Approximate region of stability of the cubic crystal of double-twist cylinders in the $\tilde{\xi}$-$\tilde{\eta}$-plane for $\tilde{\delta} = 0.25$. The line shown indicates where the free energy density has a value of -0.003 ± 0.00025, it is therefore below the transition line to the isotropic phase. Below that line, the configuration of double twist cylinders is stable for $\tilde{\eta} > 0$.

Interestingly enough, for certain values of $\tilde{\xi}$ and $\tilde{\delta}$, stable crystalline configurations exist at small positive energies: the transition from the cubic crystal to the isotropic phase is probably a weak first order transition. This leaves open the possibility that low energy excitations at finite temperature assume crystalline form, even though the ground state of the system consists of the isotropic phase.

In neutron scattering experiments, the elastic scattering cross-section $(d\sigma/d\Omega)_{el}$ at a wave vector $\boldsymbol{\kappa}$ is related to the Fourier transform of the magnetization in the following way [44]:

$$\left(\frac{d\sigma}{d\Omega}\right)_{el} \propto |\hat{\boldsymbol{\kappa}} \times (\boldsymbol{M}(\boldsymbol{\kappa}) \times \hat{\boldsymbol{\kappa}})|^2, \quad \boldsymbol{M}(\boldsymbol{\kappa}) = \int_{\text{W.–S. cell}} d\boldsymbol{r}\, \mathrm{e}^{-\mathrm{i}\boldsymbol{\kappa}\boldsymbol{r}} \boldsymbol{M}(\boldsymbol{r}), \tag{3.41}$$

where $\hat{\boldsymbol{\kappa}}$ is the unit vector in $\boldsymbol{\kappa}$-direction. For symmetry reasons, the axes of the cubic crystal of double-twist cylinders can be expected to be aligned with the axes of the crystal structure of MnSi. The lowest-order nonzero Bragg reflections are the $\langle 100 \rangle$-reflections at a wavelength of a, where a is the lattice constant. This corresponds to a magnitude of $2\pi/a = q$ in reciprocal space. The intensities of the higher order Bragg peaks of the cubic crystal depend on the specific values of the variational parameters but can be expected to be only a few percent of the intensity of the $\langle 100 \rangle$-reflection.

Is this the only three-dimensional configuration that can be contructed from cylindrical double-twist regions? For liquid crystals, it has been shown explicitly by Hornreich and Shtrikman [41] that the O^{8-} configuration can in principle be constructed without introducing π-disclinations, which makes it a candidate for a three-dimensional cubic lattice for chiral ferromagnets. If a true O^{8-}-crystal, which is essentially a bcc lattice, can be realized with a vector order parameter, then the lowest order Bragg reflexes should lie at $\langle 110 \rangle$. The construction of this structure is, however, rather involved and therefore left for future projects.

3.3.6. Phase Diagram

After having rescaled the free energy density, the coordinates and the magnetization, the free energy density (3.25) still depends on three independent parameters. A complete phase diagram as a function of these parameters is computationally expensive; instead we computed phase diagrams as a function of two parameters, setting the third to a constant value.

For all points in the phase diagram that we checked, the cubic crystal of double-twist cylinders had a lower free energy density than the square lattice. It is not at all obvious why that should be the case, since a number of qualitative differences exist between the two configurations: (1) In the square lattice of double-twist cylinders the magnetization has to drop to zero on lines in the system and not only at points, as it is the case for the arrangement with cubic symmetry. (2) In the square lattice, the magnetization rotates outwards as far as 90° from the center before cylinders touch, compared to 45° in the case of the cubic lattice, and (3) the fraction of the volume filled by the favourable double-twist regions is larger in the case of the square lattice than for the cubic crystal.

Interestingly enough, for some parameters we obtained stable crystalline structures at positive energies, which could exist as low-energy excitations well above the transition temperature to the isotropic phase.

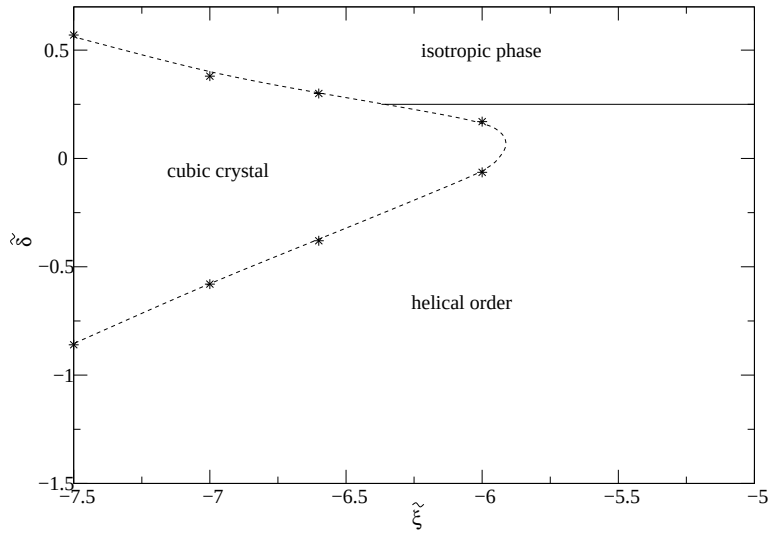

Figure 3.12.: Phase diagram in the $\tilde{\delta}$-$\tilde{\xi}$-plane for $\tilde{\eta} = 5.375$. The dashed line interpolates between the values listed in Table B.3.

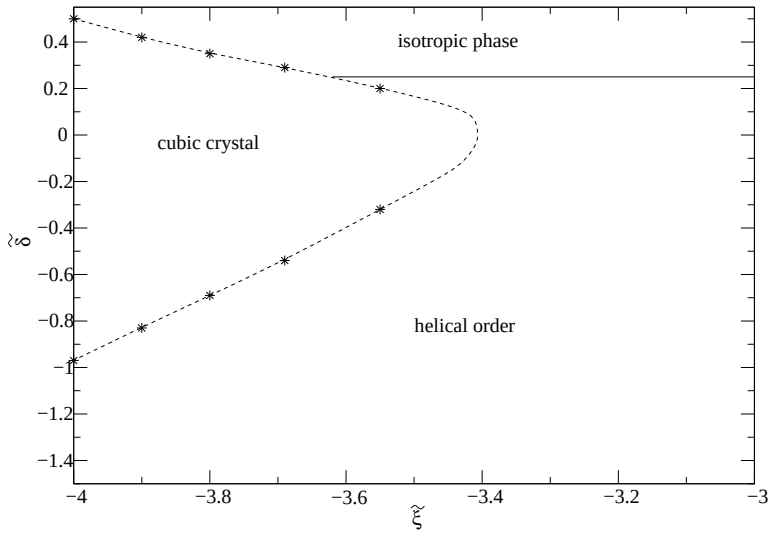

Figure 3.13.: Phase diagram in the $\tilde{\delta}$-$\tilde{\xi}$-plane for $\tilde{\eta} = 1.0$. The dashed line, which delimits the phase boundary of the cubic crystal phase, interpolates between the values listed in Table B.5.

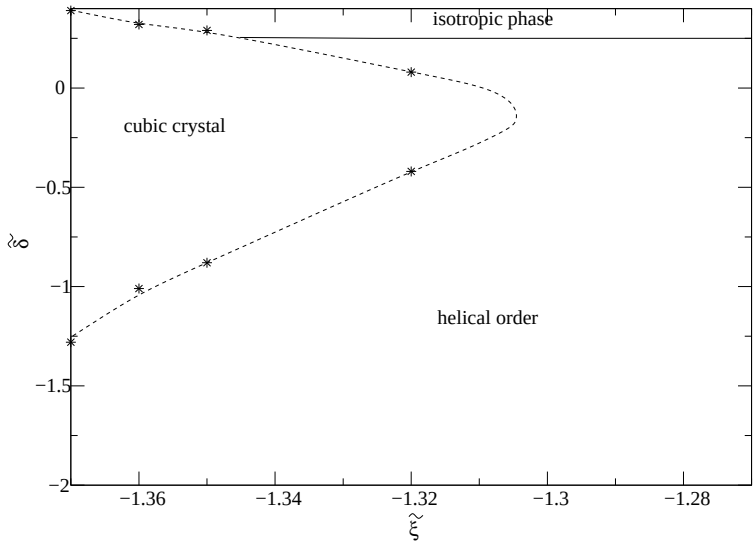

Figure 3.14.: Phase diagram in the $\tilde{\delta}$-$\tilde{\xi}$-plane for $\tilde{\eta} = 0.05$. The dashed line interpolates between the values listed in Table B.7.

Finally, the results for the free energy density obviously underestimate the extent of the "blue phase" at the border to the helical phase, but it also overestimates the extent of this phase for large ξ: at some point, amplitude fluctuations completely dominate the free energy and destroy any remnants of helical order. However, this is not captured by our variational ansatz. For a more realistic phase diagram, Monte-Carlo calculations are required.

3.3.7. Blue Phases and MnSi

Are configurations of double-twist cylinders likely to be in any way related to the partially ordered phase of MnSi? In other words, how well does this scenario compare to existing experimental data?

There are several aspects that need to be considered: (i) What are the values of ξ and η for the values of α, γ and u that are typical for MnSi? (ii) What are the thermodynamic signatures of the transition from the crystalline to the isotropic phase? And finally, (iii) how well can double-twist cylinders explain the pattern seen in neutron scattering experiments?

The first of these three issues can be addressed simultaneously for all three configurations of double-twist cylinders (single cylinder, square lattice and cubic lattice) discussed in this chapter. Since the ratio of γ and α (and with it the helical wave vector) is small in MnSi, a very low interaction u and comparatively large values of ξ and η would be needed to make double twist structures possible. While this regime might be unrealistic, there are indications that the prefactors of the quadratic and higher order terms in a Ginzburg-Landau expansion might have unusual values in MnSi: although the magnetic moment is about $0.4\mu_B$ per Mn atom

and therefore quite large for itinerant ferromagnets, the phase transition to the ferromagnetic phase (with a helical modulation) occurs at T_c =30K, which is considerably lower than the typical transition temperatures of a few hundred K in metals. From a comparison of T_c to the Fermi energy E_F, which is typically of the order of 10^4K, one might expect the magnetic moment to be a very small fraction of the free Hund's rule moment of Manganese, which is a few μ_B.

As to the second question, if the partially ordered phase is due to any kind of crystalline structure, the transition from the crystal to the isotropic phase is (weakly) first order or second order and therefore should leave signatures in thermodynamic quantities. At the crossover temperature T_0, no signatures are seen in either the a.c. susceptibility or the resistivity. But this might not be the temperature at which the crystal is destroyed, since one could imagine a scenario where the crystal structure fluctuates on timescales smaller than the one relevant for neutron diffraction. However, there would still have to be a second phase transition somewhere in the phase diagram, which is not seen at present.

Apart from the non-Fermi liquid behaviour of the electron resistivity, the most striking experimental observation in the phase diagram of MnSi is certainly the signature observed in neutron scattering experiments: In the partially ordered state, the signal is spread over the surface of a sphere of a radius close to the helical wave vector $\boldsymbol{q}_0$ and peaked at $\langle 110 \rangle$. Any model for the partially ordered state needs to explain these properties.

The anisotropic terms (3.4) present in the Ginzburg-Landau theory for MnSi orient single double-twist cylinders in a way similar to the helix: from symmetry arguments alone we can deduce that the axis of *one* double-twist cylinder, which is the only direction singled out, points into the $\langle 111 \rangle$-direction under the influence of (3.4). What are then the neutron scattering signatures of the various double-twist cylinder structures that we investigated?

In the case where the cylinders are aligned completely randomly, the length scale relevant for Bragg reflections is the radial extension of the cylinder. This would indeed give a spherical signature in neutron scattering experiments, but with a certain radial extension of the peaks, which contradicts the resolution-limited radial extension of the neutron scattering signal seen in experiment.

If the double-twist cylinders predominantly self-assemble into crystals, the maxima in neutron scattering signatures result from the Bragg peaks of the crystal structure. For the two crystal structures we investigated, we found that the double-twist wave vector q *changes* as a function of the parameters but is approximately equal to the helix wave vector q_0 at the first order phase transition from the helical to the crystalline phase.

Although we have not found any region in the phase diagram where the square lattice is energetically lower than the cubic lattice of double-twist cylinders, the existence of such regions cannot be entirely ruled out; let us therefore consider first the expected neutron scattering signature from that structure. If the cylinders are preferrably aligned locally in a square lattice, but in a direction that varies globally, in analogy to experiments with liquid crystals [40], then the relevant scale is given by the lattice constant of the square lattice. This would lead to primary Bragg reflexes at wave vectors $\sqrt{2}q$, where q is the double-twist wave-vector. In the square lattice, the anisotropic terms prefer to align the cylinder axes in the $\langle 111 \rangle$-direction, but the orientation of the lattice in the plane perpendicular to this direction is

completely random. In neutron scattering experiments, reflexes can therefore be expected on *rings* perpendicular to the $\langle 111 \rangle$-direction, and these intersect (and can therefore be expected to produce maxima) in the $\langle 110 \rangle$-direction. Since $q \approx q_0$ as the first-order transition from the helical into the double-twist phase is approached, the expected directions of the maxima in neutron scattering match those observed in MnSi, but the magnitude of the wave-vector does not.

The cubic structure we investigated can indeed be expected to produce reflexes at the double-twist wave vector $q \approx q_0$, but at $\langle 100 \rangle$ positions, which is at odds with experiments.

In contrast to the helical phase, which has a uniform magnetization, the magnetization in the crystals we investigated varies in amplitude. As was pointed out in [45], a non-uniform magnitude can couple to magnetic impurities, which could lead to the smearing out of the Bragg reflexes. The higher order anisotropic terms present in a Ginzburg-Landau theory for MnSi cannot align the reflexes as precisely any more.

3.3.8. Other propositions for helical spin crystals

In the course of this work, we became aware of two other proposals for crystalline configurations in chiral ferromagnets, which we briefly present here.

Closest to our approach is the work done by Rößler et al. [46, 47]. The "skyrmion"-configuration of the magnetization which is explicitly shown in [46, 47] is relevant to chiral ferromagnets with a crystal point group C_{nv} rather than T, and therefore not directly applicable to MnSi, but the main idea can easily be adapted.

The approach adopted in [46, 47] is best illustrated by going back to (3.22): Rößler et al. introduce an ad hoc prefactor κ_2 *not* equal to κ_1 for the chiral ferromagnet in (3.22). For sufficiently small $\kappa_2 < \kappa_1$, the cost of amplitude fluctuations is reduced far enough that double twist cylinders can appear, just as it is the case for liquid crystals. In fact, the only difference to liquid crystals that still remains is that the order parameter is a vector, not a director. In complete analogy to the work done by Hornreich and Shtrikman [36], Rößler et al. determine stable configurations of single cylindrical objects, and they proceed to calculate the free energy density of a square lattice of these cylinders, which is in fact the same configuration as discussed in subsection 3.3.4.

The authors justify their ad hoc introduction of a prefactor that reduces the cost of amplitude fluctuations by arguing that the term proportional to $(\nabla\lambda)^2$, i.e. the amplitude fluctuations, is irrelevant for the critical properties of ferromagnets and scales differently than the term proportional to $(\nabla \boldsymbol{n})^2$. Their main argument is that since the energy they use does not change the universal behaviour of an isotropic ferromagnet, they are free to use it. The authors do not, however, substantiate this claim by a detailed renormalization group calculation.

Rößler et al. explain the neutron scattering results within their square lattice approach by proposing that, since the cylindrical skyrmion tubes are oriented along the $\langle 111 \rangle$ direction, the neutron scattering intensity in reciprocal space should lie on circles which intersect and produce maxima of intensity in the $\langle 110 \rangle$ directions at $|\boldsymbol{k}| = q$, i.e. equal to the double-twist wave vector. However, since the vector rotates outwards by only 90° from the cylinder axis for

each cylinder in the square lattice, and since any Bragg reflexes in a crystalline structure are generated by the crystal structure and not by any internal structure within the Wigner-Seitz cell, our prediction for Bragg reflexes made in the previous subsection seems more likely. Furthermore, it might be worth investigating within the context of their model whether a cubic crystal of the form proposed in subsection 3.3.5 is energetically even lower than the square lattice.

A different proposal for helical spin crystals has been made by Binz et al. [45]. The authors also take the route of introducing additional terms in a Ginzburg-Landau theory for the magnetization: Similarly to Schmalian and Turlakov [20], they introduce a momentum-dependent $\boldsymbol{M}^4$-interaction $U(\boldsymbol{q}_1, \boldsymbol{q}_2, \boldsymbol{q}_3)$ and argue that it predominantly couples modes with $\boldsymbol{q}_i = \boldsymbol{q}_0$, i.e. with momenta equal to the helix wave wector. As was discussed in subsection 3.2.1, the interaction can then be parameterized by two independent angles, $U = U(\theta, \phi)$. Binz et al. expand the interaction in spherical harmonics Y_{lm} with $l \leq 2$, which adds three new interaction terms and therefore three independent parameters U_{11}, U_{20} and U_{22} to (3.1). The authors then propose various linear combinations of six helices or spin spirals (3.2) as the new ground states for suitable choices of U_{11}, U_{20} and U_{22}, and establish a phase diagram.

In which parameter regime can these structures be shown to be stable? Binz et al. claim that their higher order terms induce a crystal of helical modes already for prefactors U_{11} and U_{22} of the order of the prefactor of the momentum independent $\boldsymbol{M}^4$-term or below. This is only true, however, because a factor $(1/q_0)^2$ has already been separated out from U_{11} and U_{22} in their calculation. If this factor was absorbed in U_{11} and U_{22}, the helical spin crystals proposed in [45] would necessitate much larger prefactors. Once again, the tiny wave vector of the helical structure in MnSi penalizes higher order gradient terms.

The three dimensional structures that Binz et al. find are distinct from the cubic crystal discussed in subsection 3.3.5. For example, whereas for the cubic crystal proposed in subsection 3.3.5 time reversal is equivalent to a translation, the crystalline structures of [45] are only invariant under combined time translations and rotations. Binz et al. predict lowest order Bragg reflexes for their cubic structures along the $\langle 110 \rangle$ direction. Since their helical spin crystal is a superposition of six helices with wave vectors of equal modulus q_0, these Bragg reflexes are situated on a sphere with radius q_0 in reciprocal space and, as the authors argue, smeared out because of the varying amplitude of the magnetization within a Wigner-Seitz cell. Interestingly enough, although the three-dimensional structures proposed in [45] cannot be realized with double-twist cylinders, they nonetheless contain large, clearly identifyable regions where the magnetization twists about an axis as shown in Fig. 3.4: double-twist regions are present in these structures.

Finally, let us remark that the approach to crystalline structures in chiral ferromagnet that Binz et al. adopt is to a certain extent analogous to the "high chirality" approach to the blue phases[2]. The "high chirality" theory (see e.g. [48, 49]) reconstructs blue phases from the lowest Fourier modes of the crystal structure, as opposed to the "low chirality" approach by e.g. Meiboom et al. [37, 42], where a free energy calculation is done by stacking double-twist tubes into crystals. Our work is closely related to these "low chirality" calculations. As far as

[2] High or low chirality corresponds to large or small κ in (3.15), respectively. From that classification one would expect the low-chirality limit to be more relevant for chiral ferromagnets, as can be seen in Eq. (3.21): κ is proportional to γ, which is small due to the relativistic origin of spin-orbit coupling.

the blue phases in liquid crystals are concerned, the "high chirality" and the "low chirality" approach are complementary: although valid in different regimes of chirality, both predict double-twist structures in certain parameter regions. It is therefore interesting to see that both of these approaches also lead to stable crystalline structures in MnSi, albeit for slightly different Ginzburg-Landau theories.

3.3.9. Summary and further directions

We investigated extensions of the Ginzburg-Landau theory (3.1) for metallic magnets without inversion symmetry and found terms that can destabilize helical order in these systems. In this extended Ginzburg-Landau theory, crystalline configurations of double-twist cylinders, which are reminiscent of the structures that constitute the "blue phases" in liquid crystals, can be shown to minimize the free energy density for certain values of the parameters. To be precise, we calculated the free energy density for two different crystals, one with a square and one with a cubic lattice structure, and found the cubic lattice of double-twist cylinders to be energetically more favourable in all regions of the phase diagram that we investigated.

It is of course possible that the structures we investigated are not in fact those with the lowest free energy density, and this might be a first starting point for an extension of the work presented in this chapter. A possible candidate for another crystal of double-twist regions is the structure discovered by Hornreich and Shtrikman, who argued in [41] that there is a way to realize the O^8 structure in liquid crystals without introducing defects, which makes it a candidate for a crystalline structure in chiral ferromagnets. The possibility that chiral ferromagnets might support double-twist structures even in the absence of higher-order terms in the Ginzburg-Landau expansion is intriguing, but for a definitive answer Monte-Carlo calculations are required.

The influence of fluctuations on the phase-diagram of chiral nematic liquid crystals is considerable, as has been shown by Englert et al. [50], and the same might be true for chiral ferromagnets.

It is unclear at present whether crystalline structures are likely to play a role in the partially-ordered state of MnSi, either the structures proposed by us, by Rößler et al. or by Binz et al. If higher order Bragg reflexes could be seen in neutron scattering experiments, then this would certainly support the crystal hypothesis. In the neutron scattering experiments conducted so far, the integrated intensity on the sphere is of the same order as the intensity of the peaks in the helix phase [7]. Higher order Bragg peaks should therefore be only of very weak intensity, if they exist. However, the main problem with any kind of crystal is that there would have to be another phase transition from the crystal to the isotropic phase, and this second phase transition has not left any experimental signatures so far. It might therefore be worthwile to investigate other structures where double-twist regions play a role. For example, double-twist cylinders do not necessarily have to form crystals, they might also self-assemble in an amorphous, glassy-like state.

In the case of MnSi, however, the ongoing challenge is to explain the anomalous temperature-dependence of the electron resistivity found in the non-Fermi liquid phase. What are the consequences of extended structures of double-twist cylinders for electron scattering? A calculation that involves any kind of helical spin crystal seems rather daunting. A first calculation

could investigate the electron scattering from Goldstone modes of a *single* double-twist cylinder, assuming that in the material, cylinders are far enough apart for the electrons to scatter from only one cylinder at a time. Considering that the mean free path for electrons is 1000 Å, compared to a pitch of $1/q = 170$ Å of the original helix and therefore a radial extension of at most $\pi/(2q) \approx 300$ Å, this is only a good approximation for a configuration of cylinders that are well separated.

Appendix Part I

A. Minibands

A.1. Dzyaloshinsky-Moriya interaction

What follows is a brief sketch how a Dzyaloshinsky-Moriya interaction term such as (2.1) can be derived. Quite generally, an order parameter theory for itinerant magnets such as MnSi can be obtained by starting from a Hubbard-type model for the electronic quasiparticles, introducing a Hubbard Stratonovich field for the spin-density interaction and integrating out the electronic quasiparticles. This will be discussed in more detail in the context of quantum phase transitions in 4.1.1, and in Chapter 5 the procedure will be applied to derive the order parameter theory for a field-tuned quantum phase transition.

Here, we will not anticipate the details but instead just state that the terms bilinear in the order parameter fields that will be generated by this procedure stem from a polarization bubble diagram of the form shown in Fig. 2.7.

Spin-orbit coupling enters in the band structure of the electrons as a term of the form

$$\delta \boldsymbol{\sigma} \cdot \boldsymbol{g}(\boldsymbol{k}), \tag{A.1}$$

where the specific form of $\boldsymbol{g}(\boldsymbol{k})$ depends on the crystal structure, as discussed in section 2.2. In order to determine how this affects the effective action for the order parameter, we can treat this term as a perturbation instead of incorporating it into the electron propagator. The term to first order in spin-orbit coupling that (A.1) produces in the effective action then originates from a diagram of the form

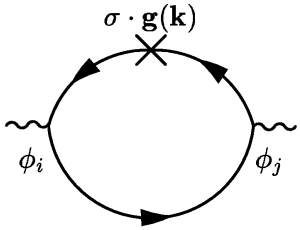

where the cross indicates an insertion of (A.1). This contribution is proportional to

$$\mathrm{Tr}[\sigma^i \sigma^m \sigma^j] \int_{\boldsymbol{k}} \frac{1}{\beta} \sum_n \mathcal{G}_0^2(\boldsymbol{k}+\boldsymbol{q}, \omega_n + \Omega) g_m(\boldsymbol{k}+\boldsymbol{q}) \mathcal{G}_0(\boldsymbol{k}, \omega_n)$$
$$= \mathrm{i}\, \epsilon_{imj} \int_{\boldsymbol{k}} \frac{1}{\beta} \sum_n \mathcal{G}_0^2(\boldsymbol{k}+\boldsymbol{q}, \omega_n + \Omega) g_m(\boldsymbol{k}+\boldsymbol{q}) \mathcal{G}_0(\boldsymbol{k}, \omega_n), \tag{A.2}$$

where $\mathcal{G}_0$ is the propagator of the electronic quasiparticles. For $\boldsymbol{g}(\boldsymbol{k}) = \boldsymbol{k}$ it is now very easy to see that the diagram generates a momentum dependent term in the effective action for the order parameter that takes the form (2.1).

	e	$3c_2, \bar{c}_2$	$4c_3$	$4c_3'$	linear functions, rotations	quadratic functions	cubic functions
A	1	1	1	1		$x^2+y^2+z^2$	xyz
${}^1E$	1	1	ε	ε^*		x^2-y^2	
${}^2E$	1	1	ε^*	ε		$3z^2-r^2$	
F	3	-1	0	0	(x,y,z)	(xy,xz,yz)	(x^3,y^3,z^3)
					(R_x,R_y,R_z)		(xy^2,x^2z,yz^2)
							(xy^2,x^2z,yz^2)

Table A.1.: Character table of irreducible representations and basis functions for the cubic group T with $\varepsilon = \exp(\mathrm{i}2\pi/3)$.

A.2. The space group $P2_13$

The space group $P2_13$ (or T^4 in Schönflies notation) consists of 12 transformations $\boldsymbol{x}' = R\boldsymbol{x} + \boldsymbol{t}$:

$$R_1 = \begin{pmatrix} 1 & 0 & 0 \\ 0 & 1 & 0 \\ 0 & 0 & 1 \end{pmatrix}, \boldsymbol{t}_1 = \begin{pmatrix} 0 \\ 0 \\ 0 \end{pmatrix} \qquad R_2 = \begin{pmatrix} 1 & 0 & 0 \\ 0 & -1 & 0 \\ 0 & 0 & -1 \end{pmatrix}, \boldsymbol{t}_2 = \begin{pmatrix} \frac{1}{2} \\ \frac{1}{2} \\ 0 \end{pmatrix}$$

$$R_3 = \begin{pmatrix} -1 & 0 & 0 \\ 0 & 1 & 0 \\ 0 & 0 & -1 \end{pmatrix}, \boldsymbol{t}_3 = \begin{pmatrix} 0 \\ \frac{1}{2} \\ \frac{1}{2} \end{pmatrix} \qquad R_4 = \begin{pmatrix} -1 & 0 & 0 \\ 0 & -1 & 0 \\ 0 & 0 & 1 \end{pmatrix}, \boldsymbol{t}_4 = \begin{pmatrix} \frac{1}{2} \\ 0 \\ \frac{1}{2} \end{pmatrix}$$

$$R_5 = \begin{pmatrix} 0 & 1 & 0 \\ 0 & 0 & 1 \\ 1 & 0 & 0 \end{pmatrix}, \boldsymbol{t}_5 = \begin{pmatrix} 0 \\ 0 \\ 0 \end{pmatrix} \qquad R_6 = \begin{pmatrix} 0 & -1 & 0 \\ 0 & 0 & -1 \\ 1 & 0 & 0 \end{pmatrix}, \boldsymbol{t}_6 = \begin{pmatrix} \frac{1}{2} \\ 0 \\ \frac{1}{2} \end{pmatrix}$$

$$R_7 = \begin{pmatrix} 0 & 1 & 0 \\ 0 & 0 & -1 \\ -1 & 0 & 0 \end{pmatrix}, \boldsymbol{t}_7 = \begin{pmatrix} \frac{1}{2} \\ \frac{1}{2} \\ 0 \end{pmatrix} \qquad R_8 = \begin{pmatrix} 0 & -1 & 0 \\ 0 & 0 & 1 \\ -1 & 0 & 0 \end{pmatrix}, \boldsymbol{t}_8 = \begin{pmatrix} 0 \\ \frac{1}{2} \\ \frac{1}{2} \end{pmatrix}$$

$$R_9 = \begin{pmatrix} 0 & 0 & 1 \\ 1 & 0 & 0 \\ 0 & 1 & 0 \end{pmatrix}, \boldsymbol{t}_9 = \begin{pmatrix} 0 \\ 0 \\ 0 \end{pmatrix} \qquad R_{10} = \begin{pmatrix} 0 & 0 & -1 \\ 1 & 0 & 0 \\ 0 & -1 & 0 \end{pmatrix}, \boldsymbol{t}_{10} = \begin{pmatrix} 0 \\ \frac{1}{2} \\ \frac{1}{2} \end{pmatrix}$$

$$R_{11} = \begin{pmatrix} 0 & 0 & -1 \\ -1 & 0 & 0 \\ 0 & 1 & 0 \end{pmatrix}, \boldsymbol{t}_{11} = \begin{pmatrix} \frac{1}{2} \\ 0 \\ \frac{1}{2} \end{pmatrix} \qquad R_{12} = \begin{pmatrix} 0 & 0 & 1 \\ -1 & 0 & 0 \\ 0 & -1 & 0 \end{pmatrix}, \boldsymbol{t}_{12} = \begin{pmatrix} \frac{1}{2} \\ \frac{1}{2} \\ 0 \end{pmatrix}$$

A.3. Representations and multiplication tables for T

The cubic group T is the point group of T^4, i.e. the group consisting of the rotations contained in T^4. T is a non-abelian group with 12 symmetry elements, it has 4 irreducible representations whose character tables [51] are given in A.1.

Direct products of representations can be reduced to direct sums of irreducible representations. For T, the results are listed in A.2.

	A	${}^1E$	${}^2E$	F
A	A	${}^1E$	${}^2E$	F
${}^1E$		${}^2E$	A	F
${}^2E$			${}^1E$	F
F				$A \oplus {}^1E \oplus {}^2E \oplus 2F$

Table A.2.: Reduction table for direct products of irreducible representations. Taken from [51].

A.4. Polarization bubble: Calculations

To determine the effect that the belt of minibands has on the order parameter susceptibility, expression (2.65) has to be evaluated. We restrict the calculation to the case $0 \leq q_z < q_0/2$, where q_z is the part of the external momentum that is parallel to the helix.

$$
\begin{aligned}
&\mathrm{Re}\,\Pi^{\perp}(\boldsymbol{q}_\perp, q_z, 0) \\
&= c\,\mathcal{P} \sum_{N_1,N_2} \int d\boldsymbol{\kappa}_\perp \int_{q_0/2}^{q_0/2} d\kappa_z \left(\delta_{N_1,N_2} \Theta\left(\frac{q_0}{2} - (\kappa_z + q_z)\right) + A^{+}_{N_1,N_2} A^{-}_{N_2,N_1} \Theta\left(\kappa_z + q_z - \frac{q_0}{2}\right)\right) \\
&\qquad \times \frac{n_F(\xi^{N_1}_{\kappa_\perp}) - n_F(\xi^{N_2}_{\kappa_\perp+q_\perp})}{\xi^{N_2}_{\kappa_\perp+q_\perp} - \xi^{N_1}_{\kappa_\perp}} \qquad \text{(A.3)} \\
&= c\,\mathcal{P} \sum_{N} \int d\boldsymbol{\kappa}_\perp \, \frac{n_F(\xi^{N}_{\kappa_\perp}) - n_F(\xi^{N}_{\kappa_\perp+q_\perp})}{\xi^{N}_{\kappa_\perp+q_\perp} - \xi^{N}_{\kappa_\perp}} \, (q_0 - q_z) \\
&\quad + c\,\mathcal{P} \sum_{N_1,N_2} \int d\boldsymbol{\kappa}_\perp \, A^{+}_{N_1,N_2} A^{-}_{N_2,N_1} \left(\frac{n_F(\xi^{N_1}_{\kappa_\perp}) - n_F(\xi^{N_2}_{\kappa_\perp+q_\perp})}{\xi^{N_2}_{\kappa_\perp+q_\perp} - \xi^{N_1}_{\kappa_\perp}} \right) q_z \qquad \text{(A.4)} \\
&= c\,\mathcal{P} \sum_{N} \int d\boldsymbol{\kappa}_\perp \, n_F(\xi^{N}_{\kappa_\perp}) \left(\frac{1}{\xi^{N}_{\kappa_\perp+q_\perp} - \xi^{N}_{\kappa_\perp}} - \frac{1}{\xi^{N}_{\kappa_\perp} - \xi^{N}_{\kappa_\perp-q_\perp}} \right) (q_0 - q_z) \\
&\quad + c\,\mathcal{P} \sum_{N_1,N_2} \int d\boldsymbol{\kappa}_\perp \, n_F(\xi^{N_1}_{\kappa_\perp}) \left(\frac{A^{+}_{N_1,N_2} A^{-}_{N_2,N_1}}{\xi^{N_2}_{\kappa_\perp+q_\perp} - \xi^{N_1}_{\kappa_\perp}} - \frac{A^{+}_{N_2,N_1} A^{-}_{N_1,N_2}}{\xi^{N_1}_{\kappa_\perp} - \xi^{N_2}_{\kappa_\perp-q_\perp}} \right) q_z \qquad \text{(A.5)} \\
&= c\,\mathcal{P} \sum_{N} \int_0^{\kappa_\perp^{max}(N)} d\kappa_\perp \, \kappa_\perp \int_0^{2\pi} d\phi \left(\frac{1}{\kappa_\perp q_\perp \cos\phi - q_\perp^2/2} - \frac{1}{\kappa_\perp q_\perp \cos\phi + q_\perp^2/2} \right) m\,(q_0 - q_z) \\
&\quad + c\,\mathcal{P} \sum_{N_1,N_2} \int_0^{\kappa_\perp^{max}(N_1)} d\kappa_\perp \, \kappa_\perp \int_0^{2\pi} d\phi \left(\frac{A^{+}_{N_1,N_2} A^{-}_{N_2,N_1}}{\kappa_\perp q_\perp \cos\phi + q_\perp^2/2 + (N_2 - N_1)\, m\, \omega_0} \right. \\
&\qquad \left. - \frac{A^{+}_{N_2,N_1} A^{-}_{N_1,N_2}}{\kappa_\perp q_\perp \cos\phi - q_\perp^2/2 + (N_1 - N_2)\, m\, \omega_0} \right) m\, q_z, \qquad \text{(A.6)}
\end{aligned}
$$

where the prefactor $c = 1/(8(2\pi)^4)$. In the last line, ϕ has been introduced as the angle between $\boldsymbol{\kappa}_\perp$ and $\boldsymbol{q}_\perp$, and $\kappa_\perp^{max}(N)$. Using

$$\int_0^{2\pi} d\phi \int_0^R dr\, r\, \frac{m}{rq\cos\phi + C} = \frac{2m}{q^2} C\pi, \tag{A.7}$$

the integrals can now be evaluated, and the result is

$$\mathrm{Re}\,\Pi^\perp(\boldsymbol{q}_\perp, q_z, 0) = \frac{1}{8}\frac{1}{(2\pi)^3}\, m\, q_0\, n_{max}, \tag{A.8}$$

i.e. the real part of the susceptibility at zero external frequency is constant and proportional to the width $n_{max}q_0$ of the belt. In the calculation, ω_0 has been taken to be constant although it actually acquires a momentum dependence for n approaching n_{max} through its dependence on $c_1 = |g^x_{k_\perp,k_z^0} - \mathrm{i}g^y_{k_\perp,k_z^0}|/(2\delta_B\epsilon_F)$, see (2.26), which will introduce a momentum dependence in (A.8) in turn.

It is convenient to evaluate the imaginary part of the susceptibility at finite external frequency separately for interband and intraband contributions.

$$\begin{aligned}
&\mathrm{Im}\,\Pi^\perp_{intra}(\boldsymbol{q}_\perp, q_z, \omega) \\
&\quad = \frac{1}{16\pi}\frac{1}{(2\pi)^3}\sum_N \int d\boldsymbol{\kappa}_\perp \left(n_F(\xi^N_{\kappa_\perp}) - n_F(\xi^N_{\kappa_\perp+q_\perp})\right)\delta\left(\xi^N_{\kappa_\perp+q_\perp} - \xi^N_{\kappa_\perp} - \omega\right)(q_0 - q_z) \\
&\quad \approx \frac{1}{16\pi}\frac{1}{(2\pi)^3}\sum_N \int_0^\infty d\kappa_\perp\, \kappa_\perp \int_0^{2\pi} d\phi\, (q_0 - q_z)\, q_\perp \kappa_\perp \cos\phi \\
&\qquad\qquad \times \delta\left(\frac{\kappa_\perp^2}{2m} + N\omega_0 - E_F\right)\delta\left(\frac{q_\perp\kappa_\perp}{m}\cos\phi - \omega\right)
\end{aligned} \tag{A.9}$$

This can be evaluated to

$$\mathrm{Im}\,\Pi^\perp_{intra}(\boldsymbol{q}_\perp, q_z, \omega) \approx \frac{m^2}{8(2\pi)^4}\frac{\omega}{q_\perp}(q_0 - q_z)\sum_N \frac{1}{2m(E_F - N\omega_0)} \propto \frac{\omega}{q_\perp}(q_0 - q_z) n_{max}. \tag{A.10}$$

The interband contributions are given by

$$\begin{aligned}
&\mathrm{Im}\,\Pi^\perp_{inter}(\boldsymbol{q}_\perp, q_z, \omega) \\
&\quad = \frac{1}{16\pi}\frac{1}{(2\pi)^3}\sum_{N_1,N_2} \int d\boldsymbol{\kappa}_\perp\, A^+_{N_1,N_2} A^-_{N_2,N_1} \left(n_F(\xi^{N_1}_{\kappa_\perp}) - n_F(\xi^{N_2}_{\kappa_\perp+q_\perp})\right) q_z \\
&\qquad\qquad \times \delta\left(\xi^{N_2}_{\kappa_\perp+q_\perp} - \xi^{N_1}_{\kappa_\perp} - \omega\right).
\end{aligned} \tag{A.11}$$

For small $(q_\perp, q_z)$ and $T = 0$,

$$n_F(\xi^{N_1}_{\kappa_\perp}) = \Theta(\xi^{N_1}_{\kappa_\perp}), \tag{A.12}$$

$$n_F(\xi^{N_2}_{\kappa_\perp+q_\perp}) \approx \Theta(\xi^{N_2}_{\kappa_\perp}) + \delta(\xi^{N_2}_{\kappa_\perp})\frac{q_\perp\cos\phi}{m}, \tag{A.13}$$

and therefore

$$
\begin{aligned}
&\operatorname{Im}\Pi^{\perp}_{inter}(\boldsymbol{q}_\perp, q_z, \omega) \\
&= \frac{1}{16\pi}\frac{1}{(2\pi)^3}\sum_{N_1,N_2}\int d\boldsymbol{\kappa}_\perp\, A^{+}_{N_1,N_2}A^{-}_{N_2,N_1}\left(\Theta(\xi^{N_1}_{\kappa_\perp}) - \Theta(\xi^{N_2}_{\kappa_\perp}) - \delta(\xi^{N_2}_{\kappa_\perp})\frac{q_\perp\cos\phi}{m}\right) q_z \\
&\qquad\qquad \times\delta\left(\xi^{N_2}_{\kappa_\perp+q_\perp} - \xi^{N_1}_{\kappa_\perp} - \omega\right) \\
&\approx \frac{m^2}{8(2\pi)^4}\, q_z \sum_{N_1,N_2} A^{+}_{N_1,N_2}A^{-}_{N_2,N_1}\frac{q_z}{q_\perp}\left(\sqrt{2m(E_F - N_2\omega_0)} - \sqrt{2m(E_F - N_1\omega_0)}\right) \\
&\quad + \frac{m^2}{8(2\pi)^4}\, q_z \sum_{N_1,N_2} \frac{\omega - (N_2 - N_1)\,\omega_0}{q_\perp}\frac{A^{+}_{N_1,N_2}A^{-}_{N_2,N_1}}{2m(E_F - N_2\,\omega_0)}.
\end{aligned}
\tag{A.14}
$$

Together with (A.10) we obtain the familiar result $\mathrm{Im}\Pi^{\perp}(\boldsymbol{q}_\perp, q_z, \omega) \propto \omega/q_\perp$ for a two-dimensional ferromagnetic metal.

B. New Phases from a Ginzburg-Landau Theory

B.1. Square lattice

$\tilde{\xi}$	$\tilde{\delta}$	$\tilde{f}$	y_0	r_1	q/q_0
-6.6	-0.2	-0.0634299	1.22811	2.84315	0.881585
-6.6	-0.1	-0.042926	1.22131	2.57234	0.862542
-6.6	0.0	-0.02651	1.22113	2.32886	0.824992
-6.6	0.1	-0.0139301	1.22039	2.08994	0.773794
-6.6	0.2	-0.00506722	1.22131	1.85845	0.685905
-6.6	0.3	0.000130559	1.22197	1.584	0.51865
-7.0	-0.4	-0.127685	1.33299	3.1475	0.898715
-7.0	-0.3	-0.0980199	1.32993	2.90271	0.884973
-7.0	-0.2	-0.0725359	1.32565	2.68434	0.866063
-7.0	-0.1	-0.0511522	1.31815	2.47478	0.842907
-7.0	0.0	-0.0337603	1.30963	2.27157	0.811973
-7.0	0.1	-0.0201183	1.3023	2.07653	0.767493
-7.0	0.2	-0.00999969	1.29835	1.88485	0.699498
-7.0	0.3	-0.00319207	1.29561	1.68857	0.601269
-7.5	-0.8	-0.31062	1.40782	3.9259	0.938045
-7.5	-0.7	-0.262095	1.41924	3.64668	0.920061
-7.5	-0.6	-0.218189	1.41566	3.44731	0.910453
-7.5	-0.5	-0.178701	1.42525	3.17356	0.90391
-7.5	-0.4	-0.143514	1.4106	2.97908	0.895536
-7.5	-0.3	-0.112828	1.41893	2.77911	0.87391
-7.5	-0.2	-0.0862552	1.40372	2.59201	0.860076
-7.5	-0.1	-0.0636989	1.40443	2.41482	0.833258
-7.5	0.0	-0.0449836	1.38996	2.23794	0.807089
-7.5	0.1	-0.0299032	1.38541	2.07442	0.767499
-7.5	0.2	-0.0181684	1.37703	1.91061	0.718022
-7.5	0.3	-0.00950419	1.3722	1.75894	0.652483
-7.5	0.4	-0.00354041	1.3605	1.60575	0.566954

Table B.1.: Results for the free energy density and the variational parameters for $\tilde{\eta} = 5.375$ and various values of $\tilde{\delta}$ and $\tilde{\xi}$. The results for the wave vector q are given as the ratio of q to the helical wave vector q_0. The free energy density is always *above* the free energy density of the cubic lattice of double-twist cylinders for the same parameters, compare to Table B.2.

B.2. Cubic lattice

$\tilde{\xi}$	$\tilde{\delta}$	$\tilde{f}$	y_0	r_1	q/q_0
-6.0	-0.4	-0.0867203	1.01602	2.34577	0.942959
-6.0	-0.2	-0.045515	1.05916	2.04732	0.0.851659
-6.0	0.0	-0.0168056	1.08609	1.80318	0.745792
-6.0	0.075	-0.00907941	1.10577	1.73741	0.686446
-6.0	0.15	-0.00299682	1.10281	1.66106	0.626629
-6.0	0.17	-0.00166924	1.10186	1.6393	0.605928
-6.6	-0.3	-0.0807239	1.15075	2.07356	0.879173
-6.6	0.0	-0.0273827	1.21797	1.78286	0.731533
-6.6	0.1	-0.0153748	1.20266	1.70698	0.689828
-6.6	0.2	-0.00614206	1.21837	1.62375	0.613024
-6.6	0.3	0.00011378	1.22187	1.524	0.506723
-7.0	-0.5	-0.147666	1.22129	2.22282	0.908292
-7.0	-0.2	-0.0721489	1.2214	1.94029	0.841514
-7.0	-0.1	-0.0529395	1.22227	1.84778	0.811657
-7.0	0.0	-0.0365803	1.22344	1.77131	0.774349
-7.0	0.1	-0.0231284	1.25907	1.70463	0.702427
-7.0	0.2	-0.0123396	1.26066	1.6312	0.654066
-7.0	0.3	-0.00428697	1.26341	1.54717	0.577466
-7.0	0.4	0.000771441	1.27939	1.44023	0.419571
-7.5	-0.9	-0.32584	1.22344	2.62781	0.995465
-7.5	-0.3	-0.11434	1.23194	2.0256	0.904934
-7.5	-0.2	-0.0900146	1.22791	1.92127	0.889297
-7.5	-0.1	-0.0687209	1.22864	1.84122	0.860896
-7.5	0.0	-0.0503419	1.22942	1.76555	0.8264
-7.5	0.1	-0.0354937	1.32542	1.71275	0.718334
-7.5	0.2	-0.0226664	1.32489	1.64472	0.674869
-7.5	0.3	-0.012446	1.3309	1.58057	0.618885
-7.5	0.4	-0.00481807	1.33225	1.51314	0.54933

Table B.2.: Results for the free energy density and the variational parameters for $\tilde{\eta} = 5.375$ and various values of $\tilde{\delta}$ and $\tilde{\xi}$. The results for the wave vector q are given as the ratio of q to the helical wave vector q_0.

$\tilde{\xi}$	a	b	c	δ_{c1}	δ_{c2}
-6.0	-0.151958	0.375493	0.00470287	{-0.064, 0.17}	-
-6.6	-0.143454	0.469668	0.00425618	-0.38	0.30
-7.0	-0.143333	0.524621	0.00289974	-0.58	0.38
-7.5	-0.149879	0.570923	0.00134286	-0.86	0.57

Table B.3.: Parameters for the fit of the free energy of B.2 to the curve $a(\tilde{\delta} - b)^2 + c$ at fixed $\tilde{\xi}$. This gives a value for δ_{c1} at which the first order phase transition from the helix to the cubic crystal of double twist cylinders takes place, and a value δ_{c2} for the transition to the isotropic phase.

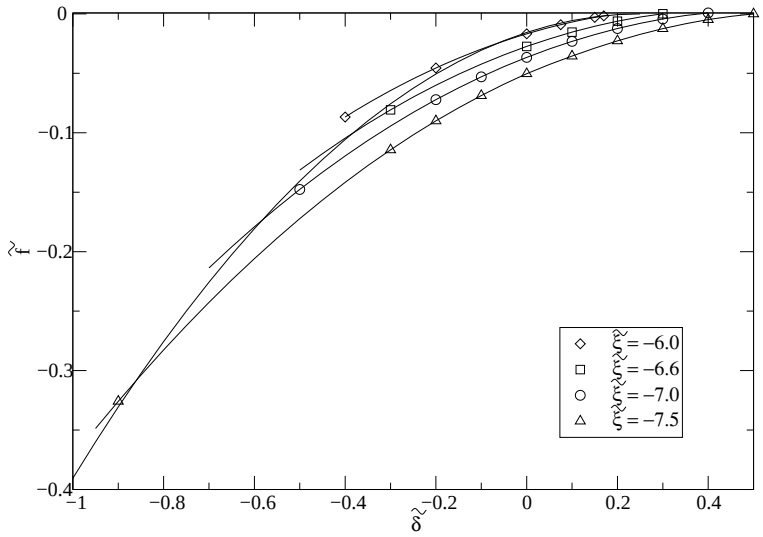

Figure B.1.: Free energy density of the helix (straight line) and the cubic crystal of double twist cylinders for $\tilde{\eta} = 5.375$ and various values of $\tilde{\xi}$ as a function of $\tilde{\delta}$.

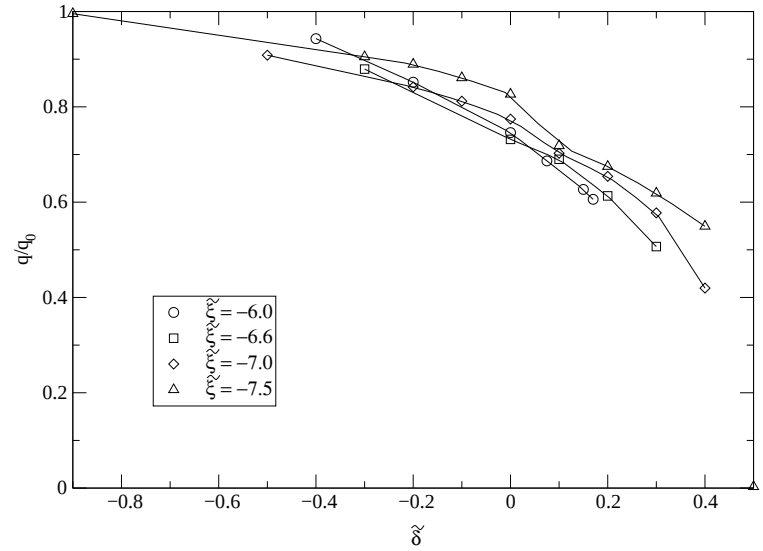

Figure B.2.: The ratio q/q_0 of the double-twist to the helical wave vector for $\tilde{\eta} = 5.375$ and various values of $\tilde{\xi}$ as a function of $\tilde{\delta}$.

$\tilde{\xi}$	$\tilde{\delta}$	$\tilde{f}$	y_0	r_1	q/q_0
-3.55	-0.6	-0.156433	1.58189	1.56473	0.978807
-3.55	-0.5	-0.127041	1.58128	1.51396	0.956831
-3.55	-0.4	-0.100609	1.58152	1.47817	0.930315
-3.55	-0.2	-0.056016	1.58065	1.40108	0.864947
-3.55	0.0	-0.0228019	1.61507	1.32084	0.759843
-3.69	-0.3	-0.0912361	1.67196	1.42478	0.885421
-3.69	-0.15	-0.0588059	1.67225	1.37382	0.835213
-3.69	0.0	-0.0326011	1.67238	1.31886	0.774516
-3.69	0.15	-0.012668	1.67042	1.26024	0.692765
-3.69	0.3	0.000326631	1.67299	1.17876	0.544219
-3.8	-0.6	-0.190515	1.70102	1.52373	0.967482
-3.8	-0.45	-0.144018	1.70136	1.46966	0.934662
-3.8	-0.3	-0.103721	1.70175	1.41642	0.895867
-3.8	-0.15	-0.0695865	1.70192	1.36686	0.848886
-3.8	0.0	-0.0415821	1.70224	1.31472	0.792735
-3.8	0.15	-0.0196921	1.70233	1.26042	0.719528
-3.8	0.3	-0.00422413	1.70248	1.19472	0.610247
-3.9	-0.75	-0.260746	1.73448	1.5683	0.99557
-3.9	-0.45	-0.158154	1.73592	1.45501	0.935811
-3.9	-0.3	-0.116186	1.73596	1.41248	0.899951
-3.9	-0.15	-0.0804703	1.73646	1.36527	0.854781
-3.9	0.0	-0.0507799	1.73657	1.31434	0.803666
-3.9	0.15	-0.0270963	1.73667	1.26437	0.738075
-3.9	0.3	-0.00956019	1.7368	1.2064	0.64772
-4.0	-0.9	-0.341223	1.76574	1.60608	1.02417
-4.0	-0.6	-0.223116	1.76675	1.50866	0.96913
-4.0	-0.3	-0.129822	1.7676	1.412	0.902527
-4.0	0.0	-0.0610129	1.76834	1.31476	0.814529
-4.0	0.3	-0.015976	1.76857	1.21693	0.677644

Table B.4.: Results for the free energy density and the variational parameters for $\tilde{\eta} = 1.0$ and various values of $\tilde{\delta}$ and $\tilde{\xi}$. The results for the wave vector q are given as the ratio of q to the helical wave vector q_0.

$\tilde{\xi}$	a	b	c	δ_{c1}	δ_{c2}
-3.55	-0.141379	0.487607	0.0108152	{-0.32, 0.20 }	-
-3.69	-0.138855	0.553734	0.00996785	-0.54	0.29
-3.8	-0.13727	0.604216	0.00853375	-0.69	0.35
-3.9	-0.136392	0.651529	0.00722641	-0.83	0.42
-4.0	-0.135416	0.700124	0.00559444	-0.97	0.50

Table B.5.: Parameters for the fit of the free energy of B.4 to the curve $a(\tilde{\delta} - b)^2 + c$ at fixed $\tilde{\xi}$. This gives a value for δ_{c1} at which the first order phase transition from the helix to the cubic crystal of double twist cylinders takes place, and a value δ_{c2} for the transition to the isotropic phase.

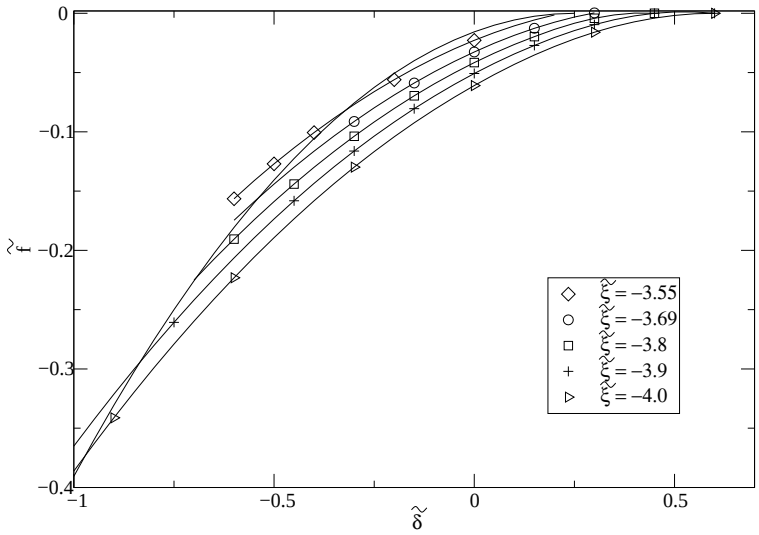

Figure B.3.: Free energy density of the helix (straight line) and the cubic crystal of double twist cylinders for $\tilde{\eta} = 1.0$ and various values of $\tilde{\xi}$ as a function of $\tilde{\delta}$.

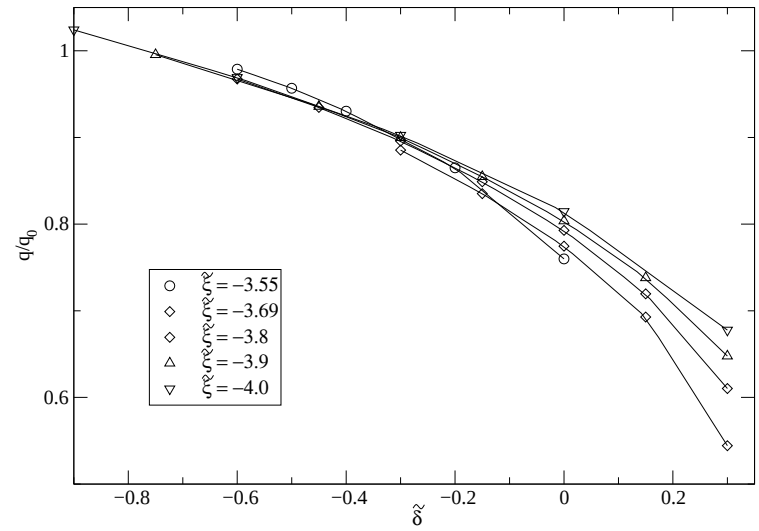

Figure B.4.: The ratio q/q_0 of the double-twist to the helical wave vector for $\tilde{\eta} = 1.0$ and various values of $\tilde{\xi}$ as a function of $\tilde{\delta}$.

$\tilde{\xi}$	$\tilde{\delta}$	$\tilde{f}$	y_0	r_1	q/q_0
-1.32	-0.6	-0.169369	2.8514	0.832457	1.0749
-1.32	-0.5	-0.136708	2.84956	0.822066	1.04407
-1.32	-0.4	-0.106921	2.84826	0.811173	1.00935
-1.32	-0.2	-0.0563214	2.84598	0.787092	0.925239
-1.32	-0.1	-0.0358113	2.85213	0.772832	0.864438
-1.32	0.0	-0.0188421	2.8589	0.756033	0.787998
-1.35	-1.0	-0.375309	2.91125	0.865703	1.18747
-1.35	-0.4	-0.140288	2.89919	0.810531	1.036
-1.35	-0.2	-0.0842116	2.89796	0.789025	0.961806
-1.35	0.0	-0.040164	2.90032	0.76364	0.860432
-1.35	0.2	-0.00967793	2.91246	0.729753	0.694391
-1.35	0.25	-0.00454059	2.91812	0.717708	0.628769
-1.36	-1.0	-0.392143	2.92908	0.86473	1.19064
-1.36	-0.6	-0.22144	2.92015	0.829731	1.10076
-1.36	-0.4	-0.152365	2.91634	0.81052	1.04408
-1.36	-0.2	-0.0944851	2.91429	0.789621	0.973684
-1.36	0.0	-0.0483743	2.91494	0.765539	0.8808
-1.36	0.2	-0.0152335	2.92551	0.73543	0.736227
-1.37	-1.2	-0.512635	2.94451	0.878105	1.23712
-1.37	-1.0	-0.409492	2.94611	0.864042	1.19388
-1.37	-0.8	-0.317231	2.93845	0.847286	1.1553
-1.37	-0.6	-0.235672	2.93593	0.829198	1.10717
-1.37	-0.4	-0.164928	2.93388	0.810439	1.05204
-1.37	-0.2	-0.105251	2.93361	0.790757	0.982419
-1.37	0.0	-0.0571224	2.93055	0.767299	0.896506
-1.37	0.2	-0.0214872	2.93475	0.739033	0.768657
-1.37	0.4	-0.000449464	2.95104	0.695845	0.517654

Table B.6.: Results for the free energy density and the variational parameters for $\tilde{\eta} = 0.05$ and various values of $\tilde{\delta}$ and $\tilde{\xi}$. The results for the wave vector q are given as the ratio of q to the helical wave vector q_0.

$\tilde{\xi}$	a	b	c	δ_{c1}	δ_{c2}
-1.32	-0.156146	0.505081	0.0211646	{-0.42, 0.08}	-
-1.35	-0.147875	0.630251	0.0175338	-0.88	0.29
-1.36	-0.142752	0.702521	0.0213714	-1.01	0.32
-1.37	-0.14324	0.723814	0.0164064	-1.28	0.39

Table B.7.: Parameters for the fit of the free energy of B.6 to the curve $a(\tilde{\delta} - b)^2 + c$ at fixed $\tilde{\xi}$. This gives a value for δ_{c1} at which the first order phase transition from the helix to the cubic crystal of double twist cylinders takes place, and a value δ_{c2} for the transition to the isotropic phase.

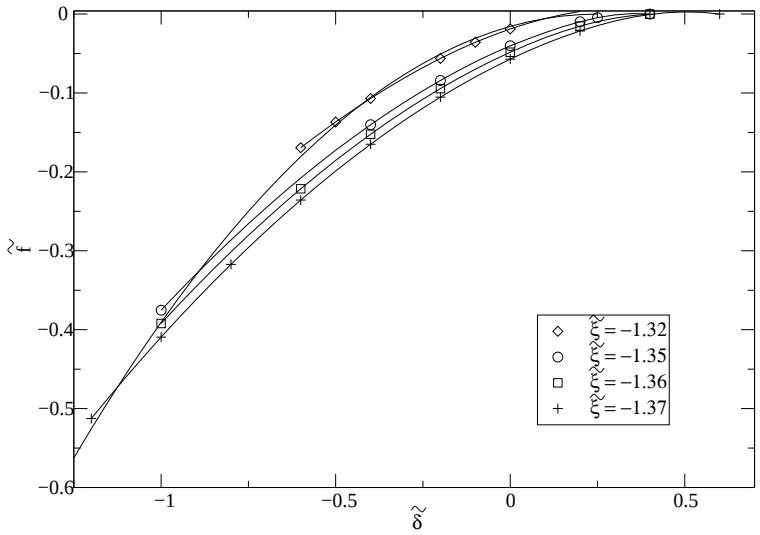

Figure B.5.: Free energy density of the helix (straight line) and the cubic crystal of double twist cylinders for $\tilde{\eta} = 0.05$ and various values of $\tilde{\xi}$ as a function of $\tilde{\delta}$.

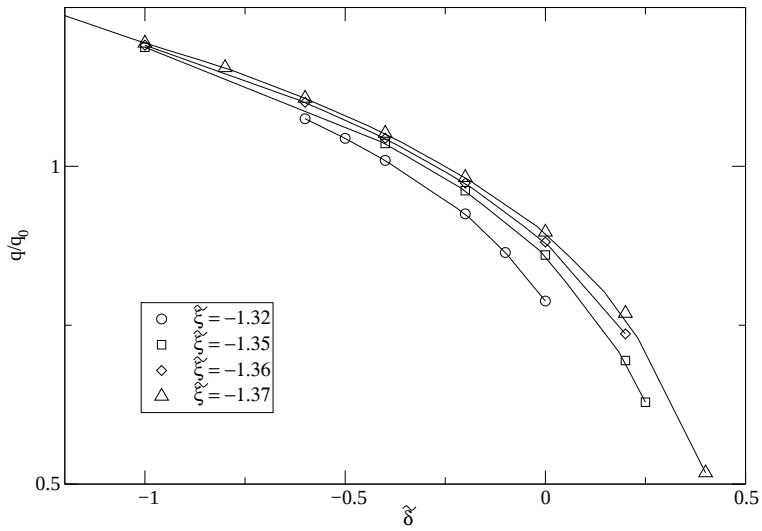

Figure B.6.: The ratio q/q_0 of the double-twist to the helical wave vector for $\tilde{\eta} = 0.05$ and various values of $\tilde{\xi}$ as a function of $\tilde{\delta}$.

Part II.

Quantum Phase Transitions in Antiferromagnetic Metals

4. Introduction

The study of quantum phase transitions is currently a very active field of research in theoretical as well as experimental condensed matter physics. Particularly in a large number of metals – mostly heavy Fermion or transition metal compounds – the critical fluctuations associated with a quantum phase transition induce anomalous behaviour in thermodynamic and transport quantities like diverging specific heat coefficients or a linear resistivity quite distinct from the behavior of a conventional Fermi liquid.

4.1. Theory

Phase transitions are omnipresent in nature: From the condensation of the Higgs particle to the boiling of water, they influenced the physics of the early universe and continue to occur in our daily lives. At a phase transition, a system undergoes a qualitative change in its properties: it changes from one phase, such as water, to the next, such as steam. This change can happen discontinuously, in which case both phases coexist at some stage, or continuously. A continuous phase transition can usually be characterized by an order parameter, such as the magnetization in the case of a magnetic ordering transition, whose expectation value is non-zero in the ordered and zero in the disordered phase. As the phase transition is approached, the order-parameter fluctuations become increasingly long-ranged in space as well as in time. The fluctuations are characterized by a diverging length scale ξ, which is itself proportional to the distance r to the critical point to some power, $\xi \propto |r|^{-\nu}$, and a corresponding diverging time scale $\tau_c \propto \xi^z \propto |r|^{-\nu z}$, where the so-called dynamical critical exponent z is not necessarily equal to one.

The temporal fluctuations of a system are caused by quantum effects, which can only become important at $T \to 0$. At finite temperatures, the thermal energy scale $k_B T$ acts as a cutoff for the temporal fluctuations if it is larger than the typical energy scale $\hbar\omega_c$ of the quantum fluctuations, and the phase transition is a so-called "classical" one. In this case, r is proportional to $|T - T_c|/T_c$, where T_c is the transition temperature. The behaviour of a system close to a finite-temperature, second-order phase transition is dominated by long-range spatial fluctuations of its order parameter and can be described by a local continuum field theory, the Ginzburg-Landau-Wilson theory. At the phase boundary, macroscopic order is destroyed by thermal fluctuations.

For $T \to 0$, however, thermal fluctuations are suppressed, and quantum fluctuations can dominate the behaviour of the system. A non-thermal control parameter then allows to tune from one ground state of the system to the next. In the case of a magnetic quantum phase transition, this control parameter can for example be an external magnetic field, which can induce a transition from a paramagnetic into a magnetic phase.

Second order phase transitions are in most cases linked with the phenomenon of symmetry breaking. There are exceptions such as topological quantum phase transitions, but usually, a symmetry of the system (either continuous or discrete) is broken by the ground state of the system upon entering the ordered phase. A Heisenberg spin system, for example, is invariant with respect to spin rotations, but this rotational symmetry is spontaneously broken by a ferromagnetic ground state, where all spins point into the same direction.

Close to the phase transition, the correlation length ξ is the only relevant length scale and τ_c is the only relevant time scale, which means that physical properties must remain unchanged if all lengths are rescaled by a common factor b, if time is rescaled by b^z and if at the same time the parameters of the system (such as r and the field conjugate to the order parameter B, e.g. a magnetic field if the order parameter is the magnetization) are adjusted so that ξ is unchanged. This scale invariance is one of the fundamental principles underlying phase transitions, it leads to a homogeneity law for the singular part of the free energy density $f = -(T/V)\ln Z$ of the form

$$f_s(r, B, T) = b^{-(d+z)} f_s(r\, b^{1/\nu}, B\, b^{y_B}, T\, b^z), \tag{4.1}$$

from which similar laws for thermodynamic quantities can be obtained. The exponents ν and y_B are the so-called critical exponents; other exponents are defined for thermodynamic quantities. These sets of critical exponents characterize the critical behaviour of very different systems independently of the underlying microscopic details; this is the principle of universality.

Correspondingly, the momentum- and frequency-dependent correlation functions also exhibit scaling behaviour:

$$Q(r, B, T; k, \omega) = b^{-[Q]} Q(r\, b^{1/\nu}, B\, b^{y_B}, T\, b^z; k\, b, \omega\, b^z). \tag{4.2}$$

By choosing e.g. $b = 1/T^{1/z}$, one obtains

$$Q(r, B, T; k, \omega) = \frac{1}{T^{-[Q]/z}} Q\left(\frac{r}{T^{1/(\nu z)}}, \frac{B}{T^{y_B/z}}, 1; \frac{k}{T^{1/z}}, \frac{\omega}{T}\right), \tag{4.3}$$

which means that Q is e.g. a function of the combination ω/T and not of ω and T separately: the data collapses on a single scaling curve, which is important for the confirmation of scaling behaviour at a phase transition in experiment.

The dimensionality of a system plays a decisive role in determining its critical behaviour, or indeed if phase transitions are even possible. Mermin and Wagner identified a so-called lower critical dimension d_c^- for phase transitions where a continuous symmetry is broken; below d_c^- no phase transition can take place, since fluctuations are strong enough to completely suppress the ordered phase. There is another special dimension, the upper critical dimension d_c^+, above which fluctuations are irrelevant, and the critical behaviour is correctly predicted by mean-field theory. For systems above the lower but below the upper critical dimension, the critical behaviour is strongly influenced by fluctuations. In this case, the system exhibits truly universal behaviour, where scaling laws of the form mentioned above are obeyed exactly, and where exponents will fulfill so-called hyperscaling relations. In systems above the upper critical dimension, on the other hand, thermodynamic quantities can depend singularly on

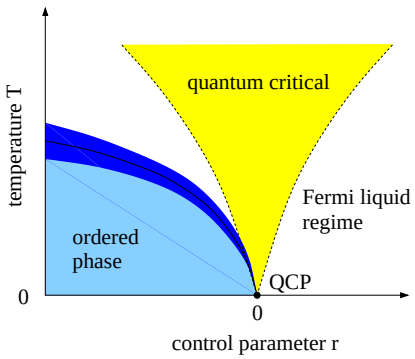

Figure 4.1.: Schematic phase diagram of a quantum phase transition with a control parameter $r \propto B - B_c$.

dangerously irrelevant operators, which have negative scaling dimension and therefore scale to zero. In this case, scaling behaviour is modified.

It seemed to be a reasonable assumption that one can straightforwardly generalize the order parameter theory for a classical phase transition to the corresponding quantum phase transition by introducing an additional time-dependence for the order parameter field. Assuming this is possible, it is then easy to see that quantum phase transitions are qualitatively different from their finite temperature counterparts, in that the dynamics, i.e. the temporal quantum fluctuations, of the order parameter determines the nature and universality class of a quantum phase transition. At $T = 0$, a system in d spatial dimensions effectively behaves like a $d + z$-dimensional system, and the universality class of a quantum phase transition can therefore be expected to be qualitatively different from a finite temperature phase transition. In particular, z is not necessarily equal to one, i.e. time is not simply one extra dimension. For example, at the critical point of an insulating antiferromagnet, the dynamics of the order parameter Φ can be described [52] as in a Klein Gordon equation $(\partial_t^2 - \nabla^2)\Phi$. In such a system, typical frequencies ω scale linearly with the momentum, $\omega \propto q^z$, where $z = 1$ is the dynamical critical exponent. In contrast, in a metal the excitation of particle-hole pairs leads to a Landau damping [53] of the antiferromagnetic order parameter, $(\partial_t + \nabla^2)\Phi$ and therefore $z = 2$.

There are many distinct kinds of quantum phase transitions to be found in nature. Examples are metal-insulator transitions, superfluid-insulator transitions, phase transitions involving topological order such as the Kosterlitz-Thouless transition, and magnetic phase transitions. Thorough discussions of all these quantum phase transitions can be found e.g. in [52, 54]. This part of the thesis concentrates on quantum phase transitions in metallic magnets, which are therefore also the subject of the remainder of this brief introduction.

4.1.1. Hertz-Millis theory of Quantum Critical Points in Metals

Starting from the assumption that one can generalize the theory of a position-dependent magnetization, i.e. the order parameter of a finite-temperature magnetic phase transition

in a metal, to the corresponding quantum phase transition by considering a position- and time-dependent order parameter, a Ginzburg-Landau theory for the (anti-) ferromagnetic quantum phase transition in metals has first been derived by Hertz [53], and later corrected and supplemented by Millis [55]. The procedure how to obtain an order parameter theory from a microscopic model of interacting electrons is described in more detail in chapter 5, where it is applied to derive the effective action for a field-tuned quantum phase transition in a three-dimensional antiferromagnetic metal; it will only be sketched here. A much more thorough derivation, correcting some factors of two of the original work [53, 55], can also be found in [56].

According to Hertz, an order parameter theory for metallic magnets can be derived in the following way: starting from a microscopic Hubbard-type Hamiltonian for the electronic quasiparticles, (1) introduce a real order parameter vector $\mathbf{\Phi}(\boldsymbol{x})$ as a Hubbard-Stratonovich field which decouples the interaction term, (2) integrate out the electronic quasiparticles to obtain an effective local action for the order parameter which has the following form:

$$S = \frac{1}{2}\int \frac{d^d k}{(2\pi)^d}\frac{1}{\beta}\sum_n \chi^{-1}(\omega_n, \boldsymbol{k})\mathbf{\Phi}^2_{\omega_n,\boldsymbol{k}} + \sum_{i=2}^{\infty}\int\left(\frac{d^d k}{(2\pi)^d}\frac{1}{\beta}\sum_n\right)^{2i-1} b_{2i}(\mathbf{\Phi}_{\omega_n,\boldsymbol{k}})^{2i} \tag{4.4}$$

The propagator $\chi^{-1}(\omega_n, \boldsymbol{k})$ and the coefficients b_{2i} are to be calculated from diagrams as shown in Fig. 5.1 in chapter 5. Hertz and Millis assumed that the vertices b_{2i} are local and can therefore be calculated by evaluating the corresponding diagrams at bosonic frequencies equal to zero and momenta equal to the ordering wave vector. They argued that for $i > 2$, the b_{2i}-vertices are irrelevant and can therefore be neglected, whereas the b_4-vertex is marginal for $z = 2$ and $d = 2$ and irrelevant otherwise. Therefore, as a last step (3), the effective action is truncated such that only the frequency and momentum contributions to the gaussian part of the action and a constant $\mathbf{\Phi}^4$ interaction term are retained. The resulting local order parameter theory reads

$$S = \frac{1}{2}\int \frac{d^d k}{(2\pi)^d}\frac{1}{\beta}\sum_n \left(\boldsymbol{k}^2 + r + \frac{|\omega_n|}{k^{z-2}}\right)\mathbf{\Phi}^2_{\omega_n,\boldsymbol{k}} + u\int_{\boldsymbol{k}}\mathbf{\Phi}^4 \tag{4.5}$$

where $\boldsymbol{k}$ is measured from the order parameter wave vector, and $z = 3$ and $z = 2$ for a ferromagnet and an antiferromagnet, respectively. The dynamics of the order parameter is governed by the damping term $|\omega|/k^{z-2}$, which comes from order parameter fluctuations coupling to electron-hole pairs on the Fermi surface. In the case of a ferromagnet, where the wave-vector of the order parameter is zero, these electron-hole pairs can originate from everywhere on the Fermi surface; for an antiferromagnet at very low temperatures, only electron-hole pairs from so-called "hot manifolds" (points on the Fermi surface separated by the antiferromagnetic wave vector $\boldsymbol{Q}$) can couple to the order parameter.

It should be noted that this theory can only describe the metallic magnet on the paramagnetic side of the quantum phase transition. In the ordered phase, the non-zero vacuum expectation value of the order parameter couples to the fermionic quasiparticles and gives rise to a gap in their excitation spectrum, which is not captured by Hertz-Millis theory.

The dimensionality of (4.5) is given by $(d + z)$, where d is the spatial dimensionality and z its dynamical critical exponent, which can be read off from the dynamical term: $z = 2$ for an

quantum critical	$d = 2,\ z = 3$	$d = 3,\ z = 2$	$d = 3,\ z = 3$	$d = 2,\ z = 2$
$\alpha_{cr} \sim$	$\log \frac{1}{T}$	$T^{1/2}$	$T^{1/3}$	$\log \log \frac{1}{T}$
$c_{cr} \sim$	$T^{2/3}$	$-T^{3/2}$	$T \log \frac{1}{T}$	$T \log \frac{1}{T}$

Table 4.1.: Critical exponents of the Hertz-Milliz-Moriya spin-fluctuation theory for three- and two-dimensional ferromagnetic ($z = 3$) and antiferromagnetic ($z = 2$) metals.

antiferromagnet and $z = 3$ for a ferromagnet. The order parameter theory is therefore at its upper critical dimension $d_c^+ = 4$ for a two-dimensional antiferromagnet or *above* d_c^+ otherwise. As a consequence, the interaction constant u is a (dangerously) irrelevant variable: scaling might be violated and in a renormalization group calculation the theory flows towards a Gaussian fixed point.

Starting from (4.5), critical exponents for thermodynamic quantities can be derived and used for comparison with experiments. Results for the critical contributions to the thermal expansion coefficient and the specific heat are summed up in table 4.1.

Spin fluctuation theory has been challenged both from the experimental and from the theoretical side. As will be briefly discussed in the next section, there are numerous experimental results that contradict spin fluctuation theory and would, by themselves, raise questions concerning the validity of Hertz-Millis theory. In particular, the specific heat coefficient in many three-dimensional antiferromagnets *diverges* logarithmically in contrast to spin-fluctuation theory, as can be seen in table 4.1. This behaviour is, however, to be expected for two-dimensional systems. It has been suggested [57] that $CeCu_{6-x}Au_x$, which is one of the systems where a logarithmically diverging specific heat coefficient has been observed, exhibits antiferromagnetic order in pairs of *planes*, but that different pairs of planes are incoherent. In this case, the critical fluctuations of the magnetization would indeed be two-dimensional.

Another experimental fact which seems to contradict Hertz-Millis theory in some systems is the ω/T-scaling behaviour seen in the magnetic susceptibility e.g. of $CeCu_{6-x}Au_x$ [58]. Any system below its upper critical dimension has to obey scaling laws of the form 4.2. Hertz-Millis theory, however, is at or above the upper critical dimension for two- and three-dimensional metals, respectively, and ω/T-scaling can be violated. And indeed, e.g. in case of a three-dimensional antiferromagnet, it can be shown that the inverse square of the correlation length $\xi^{-2} \sim \tau^{-1}$ behaves as $uT^{3/2}$ in the quantum critical regime (c.f. eq. 5.19), which corresponds to $\omega/T^{3/2}$-scaling as can be seen from 4.2 by setting $b = 1/r^{\nu}$.

4.1.2. Quantum critical points in itinerant ferromagnets

As we will see in the next section, quantum critical points that can be described by Hertz-Millis theory are surprisingly rare. But even before putting the theory to the test, there are problems inherent in the approach, as has first been pointed out by Belitz and Kirkpatrick in the context of ferromagnetic quantum critical points.

Belitz and Kirkpatrick took a closer look at the second step of the derivation of the critical theory, where electronic quasiparticles are integrated out to obtain an effective order parameter theory. A careful calculation of the static spin susceptibility in clean, ferromagnetic systems in the disordered phase shows that it exhibits non-analytic wave vector dependencies of the form [59]

$$\chi^{(2)}(\boldsymbol{q}) = \begin{cases} const. + c_1 \log\frac{1}{|\boldsymbol{q}|}, & d = 1, \\ const. + c_2 \, |\boldsymbol{q}|, & d = 2, \\ const. + c_3 \, \boldsymbol{q}^2 \log\frac{1}{|\boldsymbol{q}|}, & d = 3. \end{cases} \tag{4.6}$$

At zero wave-vector, these non-analyticities translate to diverging coefficients in a Landau-Ginzburg-Wilson order parameter theory; a *local* Landau-Ginzburg-Wilson theory that describes the critical behaviour of the system does not exist.

Moreover, the authors subsequently found that even a non-local order parameter field theory, with propagator and vertices given by the results cited above, fails to produce the exact critical behaviour. When comparing the Gaussian critical behaviour of the non-local order parameter theory to the critical behaviour of a model where the fermionic degrees of freedom are explicitly kept, it turns out that the order-parameter theory fails to take certain marginal operators into account which lead to additional logarithmic corrections to scaling [60].

A more physical interpretation of this result is that any step in which soft modes that couple sufficiently strongly to the order parameter are integrated out, is potentially dangerous: the quantum critical behaviour is instead determined by all of the soft (i.e. massless) modes in the system, not only those corresponding to order parameter fluctuations. In other words, an effective description in terms of an order parameter alone is impossible.

Belitz and Kirkpatrick put their findings in a more general context and concluded [61] that Hertz-Millis theory breaks down if a quantum phase transition has a zero-wave-number order parameter and if a source term H for the order parameter field changes the soft-mode spectrum of the fermionic part of the action. The second condition ensures that the coupling of the fermionic soft modes to the order parameter is indeed sufficiently strong. If the order parameter is the magnetization, for example, the source term is an external magnetic field, which can couple to the electronic quasiparticles via a Zeeman term, i.e. the magnetic field generates a mass for the electronic quasiparticles.

4.1.3. Hertz-Millis theory and antiferromagnets

Belitz and Kirkpatrick showed that Hertz-Millis theory fails to properly describe ferromagnetic quantum phase transitions, but their findings do not apply to antiferromagnetic quantum critical points, which are after all characterized by an order parameter with non-zero wave vector equal to the antiferromagnetic ordering wave vector $\boldsymbol{Q}$.

However, while no problems have yet been found concerning Hertz-Millis theory in three-dimensional antiferromagnets, various groups have found reasons to question the applicability of Hertz-Millis theory to two-dimensional systems [62, 63, 64, 65].

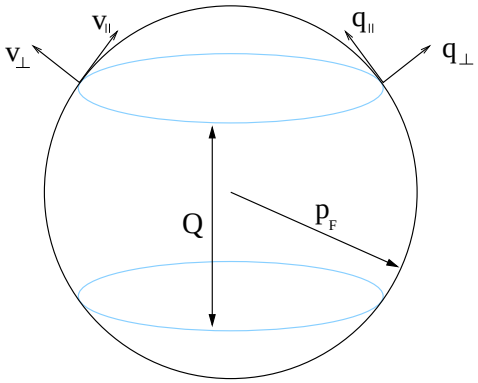

Figure 4.2.: Hot lines on a spherical Fermi surface in three spatial dimensions separated by the antiferromagnetic wave vector $\boldsymbol{Q}$.

Abanov and Chubukov [62] investigated a two-dimensional spin-fermion model of the form

$$H_{SF} = \sum_{\boldsymbol{k},\alpha} \boldsymbol{v}_F(\boldsymbol{k}-\boldsymbol{k}_F) c^\dagger_{\boldsymbol{k},\alpha} c_{\boldsymbol{k},\alpha} + \sum_q \chi_0^{-1}(\boldsymbol{q}) \boldsymbol{S}_{\boldsymbol{q}} \boldsymbol{S}_{-\boldsymbol{q}} + g \sum_{\boldsymbol{q},\boldsymbol{k},\alpha,\beta} c^\dagger_{\boldsymbol{k}+\boldsymbol{q},\alpha} \boldsymbol{\sigma}_{\alpha\beta} c_{\boldsymbol{k},\beta} \cdot \boldsymbol{S}_{-\boldsymbol{q}}, \quad (4.7)$$

in which low-energy fermions interact with their own collective spin degrees of freedom: $c^\dagger_{\boldsymbol{k},\alpha}$ creates a fermion of wave vector $\boldsymbol{k}$ and spin α, and $\boldsymbol{S}_{\boldsymbol{q}}$ are the collective bosonic spin degrees of freedom. The bare spin susceptibility χ_0^{-1} is generated by integrating out high-energy fermions. This model can be thought to arise from a Hubbard type Hamiltonian, in which the collective bosonic spin degrees of freedom have been introduced to decouple the spin-density interaction just as in the first step of the derivation of Hertz-Millis theory, but where the electronic quasiparticles have *not* been integrated out. Perturbative one-loop corrections generate a Landau damping term in the ϕ-propagator, but when the authors analyzed the theory in the framework of a renormalization group calculation they found that, due to singular vertex corrections, the frequency dependence of the spin damping term at the quantum critical point is actually $\omega^{1-\alpha}$, where the exponent depends on the number of hot spots N and $\alpha \sim 0.25$ for $N = 8$. This is clearly in contrast to Hertz-Millis theory, as it would lead to a dynamical critical exponent $z \approx 2.67$ for the bosonic degrees of freedom. In a later publication, Abanov, Chubokov and Schmalian [63] re-examined this result in the framework of an iterative perturbative calculation and argued that the dynamical spin susceptibility should have the form $\chi(\Omega, \boldsymbol{q}) \propto ((\boldsymbol{Q}-\boldsymbol{q})^2 + |\Omega_m|)^{-1+\alpha}$ instead, again with $\alpha \sim 0.25$. This would leave z unchanged from the Hertz-Millis value.

Rosch investigated the possibility of a breakdown of Hertz-Millis theory due to pseudogaps in the paramagnetic phase of an antiferromagnet [64]. In the antiferromagnetically ordered phase, the coupling of the electrons to the order parameter Φ causes gaps to open on the Fermi surface.

On the paramagnetic side and close to the quantum critical point, the antiferromagnetic background fluctuates, but if the electrons can adjust adiabatically to this background, precursors of gaps – pseudogaps – could develop even in the disordered phase. Damping of the spin fluctuations would then be reduced, and the dynamical critical exponent z_Φ of the order parameter might be different from what Hertz-Millis theory predicts. In order to determine under which conditions such pseudogaps can form and influence the electron behaviour,

Rosch estimates the effective size of the quasi-static antiferromagnetic order $\langle\Phi\rangle^{\rm eff}_{k^*,\omega^*}$ from the (imaginary part of the) spin susceptibility $1/\chi_{\boldsymbol{q}\pm\boldsymbol{Q}}(\omega) \sim \boldsymbol{q}^2 + (\mathrm{i}\omega)^{2/z_\Phi}$ to be

$$\begin{aligned}\left(\langle\Phi\rangle^{\rm eff}_{k^*,\omega^*}\right)^2 &\lesssim \int_0^{\omega^*} d\omega \int_{q_\perp<k^*} d^2q_\perp \int_{-\infty}^{\infty} d^{d-2}q_\parallel \mathrm{Im}\chi_{\boldsymbol{q}\pm\boldsymbol{Q}}(\omega)\\ &\sim (k^*)^{d+z_\Phi-2} + (k^*)^2(\omega^*)^{(d+z_\Phi-4)/z_\Phi}\\ &\sim \Delta^{(d+z_\Phi-4)(z_F/z_\Phi)+2},\end{aligned}$$

where the momentum integration takes into account that the momentum $q_\parallel$ of the electrons parallel to the hot line can vary on the scale k_F, see Fig. 4.2. In the last line, the mean-field results have been used, according to which the width of the stripe in momentum space, on which the gap opens, is $k^* \sim \Delta/v_F$, and the size of the gap is $\omega^* \sim (k^*)^{z_F} \sim \Delta^{z_F}$. Electrons can see this quasi-static antiferromagnetic order on timescales $\tau^* \sim 1/\omega^*$ and lengthscales $\xi^* \sim k^*$, and if $\Delta^{(d+z_\Phi-4)(z_F/z_\Phi)+2}$ is *larger* than the mean-field result Δ^2, i.e. for

$$d + z_\Phi \leq 4, \tag{4.8}$$

pseudogaps should appear. This suggests that the Hertz-Millis analysis is not valid in $d = 2$.

Finally, Abanov and Chubukov re-examined the Hertz-Millis derivation of an order parameter field theory for two-dimensional antiferromagnets [65]. To be more precise, they carefully re-examined the susceptibilities that are generated by integrating out the electrons, i.e. the coefficients of the effective action (4.4). Hertz and Millis argued that the coefficients b_{2n} of the $\boldsymbol{\phi}^{2n}$-terms, $n \geq 2$, are constant and can be obtained from the zero frequency and zero wave-number limit. Abanov and Chubukov find that when the diagrams are evaluated at finite bosonic frequencies $\Omega_i \to 0$ and momenta $\boldsymbol{q}_i \neq \boldsymbol{Q}$ instead, the $\boldsymbol{\phi}^{2n}$-terms (for $d = 2$) have the form

$$g_{2n} \int (d^2q\, d\Omega)^{2n-1} b_{2n} (\phi_{\boldsymbol{Q},\boldsymbol{q}})^{2n} \quad \text{with} \quad b_{2n} \propto \frac{g^{2n}}{v_F^2} \frac{|\Omega|}{(\Omega - v_F q + \mathrm{i}\delta)^{2(n-1)}}. \tag{4.9}$$

Considering that momenta, frequencies and fields have the scaling dimensions 1, z and $-1-(d+z)/2$, respectively, a scaling dimension $(2-z)n$ is obtained for the coupling constant g_{2n}. This means that for $z = 2$, all vertices are marginal in $d = 2$, in contrast to Hertz-Millis theory. Each of these marginal vertices leads to logarithmic corrections to the spin susceptibility χ, and Abanov and Chubukov argue that the logarithmic corrections sum up to a susceptibility of the form

$$\chi^{-1}(\Omega, \boldsymbol{q}) \propto ((\boldsymbol{q} - \boldsymbol{Q})^2 + |\Omega|)^{1-\gamma} \tag{4.10}$$

at the quantum critical point. This result is similar to what was obtained in [63].

Once again, these results suggest that all soft modes of a system are indeed necessary for a correct description of its quantum critical behaviour.

4.1.4. Other theories for heavy fermion criticality

The critical theory of a ferromagnetic metal cannot be a local order parameter field theory, and even for a two-dimensional antiferromagnet, the applicability of Hertz-Millis theory has been questioned. So far, no inconsistencies within Hertz-Millis theory have been found in the case of a three-dimensional antiferromagnet, but as will be discussed in the following section, the theory nonetheless fails to describe the physics at many of the putative quantum critical points in three-dimensional antiferromagnetic metals such as $CeCu_{6-x}Ag_x$ and $CeCu_{6-x}Au_x$. In addition to the intrinsic problems of Hertz-Millis theory, there seem to exist a number of metals whose quantum critical behaviour is not captured by spin-wave theory.

The metals in which quantum critical points are thought to exist are almost exclusively heavy fermion metals: these substances are characterized by a conduction band c and a band of localized f-electrons, which can hybridize to an extremely flat quasiparticle band. This leads to an effective mass for the quasiparticles which is 100 or 1000 times in excess of the mass of the free electron, which is at the origin of the name "heavy fermion" systems.

A starting point for the description of heavy fermion systems is the Kondo lattice, i.e. a Hamiltonian of the form

$$H_{HF} = \sum_k \varepsilon_k c^\dagger_{k\alpha} c_{k\alpha} + \frac{J_K}{2} \sum_r \boldsymbol{S}_r c^\dagger_{r\alpha} \boldsymbol{\sigma}_{\alpha\alpha'} c_{r\alpha'} + \sum_{\langle rr' \rangle} I_{r,r'} \boldsymbol{S}_r \cdot \boldsymbol{S}_{r'}, \tag{4.11}$$

where the first term describes the conduction electrons, the second term couples the conduction electrons to localized spin-1/2-moments $\boldsymbol{S}_r$ on the lattice, and the third term, the so-called RKKY exchange coupling, describes a Heisenberg exchange between the local moments. Almost three decades ago, Doniach suggested that the ratio δ of the RKKY interaction to the Kondo temperature is crucial for the interpretation of the behaviour of the system [66]. As long as δ is small, the quenching of the local moment through its Kondo coupling to the conduction electrons dominates, and these metals can be described by Hertz-Millis theory: the local moments hybridize with the conduction electrons and form quasiparticles. The screening of the local moments becomes imperfect at the quantum critical point, and a spin-density wave instability develops; the system becomes magnetically ordered. However, if δ gets large, one could also imagine a scenario where Kondo-screening breaks down and the local moments are polarized along the direction of the fluctuating magnetization via the RKKY exchange coupling. This state is then no longer described by Hertz-Millis theory.

Several theories have been put forward to describe the breakup of the heavy fermion quasiparticles and the role of the local moments at the quantum phase transition: Coleman et al. [67] investigate spin-charge separation, Si et al. [68] introduce the concept of local quantum criticality, and Senthil et al. [69] postulate the existence of so-called fractionalized Fermi liquids. These theories have the Kondo lattice of local moments as their common starting point for a description of heavy fermion quantum criticality, but they vary considerably in their predictions for the physics behind the quantum critical behaviour.

In several articles [67, 70], Coleman, Pépin and coworkers put forward the idea of spin-charge separation as a mechanism for the breakdown of Kondo screening. In this scenario, the heavy fermion quasiparticles decay into a neutral "spinon" and a spinless charge e fermion $e^-_\sigma \rightleftharpoons s_\sigma + \phi^-$. A magnetic phase could then come about from a condensation of the magnetic

spinors, while the ϕ fermion would propagate coherently. In this approach, it is not completely clear, however, why the breakup of the heavy fermion quasiparticles should coincide with the onset of magnetic order. In a later publication, Pépin [71] proposes the dynamics of the spinless fermion to be the key to a description of various properties of $YbRh_2Si_2$, such as a $T^{-1/3}$-upturn in the specific heat coefficient or the $\rho \sim T$-behaviour of the resistivity.

Si and coworkers [68], introduce the concept of local quantum criticality. Their basic idea is that, in addition to the fluctuating magnetization, the magnetic moments constitute local degrees of freedom that become critical at the quantum phase transition. These degrees of freedom can only fluctuate in time and not in space, hence the name. The authors treat the competition between Kondo screening and the RKKY-interaction between the local moments in the framework of an EDMFT calculation, which maps (4.11) to an effective single-site Bose-Fermi Kondo model of the form

$$H_{loc} = \frac{J_K}{2}\boldsymbol{S}(c^\dagger_\alpha \boldsymbol{\sigma}_{\alpha\alpha'} c_{\alpha'}) + \sum_k \varepsilon_k c^\dagger_{k\alpha} c_{k\alpha} + g\sum_k \boldsymbol{S}\cdot(\phi_k + \phi^\dagger_{-k}) + \sum_k w_k \phi^\dagger_k \cdot \phi_k. \qquad (4.12)$$

In an extension of DMFT, the electron-self-energy $\Sigma(\omega)$ as well as the spin self-energy $M(\omega)$ are determined self-consistently by requiring the local electron Green's function $G_{\rm loc}(\omega)$ and the local susceptibility $\chi_{\rm loc}(\omega)$ to be equal to the wavevector averages of the lattice Green's function and the lattice susceptibility:

$$M(\omega) = \chi_0^{-1}(\omega) + \frac{1}{\chi_{\rm loc}(\omega)}, \qquad \chi_{\rm loc}(\omega) = \int d\varepsilon \frac{\rho_l(\varepsilon)}{M(\omega)+\varepsilon}, \qquad (4.13)$$

$$\Sigma(\omega) = G_0^{-1}(\omega) - \frac{1}{G_{\rm loc}(\omega)}, \qquad G_{\rm loc}(\omega) = \int d\varepsilon \frac{\rho_0(\varepsilon)}{\omega - \varepsilon - \Sigma(\omega)}, \qquad (4.14)$$

where ρ_0 is the bare conduction electron density of states, and $\rho_l(\varepsilon) = \sum_{\boldsymbol{q}} \delta(\varepsilon - I_{\boldsymbol{q}})$. The result for the spin self-energy $M(\omega)$ now depends crucially on the form of $\rho_l(\varepsilon)$. If $\rho_l(\varepsilon)$ has a square-root onset from the lower band-edge, which is characteristic for three-dimensional magnetic fluctuations with e.g. $I_{\boldsymbol{q}} = I(\cos q_x a + \cos q_y a + \cos q_z a)$, then $M(\omega) \approx -I_{\boldsymbol{Q}} - {\rm i}a\omega$: Landau-damping of the spin-fluctuations is recovered. If, on the other hand, $\rho_l(\varepsilon)$ increases from zero with a jump, which would be generated by magnetic fluctuations in two dimensions with e.g. $I_{\boldsymbol{q}} = I(\cos q_x a + \cos q_y a)$, a spin self-energy of the form $M(\omega) \approx -I_{\boldsymbol{Q}} + A\omega^\alpha$ or, at finite temperature, $M(\omega, T) \approx -I_{\boldsymbol{Q}} + AT^\alpha W(\omega/T)$ is obtained. This reproduces the ω/T-scaling for the susceptibility seen in experiment, but it is unclear at present what mechanism could cause the magnetic fluctuations to become two-dimensional.

Finally, Senthil et al. [69] extended the concept of deconfined criticality to magnetic quantum critical points in heavy electron systems. The authors start from the assumption that the Kondo effect becomes suppressed and that the local moments are removed from the Fermi volume *before* the magnetic transition is reached: It is possible for the system to be non-magnetic if the local moments are in a disordered ground state (e.g. a RVB spin liquid [72]) instead of ordering magnetically; this state is dubbed FL*. In this state, fluctuations of a $U(1)$-gauge field, which formally arises from a "slave-particle" representation of the local moments $\boldsymbol{S}_r = 1/2 f^\dagger_{r\alpha} \boldsymbol{\sigma}_{\alpha\alpha'} f_{r\alpha'}$ and the subsequent implementation of a constraint, play a crucial role and serve to produce e.g. a $T \log 1/T$ singularity in the low-temperature specific heat [73]. The "conventional" FL-state, in which the local moments hybridize with the conduction electrons, can be reached from the FL*-state via a $z = 2$ quantum phase transition [73].

If Kondo screening is lost, the number of charge carriers should change discontinuously at the quantum critical point. It has been shown [74] that, if the Kondo lattice can be described as a Fermi liquid, Luttinger's theorem guarantees that the c- as well as the f-electrons contribute to the Fermi volume. If the quasiparticles are broken up, no matter how, then this is no longer true, and the Fermi surface only encompasses states whose number equals the number of c-electrons. This discontinuous change should be observable in experiment. Coleman et al. [75] suggested measuring the Hall constant in the vicinity of the quantum critical point. While a spin density wave picture predicts a continuous change in the Hall constant at the quantum critical point, any theory which describes a break-up of composite heavy fermions necessarily has a jump of the Hall constant at the phase transition as a consequence. Possible experimental evidence for a discontinuous change of the Hall constant at the quantum critical point has been reported in the compound $YbRh_2Si_2$ [76].

4.2. Antiferromagnetic QCPs in Experiments

Is the behaviour predicted by spin-fluctuation theory really seen in experiments? Antiferromagnetic quantum critical points have been suspected in a number of systems, most notably metals (heavy fermion compounds or transition metal compounds such as $CeCu_{6-x}Ag_x$, $CeCu_{6-x}Au_x$, $YbCu_{5-x}Al_x$, $CeCoIn_5$, and $YbRh_2Si_2$), and rare-earth magnetic insulators (such as $TlCuCl_3$ and $BaCuSi_2O_6$). In such systems, anomalous behaviour in thermodynamic and transport quantities is observed and cannot be explained in the framework of Fermi-liquid theory. In some of these systems, the predictions of spin-fluctuation theory fit the experimental data surprisingly well, in other systems, the critical exponents do not match at all (Fig. 4.3).

Only a few systems (e.g. $CeNi_2Ge_2$ [77]) have been found, which, upon cooling, already display non-Fermi liquid behaviour and might therefore be very close to a quantum critical point. In most heavy fermion systems, non-Fermi liquid behaviour has to be induced. Experimentally there are three main methods to tune a system towards a quantum critical point: doping, pressure, and magnetic field. Doping has the disadvantage that it induces disorder and it cannot be easily adjusted within a single sample. These problems are absent if pressure is used as the control parameter of the quantum phase transitions. However, the presence of a pressure cell makes many experiments difficult. For this reason, many recent experiments [78, 79, 80, 81, 82, 83, 84, 85, 86, 87, 88, 89] investigate field-tuned quantum critical behaviour, where an external magnetic field is used to control the distance from the quantum critical point.

A thorough discussion of antiferromagnetic quantum critical points tuned by doping, pressure, or by field is presented in [90]. We will just list a few examples for doping- and pressure-induced non-Fermi liquid behaviour and provide a slightly more comprehensive overview of field-tuned quantum critical points, since this will be the topic of chapter 5.

Doping has been used in a large number of systems, e.g. $CePtSi_{0.9}Ge_{0.1}$ [91], $UCu_5.6Al_6.4$ [91] and $CeCo_{1.2}Cu_{0.8}Ge_2$ [92]. In these three substances, the specific heat coefficient diverges logarithmically with temperature, which is at odds with Hertz-Millis theory.

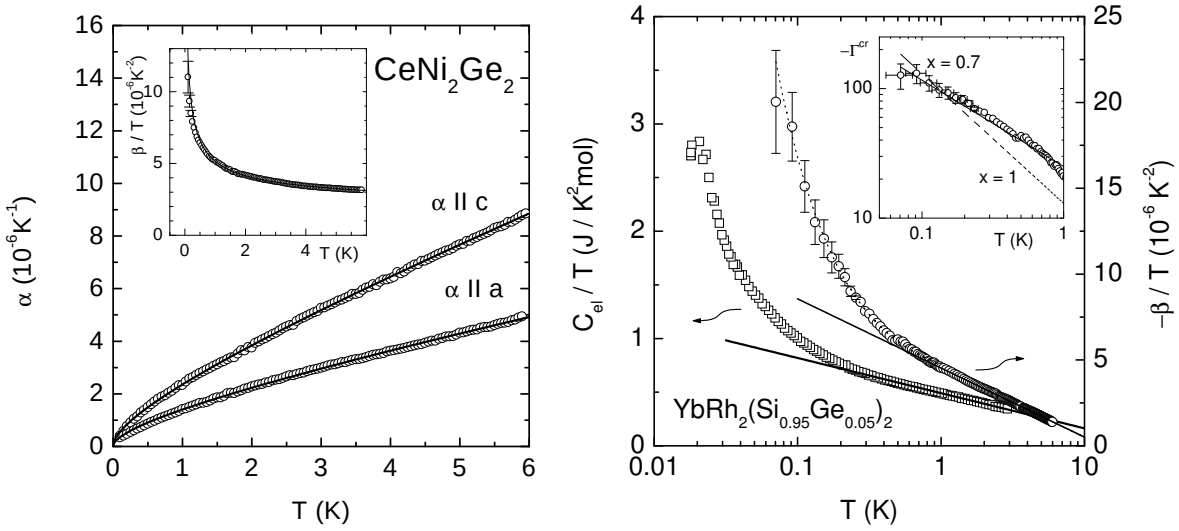

Figure 4.3.: Measurements of the thermal expansion coefficient at $B = 0$ in $CeNi_2Ge_2$ (left) and $YbRh_2(Si_{0.95}Ge_{0.05})_2$ (right). For $CeNi_2Ge_2$, $\alpha(T) = a\sqrt{T} + bT$, which fits spin-fluctuation theory (compare 4.1). In $YbRh_2(Si_{0.95}Ge_{0.05})_2$, neither of the two regimes is explained with spin-fluctuation theory: For $T > 1K$, $\beta/T \sim -\log(T_0/T)$ and for $T < 1K$, $\beta/T \sim a_0 + a_1/T$. Taken from [77].

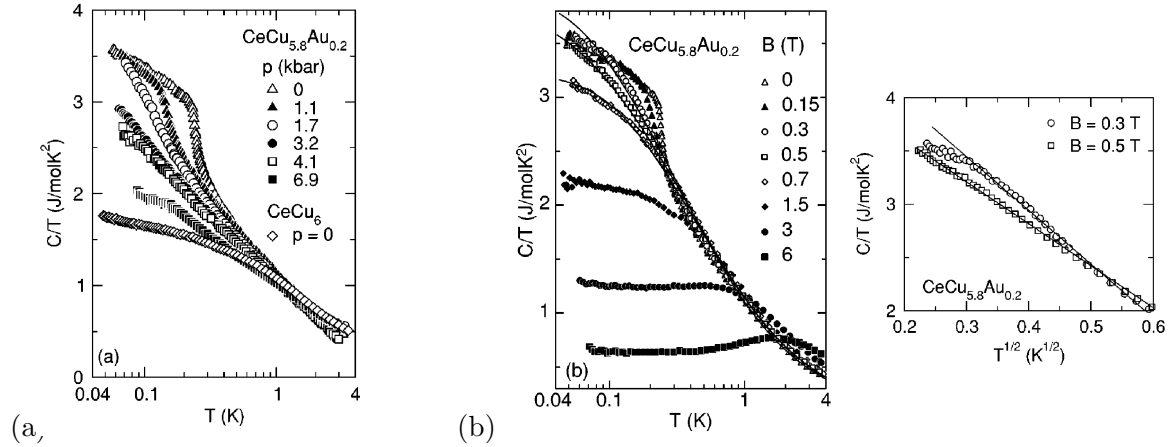

(a) (b)

Figure 4.4.: Pressure tuning (a) vs. field tuning (b) in $CeCu_{5.8}Au_{0.2}$: On the left, $C/T = a\log(T_0/T)$ whereas on the right, $C/T = \gamma_0 - a'T^{0.5}$. Taken from [79].

Pressure-tuned quantum critical points have been investigated in materials such as $CeRu_2Ge_2$, in which C/T is constant between 0.4 and 5 K [93], $CeCu_{5.8}Au_{0.2}$, in which $C/T \sim -\log T$ [94], and Ce_7Ni_3, whose specific heat coefficient also diverges logarithmically with temperature between 0.45 and 6 K [95].

Field-tuned quantum critical points have also been investigated in a number of experiments [78, 79, 80, 81, 82, 83]. For example in $CeCu_{5.2}Ag_{0.8}$ [78] and $CeCu_{5.8}Au_{0.2}$ [79] magnetic order can be suppressed by moderate magnetic fields. In these systems the quantum critical behaviour induced by a magnetic field B appears to be qualitatively different compared to the critical properties for vanishing field (controlled by pressure or doping) (see Fig. 4.4). In the presence of a field these systems seem to follow [78] the predictions from spin-fluctuation theory [53, 55, 96] for three-dimensional nearly antiferromagnetic metals, while this is not the case for $B = 0$ [94]. Similarly experiments [80] in field tuned $YbCu_{5-x}Al_x$ appear to be consistent with spin-fluctuation theory, which is not found to be the case in $YbRh_2Si_2$ where magnetic order is suppressed by tiny magnetic fields [81]. Recently, in $CeCoIn_5$ [84, 85] the superconducting order was suppressed by a magnetic field – it is at the moment a controversial question whether the observed anomalous behaviour is related to a superconducting quantum critical point or whether magnetism plays a role in this system. Very recent resistivity data under pressure [97] seems to indicate that the quantum critical point moves inside the superconducting dome to lower fields as pressure is increased. This points towards an antiferromagnetic quantum critical point.

Aside from (heavy fermion) metals, another interesting class of systems are insulators like $TlCuCl_3$ [87], $SrCu_2(BO_3)_2$ [88] or $BaCuSi_2O_6$ [89] where antiferromagnetic order can be induced by the application of a magnetic field B. These transitions [87] can be interpreted as a Bose-Einstein condensation of spin-1 excitations. The energy of the "spin-up" component of such triplets is lowered by B until it condenses at a critical field, $B = B_c$, thereby inducing antiferromagnetic order perpendicular to the magnetic field.

5. Field-tuned Quantum Phase Transitions

A large number of experiments on (possible) quantum critical points in metals have been carried out by using a magnetic field to tune through the phase diagram. Generally it is expected that the presence of a magnetic field changes the universality class of the transition as in its presence time reversal invariance is broken. We will therefore extend the original Hertz-Millis-Moriya theory of quantum critical points in metals and analyze theoretically the quantum critical behavior of a clean itinerant antiferromagnet in three dimensions subject to a static, spatially uniform external magnetic field B.

A magnetic field will have two main effects: first it will suppress (or in some cases [82] also induce) magnetic order. More interesting is the second effect: It induces a precession of the magnetic moments $\boldsymbol{S}$ perpendicular to the magnetic field

$$\partial_t \boldsymbol{S} = \boldsymbol{B} \times \boldsymbol{S} \tag{5.1}$$

and therefore modifies the dynamics of the order parameter. The linear time-derivative also translates to a dynamical exponent $z = 2$, and therefore the question arises how the precession competes with damping in a metal, which is characterized by the same dynamical critical exponent. For precession to occur, however, the system has to be reasonably isotropic, which is not the case for systems like $CeCu_{5.2}Ag_{0.8}$ [78] or $CeCu_{5.8}Au_{0.2}$ [79], where strong anisotropies prohibit the precession of the spin.

In the following, we study the interplay of ohmic damping and spin precession terms in the case of a nearly antiferromagnetic metal. First we present the model for the order parameter field and a short derivation of the effective action. Then we list the renormalization group equations for the parameters of the model and use them to derive the behavior of the correlation length. In the following sections we calculate the specific heat, thermal expansion, magnetocaloric effect, and susceptibility. We show for example that sufficiently large magnetic fields can induce sign changes in the critical contribution to the specific heat and that the susceptibility is particularly suited to probe the vicinity of the quantum critical point. Finally, we investigate the influence of the B-field on the scattering rate of the electrons. The work presented in this chapter has been published in [98].

5.1. Model and Effective action

Following the original arguments by Hertz [53], we describe the critical behaviour of an antiferromagnetic metal entirely in terms of an effective Ginzburg-Landau-Wilson theory of an order parameter field $\boldsymbol{\Phi}(\boldsymbol{r}, t)$ which represents the fluctuating (staggered) magnetization of the system. We restrict our considerations to the three-dimensional case, for which no argument against an order-parameter field theory has been found yet, see next chapter.

In the absence of a magnetic field the quadratic part of the action takes the form[53] (assuming negligible spin-orbit coupling)

$$S_2'[\mathbf{\Phi}] = \frac{1}{\beta}\int \frac{d^3k}{(2\pi)^3}\sum_n \Phi^*(r + k^2 + |\omega_n|)\Phi, \tag{5.2}$$

where r is a measure of the distance from the quantum critical point and momenta $\boldsymbol{k}$ are given relative to the antiferromagnetic ordering wave vector $\boldsymbol{Q}$. In the derivation of (5.2), the $|\omega_n|$ term results from the (Landau-) damping of the spin-fluctuations by gapless fermionic excitations in the vicinity of points on the Fermi surface that are connected by $\boldsymbol{Q}$ (assuming $Q < 2k_F$). In the low-frequency limit, damping dominates over a term $\propto \omega^2$, which is allowed by symmetry. Since frequencies scale quadratically with momentum in (5.2), the model has a dynamical critical exponent $z = 2$. In the case of a ferromagnet, Landau damping would assume the form $|\omega_n|/k$ and result in a dynamical critical exponent $z = 3$.

Three modifications to (5.2) will arise in the presence of a magnetic field. First, $r = r(B)$ will acquire a magnetic field dependence, for example, r will grow for larger fields in systems where antiferromagnetism is suppressed by B. Second, the magnetic field breaks the rotational invariance and components of Φ parallel and perpendicular to $\boldsymbol{B}$ will have different masses, r_z and $r_\perp$, respectively. Third, as argued above, the magnetization will precess around $\boldsymbol{B}$; this is described by an extra term (in coordinate and time space for convenience)

$$\begin{aligned} S_2^{pr}[\mathbf{\Phi}] &= \int_0^\beta d\tau \int d\mathbf{r}\, \boldsymbol{b}\cdot \mathrm{i}(\mathbf{\Phi}\times\partial_t\mathbf{\Phi}) \\ &= \iint b(\mathrm{i}\Phi_x\partial_t\Phi_y - \mathrm{i}\Phi_y\partial_t\Phi_x) = \iint b\tilde{\Phi}_\perp^*\partial_t\tilde{\Phi}_\perp \end{aligned} \tag{5.3}$$

in the effective action, where $\boldsymbol{b}$ is parallel to $\boldsymbol{B}$ (taken to point into the $\hat{z}$-direction) and we have introduced the complex field $\tilde{\Phi}_\perp = \Phi_x + \mathrm{i}\Phi_y$. The term (5.3) arises when $(\partial_t\mathbf{\Phi})^2$ is replaced by $(\partial_t\mathbf{\Phi} - \mathrm{i}\boldsymbol{B}\times\mathbf{\Phi})^2$, since the field acquires an additional precession $d\mathbf{\Phi} = \boldsymbol{B}\times\mathbf{\Phi}dt$ in the time dt. Note that (5.3) breaks time-reversal invariance, and such a term is therefore absent for $\boldsymbol{B} = 0$.

We have deduced the form of the effective action on phenomenological grounds but it can also be derived from a more explicit calculation. Starting point is a Hubbard-type model of electrons moving in the presence of a magnetic field:

$$H = \sum_{\boldsymbol{k}\sigma}(\epsilon_{\boldsymbol{k}} + B\sigma^z_{\sigma\sigma})\psi^\dagger_{\boldsymbol{k}\sigma}\psi_{\boldsymbol{k}\sigma} + U\sum n_\downarrow n_\uparrow. \tag{5.4}$$

Here, the magnetic field, which is taken to point along the z-direction, enters only via a Zeeman-term; orbital effects are neglected, assuming that Landau levels are broadened by disorder or thermal effects. Indeed, in the experimentally most relevant heavy Fermion systems, orbital effects are strongly suppressed compared to contributions from the Zeeman term as the effective masses and magnetic susceptibilities are very large in those systems [99].

For simplicity, a commensurate antiferromagnet will be assumed; incommensurate antiferromagnets show the same qualitative behavior for all quantities discussed below. Following

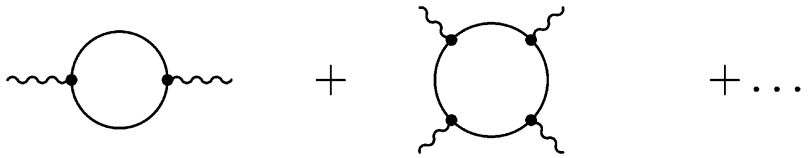

Figure 5.1.: When the fermionic fields are integrated out in (5.6) to obtain an effective action for the bosonic order parameter field, one-loop diagrams with fermionic internal lines and an even number of bosonic external lines are created.

Hertz's scheme outlined in the introduction, we introduce a real order parameter vector $\mathbf{\Phi}(\boldsymbol{x}, t)$ as a Hubbard-Stratonovich field by inserting a Gaussian integral

$$\int \mathcal{D}\mathbf{\Phi} \exp\left\{ \int d\tau \int d^3x \, \frac{1}{J} \mathbf{\Phi}^2_{\boldsymbol{x},\tau} \right\} \tag{5.5}$$

in the partition sum for the system, where J is the interaction in the spin-spin channel. The field $\mathbf{\Phi}$ is shifted, $\mathbf{\Phi} \to \mathbf{\Phi} + \mathrm{i}(\psi^\dagger \boldsymbol{\sigma} \psi)/2$, to decouple the spin-density part $J(\psi^\dagger \boldsymbol{\sigma} \psi)^2/4$ of the interaction term of (5.4). This leads to the following action:

$$S = \int d\tau \int d^3x \left(\psi^\dagger_{\tau,\boldsymbol{x},\sigma} \left((g_0)^{-1} \delta_{\sigma\sigma'} + \mathrm{i} \mathbf{\Phi}_{\tau,\boldsymbol{x}} \, \boldsymbol{\sigma}_{\sigma\sigma'} \right) \psi_{\tau\boldsymbol{x},\sigma'} + \frac{1}{J} \mathbf{\Phi}^2_{\tau,\boldsymbol{x}} \right), \tag{5.6}$$

where $g_0^{-1} = \mathrm{i}\omega_n - \epsilon_{\boldsymbol{k}} - B\sigma^z$ in momentum and frequency space. The action is now quadratic in the fermionic field as well as the order parameter field, and the electronic quasiparticles can subsequently be integrated out to obtain an effective action for the order parameter alone:

$$\begin{aligned} \int \mathcal{D}\psi^\dagger \mathcal{D}\psi \exp\left\{ \int d\tau \int d^3x \, \psi^\dagger (g_0^{-1} + \mathrm{i}\mathbf{\Phi}\boldsymbol{\sigma}) \psi \right\} &= \det\left[g_0^{-1} + \mathrm{i}\boldsymbol{\sigma}\mathbf{\Phi} \right] \\ &= \det\left[g_0^{-1} (1 + \mathrm{i} g_0 \boldsymbol{\sigma}\mathbf{\Phi}) \right] \\ &= C \exp\left\{ \mathrm{Tr} \ln(1 + \mathrm{i} g_0 \boldsymbol{\sigma}\mathbf{\Phi}) \right\} \\ &= C \exp\left\{ \sum_{n=1}^{\infty} \frac{(-1)^n}{n!} \mathrm{Tr} (\mathrm{i} g_0 \boldsymbol{\sigma}\mathbf{\Phi})^n \right\} \end{aligned}$$

This generates infinitely many interaction terms with coefficients given by diagrams of the form shown in Fig. 5.1. We truncate the effective action, retaining the leading frequency and momentum dependence of the Gaussian part of the action as well as a constant $\mathbf{\Phi}^4$ interaction term, since all other terms are irrelevant in the renormalization group sense [53, 55] (cubic terms are discussed in appendix A.1). For the quadratic part one obtains $S_2 = \frac{1}{\beta} \sum_{\omega,\boldsymbol{k}} \Phi^\alpha_{\omega_n,\boldsymbol{k}} (\delta_{\alpha\alpha'}/J + \chi^0_{\alpha\alpha'}(\boldsymbol{k}, \mathrm{i}\omega_n)) \Phi^{\alpha'}_{-\omega_n,-\boldsymbol{k}}$ where $\chi^0_{\alpha\alpha'}(\boldsymbol{k}, i\omega_n)$ is the susceptibility in the presence of the finite field $\boldsymbol{B}$ evaluated at $J = 0$ (first diagram in fig. 5.1). These susceptibilities can now be calculated on the paramagnetic side of the transition, see e.g. [100]. We obtain in momentum space

$$S = S_2[\mathbf{\Phi}] + S_4[\mathbf{\Phi}], \tag{5.7}$$

where

$$S_2[\mathbf{\Phi}] = \frac{1}{\beta}\int \frac{d^3k}{(2\pi)^3}\sum_n \mathbf{\Phi}^T_{\omega_n,\boldsymbol{k}} \begin{pmatrix} r_\perp + |\omega_n|\cos\theta + k^2 & \omega_n \sin\theta & 0 \\ -\omega_n \sin\theta & r_\perp + |\omega_n|\cos\theta + k^2 & 0 \\ 0 & 0 & r_z + |\omega_n| + k^2 \end{pmatrix} \mathbf{\Phi}_{\omega_{-n},-\boldsymbol{k}}$$

$$S_4[\mathbf{\Phi}] = \frac{g}{\beta^4}\int \frac{d^3k_1}{(2\pi)^3}\cdots\frac{d^3k_4}{(2\pi)^3}\sum_{n_1\ldots n_4}\delta(\boldsymbol{k}_1+\boldsymbol{k}_2+\boldsymbol{k}_3+\boldsymbol{k}_4)\delta_{n_1+n_2+n_3+n_4}\times (\mathbf{\Phi}_{\omega_{n_1},\boldsymbol{k}_1}\cdot\mathbf{\Phi}_{\omega_{n_2},\boldsymbol{k}_2})(\mathbf{\Phi}_{\omega_{n_3},\boldsymbol{k}_3}\cdot\mathbf{\Phi}_{\omega_{n_4},\boldsymbol{k}_4}). \tag{5.8}$$

Here $\beta = 1/k_BT$ and $\omega_n = 2\pi n/\beta$ is a Matsubara frequency and $\boldsymbol{k}$ is measured again from the ordering wave vector. The coefficients of $\boldsymbol{k}^2$ and $|\omega_n|\cos\theta$ have been made unity by an appropriate choice of the bare length scale ξ_0 and temperature/energy scale T_0. In general the prefactors of the k^2 and $|\omega|$ terms for Φ_z and $\Phi_{x/y}$ will be different (even after rescaling), we suppress these prefactors to keep the notations simple as they will not lead to any qualitative changes in the results. It is, however, essential to keep track of the dynamics of $\Phi_{x/y}$, i.e. of the ratio of precession and damping terms parametrized by an angle θ. For small θ the dynamics is overdamped, while for $\theta \sim \pi/2$ precession dominates. The value of θ depends on details of the band-structure and the size of the magnetic field with $\theta \propto B$ for small magnetic fields.

As anticipated in (5.3), the $x-$ and $y-$direction are coupled for $\theta > 0$. The Gaussian part of the action can be diagonalized by introducing the complex field $\Phi^\perp \equiv (\Phi_x + \mathrm{i}\Phi_y)/\sqrt{2}$ as above, and we obtain

$$S_2[\Phi^\perp,\Phi^z] = \int \frac{d^3k}{(2\pi)^3\beta}\sum_n \Phi^\perp_{\omega_n,\boldsymbol{k}}{}^*(2\chi_{\boldsymbol{k}}(\mathrm{i}\omega_n)^{-1})\Phi^\perp_{\omega_n,\boldsymbol{k}} + \Phi^z_{\omega_n,\boldsymbol{k}}(k^2+r_z+|\omega_n|)\Phi^z_{-\omega_n,-\boldsymbol{k}}, \tag{5.9}$$

where

$$\chi_{\boldsymbol{k}}(\mathrm{i}\omega_n) \equiv (k^2 + r_\perp + |\omega_n|\cos\theta - \mathrm{i}\omega_n\sin\theta)^{-1} \tag{5.10}$$

is the propagator of $\Phi^\perp$.

As expected from the symmetry arguments given above, $r_\perp$ and r_z turn out to be different with $r_z > r_\perp$ and $r_z - r_\perp \propto B^2$ for small B. As $r_{z/\perp}$ increases for increasing fields ($r(B) \approx r(0) + cB^2$ for small B), an antiferromagnetic system sufficiently close to its quantum critical point can be tuned to the paramagnetic phase by applying a magnetic field (assuming that no first order transition is induced).

For the discussion of the behaviour close to the quantum critical point it is important to note that the magnetic field enters into the calculations in the form of a B-dependent r as well as through the B-dependence of the angle θ. We will see that whereas θ is marginal (in the renormalization group sense), r is a relevant operator close to the quantum critical point. If the quantum critical point can be reached with a finite magnetic field B_c, $\theta(B) \approx \theta(B_c)$ can be approximated by a constant (as checked below) while it is obviously essential to keep track of the leading B dependence of the control parameter $r(B) \propto B - B_c$.

5.1.1. Magnetic insulators

The derivation of the effective action sketched above is obviously geared towards a metallic magnet, not an insulator. It turns out, however, that a critical theory for magnetic insulators such as $TlCuCl_3$ [87] or $SrCu_2(BO_3)_2$ [88] is already captured by (5.8) with $\theta = \pi/2$. Note that the situation is different for $BaCuSi_2O_6$ [89], which is – in its ordered phase – a frustrated antiferromagnet; a brief discussion of the expected critical behaviour will be presented in Appendix A.2.

The insulators we want to describe with (5.8) are dimer spin systems where the ground state consists of a singlet configuration of spin-1/2-particles on each dimer site in the absence of pressure or magnetic field. Excitations in the form of triplets are gapped. Either pressure or an external magnetic field reduces this gap and can be used to tune the system into an antiferromagnetic phase where the ground state consists of triplet configurations on each dimer site, making the system effectively a spin-1 system. The low-energy properties of antiferromagnetically coupled spin systems can be extracted from an $O(3)$ quantum rotor model (for $S = 1$), which describes a particle constrained to move on the surface of a 3-dimensional sphere via a 3-component unit vector $\hat{\boldsymbol{n}}$ with $\hat{\boldsymbol{n}}^2 = 1$. The form of the action for such a rotor model is determined by symmetry requirements [52]:

$$S = \int d\tau \int d^3x ((\partial_\tau \hat{\boldsymbol{n}})^2 + c^2 (\nabla_x \hat{\boldsymbol{n}})^2). \tag{5.11}$$

If the constraint $\hat{\boldsymbol{n}}^2 = 1$ is relaxed by introducing a coarse-grained field $\boldsymbol{\Phi}_{\tau,x} = \sum_{\mathcal{N}_x} \hat{\boldsymbol{n}}_{\tau,x}$, where $\mathcal{N}_x$ is a neighbourhood of x, then the amplitude of $\boldsymbol{\Phi}$ is allowed to vary over a wide range. As a consequence, the action for $\boldsymbol{\Phi}$ now has to contain a potential $V(\boldsymbol{\Phi})$ as well to restrict amplitude fluctuations, which leads to an action of the form

$$S = \int d\tau \int d^3x \left((\partial_\tau \boldsymbol{\Phi})^2 + c^2 (\nabla_x \boldsymbol{\Phi})^2 + m\, \boldsymbol{\Phi}^2 + u\, \boldsymbol{\Phi}^4 \right). \tag{5.12}$$

In this action, an external magnetic field is incorporated by replacing the time derivative ∂_τ (in imaginary time) with $(\partial_\tau + \mathrm{i}\boldsymbol{B}\times)$, and one retrieves (5.8) for $\theta = \pi/2$.

For insulating systems the physics of the precession term has been widely discussed [52, 101, 102, 103, 104, 105]. The corresponding quantum critical behaviour as a function of magnetic field of such an insulating magnet in an external field is actually well known: it is expected to be in the same universality class as the quantum phase transition of a low-density interacting Bose-Einstein condensate as a function of chemical potential. The relation of (5.8) to Bose-Einstein condensation for $\theta = \pi/2$ can be made apparent in the following way. We consider $S_2[\Phi^\perp]|_{\theta=\pi/2}$ in coordinate and time space. The Gaussian part of $S_2[\Phi^\perp]$ is minimized for a field $\Phi^\perp$ that obeys the equation

$$\mathrm{i}\partial_t \Phi^\perp = H\Phi^\perp, \quad H = (-\nabla^2 + r_\perp). \tag{5.13}$$

This has the form of a Schrödinger equation for a particle in a constant potential given by $V = r_\perp$. When the interaction is added, this is turned into a non-linear Schrödinger equation or Gross-Pitaevskii equation which describes the physics of weakly interacting Bosons. In this interpretation, $r_\perp$ takes over the role of the chemical potential, and the quantum critical

point of a field tuned insulating antiferromagnet ($\theta = \pi/2$) is therefore in the same universality class as the quantum phase transition of a dilute gas of Bosons driven by a chemical potential. The non-magnetic phase ($r_\perp > 0$) corresponds to a phase with negative chemical potential where no Bosons are present in the $T \to 0$ limit, while the Bose-Einstein condensed phase corresponds to the magnetically ordered phase.

5.2. Renormalization group equations and correlation length

The physical properties of the effective action (5.8) can be analyzed with the help of renormalization group equations. As a first step it is useful to perform a simple scaling analysis of $S[\mathbf{\Phi}]$. When momenta, frequencies and fields are rescaled as $k' = kb$, $\omega' = \omega b^z$, where z is the dynamical critical exponent, and $\Phi' = \Phi b^{-\frac{d+z+2}{2}}$, $S[\mathbf{\Phi}]$ remains invariant under scaling provided that $z = 2$. The masses $r^{\perp,z}$ and the dimensionless coupling constant $u \equiv g\xi_0^d/T_0$ have the scaling dimensions 2 and $4-(d+z)$, respectively. In an antiferromagnetic metal, damping as well as precession are linear in frequency and the terms therefore behave in the same way under scaling. In the renormalization group terminology this implies that the precession term is an "exactly marginal" perturbation with respect to Hertz' fix-point ($\theta = 0, u = 0$) which can be expected to modify the behavior of the system at the quantum critical point.

The scaling dimension of r and the dynamical critical exponent z determine the crossover line between quantum critical and Fermi liquid behaviour for the antiferromagnetic metal, where thermal and quantum fluctuations are of comparable energy:

$$k_B T \sim \hbar\omega_c \sim \hbar\xi_\tau^{-1} \sim \hbar\xi_r^{-z} \sim \hbar r^{z/2} \overset{z=2}{\sim} \hbar r. \tag{5.14}$$

We therefore have to distinguish two regimes: for $T \ll r$, quantum fluctuations are negligible and the system behaves like a Fermi liquid (or thermally activated for $\theta = \pi/2$). For $r \ll T$, the system will exhibit quantum critical behaviour.

The total dimensionality of a three-dimensional antiferromagnet is $d + z = 5$, which puts the system above its upper critical dimension $d_c^+ = 4$. As a consequence, the critical behaviour should be identical to that predicted by mean-field theory, and it is possible that non-universal corrections to thermodynamic quantities arise from the Φ^4-interaction term. We will see later that this is indeed the case in this model.

Close to a (quantum) phase transition, the behaviour of a system is dominated by low-energy, long-wavelength fluctuations. This can best be extracted from a RG-calculation, in which the high-energy degrees of freedom are successively integrated out until a fixed point is reached in the low-energy limit. Since the three-dimensional antiferromagnet is above its upper critical dimension, we already know that this fixed point will be Gaussian, but we can still use the RG-equations to determine the correlation length of the system.

The renormalization group equations for the parameters T, r, and u with corrections to scaling can be obtained by closely following the procedure employed by Millis [55]: We introduce UV-cutoffs in the momentum and frequency integrals of a linked cluster expansion of the

free energy and express changes of these cutoffs in terms of changes of the parameters of the model. The RG equations are as follows:

$$\frac{\partial \mathcal{T}(b)}{\partial \log b} = z\,\mathcal{T}(b), \tag{5.15}$$

$$\frac{\partial r_\perp(b)}{\partial \log b} = 2r_\perp(b) + 4u(b)\big(2f_2^\perp(r_\perp(b),\mathcal{T}(b)) + f_2^z(r_z(b),\mathcal{T}(b))\big), \tag{5.16}$$

$$\frac{\partial r_z(b)}{\partial \log b} = 2r_z(b) + 4u(b)\big(f_2^\perp(r_\perp(b),\mathcal{T}(b)) + 3f_2^z(r_z(b),\mathcal{T}(b))\big), \tag{5.17}$$

$$\frac{\partial u(b)}{\partial \log b} = (4-(d+z))u(b), \tag{5.18}$$

where $\mathcal{T}$ is the running temperature. The expressions for $f_2^{\perp,z}$ as well as details of the calculation can be found in appendix A.3. For an antiferromagnetic system in 3 spatial dimensions, $d+z=5$; the scaling dimension for u is therefore negative, and we only need to consider contributions up to and including first order in u. To this order, the scaling law for u remains unmodified. In addition, since θ can only get finite corrections from contributions at least of order $\mathcal{O}(u^2)$, θ remains unrenormalized to first order in u.

Equations (5.15) and (5.18) are solved trivially. As $r_z(b) > r_\perp(b)$, Φ_z remains massive at the quantum critical point ($r_z > 0$ for $r_\perp = 0$). In the following we will concentrate on the regime $T < r_z$, where the influence of the parallel mode Φ_z can be absorbed in a redefinition of the bare $r_\perp$.

Eq. (5.16) can be solved for low temperatures in the limits $r_\perp/T \ll 1$ and $r_\perp/T \gg 1$, corresponding to the quantum critical and (renormalized) Fermi liquid regime, respectively (see Fig. 4.1). This provides us with an expression for the correlation length $\xi_\perp$. We refer to appendix A.3 for details of the calculation. In the quantum critical regime $\xi_\perp^{-2}$ is given by

$$\xi_\perp^{-2}(r_\perp \ll T) = r_\perp + 16\sqrt{2}\pi^{3/2}\,\zeta(3/2)\,uT^{3/2}\,\cos(\theta/2), \tag{5.19}$$

and in the Fermi liquid regime it has the form

$$\xi_\perp^{-2}(T \ll r_\perp) = r_\perp + \frac{16}{3}\pi^3 uT^2 r_\perp^{1/2}\cos\theta. \tag{5.20}$$

For all $\theta < \pi/2$ one obtains the same qualitative behavior as in the case of vanishing external magnetic field [55]. Only in the Fermi liquid regime for $\theta = \pi/2$, the T^2 correction is suppressed as Landau damping is absent in this limit and our model is characterized by an energy gap which leads to an exponential dependence $\exp(-r_\perp/T)$ of the correlation length.

5.3. Thermodynamic quantities

Predictions for thermodynamic quantities are particularly suited for making contact with experimental data. Quantum critical behaviour shows up in the form of unusual exponents in the temperature and field dependence of e.g. the specific heat, and a large body of experimental data is available for comparison.

The free energy can be calculated directly from RG equations following again Ref. [55]. However, as the quartic coupling u is irrelevant, the leading behavior in the paramagnetic phase can equivalently be extracted just from the Gaussian free energy (measured in units of T_0V/ξ_0^3):

$$\begin{aligned} e^{-\beta F} &= \frac{1}{Z}\int \mathcal{D}\Phi_\perp e^{-S_2[\Phi_\perp]} \\ \Longrightarrow F = -T\ln Z &= \frac{T}{2}\frac{T_0V}{\xi_0^3}\int\frac{d^3k}{(2\pi)^3}\sum_n \ln\left[\det\begin{pmatrix}\chi^{-1} & 0\\ 0 & (\chi^{-1})^*\end{pmatrix}\right] \\ &= -\frac{1}{4}\frac{T_0V}{\xi_0^3}\int\frac{d^3k}{(2\pi)^3}\int\frac{d\omega}{\pi}\coth\left(\frac{\beta\omega}{2}\right)\arctan\left(\frac{2(r+k^2)\omega\cos\theta}{(r+k^2)^2-\omega^2}\right), \end{aligned} \tag{5.21}$$

where χ is given in 5.10 and we have set $r \equiv r_\perp$. We will compute thermodynamic quantities from the dimensionless free energy density defined as

$$\begin{aligned} \mathcal{F} &\equiv \frac{\xi_0^3}{T_0V}(F - F(T=0)) \\ &= -\frac{1}{4}\int\frac{d^3k}{(2\pi)^3}\int\frac{d\omega}{\pi}\left[\coth\left(\frac{\beta\omega}{2}\right)-1\right]\arctan\left(\frac{2(r+k^2)\omega\cos\theta}{(r+k^2)^2-\omega^2}\right), \end{aligned} \tag{5.22}$$

where the zero temperature contribution to the free energy has been subtracted so that $\mathcal{F}(T=0)=0$. The expression for the free energy simplifies greatly for $\theta=\pi/2$ and $T \ll r$:

$$\mathcal{F}_{\theta=\pi/2} = \frac{\sqrt{\pi}}{(2\pi)^3}\,T^{5/2}\,e^{-r/T}. \tag{5.23}$$

In this case, the free energy depends exponentially on $-r/T$, and so will thermodynamic quantities. This thermally activated behaviour is to be expected for systems with a gapped spectrum (5.13).

In Eq. (5.22) and in the results shown below we ignore contributions from the mode Φ_z, which is after all characterized by a finite mass r_z at $r_\perp = 0$ and therefore non-critical. To leading order, the corresponding (analytic) corrections to the free energy and its derivative are just additive and can be obtained by replacing r by r_z, by setting $\theta = 0$ and by dividing the result by a factor 2 (as there are two modes perpendicular to B) in all formulas for thermodynamic quantities given below.

In the following subsections we calculate the specific heat γ, the temperature dependence of the magnetization, the magnetocaloric effect Γ_B, and the susceptibility.

5.3.1. Specific heat

We first consider the specific heat coefficient $c/T = \gamma(T,r) = -\partial^2\mathcal{F}/\partial T^2$. More precisely, to obtain a finite result, we calculate the critical contribution to the specific heat coefficient, i.e. $\tilde{\gamma} \equiv \gamma(T,r) - \gamma(T=0,r=0)$:

$$\begin{aligned} \tilde{\gamma} = \frac{1}{4}\int\frac{d^3k}{(2\pi)^3}\int\frac{dx}{\pi}\frac{2x}{e^x-1} \\ \left[\frac{(k^2+r)^3\left(4(k^2+r)^2((k^2+r)^2+2T^2x^2)\cos\theta + 4T^4x^4\cos(3\theta)\right)}{\left((k^2+r)^4+T^4x^4+2(k^2+r)^2T^2x^2\cos(2\theta)\right)^2} - \frac{4\cos\theta}{k^2}\right], \end{aligned} \tag{5.24}$$

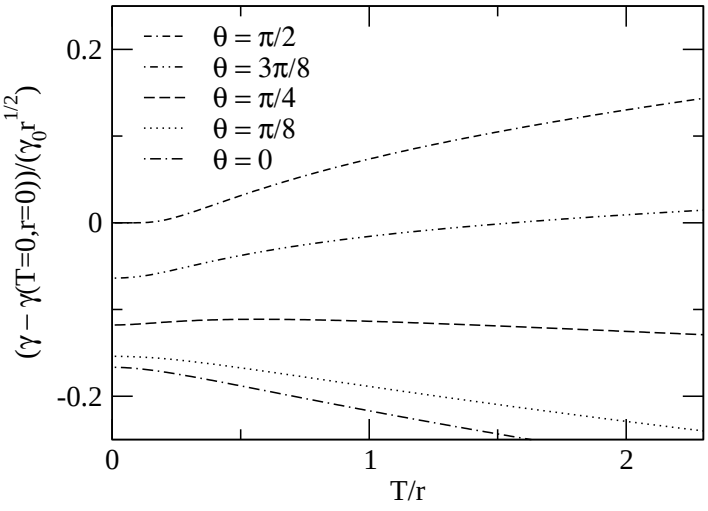

Figure 5.2.: Scaling function for the specific heat coefficient $\frac{1}{\sqrt{r}}\tilde{\gamma}$, where a non-critical contribution has been subtracted, $\tilde{\gamma} = \gamma(T,r) - \gamma(T=0,r=0)$. The function is not completely universal but depends on the parameter θ. A crossover from $\tilde{\gamma} \propto \pm T^2$ for $T \ll r$ to $\tilde{\gamma} \sim \pm\sqrt{T}$ for $r \ll T$ can be observed, where the signs depend on the value of θ. $\tilde{\gamma}(T)$ shows a maximum for $\pi/6 < \theta < \pi/3$ as can be seen more clearly in Fig. 5.3.

this differs from the physical specific heat by a $T-$independent (but UV-cutoff-dependent) constant $\gamma_c \cos\theta$.

The integrals can be evaluated exactly in certain limits. For $\theta = \pi/2$ and low $T \ll r$ the specific heat shows thermally activated behavior

$$\gamma(\theta = \pi/2, T \to 0) = \frac{\sqrt{\pi}}{(2\pi)^3} \frac{r^2}{T^{3/2}} \exp\Big[-\frac{r}{T}\Big]. \tag{5.25}$$

For $r \ll T$ and $T \ll r$, i.e. in the quantum critical regime and Fermi liquid regime, respectively, we obtain for $\theta < \pi/2$:

$$\tilde{\gamma}(r \ll T) = -\frac{15\sqrt{2\pi}}{32\,\pi^2}\zeta\left(\frac{5}{2}\right) T^{1/2} \cos\left(\frac{3}{2}\theta\right), \tag{5.26}$$

$$\tilde{\gamma}(T \ll r) = -\frac{1}{6} r^{1/2}\cos\theta - \frac{\pi^2}{60}\frac{T^2}{r^{3/2}}\cos(3\theta). \tag{5.27}$$

For $\theta = 0$, this reproduces well-known results [55] (correcting some factors of 2), and as expected from scaling, exponents remain unchanged in the presence of the precession term. However, precession influences not only the size of the prefactors but interestingly also induces sign changes when the dynamics begins to be dominated by precession rather than damping. In the quantum-critical regime the $\sqrt{T}$ correction is negative for $\theta < \pi/3$ and positive for $\theta > \pi/3$. In the Fermi liquid regime a sign change can be observed in the $T^2/r^{3/2}$ contribution at $\theta = \pi/6$.

Fig. 5.2 shows the scaling function $\frac{\tilde{\gamma}(T,r)}{\sqrt{r}} = f_\theta(T/r)$, which was obtained from a numerical integration of (5.24). Due to the presence of an exactly marginal perturbation, the scaling

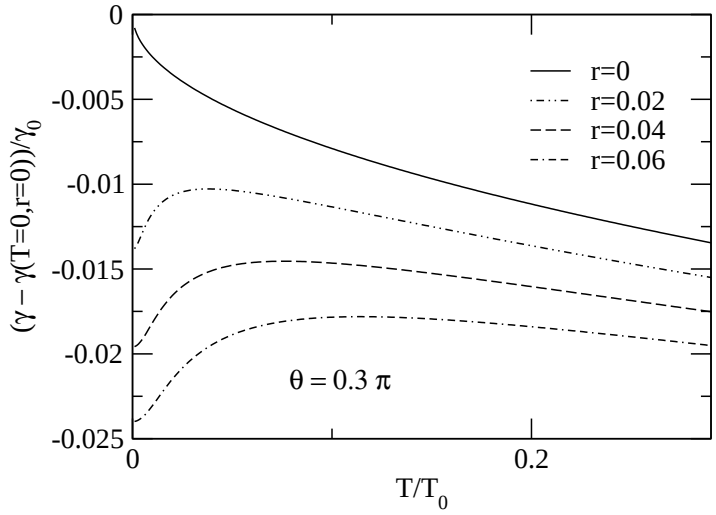

Figure 5.3.: Specific heat coefficient as a function of temperature for $\theta = 0.3\pi$ and different values of r. Note that the total specific heat coefficient γ is always positive. The maximum for $r > 0$ is characteristic for systems with $\pi/6 < \theta < \pi/3$.

function is not completely universal but depends on the parameter θ. In an intermediate regime, $\pi/6 < \theta < \pi/3$, $\gamma(T, r)$ (and the universal scaling function $\frac{\tilde{\gamma}(T,r)}{\sqrt{r}}$) shows a characteristic maximum as a function of temperature as can be read off from the asymptotical results (5.26) and (5.27). This maximum cannot be seen directly at the quantum critical point ($r = 0$) but for any finite $r > 0$ as long as the critical corrections to the specific heat dominate the non-critical ones.

5.3.2. Magnetization, magnetocaloric effect and Grüneisen parameter

As was argued in Ref. [106], the specific heat is not the most sensitive thermodynamic quantity close to a quantum critical point as it tracks only variations of the free energy with respect to temperature (vertical axis in Fig. 4.1) but not with respect to the control parameter B (horizontal axis). Quantities that depend also on the control parameter are e.g. the magnetization $M = -\partial F/\partial B$, the susceptibility $\chi = -\partial^2 F/\partial B^2$, and the T-derivative of M, $\partial M/\partial T = -\partial^2 F/(\partial B \partial T) = -\partial S/\partial B$. The mixed derivative has the advantage that – in contrast to specific heat coefficient and susceptibility – it vanishes in the $T \to 0$ limit due to the second law of thermodynamics. This makes a comparison to measurements of $\partial M/\partial T$ easier, since it is not necessary to subtract any constant non-critical contributions from experimental data.

Not only the termodynamic derivatives themselves but also their ratios can yield valuable information on the nature of a quantum critical point [106]. For a field tuned critical point, one such combination is

$$\Gamma_B = -\frac{(\partial M/\partial T)_B}{T\gamma} = -\frac{1}{T}\frac{(\partial S/\partial B)_T}{(\partial S/\partial T)_B} = \frac{1}{T}\left.\frac{\partial T}{\partial B}\right|_S . \tag{5.28}$$

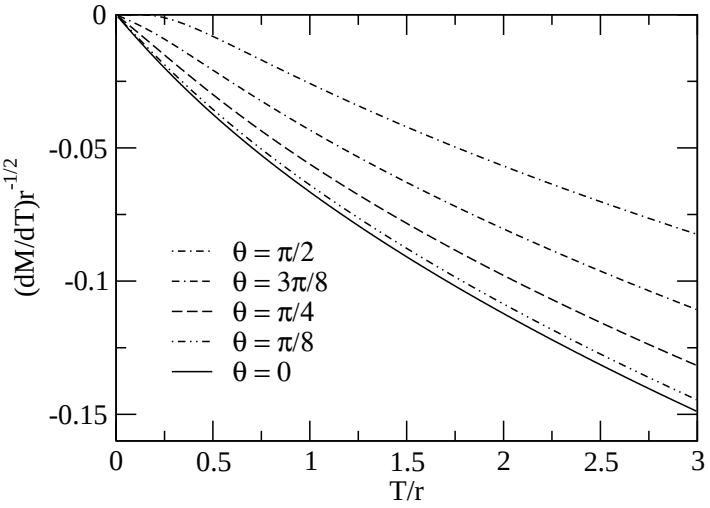

Figure 5.4.: Scaling function $\frac{1}{\sqrt{r}}\frac{\partial M}{\partial T}$. While for the specific heat shown in Fig.5.3 it was necessary to subtract a non-critical constant contribution such a background does not exist for $\frac{\partial M}{\partial T}$.

This describes the temperature change in the sample after an adiabatic change of the magnetic field, the so-called magnetocaloric effect. This quantity is constant close to a classical transition but has been shown to diverge as $T^{-1/(\nu z)}$ at a quantum critical point [106], which makes it ideally suited for identifying quantum critical points.

For pressure-tuned quantum phase transitions, where $\partial/\partial B$ is replaced by $\partial/\partial p$, the quantities related to $\partial M/\partial T$, χ and Γ_B are the thermal expansion, the compressibility (and therefore also to the sound velocity), and the Grüneisen parameter [106].

Both the control parameter r and θ depend on B; we can therefore expect two independent critical contributions to $\partial M/\partial T$:

$$\begin{aligned}\frac{\partial M}{\partial T} &= -\frac{\partial^2 \mathcal{F}}{\partial T \partial r}\frac{\partial r}{\partial B} - \frac{\partial^2 \mathcal{F}}{\partial T \partial \theta}\frac{\partial \theta}{\partial B} \\ &= \frac{1}{4}\int \frac{d^3k}{(2\pi)^3}\int \frac{d\omega}{\pi}\left(\frac{2e^{\omega/(2T)}}{e^{\omega/T}-1}\right)^2 \frac{\omega^2}{T^2}\Bigg(\frac{((k^2+r)^2+\omega^2)\cos\theta}{((k^2+r)^4+\omega^4+2(k^2+r)^2\omega^2\cos(2\theta)}\frac{\partial r}{\partial B} \\ &\quad + \frac{(k^2+r)^2((k^2+r)^2-\omega^2)\sin\theta}{((k^2+r)^2-\omega^2)^2+4(k^2+r)^2\omega^2\cos^2(\theta)}\frac{\partial \theta}{\partial B}\Bigg). \end{aligned} \tag{5.29}$$

In the limits $r, T \to 0$ we obtain

$$\begin{aligned}\frac{\partial M}{\partial T}_{r\ll T} &= -\frac{3\sqrt{2\pi}}{16\pi^2}\zeta\left(\frac{3}{2}\right)\sqrt{T}\cos\left(\frac{\theta}{2}\right)\frac{\partial r}{\partial B} \\ &\quad - \frac{15\sqrt{2\pi}}{32\pi^2}\zeta\left(\frac{5}{2}\right)T^{3/2}\sin\left(\frac{3}{2}\theta\right)\frac{\partial \theta}{\partial B}, \end{aligned} \tag{5.30}$$

$$\frac{\partial M}{\partial T}_{T\ll r} = -\frac{1}{12}\frac{T}{\sqrt{r}}\cos\theta\frac{\partial r}{\partial B} - \frac{1}{6}\sqrt{r}T\sin\theta\frac{\partial \theta}{\partial B}. \tag{5.31}$$

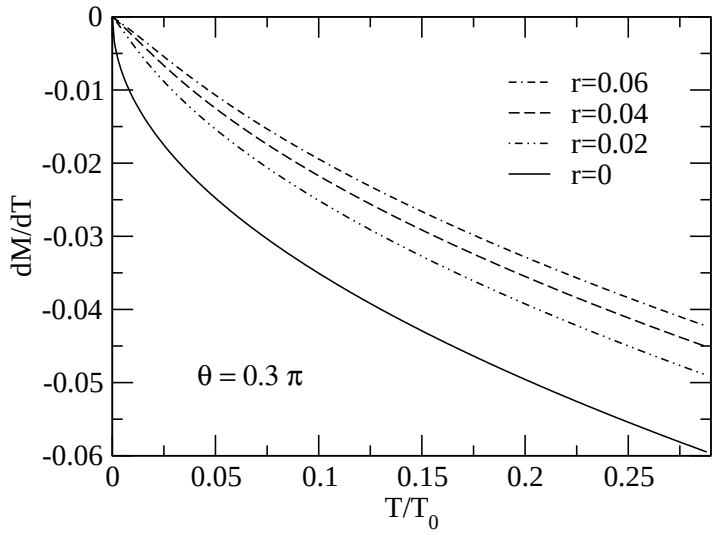

Figure 5.5.: $\frac{\partial M}{\partial T}$ as a function of temperature for $\theta = 0.3\pi$ and different values of r. At the quantum critical point we obtain $\frac{\partial M}{\partial T} \sim -\sqrt{T}$ while $\frac{\partial M}{\partial T} \sim -T/\sqrt{r}$ for $T \ll r$.

As r is a relevant perturbation at the quantum critical point while θ is only marginal, the contributions due to the B-dependence of θ are subleading and can therefore be neglected.

With $r \propto B - B_c$, we therefore find

$$\frac{\partial M}{\partial T}_{r \ll T} \propto -\sqrt{T} \cos\left(\frac{\theta}{2}\right), \tag{5.32}$$

$$\frac{\partial M}{\partial T}_{T \ll r} \propto -\frac{T}{\sqrt{B - B_c}} \cos\theta. \tag{5.33}$$

Neither $(\partial M/\partial T)_{r \ll T}$ nor $(\partial M/\partial T)_{T \ll r}$ changes sign as a function of θ, and indeed, a numerical evaluation of $(\partial M/\partial T)_{T,r}$ shows it to be a monotonic function of T for all values of θ (see Fig. 5.4).

For $\theta = \pi/2$ and at low T, the temperature derivative of the magnetization also shows thermally activated behavior

$$\frac{\partial M}{\partial T}_{\theta=\pi/2, T\to 0} = -\frac{\sqrt{\pi}}{(2\pi)^3} \frac{r}{\sqrt{T}} \exp\left[-\frac{r}{T}\right] \frac{\partial r}{\partial B}. \tag{5.34}$$

Finally, we evaluate the magnetocaloric effect

$$\Gamma_B = -\frac{(\partial M/\partial T)_B}{T(\tilde{\gamma} + \gamma_c \cos\theta)}, \tag{5.35}$$

which is given by:

$$\Gamma_B(r \ll T) = -\frac{6\sqrt{2}\cos(\frac{\theta}{2})\zeta(\frac{3}{2})}{32\sqrt{T\pi^3}\,\gamma_c \cos\theta - 15\sqrt{2}\,T\cos(\frac{3}{2}\theta)\zeta(\frac{5}{2})}, \tag{5.36}$$

$$\Gamma_B(T \ll r) = -\frac{1}{2(6\gamma_c\sqrt{r} - r)} \tag{5.37}$$

in the limits $r, T \to 0$. As the non-critical contribution γ_c enters Eq. (5.36), the result for $T \to 0$ is not fully universal [106].

5.3.3. Susceptibility

Since $r \sim B - B_c$ and T have the same scaling exponents, one might expect that the susceptibility $\chi = \partial M/\partial B = -\partial^2 F/\partial B^2$ and the specific heat coefficient $\gamma = -\partial^2 F/\partial T^2$ show very similar behavior. This, however, turns out to be not correct. The technical reason for this is that the susceptibility in the quantum critical regime is a singular function of the (dangerously irrelevant) spin-spin interaction u. Practically, this implies that a measurement of the susceptibility is complementary to other thermodynamic measurements as it is highly sensitive to a quantity which can otherwise be determined only by neutron scattering measurements of the correlation length.

The susceptibility $\chi = -\partial^2 F/\partial B^2$ gets contributions both from the B-field dependence of θ and of r. We only consider the leading corrections due to r (see discussion above) and evaluate the quantity $\tilde{\chi}(r,T) = \chi(r,T) - \chi(r=0,T=0)$ with

$$\tilde{\chi} = \int \frac{d^3k}{(2\pi)^3} \int \frac{d\omega}{\pi} \left[n_B(\omega) \mathrm{Im} \frac{1}{(k^2 + r + \mathrm{i}\omega\cos\theta - \omega\sin\theta)^2} + \Theta(-\omega) \mathrm{Im} \frac{1}{(k^2 + \mathrm{i}\omega\cos\theta - \omega\sin\theta)^2} \right] \left(\frac{\partial r}{\partial B} \right)^2 . \tag{5.38}$$

Most interesting is the quantum critical regime, where the leading correction to the susceptibility takes the form

$$\tilde{\chi}(r \ll T) \approx \left(\frac{1}{8\pi} \frac{T}{\sqrt{r}} - \frac{\sqrt{2}}{4\pi^2} \sqrt{T} \cos\left(\frac{\theta}{2}\right) \right) \left(\frac{\partial r}{\partial B} \right)^2 . \tag{5.39}$$

This expression formally diverges for $r \to 0$, which implies that we have to take into account the interaction effects discussed in Section 5.2 and we have to replace the control parameter r by $\xi_\perp^{-2}(T) \sim r + uT^{3/2}$ given by Eq. (5.19). One therefore finds

$$\tilde{\chi} \propto \frac{T}{\sqrt{r}} \qquad \text{for} \quad r < T < (r/u)^{2/3}, \tag{5.40}$$

but

$$\tilde{\chi} \propto \frac{T^{1/4}}{\sqrt{u}} \qquad \text{for} \quad T > (r/u)^{2/3}. \tag{5.41}$$

There is a crossover line within the quantum critical regime, depending on whether the control parameter itself or the temperature dependent correction $uT^{3/2}$ is the dominant contribution to the correlation length $\xi_\perp^{-2}(T)$. In the latter case, scaling is violated, i.e. the susceptibility is no longer of the form $\tilde{\chi}(r,T) = f_\theta(T/r)/\sqrt{r}$, as the dangerously irrelevant coupling u determines $\tilde{\chi}$ in this regime. It is interesting to trace back the origin of the $1/\sqrt{r}$ contribution in (5.39). It arises from the $\omega_n = 0$ mode of the Gaussian theory (5.9) which leads to a contribution of the form $T\sum_k \left(\frac{1}{k^2+r}\right)^2$ to the susceptibility. Note that the static $\omega = 0$ contribution does not depend on the dynamics, i.e. it does not depend on θ. However, the correlation length $\xi_\perp(T)$ given in Eq. (5.19) does depend smoothly on θ which leads to a slight θ-dependence of $\tilde{\chi}$.

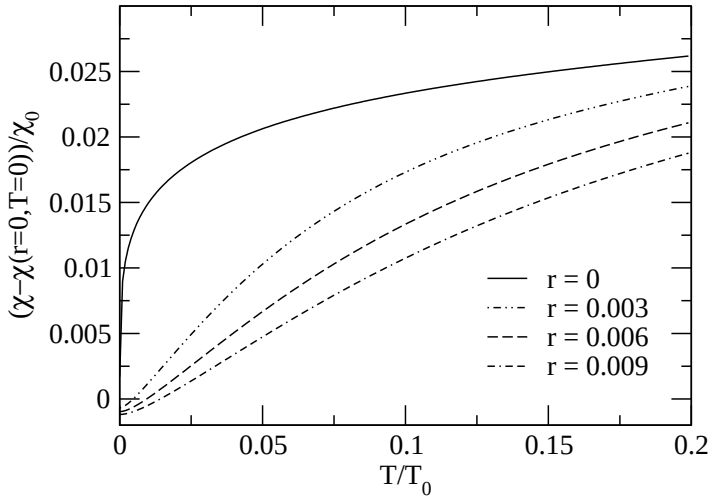

Figure 5.6.: Susceptibility as a function of temperature for $u = 0.2$, $\theta = 0.01$, and different values of r. Curves for other values of θ look essentially identical and are not shown. Note that the susceptibility is *much more* sensitive to small deviations from the quantum critical point than the specific heat coefficient or $\partial M/\partial T$ (c.f. Fig. 5.3, 5.5, where much larger values for r have been used). The $T^{1/4}$ cusp at the quantum critical point [Eq. 5.41] is rapidly washed out by tiny deviations from the critical magnetic field and replaced by the linear dependence of Eq. (5.40).

In the Fermi liquid regime, the susceptibility is given by

$$\tilde{\chi}(T \ll r) = \left(-\frac{1}{4\pi^2}\sqrt{r}\cos\theta + \frac{1}{48}\frac{T^2}{r^{3/2}}\cos\theta \right) \left(\frac{\partial r}{\partial B} \right)^2 , \tag{5.42}$$

while for $\theta = \pi/2$ and low $T \ll r$ it shows thermally activated behavior

$$\chi(\theta = \pi/2, T \to 0) = \left(\frac{\sqrt{\pi}}{(2\pi)^3}\sqrt{T}\exp\left[-\frac{r}{T}\right] \right) \left(\frac{\partial r}{\partial B} \right)^2 . \tag{5.43}$$

The rapid crossovers between the T^2, T and $T^{1/4}$ regimes are shown in Fig. 5.6.

The results for $-\partial^2 F/\partial B^2$ given in this section are also valid qualitatively for a different kind of susceptibility, namely the magnetostriction β. This quantity is given by

$$\beta = \frac{\partial^2 \mathcal{F}}{\partial p \partial B} = \frac{\partial^2 \mathcal{F}}{(\partial r)^2}\frac{\partial r}{\partial p}\frac{\partial r}{\partial B} \tag{5.44}$$

and can be determined experimentally by measuring the length change of the material as a function of magnetic field.

5.4. Scattering rate

Due to energy and momentum conservation, the scattering of electrons from spin-fluctuations is most efficient close to "hot lines" on the Fermi surface, where $E_{\boldsymbol{k}} = E_{\boldsymbol{k}\pm\boldsymbol{Q}} = 0$, where $\boldsymbol{Q}$ is

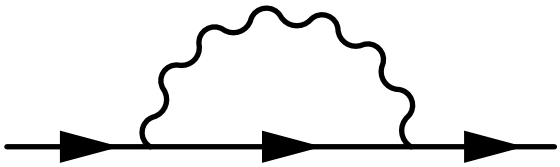

Figure 5.7.: Lowest-order contribution from scattering of the electrons from the fluctuating magnetization to the electron self-energy.

the ordering vector of the antiferromagnet. In order to determine how spin precession modifies the results we calculate the scattering rate as a function of θ. We will neglect all orbital effects of the magnetic field and will not try to calculate the conductivity and the Hall effect. For an extensive discussion of orbital effects and magnetotransport in nearly antiferromagnetic metals see Ref. [99] which does, however, not consider effects of spin precession.

The lifetime of the spin-up electron scattering from fluctuations of $\Phi_\perp$ at $T = 0$ is given by the imaginary part of the electron self-energy, which – to lowest order – consists of the diagram shown in fig. 5.7. In second order perturbation theory, τ is therefore given by [107]

$$\frac{1}{\tau^\uparrow_{\boldsymbol{k}}} = 2g_s^2 \sum_{\boldsymbol{k}'} \int_0^{\epsilon_{\boldsymbol{k}}} d\omega \, \mathrm{Im}\chi_{\boldsymbol{k}-\boldsymbol{k}'}(\omega)\delta[\omega - (E^+_{\boldsymbol{k}} - E^-_{\boldsymbol{k}'})], \tag{5.45}$$

where g_s is a coupling constant, $E^{+/-}_{\boldsymbol{k}}$ and $v_F^{+/-}$ the energy and velocity of spin up/down electrons and χ is the spin fluctuation spectrum of Eq. (5.10),

$$\chi_{\boldsymbol{q}}(\omega) = \frac{1}{\omega_{\boldsymbol{q}} + r + \mathrm{i}\omega\cos\theta - \omega\sin\theta}, \tag{5.46}$$

with $\omega_{\boldsymbol{q}} = (\boldsymbol{q} \pm \boldsymbol{Q})^2/q_0^2$. We split the momentum integration in an integral over the Fermi surface and an energy integration $\int d^3\boldsymbol{k}' = \int\int d\boldsymbol{k}'/v_F^- \int dE^-_{k'}$ and integrate first over $E^-_{k'}$, then over ω to obtain

$$\begin{aligned}\frac{1}{\tau^\uparrow_{\boldsymbol{k}}} &\approx \frac{g_s^2}{v_F^-(2\pi)^3} \int\int d\boldsymbol{k}' \left(\cos\theta \ln\left[\frac{(\omega_{\boldsymbol{k}-\boldsymbol{k}'} + r)^2 + 2E^+_{\boldsymbol{k}}\sin\theta + (E^+_{\boldsymbol{k}})^2}{(\omega_{\boldsymbol{k}-\boldsymbol{k}'} + r)^2}\right] \right. \\ &\qquad \left. + \sin\theta \arctan\left[\frac{-E^+_{\boldsymbol{k}}\cos\theta}{\omega_{\boldsymbol{k}-\boldsymbol{k}'} + r + E^+_{\boldsymbol{k}}\sin\theta}\right] \right) \qquad (5.47) \\ &\approx \frac{g_s^2 q_0^2}{v_F^-(2\pi)^2} E^+_{\boldsymbol{k}} \min\left\{\frac{E^+_{\boldsymbol{k}}}{2\delta_k^2}\cos\theta, \frac{\pi}{2} - \theta\right\}, \qquad (5.48)\end{aligned}$$

where $\delta_k = r + (\delta\boldsymbol{k}/q_0)^2$ and $\delta\boldsymbol{k}$ is the distance of $\boldsymbol{k} + \boldsymbol{Q}$ from the Fermi surface or, approximately, the distance of $\boldsymbol{k}$ from hot lines on the Fermi surface. Analogously we obtain for spin-down electrons

$$\frac{1}{\tau^\downarrow_{\boldsymbol{k}}} \approx \frac{g_s^2 q_0^2}{v_F^+(2\pi)^2} E^-_{\boldsymbol{k}} \min\left\{\frac{E^-_{\boldsymbol{k}}}{2\delta_k^2}\cos\theta, \frac{\pi}{2} - \theta\right\}, \tag{5.49}$$

where the indices + and − have been exchanged w.r.t. (5.47). The scattering rate is strongly dependent on the distance from the hot lines: at the quantum critical point and for $\delta\boldsymbol{k}/q_0 \approx 0$

the scattering rate is linear in the quasiparticle energy. Far away from the hot lines and the quantum critical point the usual scattering rate $1/\tau_{\boldsymbol{k}}^{\uparrow,\downarrow} \propto E_{\boldsymbol{k}}^{+,-2}$ is recovered [99]. Spin-precession does not lead to a qualitative change in the scattering rate.

5.5. Discussion

In this chapter, we have discussed the field-induced quantum phase transition of a clean, three-dimensional antiferromagnetic metal, restricting our attention to the non-magnetic side of the phase diagram. The main question was how the interplay of precession of the spins in the presence of a finite magnetic field and Landau damping modifies the quantum critical behavior.

Our analysis is not valid for (i) systems like $CeCu_{5.2}Ag_{0.8}$ [78] or $CeCu_{5.8}Au_{0.2}$ [79], where strong anisotropies prohibit the precession of the spin ($\theta = 0$), (ii) systems where the two modes $\Phi_{x,y}$ perpendicular to the magnetic field have different masses (in the presence of sizable spin-orbit couplings, the masses will only be similar if the crystal has a sufficiently high symmetry and if furthermore the external magnetic field is applied along a symmetry axis of a crystal) and (iii), in the case of magnetic insulators, frustrated systems. The last condition excludes e.g. $BaCuSi_2O_2$; an approach to the critical theory for this system is briefly discussed in Appendix A.2.

The analysis for $\theta = \pi/2$ is not only relevant for magnetic insulators but also for certain magnetic metals: As long as the ordering vector $\boldsymbol{Q}$ of the antiferromagnet can connect the spin-up and spin-down Fermi surfaces ($Q < k_F^+ + k_F^-$ or, more precisely, $E_{\boldsymbol{k}}^+ = E_{\boldsymbol{k}\pm\boldsymbol{Q}}^- = 0$ for a line of momenta $\boldsymbol{k}$), Landau damping is present and $\theta < \pi/2$. In contrast, one finds $\theta = \pi/2$ in all systems where no such connection exists ($Q > k_F^+ + k_F^-$). However, the transition from $\theta < \pi/2$ to $\theta = \pi/2$ is not expected to be smooth, as the interactions of the spin-fluctuations diverge and become relevant[55, 108] at the point where $Q = k_F^+ + k_F^-$.

One main qualitative result of our analysis is that the critical behavior is not completely universal: it depends on the continuous variable θ, which parametrizes the ratio of precession and damping terms in the effective action. While critical exponents do not depend on θ, this parameter strongly changes the scaling functions and even the sign of leading corrections e.g. to the specific heat.

Presently, we are not aware of any experiments which show the maximum in the T dependence of the specific heat coefficient which we predict for $\pi/6 < \theta < \pi/3$. Under what conditions can large values of θ be expected? Obviously, large uniform magnetizations are required. In heavy Fermion systems with Kondo temperatures of the order of a few Kelvin, one can introduce strong magnetic polarizations with moderate external fields and it should therefore be possible to induce sizable values of θ. A different class of systems which might be of interest in this context are ferrimagnetic materials. If it is possible to suppress only the staggered component of the magnetization in such systems either by external fields, pressure or doping, the critical theory within the Hertz approach will be characterized by a finite (and again sizable) θ.

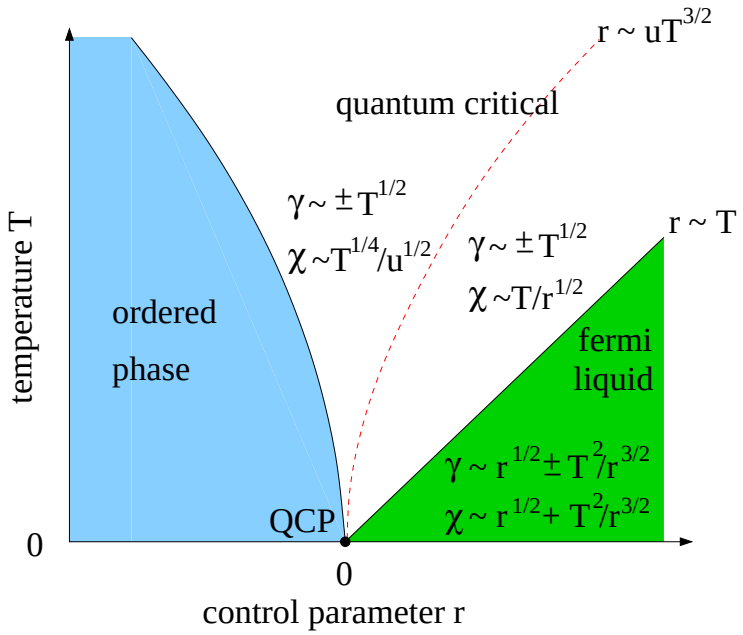

Figure 5.8.: Qualitative behavior of specific heat coefficient γ and magnetic susceptibility χ in various regimes of the phase diagram.

According to our analysis, the susceptibility $\partial M/\partial B$ is a particularly interesting experimental quantity to study close to a field-driven quantum critical point. First of all, it is expected to be much more sensitive to small deviations from criticality compared to other thermodynamic quantities (see Fig. 5.6). Second, it allows to measure the correlation length, a quantity which cannot be extracted from other thermodynamic quantities, as for $B = B_c$ we obtain from (5.39)

$$\frac{\chi(T) - \chi(T=0)}{T} \propto \xi(T). \tag{5.50}$$

Third, it strongly violates the $T/(B - B_c)$ scaling. This deviation from scaling for χ can be used to show that the relevant critical theory is above its upper critical dimension, a central question for the interpretation of quantum criticality in systems like $CeCu_{6-x}Au_x$ or $YbRh_2Si_2$ [79, 81]. All these three statements are actually independent of the value of θ: they apply equally for a dynamics which is overdamped, $\theta \ll 1$, or for a BEC system like $TlCuCl_3$ with $\theta = \pi/2$. Note that in pressure-tuned quantum critical points the compressibility κ (and therefore the sound velocity) plays the same role as χ for field tuned quantum phase transitions. An overview of the qualitative T dependence of the specific heat and susceptibility is shown in Fig. 5.8.

Once again, this behaviour has not yet been observed in experiment, as far as we know. Most experiments do not, in fact, probe $\partial M/\partial B$, but M/B instead.

Field tuned quantum-phase transitions in metals allow to study quantum critical behaviour with a tuning parameter which can easily be controlled and with a conjugate field – the uniform magnetization – which can directly be measured. They are therefore especially well

suited to answer some of the central questions in the field of quantum critical metals, for example, whether or not such systems can be described in terms of simple spin-fluctuation theories.

6. Beyond Hertz-Millis Theory

The underlying assumption of the Hertz-Millis theory of quantum phase transitions is that the transition can be described by an effective field theory for the order parameter only. While this assumption is justified in the case of classical phase transitions, where the behaviour of the system can be successfully predicted from Ginzburg-Landau theory, this is not necessarily the case for quantum phase transitions. In fact, a prerequisite for the LGW functional approach to work is that the order parameter fluctuations are the only soft modes in the system. If this is not the case, i.e. if there are other soft modes in the system which couple to the order parameter, an attempt to integrate out those soft modes leads in general to an effective action with singular and non-local vertices which precludes the application of the usual RG methods. In the case of a ferromagnet, the non-local order parameter theory has moreover been shown to be insufficient to describe the critical behaviour of the system.

In this chapter, we analyze two-dimensional antiferromagnetic metals in the vicinity of a quantum critical point within a functional renormalization group approach, keeping both the collective bosonic and the underlying fermionic degrees of freedom.

6.1. Functional Renormalization Group

All renormalization group schemes are based on the idea that degrees of freedom are treated successively, depending on their energy scale, usually descending from the highest scale present. In the functional Renormalization Group (fRG), this idea is implemented by introducing an infrared-cutoff Λ in the propagator C of the bare action, which suppresses modes with energies below Λ. If, for example, a cutoff-dependent propagator C^Λ is defined as $C^\Lambda(\omega, \boldsymbol{k}) = \Theta(|\omega| - \Lambda)C(\omega, \boldsymbol{k})$, the propagation of modes with frequencies below Λ is suppressed in all internal lines of diagrams that contribute to the Green's functions of the theory.

Starting from a bare action with an infrared cutoff in the propagator, one can now track the evolution of the free energy $\mathcal{F}$ (i.e. the generating functional for the connected Green's functions) and the evolution of the Legendre transform Γ of $\mathcal{F}$, the so-called effective action, which is the generating functional for the 1-PI vertex functions, under a change of Λ. As the cutoff goes from infinity to zero, the cutoff-dependent effective action interpolates smoothly between the bare action of the system and the final effective action, from which all physical properties of the system can be derived. The strength of the fRG now lies in the fact that the flow equations for the 1-PI vertex functions, which can be obtained from the cutoff-dependent effective action, have a comparatively simple form[1], as we will see by applying this procedure

[1] It is also possible to derive flow equations for the connected amputated Green's functions, but this implementation of the fRG scheme will not be used in this chapter.

to the spin-Fermion model in the following sections. By introducing suitable approximations, the flow equations for the 1-PI vertex functions can then be used to obtain results that go beyond perturbative RG calculations.

Comprehensive introductions to the fRG can be found e.g. in [109, 110].

6.2. Model and fRG-equations

As already mentioned in the introduction, the spin-fermion model can be derived from a Hubbard type Hamiltionian with a spin-density interaction term by introducing collective bosonic degrees of freedom to decouple the interaction term. This is in fact the first step of the derivation of Hertz-Millis theory, but we stop at this point and keep the fermionic degrees of freedom in the theory explicitly. The partition sum of the resulting spin-Fermion model reads

$$\mathcal{Z}[\eta,\bar{\eta},\mathrm{A}] = \frac{1}{\mathcal{Z}_0}\int \mathcal{D}\left[\bar{\psi},\psi,\boldsymbol{\phi}\right]\,\exp\left\{-\int d^2x\,d\tau\left(\bar{\psi}\,Q_F\psi + \frac{\boldsymbol{\phi}^2}{4J} + \mathrm{i}\boldsymbol{\phi}(\bar{\psi}\frac{\boldsymbol{\sigma}}{2}\psi) - \bar{\eta}\psi - \bar{\psi}\eta - \mathbf{A}\boldsymbol{\phi}\right)\right\}, \tag{6.1}$$

where a real vector field $\boldsymbol{A}$ has been introduced as a source for the bosonic field $\boldsymbol{\phi}$ and Q_F is the fermionic inverse propagator. Since we will derive the fRG equations in momentum- and frequency space, we provide here also the the partition sum for the Fourier transformed action

$$\begin{aligned}\mathcal{Z} = \frac{1}{\mathcal{Z}_0}\int \mathcal{D}\Phi\,\exp\Bigg\{ &-\int_{-\infty}^{\infty}\frac{\mathrm{d}^3p}{(2\pi)^3}\frac{1}{\beta}\sum_n\left[\bar{\psi}_{\omega_n,\boldsymbol{p}}\,Q_F(\mathrm{i}\omega_n,\boldsymbol{p})\psi_{\omega_n,\boldsymbol{p}} + \boldsymbol{\phi}_{\omega_n,\boldsymbol{p}}Q_B\boldsymbol{\phi}_{-\omega_n,-\boldsymbol{p}}\right]\\ &-\mathrm{i}\int_{-\infty}^{\infty}\frac{\mathrm{d}^3p_1}{(2\pi)^3}\frac{\mathrm{d}^3p_2}{(2\pi)^3}\frac{\mathrm{d}^3p_3}{(2\pi)^3}\frac{1}{\beta^3}\sum_{n_1,n_2,n_3}\delta(\boldsymbol{p}_1-\boldsymbol{p}_2+\boldsymbol{p}_3)\delta_{\omega_{n_1}-\omega_{n_2}+\omega_{n_3},0}\boldsymbol{\phi}_{\omega_{n_1},\boldsymbol{p}_1}\left(\bar{\psi}_{\omega_{n_2},\boldsymbol{p}_2}\frac{\boldsymbol{\sigma}}{2}\psi_{\omega_{n_3},\boldsymbol{p}_3}\right)\\ &+\int_{-\infty}^{\infty}\frac{\mathrm{d}^3p}{(2\pi)^3}\frac{1}{\beta}\sum_n\left[\bar{\eta}_{\omega_n,\boldsymbol{p}}\psi_{\omega_n,\boldsymbol{p}} + \bar{\psi}_{\omega_n,\boldsymbol{p}}\eta_{\omega_n,\boldsymbol{p}} + \mathbf{A}_{-\omega_n,-\boldsymbol{p}}\boldsymbol{\phi}_{\omega_n,\boldsymbol{p}}\right]\Bigg\},\end{aligned} \tag{6.2}$$

where $Q_F = \xi_{\boldsymbol{p}} - \mathrm{i}\omega_n$, and $2Q_B = 1/(2J)$ is the inverse bosonic propagator.

6.2.1. Definitions and Notation

In this section, we briefly list the field definitions and conventions used. The generating functional for the connected Greens functions, the free energy $\mathcal{F}$, is given by

$$\mathcal{F}[\bar{\eta},\eta,\boldsymbol{A}] = -\log\mathcal{Z}[\bar{\eta},\eta,\boldsymbol{A}]. \tag{6.3}$$

The derivatives of $\mathcal{F}$ with respect to the sources $\bar{\eta}, \eta, \boldsymbol{A}$ generate the classical fields

$$\begin{aligned} -\frac{\delta \mathcal{F}}{\delta \boldsymbol{A}_{-\omega,-\boldsymbol{q}}} &= \frac{1}{(2\pi)^3}\frac{1}{\beta}\langle \boldsymbol{\phi}_{\omega,\boldsymbol{q}} \rangle \equiv \frac{1}{(2\pi)^3}\frac{1}{\beta}\boldsymbol{\phi}^c{}_{\omega,\boldsymbol{q}}, \\ -\frac{\delta \mathcal{F}}{\delta \bar{\eta}_{\omega,\boldsymbol{q}}} &= \frac{1}{(2\pi)^3}\frac{1}{\beta}\psi^c_{\omega,\boldsymbol{q}}, \\ \frac{\delta \mathcal{F}}{\delta \eta_{\omega,\boldsymbol{q}}} &= \frac{1}{(2\pi)^3}\frac{1}{\beta}\bar{\psi}^c{}_{\omega,\boldsymbol{q}}. \end{aligned} \tag{6.4}$$

In the following, the index c will be dropped. A generating functional Γ' for the 1-PI vertex functions can now be introduced via a Legendre transformation of the free energy $\mathcal{F}$:

$$\begin{aligned} \Gamma'[\bar{\psi}, \psi, \boldsymbol{\phi}] = \mathcal{F}[\bar{\eta}, \eta, \boldsymbol{A}] \\ + \int \frac{\mathrm{d}^3 p}{(2\pi)^3}\frac{1}{\beta}\sum_n \left(\bar{\eta}_{\omega_n,\boldsymbol{p}}\psi_{\omega_n,\boldsymbol{p}} + \bar{\psi}_{\omega_n,\boldsymbol{p}}\eta_{\omega_n,\boldsymbol{p}} + \boldsymbol{A}_{-\omega_n,-\boldsymbol{p}}\boldsymbol{\phi}_{\omega_n,\boldsymbol{p}} \right). \end{aligned} \tag{6.5}$$

In analogy to (6.4), we have:

$$\begin{aligned} \frac{\delta \Gamma'}{\delta \boldsymbol{\phi}_{\omega,\boldsymbol{q}}} &= \frac{1}{(2\pi)^3}\frac{1}{\beta}\boldsymbol{A}_{-\omega,-\boldsymbol{q}}, \\ \frac{\delta \Gamma'}{\delta \psi_{\omega,\boldsymbol{q}}} &= -\frac{1}{(2\pi)^3}\frac{1}{\beta}\bar{\eta}_{\omega,\boldsymbol{q}}, \\ \frac{\delta \Gamma'}{\delta \bar{\psi}_{\omega,\boldsymbol{q}}} &= \frac{1}{(2\pi)^3}\frac{1}{\beta}\eta_{\omega,\boldsymbol{q}}. \end{aligned} \tag{6.6}$$

In order to make the notation more concise, we collect the fields in superfields and introduce supersources:

$$\Phi_Q \equiv \begin{pmatrix} \boldsymbol{\phi}_{\omega,\boldsymbol{q}} \\ \bar{\psi}_{\omega,\boldsymbol{q}} \\ \psi_{\omega,\boldsymbol{q}} \end{pmatrix}, \qquad \overline{\Phi}_Q \equiv \begin{pmatrix} \boldsymbol{\phi}_{-\omega,-\boldsymbol{q}} & \bar{\psi}_{\omega,\boldsymbol{q}} & \psi_{\omega,\boldsymbol{q}} \end{pmatrix} \tag{6.7}$$

$$H_Q \equiv \begin{pmatrix} \boldsymbol{A}_{\omega,\boldsymbol{q}} \\ -\eta_{\omega,\boldsymbol{q}} \\ \bar{\eta}_{\omega,\boldsymbol{q}} \end{pmatrix}, \qquad \overline{H}_Q \equiv \begin{pmatrix} \boldsymbol{A}_{-\omega,-\boldsymbol{q}} & -\eta_{\omega,\boldsymbol{q}} & \bar{\eta}_{\omega,\boldsymbol{q}}, \end{pmatrix} \tag{6.8}$$

where we introduced a collective index Q for the frequency- and momentum-dependence. These definitions allow us to rewrite (6.4) and (6.6) as

$$\begin{pmatrix} \frac{\delta \mathcal{F}}{\delta \boldsymbol{A}_{-\omega,-\boldsymbol{q}}} \\ -\frac{\delta \mathcal{F}}{\delta \eta_{\omega,\boldsymbol{q}}} \\ \frac{\delta \mathcal{F}}{\delta \bar{\eta}_{\omega,\boldsymbol{q}}} \end{pmatrix} = \frac{\delta \mathcal{F}}{\delta \overline{H}_Q} = -\frac{1}{(2\pi)^3}\frac{1}{\beta}\Phi_Q = -\frac{1}{(2\pi)^3}\frac{1}{\beta}\begin{pmatrix} \boldsymbol{\phi}_{\omega,\boldsymbol{q}} \\ \bar{\psi}_{\omega,\boldsymbol{q}} \\ \psi_{\omega,\boldsymbol{q}} \end{pmatrix}, \tag{6.9}$$

$$\begin{pmatrix} \frac{\delta \Gamma'}{\delta \boldsymbol{\phi}_{-\omega,-\boldsymbol{q}}} \\ \frac{\delta \Gamma'}{\delta \bar{\psi}_{\omega,\boldsymbol{q}}} \\ \frac{\delta \Gamma'}{\delta \psi_{\omega,\boldsymbol{q}}} \end{pmatrix} = \frac{\delta \Gamma'}{\delta \overline{\Phi}_Q} = -\frac{1}{(2\pi)^3}\frac{1}{\beta}M H_Q = \frac{1}{(2\pi)^3}\frac{1}{\beta}\begin{pmatrix} \boldsymbol{A}_{\omega,\boldsymbol{q}} \\ \eta_{\omega,\boldsymbol{q}} \\ -\bar{\eta}_{\omega,\boldsymbol{q}} \end{pmatrix}, \tag{6.10}$$

where the matrix M is defined as

$$\begin{pmatrix} -1 & 0 & 0 \\ 0 & 1 & 0 \\ 0 & 0 & 1 \end{pmatrix}. \tag{6.11}$$

In this notation, the part of the action bilinear in the fields can be expressed as

$$\begin{aligned} \frac{1}{2}(\overline{\Phi}_P, Q(P)\Phi_P) &\equiv \begin{pmatrix} \boldsymbol{\phi}_{-\omega,-\boldsymbol{p}} & \bar{\psi}_{\omega,\boldsymbol{p}} & \psi_{\omega,\boldsymbol{p}} \end{pmatrix} \begin{pmatrix} Q_B & 0 & 0 \\ 0 & 0 & \frac{1}{2}Q_F(\mathrm{i}\omega_n,\boldsymbol{p}) \\ 0 & -\frac{1}{2}Q_F(\mathrm{i}\omega_n,\boldsymbol{p}) & 0 \end{pmatrix} \begin{pmatrix} \boldsymbol{\phi}_{\omega_n,\boldsymbol{p}} \\ \bar{\psi}_{\omega_n,\boldsymbol{p}} \\ \psi_{\omega_n,\boldsymbol{p}} \end{pmatrix} \\ &= (\boldsymbol{\phi}_{-\omega_n,-\boldsymbol{p}}, Q_B(\mathrm{i}\omega_n,\boldsymbol{p})\boldsymbol{\phi}_{\omega_n,\boldsymbol{p}}) + (\bar{\psi}_{\omega_n,\boldsymbol{p}}, Q_F(\mathrm{i}\omega_n,\boldsymbol{p})\psi_{\omega_n,\boldsymbol{p}}). \end{aligned} \tag{6.12}$$

where the inverse fermionic and bosonic propagators have been collected in the matrix Q.

By differentiating equation (6.9) with respect to the field Φ and using (6.10), the following relation between the connected two-point function and the 1-PI two-point function can be derived:

$$\mathbb{1}\delta(P_1 - P_2) = \int \mathrm{d}K (2\pi)^6 \beta^2 \frac{\delta^2\Gamma'[\Phi]}{\delta\Phi_{P_2}\delta\overline{\Phi}_K} M \frac{\delta^2\mathcal{F}[H]}{\delta H_K \delta\overline{H}_{P_1}}, \tag{6.13}$$

where

$$\frac{\delta^2}{\delta\Phi\delta\overline{\Phi}} \equiv \begin{pmatrix} \frac{\delta^2}{\delta\boldsymbol{\phi}\delta\boldsymbol{\phi}} & \frac{\delta^2}{\delta\boldsymbol{\phi}\delta\psi} & \frac{\delta^2}{\delta\boldsymbol{\phi}\delta\bar{\psi}} \\ \frac{\delta^2}{\delta\psi\delta\boldsymbol{\phi}} & \frac{\delta^2}{\delta\psi\delta\psi} & \frac{\delta^2}{\delta\psi\delta\bar{\psi}} \\ \frac{\delta^2}{\delta\bar{\psi}\delta\boldsymbol{\phi}} & \frac{\delta^2}{\delta\bar{\psi}\delta\psi} & \frac{\delta^2}{\delta\bar{\psi}\delta\bar{\psi}} \end{pmatrix}, \qquad \frac{\delta^2}{\delta H\delta\overline{H}} \equiv \begin{pmatrix} \frac{\delta^2}{\delta\boldsymbol{A}\delta\bar{\eta}} & -\frac{\delta^2}{\delta\boldsymbol{A}\delta\eta} \\ \frac{\delta^2}{\delta\bar{\eta}\delta\bar{\eta}} & -\frac{\delta^2}{\delta\bar{\eta}\delta\eta} \\ -\frac{\delta^2}{\delta\eta\delta\bar{\eta}} & \frac{\delta^2}{\delta\eta\delta\eta} \end{pmatrix}. \tag{6.14}$$

To lowest order in perturbation theory, $\delta^2\Gamma'/(\delta\Phi\delta\overline{\Phi})|_{\Phi=\overline{\Phi}=0} = Q$. When the external fields are set to zero, (6.13) becomes

$$\mathbb{1} = \Gamma'^{(2)}(P) M \mathcal{F}^{(2)}(P). \tag{6.15}$$

From this we see that $M\mathcal{F}^{(2)}(P) \equiv \mathcal{G}(P)$ is the full propagator. Further relations between connected Greens functions and 1-PI vertex functions can be obtained by taking higher-order derivatives of (6.10).

In the following, it will be convenient to work with a slightly modified generating functional for the 1-PI vertex functions defined by

$$\Gamma[\Phi] = \mathcal{F}[H] + (\bar{H}, \Phi) - \frac{1}{2}(\overline{\Phi}, Q\,\Phi). \tag{6.16}$$

In contrast to Γ' defined in (6.5), the two-point vertex function generated by Γ is now equal to the self-energy, i.e. $\Gamma^{(2)} = \delta^2\Gamma/(\delta\Phi\delta\overline{\Phi})|_{\Phi=\overline{\Phi}=0} = \Sigma$. The relations (6.13) and (6.15) are now changed to

$$\mathbb{1}\delta(P_1 - P_2) = \int \mathrm{d}K (2\pi)^6 \beta^2 \left(\frac{\delta^2\Gamma[\Phi]}{\delta\Phi_{P_2}\delta\overline{\Phi}_K} + Q(K)\delta(K - P_2) \right) M \frac{\delta^2\mathcal{F}[H]}{\delta H_K \delta\overline{H}_{P_1}}, \tag{6.17}$$

$$\mathbb{1} = (\Sigma(P_2) + Q(P_2))\, M\mathcal{F}^{(2)}(P_2). \tag{6.18}$$

6.2.2. fRG Equation for the Effective Action Γ

We now want to derive flow equations for the effective action Γ, and as a consequence for the 1-PI vertex functions of the theory. We have two kinds of fields in our model and therefore introduce two cut-offs s_B, s_F for the bosonic and fermionic degrees of freedom respectively in the inverse propagator to separate high-momentum and low-momentum modes. For evaluation of the flow equations, both cutoffs have to be expressed as (different) functions of a flow parameter Λ, i.e. $s_F = s_F(\Lambda)$ and $s_B = s_B(\Lambda)$. Differentiating w.r.t. the flow parameter Λ then generates a differential equation for the free energy as follows:

$$\begin{aligned}
\partial_\Lambda \mathcal{F} &= -\frac{1}{\mathcal{Z}}\partial_\Lambda \mathcal{Z} \\
&= -\mathcal{Z}_0 \partial_\Lambda (\mathcal{Z}_0)^{-1} - \frac{1}{e^{-\mathcal{F}}}\,\partial_\Lambda \int \mathcal{D}\Phi e^{-S[\Phi]+\int_X \overline{H}\Phi} \\
&= \partial_\Lambda \log \mathcal{Z}_0 + \frac{1}{e^{-\mathcal{F}}}\int \mathcal{D}\Phi \frac{1}{2}\left(\overline{\Phi}, \partial_\Lambda Q^\Lambda \Phi\right) e^{-S[\Phi]+\int_X \overline{H}\Phi} \\
&= \partial_\Lambda \log \mathcal{Z}_0 + \frac{1}{2}\frac{1}{e^{-\mathcal{F}}}\left(\frac{\delta}{\delta H}, \partial_\Lambda Q^\Lambda \frac{\delta}{\delta \overline{H}}\right) e^{-\mathcal{F}} \\
&= \frac{1}{2}\mathrm{Tr}\left[M(Q^\Lambda)^{-1}\partial_\Lambda Q^\Lambda\right] + \frac{1}{2}\left(\frac{\delta \mathcal{F}}{\delta H}, \partial_\Lambda Q^\Lambda \frac{\delta \mathcal{F}}{\delta \overline{H}}\right) - \frac{1}{2}\mathrm{Tr}\left[\partial_\Lambda Q^\Lambda \frac{\delta^2 \mathcal{F}}{\delta H \delta \overline{H}}\right].
\end{aligned} \tag{6.19}$$

In the above equations, a shorthand notation is used where all indices and/or arguments of the fields and of $\mathcal{F}$ are suppressed and where Tr denotes a trace over the entries of the matrices as well as an integration over momenta and a sum over Matsubara frequencies. From Eq. (6.19) we can now derive the flow equation for Γ, from which we will obtain the integro-differential equations for the 1-PI-vertex functions, which can then be solved numerically. We define Γ as

$$\Gamma[\Phi] = \mathcal{F}[H] + (\bar{H}, \Phi) - \frac{1}{2}(\overline{\Phi}\,, Q^\Lambda\,\Phi), \tag{6.20}$$

so that the two-point vertex function generated by Γ is once again equal to the self-energy, i.e. $\Gamma^{(2)} = \delta^2\Gamma/(\delta\Phi\delta\overline{\Phi})|_{\Phi=\overline{\Phi}=0} = \Sigma$. Using (6.19) and (6.16), we obtain the fRG-equation for Γ:

$$\begin{aligned}
\partial_\Lambda \Gamma &= \partial_\Lambda \mathcal{F} - \frac{1}{2}(\overline{\Phi}\,, \partial_\Lambda Q^\Lambda\,\Phi) \\
&= \frac{1}{2}\mathrm{Tr}\left[(\partial_\Lambda Q^\Lambda) M (Q^\Lambda)^{-1}\right] - \frac{1}{2}\mathrm{Tr}\left[(\partial_\Lambda Q^\Lambda) M \left(\frac{\delta^2\Gamma}{\delta\Phi\delta\overline{\Phi}} + Q^\Lambda\right)^{-1}\right]
\end{aligned} \tag{6.21}$$

If we now separate off the field-independent part from $\delta^2\Gamma/(\delta\Phi\delta\overline{\Phi})$, i.e. if we define

$$\tilde{\Gamma} \equiv \frac{\delta^2\Gamma}{\delta\Phi\delta\overline{\Phi}} - \Sigma, \tag{6.22}$$

then, using $(\Sigma + Q)^{-1} = \mathcal{G}$, the inverse of $\delta^2\Gamma/(\delta\Phi\delta\overline{\Phi}) + Q^\Lambda$ can be expanded into a power series:

$$\begin{aligned}
\left(\frac{\delta^2\Gamma}{\delta\Phi\delta\overline{\Phi}} + Q^\Lambda\right)^{-1} &= \left(1 + \mathcal{G}^\Lambda\tilde{\Gamma}\right)^{-1}\mathcal{G}^\Lambda \\
&= \left(1 - \mathcal{G}^\Lambda\tilde{\Gamma} + [\mathcal{G}^\Lambda\tilde{\Gamma}]^2 - \ldots\right)\mathcal{G}^\Lambda.
\end{aligned} \tag{6.23}$$

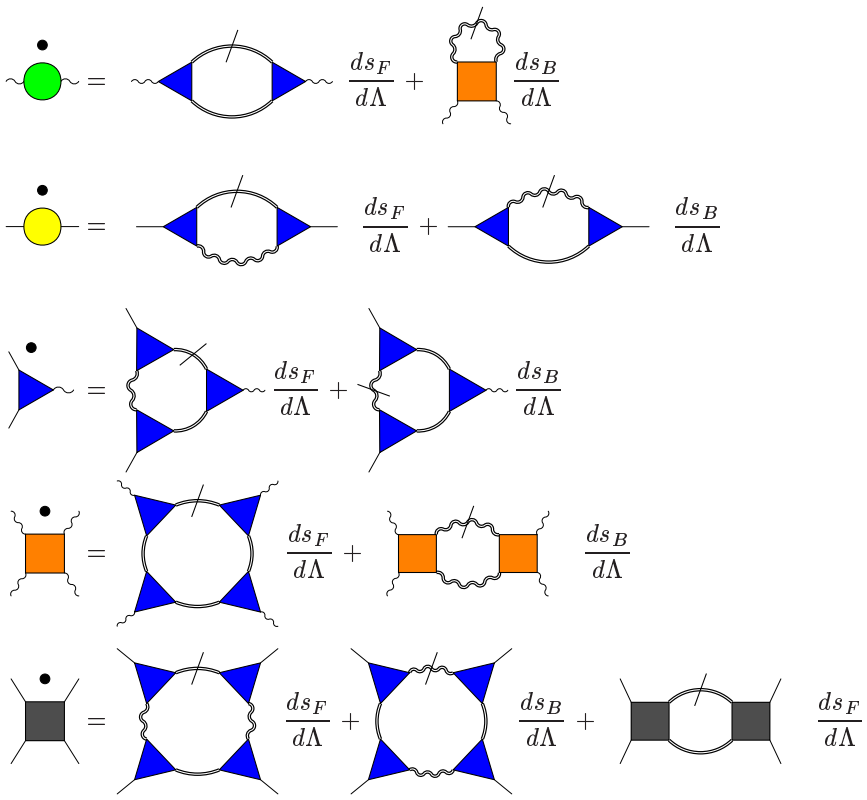

Figure 6.1.: Picture of the flow equations that can be derived from Eq. (6.24), up to and including vertices with four external legs. A dot indicates a derivative w.r.t. Λ.

Using the cyclicity of the trace and defining $S^\Lambda \equiv \mathcal{G}^\Lambda(\partial_\Lambda Q^\Lambda)M\mathcal{G}^\Lambda$, (6.21) can now be cast into the following form:

$$\begin{aligned}\partial_\Lambda \Gamma = &\frac{1}{2}\mathrm{Tr}\left[(\partial_\Lambda Q^\Lambda)M(Q^\Lambda)^{-1}\right] - \frac{1}{2}\mathrm{Tr}\left[(\partial_\Lambda Q^\Lambda)M\mathcal{G}^\Lambda\right] \\ &+ \frac{1}{2}\mathrm{Tr}\left[S^\Lambda\left(\tilde{\Gamma} - \tilde{\Gamma}\mathcal{G}^\Lambda\tilde{\Gamma} + \ldots\right)\right]. \end{aligned} \tag{6.24}$$

Here, S^Λ is the so-called single-scale propagator, since it has support only on the scale Λ in the case of a sharp cutoff – in that case, $\partial_\Lambda Q^\Lambda$ is a δ-function,

Renormalization group equations for the 1-PI vertex functions can be obtained by differentiating (6.24) with respect to the fields and setting the fields to zero. This leads to a hierarchy of infinitely many coupled differential equations for the 1-PI vertex functions, which we have to truncate before we can attempt to solve it.

At this point, let us briefly comment on the general form of the flow equations for the 1-PI vertex functions. As can be seen from (6.24) and in Fig. 6.1, the flow equations for the vertex functions have the basic shape of 1-loop renormalization group equations but with *dressed* propagators and *fully momentum and frequency dependent* vertices.

For cutoffs $s_F, s_B = \infty$, the fermionic and the bosonic propagator are identically zero:

$\Gamma^{s_F,s_B=\infty}$ is equal to the interaction part of the bare action in the exponent of (6.2), and this sets the initial conditions for flow equations for the 1-PI vertex functions.

6.2.3. Choice of Cutoff Functions

The questions to be adressed in regard to the cutoff-function are twofold: First, we have to choose between a sharp and a smooth cutoff-function. Second, we have two kinds of fields in our model that can in principle have cutoffs that are varied independently of each other.

Let us turn to the first issue: the form of the cutoff-function. In order not to obscure the discussion with notation, we will assume that there is now only one cutoff Λ in the model. A sharp cutoff of the form

$$(Q^\Lambda)^{-1}(K) = \chi^\Lambda(\omega)Q^{-1}(K) = \Theta(|\omega| - \Lambda)Q^{-1}(K) \tag{6.25}$$

is rather convenient in the sense that the frequency integration in the flow equations for the vertices is completely suppressed. However, it introduces one additional complication that has first been noted by Morris in [111]: How should combinations of $\dot{\chi}^\Lambda$ and χ^Λ, i.e. the combinations of $\Theta(|\omega| - \Lambda)$ and $-\delta(|\omega| - \Lambda)$ in the flow equations, be interpreted? It was shown [111] that expressions like these are indeed unique, if $\Theta(|\omega| - \Lambda)$ is implemented as the sharp cutoff limit of a smooth cutoff function $\Theta_\epsilon(|\omega| - \Lambda)$:

$$\Theta_\epsilon(|\omega| - \Lambda) \xrightarrow{\epsilon\to 0} \Theta(|\omega| - \Lambda). \tag{6.26}$$

$$\delta_\epsilon(|\omega| - \Lambda) f(\Theta_\epsilon(|\omega| - \Lambda)) \xrightarrow{\epsilon\to 0} \delta(|\omega| - \Lambda) \int_0^1 dt\, f(t). \tag{6.27}$$

It is precisely relation (6.27) that turns the flow equations for the vertices into meaningful equations. The question remains, however, at which stage in the derivation of the flow equations (6.27) should be applied. Indeed, one has to be careful since the vertices themselves (in the case of translational invariance) contain δ-functions that can be affected by (6.27). Let us therefore demonstrate the application of (6.27) in two particular cases: (i) for flow equations for vertices with zero external frequencies and (ii) for flow equations with external frequencies $\neq 0$, where all internal lines have different frequency arguments.

Let us first consider the case for frequency-dependent vertex functions. With the cutoff defined in (6.25), the single scale propagator S^Λ has the form

$$\begin{aligned} S^\Lambda &= \mathcal{G}^\Lambda \dot{Q}^\Lambda M \mathcal{G}^\Lambda = \mathcal{G}^\Lambda \partial_\Lambda (\chi^\Lambda)^{-1} Q M \mathcal{G}^\Lambda = -\mathcal{G}^\Lambda \dot{\chi}^\Lambda (\chi^\Lambda)^{-2} Q M \mathcal{G}^\Lambda \\ &= -\frac{1}{\chi^\Lambda \Sigma^\Lambda + Q} \dot{\chi}^\Lambda Q M \frac{1}{\chi^\Lambda \Sigma^\Lambda + Q}. \end{aligned} \tag{6.28}$$

After insertion into (6.24), relation (6.27) can be applied, assuming that the arguments appearing in the propagators are different, as indicated by different indices:

$$\begin{aligned}
&\partial_\Lambda \Gamma^\Lambda - \frac{1}{2}\mathrm{Tr}\left[(\partial_\Lambda Q^\Lambda) M((Q^\Lambda)^{-1} - \mathcal{G}^\Lambda)\right] \\
&= \frac{1}{2}\mathrm{Tr}\left[S_1^\Lambda\left(\tilde{\Gamma} - \tilde{\Gamma}\mathcal{G}_2^\Lambda\tilde{\Gamma} + \ldots\right)\right] \\
&= -\frac{1}{2}\mathrm{Tr}\left[\frac{1}{\chi_1^\Lambda\Sigma_1^\Lambda + Q_1}\dot{\chi}_1^\Lambda Q_1 M \frac{1}{\chi_1^\Lambda\Sigma_1^\Lambda + Q_1}\left(\tilde{\Gamma} - \tilde{\Gamma}\mathcal{G}_2^\Lambda\tilde{\Gamma} + \ldots\right)\right] \\
&= -\frac{1}{2}\mathrm{Tr}\left[\dot{\chi}_1^\Lambda\left(\int_0^1 \frac{1}{t\Sigma_1^\Lambda + Q_1} Q_1 M \frac{1}{t\Sigma_1^\Lambda + Q_1}\right)\left(\tilde{\Gamma} - \tilde{\Gamma}\mathcal{G}_2^\Lambda\tilde{\Gamma} + \ldots\right)\right] \\
&= -\frac{1}{2}\mathrm{Tr}\left[\dot{\chi}_1^\Lambda M(\Sigma_1^\Lambda + Q_1)^{-1}\left(\tilde{\Gamma} - \tilde{\Gamma}\mathcal{G}_2^\Lambda\tilde{\Gamma} + \ldots\right)\right]. \qquad (6.29)
\end{aligned}$$

Notice that the second term on the left hand side of (6.29) is field-independent and therefore irrelevant for the flow equations for the vertex functions.

Consider now the flow equation for a vertex where all external frequencies Ω_n have been set to 0. In this case, relation (6.27) has to be applied in a slightly different way since all propagators in the loops of the flow equations for this vertex now have identical frequency arguments. When a particular vertex is assumed to be frequency independent and is evaluated at external frequencies $\Omega = 0$, it is useful to start from (6.21) and cast the flow equation into a simpler form:

$$\begin{aligned}
2\,\partial_\Lambda \Gamma^\Lambda &= \mathrm{Tr}\dot{Q}^\Lambda M(Q^\Lambda)^{-1} - \mathrm{Tr}\left[\dot{Q}^\Lambda M\left(\frac{\delta^2\Gamma}{\delta\Phi\delta\overline{\Phi}} + Q^\Lambda\right)^{-1}\right] \\
&= \mathrm{Tr}M\dot{Q}^\Lambda(Q^\Lambda)^{-1} - \mathrm{Tr}\left[M\dot{Q}^\Lambda\left(\frac{\delta^2\Gamma}{\delta\Phi\delta\overline{\Phi}} + Q^\Lambda\right)^{-1}\right] \\
&= \partial_\Lambda \mathrm{Tr}M\log\frac{Q^\Lambda}{\frac{\delta^2\Gamma}{\delta\Phi\delta\overline{\Phi}} + Q^\Lambda}, \qquad (6.30)
\end{aligned}$$

where ∂_Λ in the third line only acts on the cutoff-dependent inverse propagator Q^Λ. Using the cutoff given in (6.25) and relation (6.27), this leads to a slightly modified flow equation for the vertex functions:

$$\begin{aligned}
2\partial_\Lambda\Gamma^\Lambda &= \partial_\Lambda \mathrm{Tr}M\log\frac{Q}{\chi^\Lambda\frac{\delta^2\Gamma}{\delta\Phi\delta\overline{\Phi}} + Q}, \\
&= \mathrm{Tr}\left(\partial_\Lambda\chi^\Lambda, \frac{\delta}{\delta\chi^\Lambda}\right) M\log\frac{Q}{\chi^\Lambda\frac{\delta^2\Gamma}{\delta\Phi\delta\overline{\Phi}} + Q} \\
&= \mathrm{Tr}(\partial_\Lambda\chi^\Lambda)M\int_0^1 dt\frac{d}{dt}\log\frac{Q}{t\frac{\delta^2\Gamma}{\delta\Phi\delta\overline{\Phi}} + Q} \\
&= \mathrm{Tr}(\partial_\Lambda\chi^\Lambda)M\log\frac{Q}{\frac{\delta^2\Gamma}{\delta\Phi\delta\overline{\Phi}} + Q}
\end{aligned}$$

$$
\begin{aligned}
&= \mathrm{Tr}(\partial_\Lambda \chi^\Lambda) M \log \frac{Q}{Q+\Sigma^\Lambda} \frac{Q+\Sigma^\Lambda}{Q+\Sigma^\Lambda+\tilde{\Gamma}^\Lambda} \\
&= -\mathrm{Tr}(\partial_\Lambda \chi^\Lambda) M \log(1+Q^{-1}\Sigma^\Lambda) - \mathrm{Tr}(\partial_\Lambda \chi^\Lambda) M \log(1+\tilde{\mathcal{G}}^\Lambda \tilde{\Gamma}^\Lambda) \\
&= -\mathrm{Tr}(\partial_\Lambda \chi^\Lambda) M \log(1+Q^{-1}\Sigma^\Lambda) + \mathrm{Tr}(\partial_\Lambda \chi^\Lambda) M \sum_k \frac{(-1)^k}{k} \left(\tilde{\mathcal{G}}^\Lambda \tilde{\Gamma}^\Lambda\right)^k, \qquad (6.31)
\end{aligned}
$$

where $\tilde{\mathcal{G}}^\Lambda = (Q+\Sigma^\Lambda)^{-1}$. For better comparison with the last line of (6.29), let us rewrite (6.31) as

$$
\partial_\Lambda \Gamma^\Lambda + \frac{1}{2}\mathrm{Tr}(\partial_\Lambda \chi^\Lambda) M \log(1+Q^{-1}\Sigma^\Lambda) = \frac{1}{2}\mathrm{Tr}(\partial_\Lambda \chi^\Lambda) M \sum_k \frac{(-1)^k}{k} \left(\tilde{\mathcal{G}}^\Lambda \tilde{\Gamma}^\Lambda\right)^k, \qquad (6.32)
$$

where the second term on the left-hand side is field-independent and therefore gives no contribution to the flow equations for the vertex functions. It is now apparent that the prefactor of the flow equation for a particular vertex depends crucially on whether its external frequencies are set to zero or not: Flow equations derived from Eq. (6.32) get extra factors $1/k$ compared to the fRG equations derived from Eq. (6.29).

The next question is how to vary the bosonic cutoff with respect to the the fermionic cutoff: writing both s_F and s_B as functions of a flow parameter Λ, what is the actual form of $s_F(\Lambda)$ and $s_B(\Lambda)$? The results at the end of the RG flow should of course be independent of the actual form of the cutoffs, but this is only strictly true for the full system of differential equations. Whenever approximations are introduced, they can influence the choice of cutoff-functions necessary to correctly model the behaviour of a system. For the spin-fermion model, this is a delicate issue, as can be seen from prior investigations of this model in the literature [62, 63, 65].

In these papers, two different routes were explored to generate a propagator for spin fluctuations different from what Hertz-Millis theory predicts. As sketched in Section 4.1.3 of the introduction, if the fermions are integrated out completely, retaining a frequency-dependence in the diagrams that contribute to the coefficients b_{2i} of Eq. (4.4) leads to the realization that all of these diagrams are in fact marginal, and it has been suggested that all of their logarithmic contributions to the bosonic self-energy add up to a susceptibility of the form $\chi^{-1}(\Omega, \boldsymbol{q}) \propto ((\boldsymbol{q}-\boldsymbol{Q})^2 + |\Omega|)^{1-\gamma}$ [65]. In the language of our functional Renormalization Group, this would mean that if we were to send s_F to zero first without letting s_B flow, we would not be able to truncate the hierarchy of flow equations. Instead, we would need to consider vertices $\Gamma_{\boldsymbol{\phi}^n}$ with arbitrary n in order to reproduce the results of [65]. Clearly, this is a scenario we have to avoid.

According to Abanov et al. [62, 63], there is another way by which an anomalous propagator can be generated, namely via the fermion-boson vertex. Let us take a closer look at their line of arguments. The lowest-order perturbative correction ΔV to the boson-fermion-vertex V has the form [62]

$$
\frac{\Delta V}{V} = \frac{4}{N\pi} \arctan\left(\frac{v_x}{v_y}\right) \log \xi, \qquad (6.33)
$$

where ξ is the correlation length, $r \sim \xi^{-2}$, N is the number of hot spots, and the fermionic dispersion was linearized and had the form $v_x k_x + v_y k_y$. Furthermore, it was assumed that damping had already been generated, i.e. a bosonic propagator of the form $\left(r + (\boldsymbol{q} - \boldsymbol{Q})^2 + |\omega|\right)^{-1}$ was used. The authors extend (6.33) to a RG-equation for the running coupling constant V^R:

$$\frac{dV^R}{dL} = \frac{4}{N\pi} \arctan\left(\frac{v_x}{v_y}\right) V^R, \tag{6.34}$$

where $L = \log \xi$, which as the authors argue gets replaced by $L = (1/2) \log \Omega$ at the quantum critical point. Using $v_x/v_y \approx N\pi/(24L)$ for $\xi \to \infty$ from a RG-calculation, Eq. (6.34) can be solved and has

$$V^R = V_0 |\Omega|^{-1/N} |\log \Omega|^{-1/6} \tag{6.35}$$

as a solution at the quantum critical point [62]. When this result is inserted back into the calculation of a frequency-dependent bosonic self-energy $\Sigma_B(\Omega)$ in lowest-order perturbation theory, one obtains

$$\Sigma_B \propto |\Omega|^{(N-2)/N} |\log \Omega|^{-1/3}. \tag{6.36}$$

In a subsequent publication [63], the authors also took the momentum-dependence of the vertex and the bosonic self-energy into account and obtained a bosonic propagator of the form

$$\chi^{-1}(\boldsymbol{q}, \Omega) \propto \left(\gamma|\Omega| + (\boldsymbol{q} - \boldsymbol{Q})^2\right)^{(N-2)/N} |\log(\gamma|\Omega| + (\boldsymbol{q} - \boldsymbol{Q})^2)|^{-1/3}. \tag{6.37}$$

However, these results are based on the assumption that damping for the magnetic fluctuations has already been generated and can influence the vertex renormalization. Since the imaginary part of the bosonic self-energy comes from *low-energy* fermions, this assumption is far from being obvious. The fRG-equations make a more careful handling of the energy scales possible and thus provide a more rigorous framework to investigate the interplay of the vertex function and the bosonic self-energy, which is what we are aiming to do in the following.

If the bosonic cut-off s_B is brought to zero at a suitable pace, we can expect the frequency-dependent bosonic self-energy to generate corrections to the fermion-boson vertex. If the vertex and the freqency dependence of the bosonic self-energy can then couple back into each other, an anomalous frequency dependence of the bosonic self-energy might be generated. If this feedback loop is generated within the flow by considering cutoffs that are suitably related, cutting off the fRG-equations can be justified.

6.3. Flow Equations for the 1-PI Vertex Functions

We first list the approximations for the vertex functions and then proceed to derive and investigate a set of coupled fRG-equations for a certain choice of cutoffs s_F and s_B.

The flow equations can be straightforwardly derived from (6.24), using (6.27) if necessary; the only complication that arises is that $\mathcal{G}$ and $\tilde{\Gamma}$ in (6.24) are actually matrices.

Since we employ a frequency cut-off and retain only the frequency dependence of the self-energies and the fermion-boson vertex, the momentum integrations in the flow equations can all be done analytically. This reduces the flow equations to a set of coupled differential equations. It is most convenient not to use Matsubara frequencies but to convert the summation over the Matsubara frequencies into contour integrals and continue analytically to real frequencies.

A word on notation: in the following, the "dot"-abbreviation for a derivative refers to $d/(d\Lambda)$, where it is assumed that the bosonic and the fermionic cutoff are both functions of Λ: $s_F = s_F(\Lambda)$ and $s_B = s_B(\Lambda)$. In order not to clutter up the following formulas, we will not write the cutoff dependence of the vertex functions explicitly.

6.3.1. Approximations in the Vertex Functions

We have already stated that the set of coupled differential equations for the vertex functions that can be derived from (6.24) has to be truncated if one wants to solve it. This is usually done by setting all vertex functions except for a very small set to zero. But even then, it is usually computationally too expensive – and also unnecessary – to keep the full momentum- and frequency-dependence of the remaining vertex functions, and further simplifications are introduced to reduce the complexity of the set of coupled differential equations. On the one hand, the approximations should not be too drastic: we want to ensure that the essential physics is captured by the fRG-equations. On the other hand, it is of course desirable to make the set of coupled differential equations as simple to solve as possible. In our model, we need to make certain that the feedback-loop between the bosonic self-energy and the fermion-fermion-boson vertex is implemented in the fRG-equations.

- Bosonic self energy Σ_B

  In the Hertz-Millis theory of antiferromagnetic quantum phase transitions, the decay of spin fluctuations into particle-hole pairs gives rise to a damping term of the form $|\omega|$ in the spin susceptibility, leading to a propagator of the form

  $$\chi_{\boldsymbol{q}}(\mathrm{i}\omega_n) = (r + (\boldsymbol{q} - \boldsymbol{Q})^2 + |\omega_n|)^{-1}. \tag{6.38}$$

  Abanov and Chubukov argued in [62] that the logarithmically divergent fermion-boson vertex will alter this propagator significantly. Our main goal is therefore to investigate how the fermion-boson vertex evolves in the fRG flow and how the boson propagator is influenced by this in turn. We are mainly interested in the evolution of the damping part of the bosonic propagator in the fRG flow. Assuming that a momentum-dependence of the propagator has already been generated by high-energy fermions, we use a bosonic propagator of the form

  $$\chi_{\boldsymbol{q}}(\omega) = (r + (\boldsymbol{q} - \boldsymbol{Q})^2 - \Sigma_B(\omega))^{-1}, \tag{6.39}$$

  where we approximate the bosonic self-energy as follows:

  $$\Sigma_B(\omega) \equiv \Sigma_B(\omega, q = \boldsymbol{Q}). \tag{6.40}$$

  We track only the change of the imaginary part of the bosonic self-energy in the flow.

- Fermionic self energy Σ_F

  We will see that the fermionic self-energy only generates subleading corrections in the fRG-equations for the fermion-boson vertex and is not relevant for the flow of the bosonic self-energy; we can therefore neglect the flow of the fermionic self-energy Σ_F for now.

- Boson-Fermion interaction $\Gamma_{\boldsymbol{\phi}\bar{\psi}\psi}$

  We consider a fully frequency dependent vertex and take the external bosonic momentum of $\Gamma_{\boldsymbol{\phi}_i\psi_\mu\bar{\psi}_\nu}$ to be at the antiferromagnetic ordering vector and the fermionic momenta to be on hot lines:

  $$V(\Omega_1,\Omega_2)\sigma^i_{\mu\nu} \equiv \Gamma_{\boldsymbol{\phi}_i\psi_\mu\bar{\psi}_\nu}(\boldsymbol{Q},\Omega_1;\boldsymbol{k}^*,\Omega_2;\boldsymbol{k}^*+\boldsymbol{Q},-\Omega_1-\Omega_2), \tag{6.41}$$

  where the first set of arguments of $\Gamma_{\boldsymbol{\phi}_i\bar{\psi}_\nu\psi_\mu}$ are the momentum and frequency arguments of $\boldsymbol{\phi}_i$, the second set of arguments are the momentum and frequency arguments of ψ_μ and so on. A full justification of this approximation is given in the next section.

- Four-boson vertex $\Gamma_{\boldsymbol{\phi}^4}$

  We want to avoid a contribution of the four-boson vertex in the flow equation for the bosonic self-energy and therefore have to determine the choice of cutoffs for which such a feedback would occur. The full vertex is a function of three frequencies and three momenta after momentum and frequency conservation has been taken into account. For $\Gamma_{\boldsymbol{\phi}^4}$ to generate a frequency-dependence in the bosonic self-energy $\Sigma_B(\Omega)$, we need to consider the dependence on two external frequencies and one external momentum and calculate the feedback in the flow equation for Σ_B. We find that for $s_B < 2s_F$, no contribution from $\Gamma_{\boldsymbol{\phi}^4}$ enters the flow equation for Σ_B. Details are given in section B.4 of the Appendix.

- Four-fermion vertex $\Gamma_{\bar{\psi}\psi\bar{\psi}\psi}$

  The four-fermion vertex will be set to zero in this version of the flow equations.

In order to avoid contributions from the vertex function $\Gamma_{\boldsymbol{\phi}^4}$ in the flow equation for Σ_B, we have to set $s_B < 2s_F$.

6.3.2. Flow for a constant Fermion-Boson Vertex

The aim of this subsection is to give a convincing argument why it is not sufficient to consider a constant fermion-boson vertex in the flow equations. For that, let us first look at the flow equation for the bosonic self-energy for the case of a constant fermion-boson vertex. Before anything else can happen, the fermions have to generate a dynamics for this object. Since the frequency arguments in the propagators of the respective diagrams are all different, the renormalization group equation for Σ_B can be derived from (6.29) and has the following form:

$$\begin{aligned}\frac{\partial}{\partial s_F}\mathrm{Im}\Sigma_B(\Omega) &= V^2\int\frac{d\omega}{\pi}\frac{d}{ds_F}\left(\chi_F(\omega+\Omega)\chi_F(\omega)\right)I_B(\omega,\Omega)\\ &= V^2\int\frac{d\omega}{\pi}\frac{d}{ds_F}\left(\chi_F(\omega+\Omega)\chi_F(\omega)\right)\frac{n_F(\omega+\Omega)-n_F(\omega)}{8\,v_x v_y},\end{aligned}$$

where $I_B(\omega, \Omega)$ contains the momentum integration and is evaluated in detail in Appendix B.3. At zero temperature, the fermionic distribution functions become step functions and combine with the cut-offs to yield a flow equation of the form

$$\frac{\partial}{\partial s_F}\mathrm{Im}\Sigma_B(\Omega) = \frac{-1}{4\pi}\frac{1}{v_x v_y}V^2\Theta(|\Omega| - 2s_F)\,\mathrm{sign}(\Omega). \tag{6.42}$$

Surprisingly enough, although the fermions generate a damping term in the bosonic self-energy, which generates damping in the fermionic self-energy in turn, the damping of the fermions does not couple back into the RG-equations for the bosonic self-energy at all. Furthermore, a contribution to the imaginary part of the bosonic self energy at frequency Ω will only be generated when s_F falls below $|\Omega|/2$.

Let us now take a look at the flow equation for a frequency-independent, constant V, i.e. $\Gamma_{\boldsymbol{\phi}\psi\bar{\psi}}$ at fixed external frequencies. Two natural choices for the external frequencies present themselves: we could set all external frequencies to zero or the external fermionic frequencies to $\pm s_F$ and only the bosonic frequency to zero. The latter choice respects at least to some extent how this vertex function enters the flow equation for Σ_B.

Let us investigate each of these two possibilities in turn. Setting all frequencies to zero first, we obtain the following flow equation for V (for a detailled calculation see Appendix B.3.1):

$$\dot{V} = V^3 \int \frac{d\omega}{\pi}\left(\delta(|\omega| - s_B)\Theta(|\omega| - s_F)\frac{ds_B}{d\Lambda} + \Theta(|\omega| - s_B)\delta(|\omega| - s_F)\frac{ds_F}{d\Lambda}\right) \frac{1}{2\pi v_x v_y}\arctan\left(\frac{v_y}{v_x}\right)\frac{\mathrm{Im}\Sigma_B^A(\omega)}{\left(\mathrm{Im}\Sigma_B^A(\omega)\right)^2 + r^2}. \tag{6.43}$$

The contribution $\propto ds_F/(d\Lambda)$ from the fermionic cutoff will set all internal lines to the fermionic cut-off: $\omega \equiv s_F$. However, we have just derived (6.42), from which we see that the imaginary part of the bosonic self-energy at frequency ω will only be generated for $s_F < |\omega|/2$, which means that the contribution $\propto ds_F/(d\Lambda)$ of (6.43) plays no role in the flow equation for V at all. For the same reason, the contribution $\propto ds_B/(d\Lambda)$ to the flow equation for V is only present for $s_B > 2s_F$ – precisely the choice of cutoffs we want to avoid.

The second choice for the external frequencies of $\Gamma_{\boldsymbol{\phi}\psi\bar{\psi}}$ consisted of setting only the bosonic frequency to zero and the fermionic frequencies to $\pm s_F$. In this case, the flow equation for V has the form (for a detailled calculation see Appendix B.3.2):

$$\dot{V} = \frac{2V^3}{(2\pi)^2}\frac{1}{v_x v_y}\arctan\left(\frac{v_y}{v_x}\right)\left(\Theta(2s_F - s_B)\frac{ds_F}{d\Lambda}\frac{\mathrm{Im}\Sigma_B^A(-2s_F)}{\left(\mathrm{Im}\Sigma_B^A(-2s_F)\right)^2 + \left(r - \mathrm{Re}\Sigma_B^A(-2s_F)\right)^2} + \Theta(s_B - 2s_F)\frac{ds_B}{d\Lambda}\frac{\mathrm{Im}\Sigma_B^A(-s_B)}{\left(\mathrm{Im}\Sigma_B^A(-s_B)\right)^2 + \left(r - \mathrm{Re}\Sigma_B^A(-s_B)\right)^2}\right).$$

Now we can immediately see the next problem: although a dependence on the fermionic cutoff now seems to be present, it requires the evaluation of the bosonic self-energy at a frequency equal to $\pm 2s_F$. However, this is precisely the frequency in the flow at which an imaginary part of the bosonic self-energy is created; the contribution from the fermionic cutoff is therefore, once again, zero, and the contribution from the bosonic cutoff is only present for $s_B > 2s_F$.

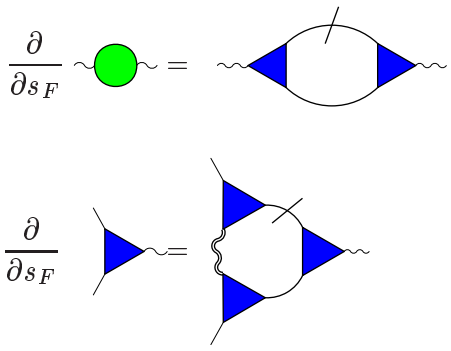

Figure 6.2.: Coupled flow equations for the bosonic self-energy and the fermion-boson interaction vertex. The feedback of the fermionic self-energy on the flow equations is negligible; as a consequence, the flow of the fermionic self-energy is not considered.

6.3.3. Flow Equations for the Vertex Functions

We have found that, in order to avoid contributions from the vertex function Γ_{ϕ^4} in the flow equation for Σ_B, we have to set $s_B < 2s_F$, which also necessitates taking into account a frequency-dependent V. As long as the condition $s_B < 2s_F$ is fulfilled, i.e. as long as the bosonic cutoff is sufficiently lower than the fermionic cutoff, the dynamics for the bosons is not generated fast enough for contributions from the bosonic cutoff to occur. In the following flow equations, we will therefore only have contributions from the dependence of the 1-PI-vertex functions on the fermionic cutoff s_F as depicted in Fig. 6.2.

We now consider a fully frequency-dependent vertex function in the flow equations. As a consequence, the flow equation for Σ_B now has the form

$$\begin{aligned}\frac{\partial}{\partial s_F}\mathrm{Im}\Sigma_B(\Omega) &= -\frac{1}{2}\int\frac{d\omega}{\pi}4V(\Omega,\omega)V(-\Omega,\omega+\Omega)\frac{d}{ds_F}\left(\chi_F(\omega+\Omega)\chi_F(\omega)\right)I_B(\omega,\Omega)\\ &= -\frac{1}{2}\int\frac{d\omega}{\pi}4V(\Omega,\omega)V(-\Omega,\omega+\Omega)\frac{d}{ds_F}\left(\chi_F(\omega+\Omega)\chi_F(\omega)\right)\\ &\qquad\qquad\frac{n_F(\omega+\Omega)-n_F(\omega)}{8\,v_xv_y},\end{aligned}$$

where $I_B(\omega,\Omega)$ contains the momentum integration and is evaluated in detail in the Appendix. At zero temperature, the fermionic distribution functions become step functions and combine with the cut-offs to yield a flow equation of the form

$$\begin{aligned}\frac{\partial}{\partial s_F}\mathrm{Im}\Sigma_B(\Omega) = \frac{-1}{4\pi v_xv_y}\Bigg[&\sum_{\omega=\pm s_F}V(\Omega,\omega)V(-\Omega,\omega+\Omega)\left(n_F(\omega)-n_F(\omega+\Omega)\right)\Theta(|\omega+\Omega|-s_F)\\ &+\sum_{\omega=\pm s_F-\Omega}V(\Omega,\omega)V(-\Omega,\omega+\Omega)\left(n_F(\omega)-n_F(\omega+\Omega)\right)\Theta(|\omega|-s_F)\Bigg].\end{aligned}\quad(6.44)$$

The second fRG-equation is the one for the fermion-boson vertex, see (B.20):

$$\begin{aligned}\frac{\partial}{\partial s_F}V(\Omega_1,\Omega_2) = \frac{-1}{4\pi v_x v_y}\Bigg[&\sum_{\omega=\pm s_F-\Omega_2} V(\omega,\Omega_2)V(\Omega_1,\omega+\Omega_2)V(-\omega,\omega+\Omega_1+\Omega_2)\times \\ &\Theta(|\Omega_1+\Omega_2+\omega|-s_F)\Theta(|\omega|-s_B)\tilde{I}_V(\omega,\Omega_1,\Omega_2) \\ &+ \sum_{\omega=\pm s_F-\Omega_1-\Omega_2} V(\omega,\Omega_2)V(\Omega_1,\omega+\Omega_2)V(-\omega,\omega+\Omega_1+\Omega_2)\times \\ &\Theta(|\Omega_2+\omega|-s_F)\Theta(|\omega|-s_B)\tilde{I}_V(\omega,\Omega_1,\Omega_2)\Bigg]. \end{aligned} \tag{6.45}$$

with

$$\begin{aligned}\tilde{I}_V(\omega,\Omega_1,\Omega_2) = &\frac{\mathrm{Im}\Sigma_B^R(\omega)}{\left(r+\frac{(2\omega+\Omega_1+2\Omega_2)^2}{4v_x^2}+\frac{\Omega_1^2}{4v_y^2}\right)^2+\left(\mathrm{Im}\Sigma_B^R(\omega)\right)^2} \\ &\left[\coth\left(\frac{\beta\omega}{2}\right)+\tanh\left(\frac{\beta(\omega+\Omega_1+\Omega_2)}{2}\right)-\tanh\left(\frac{\beta(\omega+\Omega_2)}{2}\right)\right]. \end{aligned} \tag{6.46}$$

At large Ω_1 and Ω_2, $\partial V(\Omega_1,\Omega_2)/(\partial s_F)$ is suppressed by the explicit frequency-dependence of the denominator of $\tilde{I}_V$, while for small Ω_1 and Ω_2, $\partial V(\Omega_1,\Omega_2)/(\partial s_F)$ is suppressed by r.

We can absorb the common prefactor $1/(4\pi v_x v_y)$ of (6.44) and (6.45) by setting

$$V \to 4\pi v_x v_y\, V \tag{6.47}$$

$$\mathrm{Im}\Sigma_B \to 4\pi v_x v_y\, \mathrm{Im}\Sigma_B \tag{6.48}$$

$$r \to 4\pi v_x v_y\, r. \tag{6.49}$$

This changes the prefactors of the frequency-dependent terms in the denominator of $\tilde{I}_V$:

$$\begin{aligned}\tilde{I}_V(\omega,\Omega_1,\Omega_2) = &\frac{\mathrm{Im}\Sigma_B^R(\omega)}{\left(r+\frac{(2\omega+\Omega_1+2\Omega_2)^2}{4\pi v_F^4}+\frac{\Omega_1^2}{4\pi v_F^4}\right)^2+\left(\mathrm{Im}\Sigma_B^R(\omega)\right)^2} \\ &\left[\coth\left(\frac{\beta\omega}{2}\right)+\tanh\left(\frac{\beta(\omega+\Omega_1+\Omega_2)}{2}\right)-\tanh\left(\frac{\beta(\omega+\Omega_2)}{2}\right)\right], \end{aligned} \tag{6.50}$$

where we set $v_x = v_y = v_F/\sqrt{2}$.

The scales that are present in the flow equations are now the Fermi velocity v_F, the mass r, the initial value of the interaction $V(\Omega_1,\Omega_2)$ and the frequency-cutoff ω_c, up to which the frequency-dependence of the 1-PI vertex functions is considered and which also serves as a starting value for s_F. This frequency-cutoff is in fact related to the Fermi velocity since the frequency-dependence of $\mathrm{Im}\Sigma_B$ is generated by fermions: a simple evaluation of the polarization bubble with linearized fermionic dispersion yields $\mathrm{Im}\Sigma_B(\omega)$ proportional to $\omega/(v_x v_y) \approx \omega/v_F^2$. By this argument, the frequency-cutoff ω_c should be of the order of v_F^2.

For a numerical evaluation of the flow equations we set $4\pi v_F^4 = 1$ and $\omega_c = 1$. We discretized $\mathrm{Im}\Sigma_B(\Omega)$ in the interval $-1 \le \Omega \le 1$ and $V(\Omega_1,\Omega_2)$ for $-1 \le \Omega_1, \Omega_2 \le 1$ and used the initial

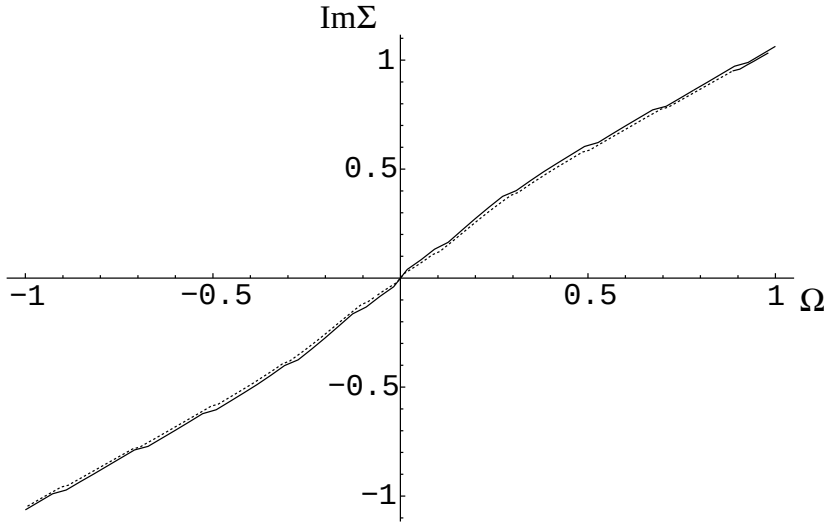

Figure 6.3.: Plot of $\mathrm{Im}\Sigma_B(\Omega)$ versus frequency Ω for $r = 0.2$ and $\Delta\Omega \approx 0.04$, $\Delta s_F = 0.01$ (straight line) as well as $\Delta\Omega \approx 0.02$, $\Delta s_F = 0.005$ (dashed line).

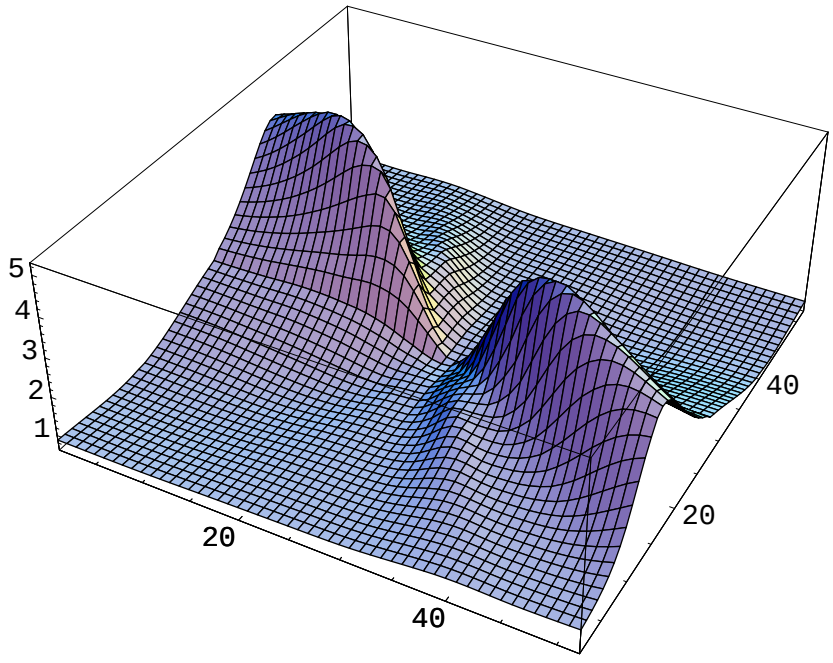

Figure 6.4.: Plot of $V(\Omega_1, \Omega_2)$ versus frequencies Ω_1, Ω_2 for $r = 0.2$, $\Delta\Omega \approx 0.04$ and $\Delta s_F = 0.01$.

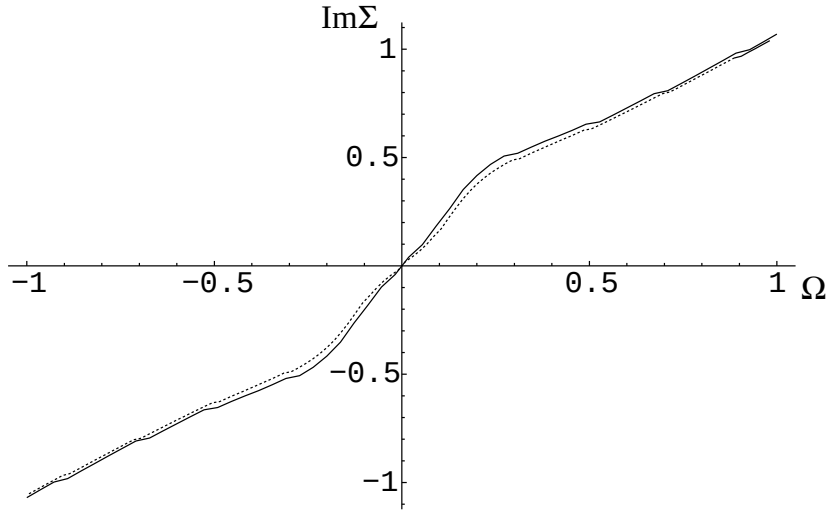

Figure 6.5.: Plot of $\mathrm{Im}\Sigma_B(\Omega)$ versus frequency Ω for $r = 0.1$ and $\Delta\Omega \approx 0.04$, $\Delta s_F = 0.01$ (straight line) as well as $\Delta\Omega \approx 0.02$, $\Delta s_F = 0.005$ (dashed line).

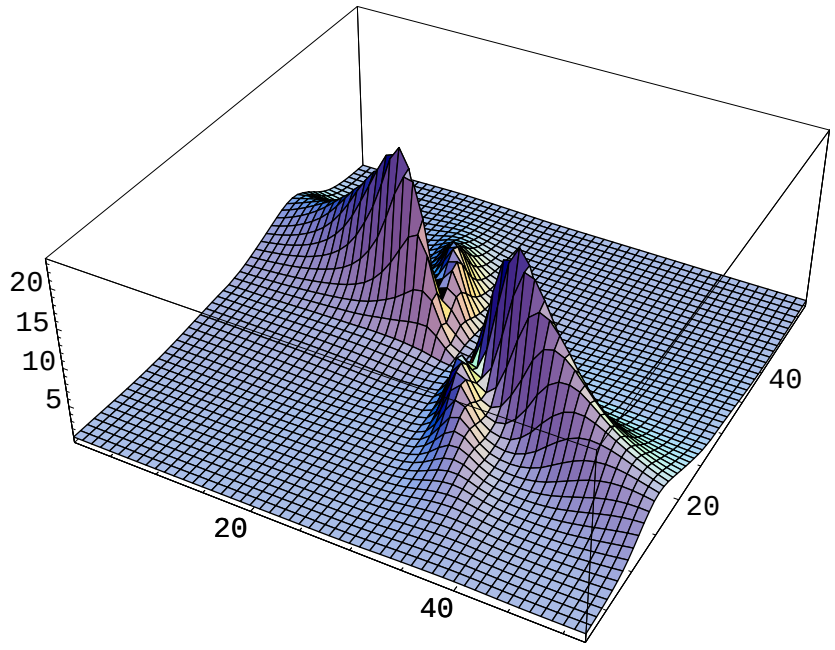

Figure 6.6.: Plot of $V(\Omega_1, \Omega_2)$ versus frequencies Ω_1, Ω_2 for $r = 0.1$, $\Delta\Omega \approx 0.04$ and $\Delta s_F = 0.01$.

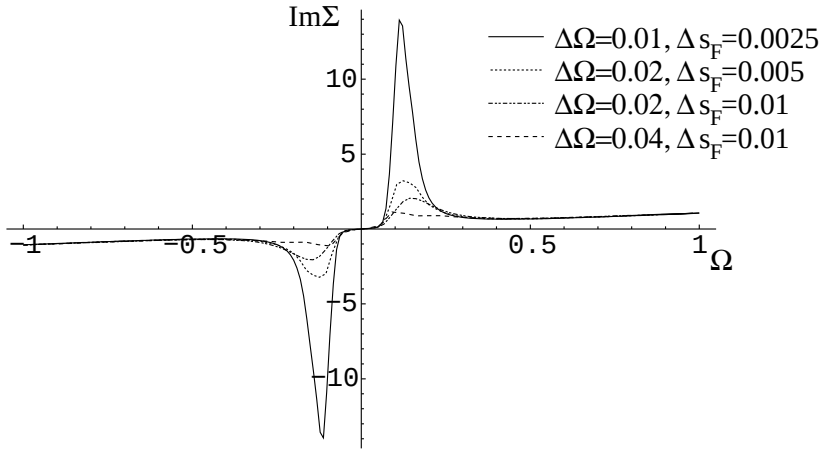

Figure 6.7.: Plot of $\mathrm{Im}\Sigma_B(\Omega)$ versus frequency Ω for $r = 0.05$. The maximum (minimum) becomes more pronounced as the number of frequencies at which $\mathrm{Im}\Sigma_B$ is sampled becomes larger: the flow for $\mathrm{Im}\Sigma_B(\Omega)$ is very likely to diverge at that point.

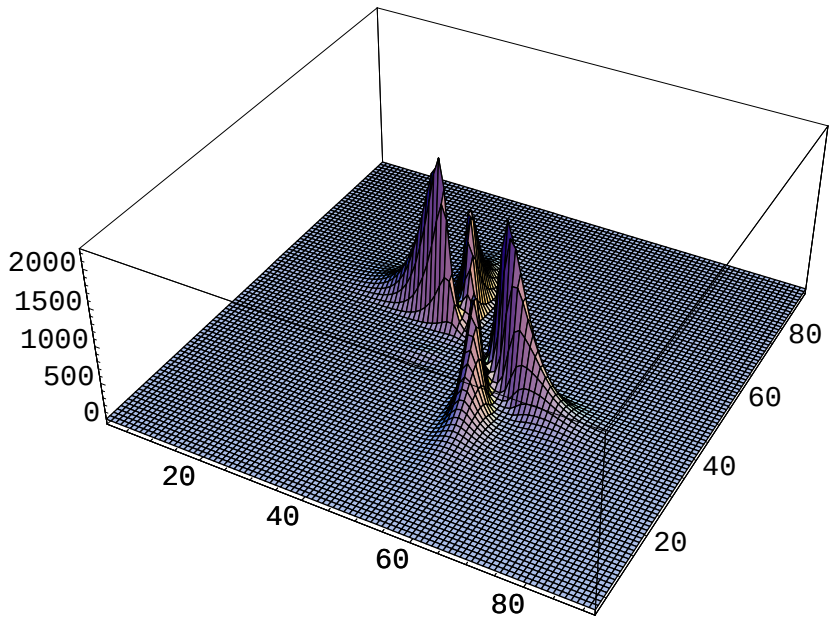

Figure 6.8.: Plot of $V(\Omega_1, \Omega_2)$ versus frequencies Ω_1, Ω_2 for $r = 0.05$, $\Delta\Omega \approx 0.02$ and $\Delta s_F = 0.005$.

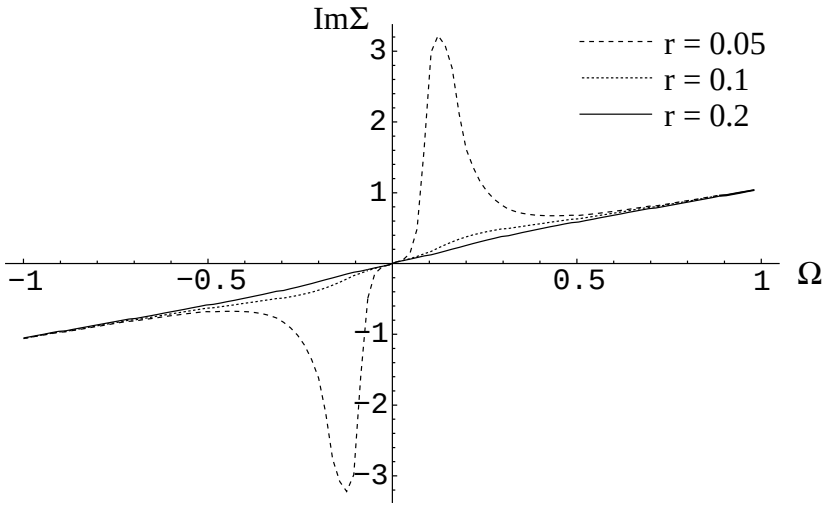

Figure 6.9.: $\mathrm{Im}\Sigma(\Omega)$ for $\Delta\Omega \approx 0.02$, $\Delta s_F = 0.005$ and various values for r. The high frequency behaviour is independent of the value of r.

values $V(\Omega_1, \Omega_2)|_{s_F=1} \equiv V_0 = 1$ and $\mathrm{Im}\Sigma_B(\Omega)|_{s_F=1} \equiv 0$. We solved the resulting system of coupled differential equations numerically, using the second-order Runge-Kutta method.

The results for $\mathrm{Im}\Sigma_B$ and V for $r = 0.2$, $r = 0.1$ and $r = 0.05$ are given in Figs 6.3 to 6.8. In order to ascertain whether the result is independent of the discretization, we varied the grid spacing $\Delta\Omega$ and the step size Δs_F for each value of r. A first thing to observe in Fig. 6.9 is that for large frequencies, the behaviour of the imaginary part of the self-energy is independent of r.

For large r we can expect V to change very little in the flow, and $\mathrm{Im}\Sigma_B(\Omega)$, which can then be computed straightforwardly from (6.44) with constant V, should be linear in Ω as a consequence. For $r = 0.2$, the resulting curve for $\mathrm{Im}\Sigma_B$ does not deviate much from the linear behaviour yet, and $V(\Omega_1, \Omega_2)$ grows only moderately for certain frequencies. For $r = 0.1$, the increase of $V(\Omega_1, \Omega_2)$ at low frequencies is already more pronounced, see Fig. 6.6, and the imaginary-part of the self-energy deviates from linearity for small frequencies Ω as shown in Fig. 6.5. For $r = 0.05$, finally, the large peak of $V(\Omega_1, \Omega_2)$ shown in Fig. 6.8 can be shown to grow with decreasing grid spacing and/or step size, which points towards a divergence in $V(\Omega_1, \Omega_2)$. The steep increase in V couples back into the flow equation for $\mathrm{Im}\Sigma_B$ in such a way that for $r = 0.05$, $\mathrm{Im}\Sigma_B$ also shows a divergence: the maximum (minimum) of $\mathrm{Im}\Sigma_B(\Omega)$ in Fig. 6.7 can be seen to increase (decrease) as the grid spacing and the step size are decreased.

How can we explain this behaviour? Previous studies [62, 63] of the fermion-boson vertex and its contribution to the bosonic self-energy in the spin-fermion model found no divergence either in the imaginary part of the self-energy or the fermion-boson vertex, see Eqs (6.35) and (6.36).

However, the vertices in our flow equations are now fully frequency-dependent – it is not at all obvious at what point in the flow which parts of the 1-PI-vertex functions couple back into each other. The following two scenarios for the flow of V serve to illustrate the significance of this fact.

If we approximate V by a constant and set $\mathrm{Im}\Sigma_B(\Omega) = V^2\Omega$, which is what one would obtain from a one-loop calculation or from the fRG equations in the presence of a constant V, the RG-equation for V can be simplified to

$$\frac{dV}{ds_F} = -\gamma V \frac{s_F}{\left(\frac{r}{V^2}\right)^2 + s_F^2} \equiv -\gamma V \frac{s_F}{\tilde{r}^2 + s_F^2} \tag{6.51}$$

$$\int_{V_0}^{V^*} \frac{dV}{V} \approx -\gamma \int_1^{\tilde{r}} \frac{ds_F}{s_F} \implies \log\left(\frac{V^*}{V_0}\right) = \gamma \log \tilde{r}, \tag{6.52}$$

where γ is a constant prefactor. In this case, the vertex function is perfectly well-behaved and the power-law behaviour of (6.35) is recovered. Alternatively, it could happen that the effective flow equation for the vertex has the form

$$\frac{dV}{ds_F} = -\frac{V^3}{2\,r}, \tag{6.53}$$

if the main contribution to V is always generated at a point in the flow where $\mathrm{Im}\Sigma_B \approx r$. Using separation of variables this reads

$$\int_{V_0}^{V^*} \frac{dV}{V^3} = \int_1^0 \frac{ds_F}{2\,r} \implies V^{*2} = \frac{r\,V_0^2}{r - V_0^2}. \tag{6.54}$$

In this scenario, V^* diverges for $r \to V_0^2$.

6.4. Summary and Outlook

In this chapter, we presented first results for a treatment of the spin-fermion model in two spatial dimensions within a functional Renormalization Group approach. With the specific goal of testing Hertz-Millis theory for two-dimensional antiferromagnets in mind, we chose the fRG-approach because it takes into consideration the feedback of the frequency-dependent 1-PI-vertex functions on each other.

We observed a divergence of the fermion-boson vertex and the imaginary part of the self-energy as the distance r to the quantum critical point falls below a certain threshold. This would indicate that the behaviour of the two-dimensional antiferromagnet is incompatible with Hertz-Millis theory [53, 55]. Although previous investigations [62, 63, 65] of the spin-fermion model arrived at the same conclusion, they did not observe a divergence in either the fermion-boson vertex or the imaginary part of the self-energy. We believe that this is due to the fact that we considered the full frequency-dependence of the fermion-boson vertex, which was previously neglected.

This flow to strong coupling of the RG-equation for r below a certain value points towards the fact that non-perturbative effects dominate for $r \to 0$. One possibility is that the quantum phase transition becomes first order, another possibility is that a pseudogap develops in the electron spectrum. Further investigations are definitely needed. In particular, we should try

to understand how the flow to strong coupling can happen in the approach where the electrons are integrated out first.

How can this calculation be expanded and improved? Possible extensions of the fRG-equations include considering the flow of Σ_F and of the real part of Σ_B. Furthermore, the results of Abanov et al. [63, 65] suggest that the momentum dependence of Σ_B should also be of interest. One should also perform a calculation analogous to the one presented in this chapter for three spatial dimensions instead of two. From a theoretical side, no inconsistencies have been found yet for Hertz-Millis theory for an antiferromagnet in three spatial dimensions. This could serve as a verification for the validity of our results.

Although the four-fermion interaction vertex has been eliminated in the bare action in the exponent of (6.2), it can be generated once again in the fRG-flow. We have neglected this vertex in our flow equations, but it is precisely this vertex which would produce an instability in the spin-density-channel in a RG-calculation in the purely fermionic model from which the spin-fermion model has been derived: this instability indicates the onset of magnetic order. Another interesting question concerns superconductivity mediated by magnetic fluctuations, indicated by a divergence in the Cooper-channel of the four-fermion interaction vertex.

It would be preferrable to consider the four-fermion vertex in the flow in some way. Rather than incorporating the four-fermion vertex with an additional fRG-equation, we have sketched a preliminary version of the flow equations with a continuous Hubbard-Stratonovich transformation in Appendix B.5. This continuous Hubbard-Stratonovich transformation can be used to set a momentum- and frequency independent spin-density interaction to zero at each point in the fRG-flow.

We conclude by stating that the functional Renormalization Group seems to be a promising tool for investigating the interplay of the electronic degrees of freedom and their collective excitations close to a quantum critical point.

Appendix Part II

A. Field-tuned Quantum Phase Transitions

A.1. Cubic terms in the effective action

In this appendix we briefly discuss whether cubic terms Φ^3 are present in the low-energy effective Lagrangian. As Φ carries the momentum $\boldsymbol{Q}$, the presence of such terms is forbidden by momentum conservation in most systems with the exception of magnetic structures (e.g. BCC lattices) where the sum of three ordering vectors adds up to 0. If such a system has Ising symmetry, then a cubic term does exist and the magnetic field driven transition will be first order. However, for xy symmetry perpendicular to the magnetic field (the case mostly discussed in chapter 5), a rotationally invariant cubic term of the form $\Phi_\perp^3$ does not exist. While terms like $B\Phi_z|\Phi_\perp|^2$ are allowed by symmetry, they lead effectively only to a renormalization of the $|\Phi_\perp|^4$ interaction as Φ_z remains massive. Such terms can therefore be neglected.

A.2. Frustration in BEC of Magnons

The insulator $BaCuSi_2O_2$ can be tuned to an antiferromagnetic quantum critical point by applying an external magnetic field. Recent experiments seem to indicate that $BaCuSi_2O_2$ exhibits quantum critical behaviour of a two dimensional system, with a phase boundary $T_c \propto (B - B_c)$ instead of $T_c \propto (B - B_c)^{2/3}$.

$BaCuSi_2O_2$ is a layered spin dimer system in which the dimers in one layer are arranged on a square lattice, but neighbouring layers are shifted such that a dimer in one layer is at the centre of a square of dimers in the next layer. In this system $J = 4.45$ meV, $J' = 0.51$ meV, and $J_f = 0.16$ meV, where J is the antiferromagnetic spin interaction, J' is the intra-layer coupling, and J_f is the inter-layer antiferromagnetic interaction. Neighbouring layers are decoupled in the ground state of the system: the inter-layer coupling is effectively removed by frustration. However, neighbouring layers inevitably get coupled by fluctuations in the so-called "order from disorder"-mechanism. The quantum critical behaviour should therefore revert to that of a three-dimensional system below a certain temperature scale. Maltseva and Coleman considered this system in the antiferromagnetically ordered phase in the framework of linear spin-wave theory and estimated the transition temperature from 2D- to 3D-behaviour to be $\sim J'/\ln(J'/J_f)$ [112].

Within the "soft spin" approach to Bose-Einstein condensation of magnons, what are the predictions for the quantum critical behaviour of a frustrated system like $BaCuSi_2O_2$? It is not the purpose of this section to give a complete answer to that question, we simply sketch how one might tackle this particular problem. In order to account for frustration,

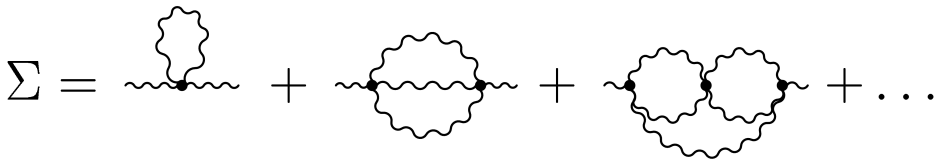

Figure A.1.: Diagrams contributing to the self energy of magnetic fluctuations.

the dispersion relation of the propagator for $\mathbf{\Phi}$ has to be modified: defining k_x and k_y to be momentum components within a layer and k_z to be perpendicular to the layer, we can account for intralayer exchange and interlayer hopping in a tight binding picture with a dispersion relation of the form

$$\varepsilon(\boldsymbol{k}) = J'(\cos(k_x a) + \cos(k_y a)) + 2J_f \cos(k_z a) \cos\frac{k_x a}{2} \cos\frac{k_y a}{2}, \tag{A.1}$$

where a is the lattice constant, and the distance between layers is taken to be equal to the lattice constant within one layer for simplicity reasons. For small deviations $\Delta k_x, \Delta k_y$ and Δk_z of the momenta from π/a, the dispersion relation (A.1) can be approximated by

$$\varepsilon(\boldsymbol{k}) = \frac{a^2}{2} J' \left((\Delta k_x)^2 + (\Delta k_y)^2\right) + 2\, J_f \frac{a^2}{4} \left(-1 + \frac{a^2}{2}(\Delta k_z)^2\right) (\Delta k_x)(\Delta k_y) + const. \tag{A.2}$$

Introducing the momentum $k_\parallel$ in the x-y-plane as well as the momentum $k_\perp$ perpendicular to it, let us approximate the inverse propagator for the order parameter field $\mathbf{\Phi}$ in the corresponding "soft spin" theory by

$$\chi_{\boldsymbol{k}}^{-1}(\mathrm{i}\omega_n) = k_\parallel^2(1 + \eta k_\perp^2) + r_0 - \mathrm{i}\omega_n, \tag{A.3}$$

where η is an anisotropy parameter related to J' and J_f. A $k_\perp^2$-term is missing in the bare propagator but will be generated at the 2-loop level by the second diagram of Fig. A.1, which leads to the following contribution to the self-energy of $\mathbf{\Phi}$ in the limit $r_0 \to 0$, where r_0 is the distance to the quantum critical point:

$$\Sigma_{2-\mathrm{loop}}(k_\parallel, k_\perp, \Omega = 0) = \frac{16}{(2\pi)^6} \frac{u^2}{\eta} \int_{-\sqrt{\eta}\Lambda}^{\sqrt{\eta}\Lambda} d\tilde{p}_\perp \int_0^\Lambda dp_\parallel p_\parallel \int_{-\sqrt{\eta}\Lambda}^{\sqrt{\eta}\Lambda} d\tilde{q}_\perp \int_0^\Lambda dq_\parallel q_\parallel$$
$$\frac{1}{p_\parallel^2(1+\tilde{p}_\perp^2) + q_\parallel^2(1+\tilde{q}_\perp^2) + (p_\parallel + q_\parallel - k_\parallel)^2 \left(1 + (\tilde{p}_\perp + \tilde{q}_\perp - \sqrt{\eta}\, k_\perp)^2\right)}. \tag{A.4}$$

where the frequency integrations have already been performed at $T = 0$ and the loop momenta have been rescaled: $\tilde{q}_\perp = \sqrt{\eta} q_\perp$ and $\tilde{p}_\perp = \sqrt{\eta} p_\perp$. The momentum integrals are dominated by high momenta and necessitate the introduction of UV-cutoffs. To calculate the prefactor of the $k_\perp^2$-term in the self-energy generated by this diagram, let us consider the first term of a Taylor expansion of $\Sigma_{2\ \mathrm{loop}}(0, k_\perp, 0) - \Sigma_{2\ \mathrm{loop}}(0, 0, 0)$ in powers of $k_\perp^2$. The remaining integrals can be calculated, but the $\tilde{p}_\perp$-integration diverges logarithmically in the UV-cutoff, which means that the validity of the Taylor expansion is in question. Also, the logarithmic divergence indicates that the main contribution to the $\tilde{p}_\perp$-integrals comes from high momenta;

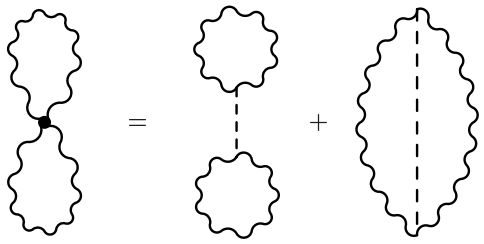

Figure A.2.: Diagram contributing to the free energy in $\mathcal{O}(u)$. The different contractions of the internal indices of the fields involved have been made explicit on the right hand side, where the dashed line represents the quartic interaction u.

an expansion of (A.1) in the momenta to obtain the propagator (A.3) is an approach that has to be reconsidered.

Assuming the Taylor expansion can indeed be done, the inverse propagator then has the following form:

$$\chi_{\boldsymbol{k}}^{-1}(\mathrm{i}\omega_n) = k_{\parallel}^2 + c_1 u^2 \log\eta\, k_{\perp}^2 + r_0 - \mathrm{i}\omega_n, \tag{A.5}$$

where $c_1 \sim \Lambda^2 \log\Lambda$ is a cutoff-dependent constant.

Anisotropic models with a propagator of this form have been investigated in [56]: The quantum critical behaviour of the system should change from two-dimensional to three-dimensional at a temperature $T \ll c_1 u^2 \Lambda^2 \log\eta$. It is obvious that a more careful calculation is required.

A.3. Derivation of RG-equations

Following Millis's treatment [55, 56], we perform the renormalization group analysis on the free energy of the system described by the action (5.8) after having converted all Matsubara sums to integrals. Although we restrict our calculations to metals in three spatial dimensions and with a dynamical critical exponent of $z = 2$, we nonetheless keep the variables d and z in the calculation in order to make the origin of certain factors more transparent.

The free energy can be obtained via a linked cluster expansion in the coupling constant u. The scaling dimension of u is $4 - (d + z)$, which is negative for an antiferromagnetic system in 3 spatial dimensions. To first order in u, only the diagram in Fig. A.2 contributes to the free energy. Up to first order in u, the free energy $\mathcal{F}$ is therefore given by

$$\mathcal{F} = \mathcal{F}_G + u[(I_\chi + I_{\chi^*} + I_{\chi^z})^2 + 2(I_\chi^2 + I_{\chi^*}^2 + I_{\chi^z}^2)], \tag{A.6}$$

where

$$\mathcal{F}_G = -\frac{1}{2}\int_0^\Lambda \frac{d^3k}{(2\pi)^3}\int_0^\Gamma \frac{d\omega}{\pi}\,\coth\left(\frac{\beta\omega}{2}\right)\arctan\left(\frac{2(r+k^2)\omega\cos\theta}{(r+k^2)^2-\omega^2}\right) \tag{A.7}$$

is the Gaussian free energy measured in units of $T_0 V/\xi_0^3$ with the cutoffs Λ and Γ, I_χ is given by

$$\begin{aligned} I_\chi &\equiv \int \frac{d^3k}{(2\pi)^3} \frac{1}{\beta} \sum_n \chi_{\boldsymbol{k}}(i\omega_n) \\ &= \int_0^\Lambda \frac{d^3k}{(2\pi)^3} \int_0^\Gamma \frac{d\omega}{\pi} \coth\left(\frac{\beta\omega}{2}\right) \frac{\omega\cos\theta}{(r+k^2)^2 - 2(r+k^2)\omega\sin\theta + \omega^2}, \end{aligned} \tag{A.8}$$

and I_{χ^*}, I_{χ^z} are defined analogously.

In order to relate changes of (A.6) under a cutoff-change to changes of $r_\perp$ and r_z, let us first rearrange (A.6):

$$\begin{aligned} \mathcal{F} &= \mathcal{F}_G + u[3(I_\chi^2 + I_{\chi^*}^2 + I_{\chi^z}^2) + 2(I_\chi I_{\chi^*} + I_\chi I_{\chi^z} + I_{\chi^*} I_{\chi^z})] \\ &= \mathcal{F}_G + \frac{u}{2}[3(I_\chi + I_{\chi^*} + I_{\chi^z})^2 + 2I_{\chi^z}^2 + (I_\chi + I_{\chi^*} - I_{\chi^z})^2], \end{aligned}$$

where we used that $I_\chi - I_{\chi^*} = 0$.

As a next step, we separate out of the momentum and frequency integrals in the expressions on the right hand side of (A.6) the regions given by $\{\Lambda \geq k \geq \Lambda/b, \Gamma \geq \omega \geq 0\}$ and $\{\Lambda \geq k \geq 0, \Gamma \geq \omega \geq \Gamma/b^2\}$. Using that

$$I_\chi + I_{\chi^*} = 2\frac{\partial \mathcal{F}_G}{\partial r_\perp},\ I_{\chi^z} = 2\frac{\partial \mathcal{F}_G}{\partial r_z}, \tag{A.9}$$

the change in $\mathcal{F}$ upon such a variation of the cutoff can be expressed as a change of $r_\perp$ and r_z:

$$\begin{aligned} \frac{\partial \mathcal{F}}{\partial \log b} &= \frac{\partial \mathcal{F}_G}{\partial \log b} + 3u\,(I_\chi + I_{\chi^*} + I_{\chi^z}) \left(\frac{\partial I_\chi}{\partial \log b} + \frac{\partial I_{\chi^*}}{\partial \log b} + \frac{\partial I_{\chi^z}}{\partial \log b}\right) \\ &\quad + 2u\, I_{\chi^z} \frac{\partial I_{\chi^z}}{\partial \log b} + u\,(I_\chi + I_{\chi^*} - I_{\chi^z}) \left(\frac{\partial I_\chi}{\partial \log b} + \frac{\partial I_{\chi^*}}{\partial \log b} - \frac{\partial I_{\chi^z}}{\partial \log b}\right) \\ &= \frac{\partial \mathcal{F}_G}{\partial \log b} + 6u \left(\frac{\partial \mathcal{F}_G}{\partial r_\perp} + \frac{\partial \mathcal{F}_G}{\partial r_z}\right) \left(\frac{\partial I_\chi}{\partial \log b} + \frac{\partial I_{\chi^*}}{\partial \log b} + \frac{\partial I_{\chi^z}}{\partial \log b}\right) \\ &\quad + 4u \frac{\partial \mathcal{F}_G}{\partial r_z} \frac{\partial I_{\chi^z}}{\partial \log b} + 2u \left(\frac{\partial \mathcal{F}_G}{\partial r_\perp} - \frac{\partial \mathcal{F}_G}{\partial r_z}\right) \left(\frac{\partial I_\chi}{\partial \log b} + \frac{\partial I_{\chi^*}}{\partial \log b} - \frac{\partial I_{\chi^z}}{\partial \log b}\right) \\ &= \frac{\partial \mathcal{F}_G}{\partial \log b} + \frac{\partial \mathcal{F}_G}{\partial r_\perp} \left(8u \left(\frac{\partial I_\chi}{\partial \log b} + \frac{\partial I_{\chi^*}}{\partial \log b}\right) + 4u \frac{\partial I_{\chi^z}}{\partial \log b}\right) \\ &\quad + \frac{\partial \mathcal{F}_G}{\partial r_z} \left(4u \left(\frac{\partial I_\chi}{\partial \log b} + \frac{\partial I_{\chi^*}}{\partial \log b}\right) + 12u \frac{\partial I_{\chi^z}}{\partial \log b}\right) \\ &\stackrel{!}{=} \frac{\partial \mathcal{F}_G}{\partial \log b} + \frac{\partial \mathcal{F}_G}{\partial r_\perp} \frac{\partial r_\perp}{\partial \log b} + \frac{\partial \mathcal{F}_G}{\partial r_z} \frac{\partial r_z}{\partial \log b}. \end{aligned} \tag{A.10}$$

This leads to the equations

$$\frac{\partial r_\perp(b)}{\partial \log b} = 2r_\perp(b) + 4u(b)\big(2f_2^\perp(r_\perp(b), \mathcal{T}(b)) + f_2^z(r_z(b), \mathcal{T}(b))\big), \tag{A.11}$$

$$\frac{\partial r_z(b)}{\partial \log b} = 2r_z(b) + 4u(b)\big(f_2^\perp(r_\perp(b), \mathcal{T}(b)) + 3f_2^z(r_z(b), \mathcal{T}(b))\big) \tag{A.12}$$

for the running masses $r_\perp(b)$, $r_z(b)$, where $f_2^\perp$ and f_2^z are given by

$$f_2^\perp(r_\perp,\mathcal{T}) = K_3\Lambda^3 \int_0^\Gamma \frac{d\omega}{\pi}\coth\left(\frac{\beta\omega}{2}\right)\frac{2\omega((\Lambda^2+r_\perp)^2+\omega^2)\cos\theta}{((\Lambda^2+r_\perp)^2+\omega^2)^2-4(\Lambda^2+r_\perp)^2\omega^2\sin^2\theta}$$
$$+\frac{z\Gamma}{\pi}\int_0^\Lambda \frac{d^3k}{(2\pi)^3}\coth\left(\frac{\beta\Gamma}{2}\right)\frac{2\Gamma((k^2+r_\perp)^2+\Gamma^2)\cos\theta}{((k^2+r_\perp)^2+\Gamma^2)^2-4(k^2+r_\perp)^2\Gamma^2\sin^2\theta},$$
$$f_2^z(r_z,\mathcal{T}) = K_3\Lambda^3 \int_0^\Gamma \frac{d\omega}{\pi}\coth\left(\frac{\beta\omega}{2}\right)\frac{\omega}{(r_z+\Lambda^2)^2+\omega^2}$$
$$+\frac{z\Gamma}{\pi}\int_0^\Lambda \frac{d^3k}{(2\pi)^3}\coth\left(\frac{\beta\Gamma}{2}\right)\frac{\Gamma}{(r_z+k^2)^2+\Gamma^2}. \tag{A.13}$$

In the following we assume that the system is close to the quantum critical point at temperatures much smaller than r_z. In this case, $f_2^z(r_z,\mathcal{T})$ can be set to zero, and the renormalization group flow of $r_\perp$ is determined by $f_2^\perp(r_\perp,\mathcal{T})$ only. There are two contributions to $f_2^\perp$, one from the renormalization due to the separated momentum shell, where momentum is set on shell $k=\Lambda$, and one from the renormalization due to the frequency shell with $\omega=\Gamma$. For subsequent calculations we note that

$$f_2^\perp(r_\perp,\mathcal{T}) - f_2^\perp(r_\perp,0) = K_3\Lambda^3\int_0^\Gamma\frac{d\omega}{\pi}\left[\coth\left(\frac{\beta\omega}{2}\right)-1\right]\times$$
$$\frac{2\omega((\Lambda^2+r_\perp)^2+\omega^2)\cos\theta}{((\Lambda^2+r_\perp)^2+\omega^2)^2-4(\Lambda^2+r_\perp)^2\omega^2\sin^2\theta}+\mathcal{O}(e^{-\Gamma/\mathcal{T}}), \tag{A.14}$$

in other words the contribution of the frequency shell renormalizes zero temperature properties only and is exponentially suppressed at finite temperatures.

In order to obtain an expression for the correlation length, we first substitute $r_\perp(b)=R_\perp(b)b^2$ to eliminate the naive scaling and then formally integrate equation (A.11):

$$R_\perp(b) = r_0^\perp + 8\int_0^{\ln b} dx e^{-2x}u(e^x)f_2^\perp(R_\perp(e^x)e^{2x},Te^{zx}). \tag{A.15}$$

We then perform an expansion in temperature

$$R_\perp(b)\sim\Delta_\perp(b)+R_T^\perp(b)+\delta R_\perp(b), \tag{A.16}$$

where three terms contribute.

The first term $\Delta_\perp(b)$ is the running mass at zero temperature,

$$\Delta_\perp(b) = r_0^\perp + 8\int_0^{\ln b} dx\, e^{-2x}u(e^x)f_2^\perp(\Delta_\perp(e^x)e^{2x},0); \tag{A.17}$$

the integrand can now be expanded in $\Delta_\perp$ which leads to the following expression

$$\begin{aligned}\Delta_\perp(b) &\sim r_0^\perp + 8 f_2^\perp(0,0)\int_0^{\ln b} dx\, e^{-2x} u(e^x) \stackrel{b\to\infty}{\to} r_0^\perp - r_c^\perp \\ &\equiv r_\perp, \end{aligned} \tag{A.18}$$

i.e. this defines the parameter which characterizes the distance from the critical point.

The other two terms in (A.16) are of first order in temperature: One contribution is due to an explicit dependence of $f_2^\perp$ on the running temperature,

$$\begin{aligned}R_T^\perp(b) &= 8\int_0^{\ln b} dx e^{-2x} u(e^x)\big(f_2^\perp(R_\perp(e^x)e^{2x}, Te^{zx}) \\ &\quad - f_2^\perp(R_\perp(e^x)e^{2x},0)\big), \end{aligned} \tag{A.19}$$

and $\delta R_\perp(b)$ originates from the temperature dependence of the running mass,

$$\begin{aligned}\delta R_\perp(b) &= 8\int_0^{\ln b} dx e^{-2x} u(e^x)\big(f_2^\perp(R_\perp(e^x)e^{2x},0) \\ &\quad - f_2^\perp(\Delta_\perp(e^x)e^{2x},0)\big). \end{aligned} \tag{A.20}$$

This term is of the order of u^2 and will be neglected from now on.

The inverse square of the correlation length $\xi_\perp$ is given by

$$\begin{aligned}\xi_\perp^{-2} &= \lim_{b\to\infty}\{\Delta_\perp(b) + R_T^\perp(b)\} = r_\perp + \lim_{b\to\infty} 8\int_0^{\ln b} dx\, e^{-2x} u(e^x) K_3 \Lambda^3 \int_0^\Gamma \frac{d\omega}{\pi}\left[\coth\left(\frac{\omega}{2Te^{zx}}\right) - 1\right]\times \\ &\quad \frac{2\omega((\Lambda^2 + R_\perp(e^x)e^{2x})^2 + \omega^2)\cos\theta}{((\Lambda^2 + R_\perp(e^x)e^{2x})^2 + \omega^2)^2 - 4(\Lambda^2 + R_\perp(e^x)e^{2x})^2\omega^2\sin^2\theta} \qquad \text{(A.21)} \\ &= r_\perp + 16\Lambda^{d+z-2} K_d T^{2/z}\int_{\ln(\frac{T^{1/z}}{\Lambda})}^\infty dx\, u(e^x\Lambda T^{-1/z}) e^{(z-2)x}\int_0^\infty \frac{dv}{\pi}(\coth v - 1) \qquad \text{(A.22)} \\ &\quad \frac{4\Lambda^z e^{zx} v\big((\Lambda^2 + R_\perp(e^x\Lambda T^{-1/z})e^{2x}\Lambda^2 T^{-2/z})^2 + 4\Lambda^{2z}e^{2zx}v^2\big)\cos\theta}{\big((\Lambda^2 + R_\perp(e^x\Lambda T^{-1/z})e^{2x}\Lambda^2 T^{-2/z})^2 + 4\Lambda^{2z}e^{2zx}v^2\big)^2 - 16(\Lambda^2 + R_\perp(e^x\Lambda T^{-1/z})e^{2x}\Lambda^2 T^{-2/z})^2 v^2\Lambda^{2x}e^{2zx}\sin^2\theta}, \end{aligned}$$

where the transformations $e^{x'} = e^x\Lambda^{-1}T^{1/z}$ and $v = \omega/2Te^{zx}$ have been introduced, and $u(e^x\Lambda T^{-1/z}) = u_0(e^x\Lambda T^{-1/z})^{4-(d+z)}$. Expression (A.22) for the correlation length can now be evaluated in the quantum critical and Fermi liquid regime.

In the quantum critical regime we can neglect the dependence of the integrand of (A.22) on $R_\perp$ and extend the lower limit of the x-integral to $-\infty$. Using the following integral

$$\int_0^\infty d\xi\,\frac{(2\xi)^n}{\sinh^2\xi} = 2n\Gamma(n)\zeta(n),\ n = 0,1,2,\ldots \tag{A.23}$$

we obtain

$$\begin{aligned}\xi_\perp^{-2} &= r_\perp + 16\frac{K_d}{z\cos\left(\frac{d-2}{2z}\pi\right)}\Gamma\left(1+\frac{d-2}{z}\right)\zeta\left(1+\frac{d-2}{z}\right)\\ &\quad\times u\,T^{\frac{d+z-2}{z}}\cos\left(\frac{d-2}{z}\theta\right).\end{aligned} \tag{A.24}$$

In the Fermi liquid regime and for low temperatures, we can replace the running mass $R_\perp$ in (A.22) by the control parameter $r_\perp$. It is convenient at this point to introduce yet another variable transformation of the form $e^{2x'} = r_\perp T^{-2/z} e^{2x}$. To lowest order we can then neglect the term $T r_\perp^{-z/2}$ in the integrand. Furthermore, we can extend the lower limit of the x-integral to $-\infty$, thereby inducing an error of order $\mathcal{O}(r_\perp^{1/2}/\Lambda)^{2-d+z}$, and obtain

$$\xi_\perp^{-2} = r_\perp + 16\frac{\pi^2}{12}\frac{d-z}{\sin\left(\frac{d-z}{2}\pi\right)}K_d u T^2 r_\perp^{\frac{d-z-2}{2}}\cos\theta \tag{A.25}$$

in the Fermi liquid regime.

B. Beyond Hertz-Millis Theory

B.1. Bosonic self-energy Σ_B

The momentum integral of the flow equation for the bosonic self-energy in two dimensions reads

$$\begin{aligned} I_B(\omega,\Omega) &= \int \frac{d^2k}{(2\pi)^2} \big([\mathrm{Im}G_R(\omega,\boldsymbol{k})]\, G_A(\omega+\Omega,\boldsymbol{k}+\boldsymbol{Q}) n_F(\omega) \\ &\qquad + G_R(\omega,\boldsymbol{k})\, [\mathrm{Im}G_R(\omega+\Omega,\boldsymbol{k}+\boldsymbol{Q})]\, n_F(\omega+\Omega)\big), \end{aligned} \tag{B.1}$$

where G_R, G_A are the full retarded and advanced electron Green's function, respectively. The main contribution to this integral comes from the hot spots $\boldsymbol{k}^*$ on the Fermi surface. It is therefore convenient to shift the integration variable $\boldsymbol{k}$ by $\boldsymbol{k}^*$, linearize the fermionic dispersion relation around the hot spots, and then set

$$\begin{aligned} \xi_{\boldsymbol{k}^*+\boldsymbol{k}+\boldsymbol{Q}} &= -v_x k_x + v_y k_y, \\ \xi_{\boldsymbol{k}^*+\boldsymbol{k}} &= -v_x k_x - v_y k_y. \end{aligned} \tag{B.2}$$

If we then perform a change of variables, setting

$$\begin{aligned} x_1 &= v_x k_x + v_y k_y, & k_x &= \frac{1}{2v_x}(x_1+x_2) \\ x_2 &= v_x k_x - v_y k_y, & k_y &= \frac{1}{2v_y}(x_1-x_2) \end{aligned} \tag{B.3}$$

so that

$$\int_0^\infty dk_x \int_{-\infty}^\infty dk_y \longrightarrow -\frac{1}{2v_x v_y} \int_{-\infty}^\infty dx_1 \int_{-x_1}^\infty dx_2 \approx -\frac{1}{2v_x v_y} \int_{-\infty}^\infty dx_1 \int_0^\infty dx_2, \tag{B.4}$$

the momentum integrals decouple and can be evaluated. For the imaginary part of $I_B(\omega,\Omega)$ we obtain

$$\begin{aligned} \mathrm{Im}\, I_B(\omega,\Omega) &= \int \frac{d^2k}{(2\pi)^2} \mathrm{Im}G_R(\omega,\boldsymbol{k})\, \mathrm{Im}G_R(\omega+\Omega,\boldsymbol{k}+\boldsymbol{Q})\, [n_F(\omega)-n_F(\omega+\Omega)] \\ &= -\frac{1}{2v_x v_y} [n_F(\omega)-n_F(\omega+\Omega)] \int_{-\infty}^\infty \frac{dx_1}{2\pi} \int_0^\infty \frac{dx_2}{2\pi} \times \\ &\qquad \mathrm{Im}\frac{1}{\omega+x_1-\Sigma_F^R(\omega)}\, \mathrm{Im}\frac{1}{\omega+\Omega+x_2-\Sigma_F^R(\omega+\Omega)} \\ &= -\frac{n_F(\omega)-n_F(\omega+\Omega)}{2(2\pi)^2 v_x v_y} \pi \left(\frac{\pi}{2} - \arctan \frac{\omega+\Omega-\mathrm{Re}\Sigma_F^R(\omega+\Omega)}{\mathrm{Im}\Sigma_F^R(\omega+\Omega)} \right). \end{aligned} \tag{B.5}$$

If the lower limit of the x_2-integral in (B.4) is extended to $-\infty$, then the integrals (B.5) still converge, and the result is

$$\mathrm{Im}\, I_B(\omega,\Omega) = -\frac{n_F(\omega)-n_F(\omega+\Omega)}{8v_x v_y}, \tag{B.6}$$

which is completely independent of the electron self-energy.

B.2. Fermionic self-energy Σ_F

For the sake of completeness, we present the flow equation for the fermionic self-energy as well. Since the frequency arguments in the propagators of the respective diagrams are all different, the renormalization group equations for Σ_F can be derived from (6.29); it has the following form:

$$\frac{d}{d\Lambda}\mathrm{Im}\Sigma_F(\Omega) = -V^2 \int \frac{d\omega}{\pi}\frac{d}{ds_F}\left(\chi^{s_F}(\omega+\Omega)\chi^{s_F}(\omega)\right) I_F(\omega,\Omega)$$

where $I_F(\omega,\Omega)$ contains the momentum integration and has the following form:

$$\begin{aligned} I_F(\omega,\Omega) &= \int \frac{d^2k}{(2\pi)^2}\Big(G_R(\omega+\Omega,\boldsymbol{k}+\boldsymbol{k}^*)\left[\mathrm{Im}D_R(\omega,\boldsymbol{k})\right] n_B(\omega) \\ &\quad + \left[\mathrm{Im}G_R(\omega+\Omega,\boldsymbol{k}+\boldsymbol{k}^*)\right] D_R(\omega,\boldsymbol{k}) n_F(\omega+\Omega)\Big), \end{aligned} \tag{B.7}$$

where G_R is the full retarded electron Green's function and D_R is the full retarded bosonic Green's function. The main contribution to this integral comes from momenta k close to the hot manifolds. Following [107], we split the momentum integration in an integral over the Fermi surface and an energy integration, $\int d^d\boldsymbol{k} = (1/v_F)\int\int dk_\perp k_\perp^{d-2}\int dE$, and consider only the energy dependence of the fermionic propagator and the dependence on $\boldsymbol{k}_\perp$ of the bosonic propagator. The integral (B.1) is then approximated by

$$\begin{aligned} I_F(\omega,\Omega) &= \frac{1}{v_F(2\pi)^2}\int_0^\infty dk_\perp \int_{-\infty}^{\infty} dE \left[\frac{1}{\omega+\Omega-E-\Sigma_F^R(\omega+\Omega)}\mathrm{Im}\left(\frac{1}{k_\perp^2+r-\Sigma_B^R(\omega)}\right) n_B(\omega)\right. \\ &\quad \left. + \mathrm{Im}\left(\frac{1}{\omega+\Omega-E-\Sigma_F^R(\omega+\Omega)}\right)\frac{1}{k_\perp^2+r-\Sigma_B^R(\omega)} n_F(\omega+\Omega)\right] \end{aligned} \tag{B.8}$$

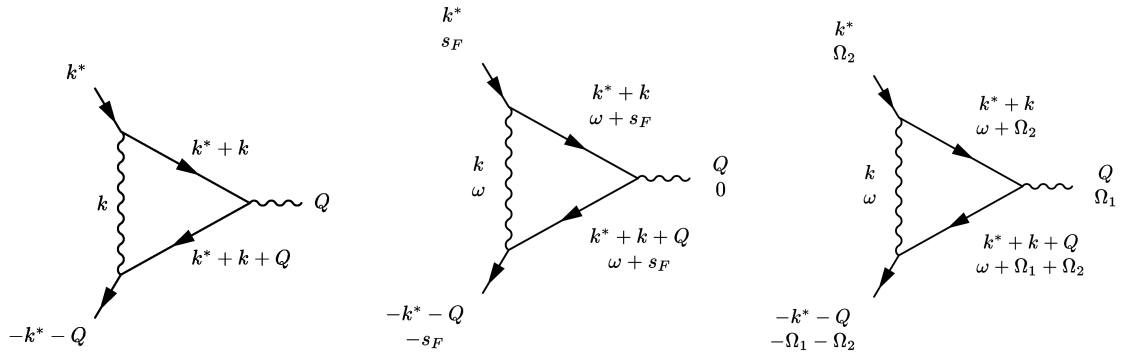

Figure B.1.: Fermion-boson vertex V (a) for external frequencies set to zero, (b) for an external fermionic frequency equal to the fermionic cutoff s_B and (c) with full frequency-dependence.

The imaginary part of the self-energy, to which the imaginary part of $I(\omega, \Omega)$ contributes, can now be computed without further approximations, and reads

$$\begin{aligned}
\mathrm{Im}I_F(\omega,\Omega) &= \frac{n_B(\omega)+n_F(\omega+\Omega)}{v_F(2\pi)^2}\int_0^\infty dk_\perp \,\mathrm{Im}\left(\frac{1}{k_\perp^2+r-\Sigma_B^R(\omega)}\right)\times \\
&\quad \int_{-\infty}^{\infty} dE\,\mathrm{Im}\left(\frac{1}{\omega+\Omega-E-\Sigma_F^R(\omega+\Omega)}\right) \\
&= \frac{n_B(\omega)+n_F(\omega+\Omega)}{v_F(2\pi)^2}\int_0^\infty dk_\perp \,\frac{\mathrm{Im}\Sigma_B^R(\omega)}{(k_\perp^2+r-\mathrm{Re}\Sigma_B^R(\omega))^2+(\mathrm{Im}\Sigma_B^R(\omega))^2}\times \\
&\quad \int_{-\infty}^{\infty} dE\,\frac{\mathrm{Im}\Sigma_F^R(\omega+\Omega)}{(\omega+\Omega-E-\mathrm{Re}\Sigma_F^R(\omega+\Omega))^2+(\mathrm{Im}\Sigma_F^R(\omega+\Omega))^2} \\
&= \frac{n_B(\omega)+n_F(\omega+\Omega)}{v_F(2\pi)^2}\left[\arctan\left(\frac{r-\mathrm{Re}\Sigma_F^R(\omega+\Omega)}{\mathrm{Im}\Sigma_F^R(\omega+\Omega)}\right)-\frac{\pi}{2}\right]\times \\
&\quad \frac{\pi}{2}\mathrm{Im}\left(r-\Sigma_B^R\right)^{-1/2}
\end{aligned} \tag{B.9}$$

If the lower limit of the $k_\perp$-integration is extended to $-\infty$, the result has the form

$$\mathrm{Im}I_F(\omega,\Omega) = \frac{n_B(\omega)+n_F(\omega+\Omega)}{v_F(2\pi)^2}\frac{\pi}{2}\mathrm{Im}\left(r-\Sigma_B^R\right)^{-1/2} \tag{B.10}$$

B.3. Fermion-boson vertex V

B.3.1. Fermion-boson vertex V at zero external frequencies

Let us first take a look at the flow equation for the vertex function at zero external frequencies and with fermionic momenta at hot spots and the bosonic momentum equal to the antiferromagnetic ordering vector, i.e. the diagram (a) in Fig. B.1. In this case,

$$\dot{V} = \frac{V^3}{2}\int \frac{d^2k}{(2\pi)^2}\frac{1}{\beta}\sum_n \left(2\chi_F(\mathrm{i}\omega_n)\dot{\chi}_B(\mathrm{i}\omega_n)\frac{ds_B}{d\Lambda} + 2\chi_B(\mathrm{i}\omega_n)\dot{\chi}_F(\mathrm{i}\omega_n)\frac{ds_F}{d\Lambda}\right) (\mathcal{D}(\mathrm{i}\omega_n,\boldsymbol{k})\mathcal{G}(\mathrm{i}\omega_n,\boldsymbol{k}+\boldsymbol{k}^*)\mathcal{G}(\mathrm{i}\omega_n,\boldsymbol{k}^*+\boldsymbol{k}+\boldsymbol{Q}))\,. \tag{B.11}$$

where we used (6.27) to take care of the cut-off functions. After converting the summation over Matsubara frequencies into an integral, the momentum integral that has to be evaluated in (B.11) has the form

$$I_V(\omega) = \int \frac{d^2k}{(2\pi)^2}\Big(G_R(\omega,\boldsymbol{k}+\boldsymbol{k}^*)G_R(\omega,\boldsymbol{k}+\boldsymbol{k}^*-\boldsymbol{Q})\mathrm{Im}\left[D_R(\omega,\boldsymbol{k})\right]n_B(\omega) + \mathrm{Im}\left[G_R(\omega,\boldsymbol{k}+\boldsymbol{k}^*)G_R(\omega,\boldsymbol{k}+\boldsymbol{k}^*-\boldsymbol{Q})\right]D_R(\omega,\boldsymbol{k})n_F(\omega)\Big). \tag{B.12}$$

The imaginary part of this integral vanishes if the external frequencies are set to zero; the real part at $T=0$, where $n_B(\omega) = -n_F(\omega) = -\Theta(-\omega)$, reads

$$\begin{aligned}\mathrm{Re}I_V(\omega) &= \int \frac{d^2k}{(2\pi)^2}\Big(-\mathrm{Re}\left[G_R(\omega,\boldsymbol{k}+\boldsymbol{k}^*)G_R(\omega,\boldsymbol{k}+\boldsymbol{k}^*-\boldsymbol{Q})\right]\mathrm{Im}\left[D_R(\omega,\boldsymbol{k})\right] \\ &\quad + \mathrm{Im}\left[G_R(\omega,\boldsymbol{k}+\boldsymbol{k}^*)G_R(\omega,\boldsymbol{k}+\boldsymbol{k}^*-\boldsymbol{Q})\right]\mathrm{Re}\left[D_R(\omega,\boldsymbol{k})\right]\Big)\Theta(-\omega) \\ &= \mathrm{Im}\int \frac{d^2k}{(2\pi)^2}\,G_R(\omega,\boldsymbol{k}+\boldsymbol{k}^*)G_R(\omega,\boldsymbol{k}+\boldsymbol{k}^*-\boldsymbol{Q})D_A(\omega,\boldsymbol{k})\Theta(-\omega)\end{aligned} \tag{B.13}$$

where it was used that

$$\mathrm{Re}D_R(\omega,\boldsymbol{k}) = \frac{1}{2}\left(D_R(\omega,\boldsymbol{k}) + D_R^*(\omega,\boldsymbol{k})\right) = \frac{1}{2}\left(D_R(\omega,\boldsymbol{k}) + D_A(\omega,\boldsymbol{k})\right) \tag{B.14}$$

and so on. Once again, we can linearize the fermionic dispersion relation around the hot spots $\boldsymbol{k}^*$, shift $\boldsymbol{k}$ and set

$$\begin{aligned}\xi_{\boldsymbol{k}^*+\boldsymbol{k}+\boldsymbol{Q}} &= -v_x k_x + v_y k_y, \\ \xi_{\boldsymbol{k}^*+\boldsymbol{k}} &= -v_x k_x - v_y k_y,\end{aligned} \tag{B.15}$$

in which case

$$\begin{aligned}&\int \frac{d^2k}{(2\pi)^2}\,G_R(\omega,\boldsymbol{k}+\boldsymbol{k}^*+\boldsymbol{Q})G_R(\omega,\boldsymbol{k}+\boldsymbol{k}^*)D_A(\omega,\boldsymbol{k}+\boldsymbol{Q}) \\ &= \frac{1}{(2\pi)^2}\int dk_x dk_y\,\frac{1}{(\omega-\Sigma_F^R(\omega)+v_x k_x)^2-(v_y k_y)^2}\,\frac{1}{r+k_x^2+k_y^2-\Sigma_B^A(\omega)}.\end{aligned}$$

Evaluating this integral we find, as already stated by Abanov et al. [63] (see Appendix A), that the contributions from the frequency dependence of the electron propagators only give subleading corrections, and we can approximate $\mathrm{Re}I_V(\omega)$ by

$$\mathrm{Re}I_V(\omega) = \frac{\Theta(-\omega)}{(2\pi)v_x v_y} \arctan\left(\frac{v_y}{v_x}\right) \frac{\mathrm{Im}\Sigma_B^A(\omega)}{\left(\mathrm{Im}\Sigma_B^A(\omega)\right)^2 + \left(r - \mathrm{Re}\Sigma_B^A(\omega)\right)^2}. \tag{B.16}$$

B.3.2. Fermion-boson vertex V at s_F

We now want to consider the frequency-dependence of the vertex function at least to some extent. The full vertex function depends on two independent external frequencies and two independent external momenta. Another possible approximation consists of setting the external bosonic frequency to zero and the remaining external frequency Ω (see diagram (b) of Fig. B.1) to the value of the fermionic cut-off s_F, since the vertex enters into the fRG-equation for the bosonic self-energy in such a way that one of its external fermionic momenta is set to s_F. The external momenta remain at the same values as above. Once again, we have to be careful how to interpret the combinations of cut-off functions and apply (6.27) if necessary. The flow equation then has the form

$$\begin{aligned}\dot{V} = -\frac{1}{2}\int \frac{d\omega}{\pi}\left(-2V^3\chi_F(\omega+s_F)\dot{\chi}_B(\omega)\frac{ds_B}{d\Lambda} - 2V^3\chi_B(\omega)\dot{\chi}_F(\omega+s_F)\frac{ds_F}{d\Lambda}\right)\times \\ \int \frac{d^2k}{(2\pi)^2}\Big(G_R(\omega+s_F,\boldsymbol{k}+\boldsymbol{k}^*)G_R(\omega+s_F,\boldsymbol{k}+\boldsymbol{k}^*-\boldsymbol{Q})\mathrm{Im}\left[D_R(\omega,\boldsymbol{k})\right]n_B(\omega) \\ + \mathrm{Im}\left[G_R(\omega+s_F,\boldsymbol{k}+\boldsymbol{k}^*)G_R(\omega+s_F,\boldsymbol{k}+\boldsymbol{k}^*-\boldsymbol{Q})\right]D_R(\omega,\boldsymbol{k})n_F(\omega+s_F)\Big).\end{aligned}$$

Using the δ-functions from the cut-offs, the frequency integration can be perfomed, and the combination of cut-off functions and fermionic and bosonic distribution functions gives

$$\begin{aligned}\dot{V} &= \frac{-1}{2\pi}\left(-2V^3\Theta(2s_F-s_B)\frac{ds_B}{d\Lambda}I_V'(-s_B) - 2V^3\Theta(s_B-2s_F)\frac{ds_F}{d\Lambda}I_V'(-2s_F)\right), \\ I_V'(\omega) &= \int\frac{d^2k}{(2\pi)^2}\Big(-\mathrm{Re}\left[G_R(\omega+s_F,\boldsymbol{k}+\boldsymbol{k}^*)G_R(\omega+s_F,\boldsymbol{k}+\boldsymbol{k}^*-\boldsymbol{Q})\right]\mathrm{Im}\left[D_R(\omega,\boldsymbol{k})\right] \\ &\quad + \mathrm{Im}\left[G_R(\omega+s_F,\boldsymbol{k}+\boldsymbol{k}^*)G_R(\omega+s_F,\boldsymbol{k}+\boldsymbol{k}^*-\boldsymbol{Q})\right]\mathrm{Re}\left[D_R(\omega,\boldsymbol{k})\right]\Big)\end{aligned} \tag{B.17}$$

The momentum integration can now be performed in complete analogy to B.13, yielding a flow equation

$$\begin{aligned}\dot{V} = \frac{-2V^3}{(2\pi)^2}\frac{1}{v_x v_y}\arctan\left(\frac{v_y}{v_x}\right)\Bigg(\Theta(2s_F-s_B)\frac{ds_F}{d\Lambda}\frac{\mathrm{Im}\Sigma_B^A(-2s_F)}{\left(\mathrm{Im}\Sigma_B^A(-2s_F)\right)^2+\left(r-\mathrm{Re}\Sigma_B^A(-2s_F)\right)^2} \\ + \Theta(s_B-2s_F)\frac{ds_B}{d\Lambda}\frac{\mathrm{Im}\Sigma_B^A(-s_B)}{\left(\mathrm{Im}\Sigma_B^A(-s_B)\right)^2+\left(r-\mathrm{Re}\Sigma_B^A(-s_B)\right)^2}\Bigg).\end{aligned}$$

B.3.3. Fully frequency-dependent V

In order to take the full feedback of the vertex in the flow equation for the bosonic self-energy into account, we should therefore consider the full frequency dependence of the vertex, taking the external momenta at the same values as above. All internal propagators now have different momenta, and the flow equation can be derived directly from (6.29):

$$\begin{aligned}\dot{V}(\Omega_1,\Omega_2) = \frac{-1}{2}\frac{1}{\beta}\sum_n 2V(\omega,\Omega_2)V(\Omega_1,\omega+\Omega_2)V(-\omega,\omega+\Omega_1+\Omega_2)\\ \frac{d}{d\Lambda}\left(\chi_F(\mathrm{i}\omega_n+\mathrm{i}\Omega_1+\mathrm{i}\Omega_2)\chi_F(\mathrm{i}\omega_n+\mathrm{i}\Omega_2)\chi_B(\mathrm{i}\omega_n)\right)\\ \int\frac{d^2k}{(2\pi)^2}\left(\mathcal{D}(\mathrm{i}\omega_n,\boldsymbol{k})\mathcal{G}(\mathrm{i}\omega_n+\mathrm{i}\Omega_2,\boldsymbol{k}+\boldsymbol{k}^*)\mathcal{G}(\mathrm{i}\omega_n+\mathrm{i}\Omega_1+\mathrm{i}\Omega_2,\boldsymbol{k}^*+\boldsymbol{k}+\boldsymbol{Q})\right).\end{aligned} \tag{B.18}$$

We neglect the fermionic self-energy right from the start. In order to perform the momentum integration, we convert the summation over Matsubara frequencies into an integral. One can show that the most singular contribution of the last line (B.18) to the flow equation for the imaginary part of the bosonic self-energy has the form

$$\begin{aligned}\frac{1}{2v_xv_y}\tilde{I}_V(\omega,\Omega_1,\Omega_2) = \frac{1}{2v_xv_y}\frac{\mathrm{Im}\Sigma_B^R(\omega)}{\left(r+\frac{(2\omega+\Omega_1+2\Omega_2)^2}{4v_x^2}+\frac{\Omega_1^2}{4v_y^2}\right)^2+\left(\mathrm{Im}\Sigma_B^R(\omega)\right)^2}\\ \left[\coth\left(\frac{\beta\omega}{2}\right)+\tanh\left(\frac{\beta(\omega+\Omega_1+\Omega_2)}{2}\right)-\tanh\left(\frac{\beta(\omega+\Omega_2)}{2}\right)\right].\end{aligned} \tag{B.19}$$

The flow equation for the vertex is now rather complicated and has the form

$$\begin{aligned}\dot{V}(\Omega_1,\Omega_2) = \frac{-1}{4\pi v_xv_y}\Bigg[\sum_{\omega=\pm s_F-\Omega_2}V(\omega,\Omega_2)V(\Omega_1,\omega+\Omega_2)V(-\omega,\omega+\Omega_1+\Omega_2)\times\\ \Theta(|\Omega_1+\Omega_2+\omega|-s_F)\Theta(|\omega|-s_B)\frac{dsF}{d\Lambda}\tilde{I}_V(\omega,\Omega_1,\Omega_2)\\ +\sum_{\omega=\pm s_F-\Omega_1-\Omega_2}V(\omega,\Omega_2)V(\Omega_1,\omega+\Omega_2)V(-\omega,\omega+\Omega_1+\Omega_2)\times\\ \Theta(|\Omega_2+\omega|-s_F)\Theta(|\omega|-s_B)\frac{dsF}{d\Lambda}\tilde{I}_V(\omega,\Omega_1,\Omega_2)\\ +\sum_{\omega=\pm s_B}V(\Omega_1,\omega+\Omega_2)V(-\omega,\omega+\Omega_1+\Omega_2)\times\\ \Theta(|\Omega_1+\Omega_2+\omega|-s_F)V(\omega,\Omega_2)\Theta(|\Omega_2+\omega|-s_F)\frac{dsB}{d\Lambda}\tilde{I}_V(\omega,\Omega_1,\Omega_2)\Bigg].\end{aligned} \tag{B.20}$$

The last contribution (third line) to $\dot{V}$ is $\neq 0$ only if $\mathrm{Im}\Sigma_B^R(s_B)\neq 0$, meaning that some imaginary part has to be generated by the dependence on s_F first.

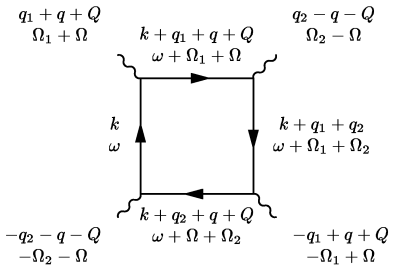

Figure B.2.: Fully frequency- and momentum-dependent four-boson vertex.

B.4. Four-boson vertex Γ_{ϕ^4}

The basic structure of the diagram that needs to be considered is shown in Fig. B.2. The diagram depends in principle on three external momenta $\boldsymbol{q}$, $\boldsymbol{q}_1$ and $\boldsymbol{q}_2$ and three external frequencies Ω, Ω_1 and Ω_2. To be consistent with the previous calculations, we neglect the fermionic self-energies in the internal lines. For simplicity, we set $T = 0$ right from the start, in which case the summation over discrete Matsubara frequencies turns into an integration:

$$U(\Omega,\Omega_1,\Omega_2;\boldsymbol{q},\boldsymbol{q}_1,\boldsymbol{q}_2) = V^4 \int \frac{d\omega\, d^2k}{(2\pi)^3} \frac{1}{\mathrm{i}\omega - \xi_{\boldsymbol{k}}} \frac{1}{\mathrm{i}(\omega+\Omega_1+\Omega) - \xi_{\boldsymbol{k}+\boldsymbol{q}_1+\boldsymbol{q}+\boldsymbol{Q}}} \times \frac{1}{\mathrm{i}(\omega+\Omega_1+\Omega_2) - \xi_{\boldsymbol{k}+\boldsymbol{q}_1+\boldsymbol{q}_2}} \frac{1}{\mathrm{i}(\omega+\Omega+\Omega_2) - \xi_{\boldsymbol{k}+\boldsymbol{q}_2+\boldsymbol{q}+\boldsymbol{Q}}}. \tag{B.21}$$

We can now linearize the fermionic dispersion near hot spots as before, and perform the momentum integrations to obtain [63]:

$$U(\Omega,\Omega_1,\Omega_2;\boldsymbol{q},\boldsymbol{q}_1,\boldsymbol{q}_2) = \frac{V^4}{16\pi v_x v_y} \int d\omega \frac{\mathrm{sign}(\omega) - \mathrm{sign}(\omega+\Omega_1+\Omega_2)}{\xi_{\boldsymbol{q}_1+\boldsymbol{q}_2} - \mathrm{i}(\Omega_1+\Omega_2)} \frac{\mathrm{sign}(\omega+\Omega_1-\Omega) - \mathrm{sign}(\omega+\Omega+\Omega_2)}{\xi_{\boldsymbol{Q}+\boldsymbol{q}_1-\boldsymbol{q}_2} - \mathrm{i}(\Omega_1-\Omega_2)}. \tag{B.22}$$

In the system of fRG-equations we investigate here, the vertex only feeds back into the self energy, see Fig. B.3. In the corresponding diagram for $(d/ds_B)\Sigma_B$, two of the external lines of the diagram shown in Fig. B.2 are contracted, and we effectively only need the dependence of Γ_{ϕ^4} on two independent external frequencies for the flow of Σ_B. When two adjacent lines of the diagram shown in Fig. B.2 are contracted, which corresponds to setting $\Omega_1 = \Omega_2$ and $\boldsymbol{q}_1 = \boldsymbol{q}_2$, the poles in (B.21) are positioned in such a way that the momentum integration gives zero. A finite contribution to the flow of Σ_B only comes from diagrams where external legs that are not adjacent to each other are contracted, i.e. where $\omega = 0$ and $\boldsymbol{q} = 0$. Furthermore, we only consider a frequency-dependent bosonic self-energy at the antiferromagnetic ordering wave vector and therefore only need the dependence of $(d/ds_F)\Gamma_{\phi^4}$ on one external momentum, which will be the loop momentum in the second contribution to the flow equation of $\dot{\Sigma}(\Omega)$ shown in Fig. B.3. In this special case the flow equations are very simple, and we can therefore take this momentum dependence of $(d/ds_F)\Gamma_{\phi^4}$ into account without introducing too many complications in the flow equations.

At this point, let us also take a look at the spin summations in the flow equation for $\Gamma_{\boldsymbol{\phi}^4}$ or, writing out spin indices more carefully,

$$\frac{\delta^4}{\delta\phi_i(\Omega_1,-Q)\delta\phi_j(-\Omega_1,-Q)\delta\phi_k(\Omega_2,Q)\delta\phi_l(-\Omega_2,Q)}\tilde{\Gamma}\big|_{\boldsymbol{\Phi}=\psi=\bar{\psi}=0}. \tag{B.23}$$

The diagrams that we consider for the flow equation of $\Gamma_{\boldsymbol{\phi}^4}$, i.e. those where ϕ_i and ϕ_j are *not* adjacent to each other, lead to the following summation over spin indices:

$$\begin{aligned}\mathrm{Tr}\big[&\sigma^i_{\mu\nu}\sigma^k_{\nu\sigma}\sigma^j_{\sigma\rho}\sigma^l_{\rho\mu}+\sigma^i_{\mu\nu}\sigma^l_{\nu\sigma}\sigma^j_{\sigma\rho}\sigma^k_{\rho\mu}+\sigma^j_{\mu\nu}\sigma^k_{\nu\sigma}\sigma^i_{\sigma\rho}\sigma^l_{\rho\mu}+\sigma^j_{\mu\nu}\sigma^l_{\nu\sigma}\sigma^i_{\sigma\rho}\sigma^k_{\rho\mu}\\ &+\sigma^k_{\mu\nu}\sigma^i_{\nu\sigma}\sigma^l_{\sigma\rho}\sigma^j_{\rho\mu}+\sigma^k_{\mu\nu}\sigma^j_{\nu\sigma}\sigma^l_{\sigma\rho}\sigma^i_{\rho\mu}+\sigma^l_{\mu\nu}\sigma^i_{\nu\sigma}\sigma^k_{\sigma\rho}\sigma^j_{\rho\mu}+\sigma^l_{\mu\nu}\sigma^j_{\nu\sigma}\sigma^k_{\sigma\rho}\sigma^i_{\rho\mu}\big]\\ &=8(-\delta_{ij}\delta_{kl}+\delta_{ik}\delta_{jl}+\delta_{il}\delta_{jk}).\end{aligned}$$

In the flow equations, the diagrams with $\omega=0$ and $\boldsymbol{q}=\boldsymbol{q}_1=0$ give the following contribution to $(d/ds_F)\Gamma_{\boldsymbol{\phi}^4}$:

$$\begin{aligned}\frac{d}{ds_F}\Gamma_{\boldsymbol{\phi}^4}(\Omega_1,\Omega_2;\boldsymbol{q}_2)=\frac{1}{2}8\frac{V^4}{16\pi v_x v_y}\int d\omega\times\\ \frac{d}{ds_F}\left(\chi_F(\omega)\chi_F(\omega+\Omega_1)\chi_F(\omega+\Omega_1+\Omega_2)\chi_F(\omega+\Omega_2)\right)\\ \frac{\mathrm{sign}(\omega)-\mathrm{sign}(\omega+\Omega_1+\Omega_2)}{\xi_{\boldsymbol{q}_2}-(\Omega_1+\Omega_2)\pm\mathrm{i}0}\frac{\mathrm{sign}(\omega+\Omega_1)-\mathrm{sign}(\omega+\Omega_2)}{\xi_{\boldsymbol{Q}-\boldsymbol{q}_2}-(\Omega_1-\Omega_2)\pm\mathrm{i}0}.\end{aligned} \tag{B.24}$$

In principle, all other diagrams also contribute to $(d/ds_F)\Gamma_{\boldsymbol{\phi}^4}$, but since we are only interested in those contributions to $\Gamma_{\boldsymbol{\phi}^4}$ that influence the flow of the self-energy, we will neglect all other contributions in the flow equation for $\Gamma_{\boldsymbol{\phi}^4}$.

The frequency integration can now be performed. The cut-off functions combine with the sign functions and one obtains

$$\begin{aligned}\frac{d}{ds_F}\Gamma_{\boldsymbol{\phi}^4}(\Omega_1,\Omega_2;\boldsymbol{q}_2)=\frac{4}{16\pi v_x v_y}\frac{\mathrm{sign}(\Omega_2-\Omega_1)}{\left[\xi_{\boldsymbol{q}_2}-(\Omega_1+\Omega_2)\pm\mathrm{i}0\right]\left[\xi_{\boldsymbol{Q}-\boldsymbol{q}_2}-(\Omega_1-\Omega_2)\pm\mathrm{i}0\right]}\\ V^4\,\Theta(|\Omega_1-\Omega_2|-2s_F).\end{aligned} \tag{B.25}$$

Note that only the terms in the second line depend on the fermionic cut-off s_F. It is this simple structure of the flow-equation for $\Gamma_{\boldsymbol{\phi}^4}$ which permits us to take its momentum dependence into account in the flow equation for the bosonic self-energy if we define a *momentum-independent* function $\gamma_{\boldsymbol{\phi}^4}(\Omega_1,\Omega_2)$ such that

$$\Gamma^{s_F}_{\boldsymbol{\phi}^4}(\Omega_1,\Omega_2;\boldsymbol{q}_2)\equiv\frac{4}{16\pi v_x v_y}\frac{1}{\left[\xi_{\boldsymbol{q}_2}-(\Omega_1+\Omega_2)\pm\mathrm{i}0\right]\left[\xi_{\boldsymbol{Q}-\boldsymbol{q}_2}-(\Omega_1-\Omega_2)\pm\mathrm{i}0\right]}\gamma^{s_F}_{\boldsymbol{\phi}^4}(\Omega_1,\Omega_2). \tag{B.26}$$

The flow equation for $\gamma_{\boldsymbol{\phi}^4}(\Omega_1,\Omega_2)$ reads

$$\frac{d}{ds_B}\gamma_{\boldsymbol{\phi}^4}(\Omega_1,\Omega_2)=V^4\,\Theta(|\Omega_1-\Omega_2|-2s_F)\mathrm{sign}(\Omega_2-\Omega_1). \tag{B.27}$$

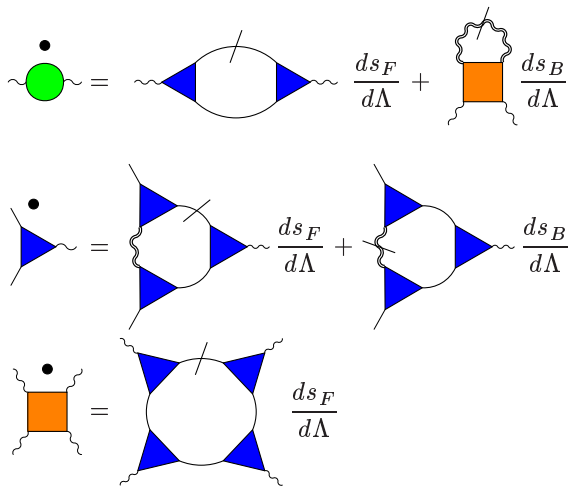

Figure B.3.: The flow equations shown in Fig. 6.2 are now supplemented by a flow for the four-boson vertex and its feedback on the bosonic self-energy.

Finally, let us calculate the feedback of (B.25) in the flow equation for the imaginary part of the bosonic self-energy, choosing $\Omega_1 \equiv \Omega$ to be the external frequency (a combinatorical factor of 2 for the two possibilities of choosing the external frequency is now required) and $\Omega_2 \equiv \omega$ to be the loop momentum of the second diagram in the flow equation for Σ_B in Fig. B.3. Leaving aside the frequency-dependent cutoff-function and γ^4_ϕ for the moment, we need to evaluate the momentum integrals of the following expression:

$$\int \frac{d^2k}{(2\pi)^2} \frac{1}{\beta} \sum_n \mathcal{D}(\mathrm{i}\omega_n, \boldsymbol{k}) \frac{1}{\mathrm{i}(\Omega + \omega_n) - \xi_{\boldsymbol{k}}} \frac{1}{\mathrm{i}(\Omega - \omega_n) - \xi_{\boldsymbol{Q}-\boldsymbol{k}}}, \tag{B.28}$$

where $\mathcal{D}$ is the dressed bosonic propagator. One can show that the most singular contribution of (B.28) to the flow equation for the imaginary part of the bosonic self-energy has the form

$$\frac{1}{2v_x v_y} \int \frac{d\omega}{2\pi} \left(\coth\left(\frac{\beta\omega}{2}\right) - \coth\left(\frac{\beta(\omega+\Omega)}{2}\right) - \coth\left(\frac{\beta(\omega-\Omega)}{2}\right) \right) \times \frac{\mathrm{Im}\Sigma_B^R(\omega)}{\left[r + \left(\frac{\omega}{v_x}\right)^2 + \left(\frac{\Omega}{v_y}\right)^2 \right]^2 + \left[\mathrm{Im}\Sigma_B^R(\omega)\right]^2}. \tag{B.29}$$

The main $\omega-$dependence of the denominator comes from the imaginary part of the bosonic self-energy, and since v_y is of the order of the Fermi velocity, the contribution $\propto \Omega/v_y$ can also be neglected. At $T = 0$, the coth-functions become sign-functions, and we obtain the following contribution to the flow equation for the imaginary part of the bosonic self-energy:

$$\frac{d}{ds_B}\mathrm{Im}\Sigma_B(\Omega) = -\frac{1}{16\pi^2}\frac{1}{(v_x v_y)^2}\mathrm{sign}(|\Omega| - s_B) \left[-\frac{\mathrm{Im}\Sigma_B^R(-s_B)}{\left(\mathrm{Im}\Sigma_B^R(-s_B)\right)^2 + r^2} \gamma_{\phi^4}(\Omega, -s_B) + \frac{\mathrm{Im}\Sigma_B^R(s_B)}{\left(\mathrm{Im}\Sigma_B^R(s_B)\right)^2 + r^2} \gamma_{\phi^4}(\Omega, s_B) \right]. \tag{B.30}$$

This contribution is $\neq 0$ only if $\mathrm{Im}\Sigma_B^R(|s_B|) \neq 0$, meaning that some imaginary part has to be generated by the dependence on s_F first. Since $(\partial/\partial s_F)\mathrm{Im}\Sigma_B(\Omega)$ is itself proportional to $\Theta(|\Omega| - 2s_F)$, we can immediately see that the contribution (B.30) to the flow equation is only present for $s_B > 2s_F$.

B.5. Continuous Hubbard–Stratonovich transformation

The Hubbard–Stratonovich transformation is originally introduced to eliminate the spin-density interaction $J(\bar{\psi}(\boldsymbol{\sigma}/2)\psi)^2$. However, this would be once again generated in the RG-flow, we therefore want to eliminate the spin-density interaction part at each point in the fRG-flow by means of a continuous Hubbard-Stratonovich transformation. The general idea of a continuous Hubbard-Stratonovich transformation has already been explored by Gies and Wetterich [113], who introduced a continuous Hubbard-Stratonovich transformation for the "classical" fields, i.e. the arguments of the Legendre effective action.

A continuous Hubbard–Stratonovich transformation can be incorporated in the RG-flow by introducing an additional, cutoff-dependent parameter. It is not possible to eliminate the full four-fermion vertex $\Gamma_{\psi\bar{\psi}\psi\bar{\psi}}$, which depends on three independent momenta and frequencies. A more reasonable approach is to eliminate the momentum- and frequency-independent part of the four-point vertex function which corresponds to the spin-density interaction, much in the way the original Hubbard-Stratonovich transformation acts. There are several possible ways to accomplish this. One could think of introducing a cutoff-dependent parameter

1. as a transformation of the (classical) fields, i.e. the arguments of Γ, as it was done in [113],
2. in the action S as a transformation of $\boldsymbol{\phi}$ during the RG-flow,
3. in S before the RG-flow starts, i.e. as a parameter in the original Hubbard–Stratonovich transformation.

In the following, the different approaches will be discussed in order to find the one which is the most convenient for the problem at hand.

The following difficulty arises in cases 2 and 3: As a result of introducing the additional, cutoff-dependent parameter in S, the RG-equations invariably become more complicated. It is therefore convenient to reduce the complexity of the RG-equations by using the field redefinition invariance of $\mathcal{Z}$, which will be discussed in the following section. This field redefinition invariance can be cast into the form of functional differential equations; in particular the following two cases will be needed:

- an infinitesimal Hubbard–Stratonovich transformation

$$\boldsymbol{\phi}(x,\tau) \to \boldsymbol{\phi}(x,\tau) + \varepsilon(x,\tau)\bar{\psi}(x,\tau)\frac{\boldsymbol{\sigma}}{2}\psi(x,\tau) \tag{B.31}$$

- an infinitesimal rescaling of the field ϕ

$$\boldsymbol{\phi}(x,\tau) \to (1+\varepsilon(x,\tau))\boldsymbol{\phi}(x,\tau) \tag{B.32}$$

B.5.1. Field redefinition invariance of the partition sum

In analogy to ordinary integrals, path integrals are left invariant by a change of integration variables.

Consider a theory with fields $\phi_i(x)$, $i = 1 \dots n$, which are collectively denoted by a vector $\Phi = (\phi_1, \dots, \phi_n)$, a Lagrangian $\mathcal{L}(\Phi, \partial_\mu \Phi)$, the vector of sources $\boldsymbol{A} = (A_1, \dots, A_n)$ and the generating functional

$$\mathcal{Z}[\boldsymbol{A}] = \int \mathcal{D}\Phi \mathrm{e}^{-\int_X (\mathcal{L} - \boldsymbol{A}\Phi)} = \int \mathcal{D}\Phi \mathrm{e}^{-S[\Phi] + \int_X \boldsymbol{A}\Phi}, \tag{B.33}$$

where the shorthand notation $X = (\boldsymbol{x}, \tau)$ has been introduced, i.e.

$$\int_X \equiv \int_0^\beta \mathrm{d}\tau \int_{-\infty}^{\infty} \mathrm{d}^3 x. \tag{B.34}$$

Consider infinitesimal field transformations of the form

$$\phi_i \to \phi_i + \delta\phi_i, \quad \delta\phi_i = \varepsilon f_i\{\Phi; x\} \tag{B.35}$$

where the f_i are arbitrary functionals of Φ subjected to the condition that they admit an expansion in powers of the ϕ_is. This ensures that the transformations may be inverted as formal series. The field transformations induce the following changes

- in the action:

$$S[\Phi + \delta\Phi] = S[\Phi] + \int_X \frac{\delta S[\Phi]}{\delta \phi_k(X)} \delta\phi_k(X) + \dots \tag{B.36}$$

$$\mathrm{e}^{-S[\Phi+\delta\Phi]} \cong \mathrm{e}^{-S[\Phi]} \left(1 - \int_X \frac{\delta S[\Phi]}{\delta \phi_k(X)} \delta\phi_k(X) + \dots\right) \tag{B.37}$$

- in the source term:

$$\mathrm{e}^{\int_X \boldsymbol{A}(\Phi+\delta\Phi)} \cong \mathrm{e}^{\int_X \boldsymbol{A}\Phi} \left(1 + \int_X \boldsymbol{A}(X)\delta\Phi(X) + \dots\right) \tag{B.38}$$

- in the Jacobian:

$$\mathcal{J} = 1 + \int_X \frac{\delta f_k\{\Phi; X\}}{\delta \phi_k(X)} \varepsilon + \dots \tag{B.39}$$

Since a change of integration variable cannot change the partition function $\mathcal{Z}[\boldsymbol{A}]$, the variation $\delta\mathcal{Z}[\boldsymbol{A}]$ must vanish. To first order in ε this requirement is expressed as

$$0 = \delta\mathcal{Z}[\boldsymbol{A}] = \int \mathcal{D}\Phi \left(\int_X \left[\frac{\delta f_k\{\Phi; X\}}{\delta \phi_k(X)} + \left(A_k(X) - \frac{\delta S[\Phi]}{\delta \phi_k(X)} \right) f_k\{\Phi; X\} \right] \right) \mathrm{e}^{-S[\Phi] + \int_X \boldsymbol{A}\Phi}. \tag{B.40}$$

Differentiating this relation with respect to the sources and setting the source terms to zero yields relations between the Greens functions.

When the reparametrization (B.35) leaves the action invariant and the Jacobian unchanged, as is generally the case for symmetry transformations, (B.40) has a particularly simple form:

$$0 = \delta\mathcal{Z}[\boldsymbol{A}] = \int \mathcal{D}\Phi \int_X \left[A_k(X) f_k\{\Phi; x\}\right] \mathrm{e}^{-S[\Phi]+\int_X \boldsymbol{A}\Phi}. \tag{B.41}$$

From this relation, Ward identities (in the case of linear field transformations) or Slavnov–Taylor identities (in the case of non-linear field transformations) can be derived.

B.5.2. Method 1

It was first put forward in [113] (and then applied to the antiferromagnetic Hubbard model in [114]) to use transformations of the classical fields, i.e. the arguments of Γ, to simplify RG-flow equations. Following the approach of Gies and Wetterich, the field variable $\boldsymbol{\phi} \to \boldsymbol{\phi}^\Lambda$ is allowed to become cutoff-dependent, and $\boldsymbol{\phi}^\Lambda$ is varied during the flow in the following manner:

$$\partial_\Lambda \boldsymbol{\phi}^\Lambda = -\left(\partial_\Lambda \alpha^\Lambda\right)(\bar{\psi}\frac{\boldsymbol{\sigma}}{2}\psi), \tag{B.42}$$

where α^Λ is an arbitrary function. The effective action $\Gamma_\Lambda[\bar{\psi}, \psi, \boldsymbol{\phi}^\Lambda]$ then obeys the modified flow equation

$$\partial_\Lambda \Gamma_\Lambda[\bar{\psi}, \psi, \boldsymbol{\phi}^\Lambda] = \partial_\Lambda \Gamma_\Lambda[\bar{\psi}, \psi, \boldsymbol{\phi}^\Lambda]\big|_{\boldsymbol{\phi}^\Lambda} \int \frac{\delta\Gamma_\Lambda[\bar{\psi}, \psi, \boldsymbol{\phi}^\Lambda]}{\delta\boldsymbol{\phi}^\Lambda} \partial_\Lambda \boldsymbol{\phi}^\Lambda. \tag{B.43}$$

The function α^Λ can now be chosen to flow in such a way that the four-fermion function (or rather the spin-spin part of it at zero external momenta and frequencies) vanishes at all scales.

When this transformation is used, it is uncelar for most transformations α which field χ has $\boldsymbol{\phi}$ as its expectation value:

$$\boldsymbol{\phi}^\Lambda := \langle \chi^\Lambda \rangle = \frac{\delta \mathcal{F}_\Lambda}{\delta \boldsymbol{A}}. \tag{B.44}$$

and the higher derivatives of $\mathcal{F}_\Lambda$ are now related to correlation functions of χ^Λ.

B.5.3. Method 2

A different approach is to introduce transformations at an earlier stage, i.e. for the quantum fields in the exponent of $\mathcal{Z}$. A possible choice is to set

$$\boldsymbol{\phi} \to \boldsymbol{\phi} + \zeta(\bar{\psi}\frac{\boldsymbol{\sigma}}{2}\psi) \tag{B.45}$$

in the RG-flow, where $\zeta = \zeta(s_B, s_F)$ is a cutoff-dependent parameter. The partition sum (6.1) is then changed to

$$\begin{aligned}\mathcal{Z} &= \int \mathcal{D}\Phi\, \mathrm{e}^{-\int_X \left(\bar\psi Q_F\psi + \left(\boldsymbol{\phi}+\zeta(\bar\psi\frac{\boldsymbol{\sigma}}{2}\psi)\right)^2 Q_B + \mathrm{i}\left(\boldsymbol{\phi}+\zeta(\bar\psi\frac{\boldsymbol{\sigma}}{2}\psi)\right)(\bar\psi\frac{\boldsymbol{\sigma}}{2}\psi) - \boldsymbol{A}\boldsymbol{\phi} - \bar\eta\psi - \bar\psi\eta\right)} \\ &= \int \mathcal{D}\Phi\, \mathrm{e}^{-\int_X \left(\bar\psi Q_F\psi + \boldsymbol{\phi}^2 Q_B + (\mathrm{i}+2\zeta Q_B)\boldsymbol{\phi}(\bar\psi\frac{\boldsymbol{\sigma}}{2}\psi) + (\mathrm{i}\zeta+\zeta^2 Q_B)(\bar\psi\frac{\boldsymbol{\sigma}}{2}\psi)^2 - \boldsymbol{A}\boldsymbol{\phi} - \bar\eta\psi - \bar\psi\eta\right)},\end{aligned} \tag{B.46}$$

and the differential equation for $\mathcal{Z}_\zeta$ has to include the flow of ζ as well. It is obvious from looking at the exponent of (B.46) that we have to pay special attention to the derivative w.r.t. the bosonic cutoff s_B, and we therefore exclusively consider $\partial_{s_B}\mathcal{Z}$ here:

$$\begin{aligned}\partial_{s_B}\mathcal{Z}_\zeta &= \int \mathcal{D}\Phi \left[-\frac{\partial S[\Phi]}{\partial Q_B}\,\partial_{s_B}Q_B - \frac{\partial S[\Phi]}{\partial\zeta}\,\partial_{s_B}\zeta\right] \mathrm{e}^{-S[\Phi]+\int_X \boldsymbol{A}\boldsymbol{\phi}+\bar\eta\psi+\bar\psi\eta} \\ &= \int \mathcal{D}\Phi \Bigg[-\int_X \left(\boldsymbol{\phi} + \zeta\bar\psi\frac{\boldsymbol{\sigma}}{2}\psi\right)^2 \partial_{s_B}Q_B \\ &\qquad - \left\{2(\boldsymbol{\phi} + \bar\psi\frac{\boldsymbol{\sigma}}{2}\psi)Q_B + \mathrm{i}(\bar\psi\frac{\boldsymbol{\sigma}}{2}\psi)\right\}(\bar\psi\frac{\boldsymbol{\sigma}}{2}\psi)\partial_{s_B}\zeta\Bigg] \mathrm{e}^{-S[\Phi]+\int_X\cdots}\end{aligned} \tag{B.47}$$

This would obviously lead to a much more complicated form of RG-equations for Γ, since three- and four-point functions would now have to be inverted.

It is however possible to simplify (B.47). By using the reparametrization invariance of $\mathcal{Z}(\Lambda)$

- with respect to the transformation $\boldsymbol{\phi} \to \boldsymbol{\phi} + \varepsilon(x)\bar\psi\frac{\boldsymbol{\sigma}}{2}\psi$:

$$0 = \int \mathcal{D}\Phi \left[\left(\boldsymbol{A} - 2(\boldsymbol{\phi} + \zeta(\bar\psi\frac{\boldsymbol{\sigma}}{2}\psi))Q_B + \mathrm{i}(\bar\psi\frac{\boldsymbol{\sigma}}{2}\psi)\right)\bar\psi\frac{\boldsymbol{\sigma}}{2}\psi\right] \mathrm{e}^{-S[\Phi]+\int_X\cdots} \tag{B.48}$$

- with respect to the transformation $\boldsymbol{\phi} \to \boldsymbol{\phi} + \varepsilon(x)\boldsymbol{\phi}$:

$$0 = \int \mathcal{D}\Phi \left[\delta(0) + \left(\boldsymbol{A} - 2(\boldsymbol{\phi} + \zeta(\bar\psi\frac{\boldsymbol{\sigma}}{2}\psi))Q_B + \mathrm{i}(\bar\psi\frac{\boldsymbol{\sigma}}{2}\psi)\right)\boldsymbol{\phi}\right] \mathrm{e}^{-S[\Phi]+\int_X\cdots} \tag{B.49}$$

equation (B.47) can be written as

$$\begin{aligned}\partial_{s_B}\mathcal{Z}_\zeta = \int \mathcal{D}\Phi \int_X \Bigg\{ &- \boldsymbol{A}(\bar\psi\frac{\boldsymbol{\sigma}}{2}\psi)\partial_{s_B}\zeta + \partial_{s_B}Q_B\left[\boldsymbol{\phi}^2 + \frac{\zeta^2}{2\zeta Q_B + \mathrm{i}}\boldsymbol{A}(\bar\psi\frac{\boldsymbol{\sigma}}{2}\psi)\right. \\ &\left. + \left(2\zeta - \frac{2Q_B\zeta^2}{2\zeta Q_B + \mathrm{i}}\right)\frac{1}{2\zeta Q_B + \mathrm{i}}(\delta(0) + \boldsymbol{A}\boldsymbol{\phi} - 2Q_B\boldsymbol{\phi}^2)\right]\Bigg\} \mathrm{e}^{-S[\Phi]+\int_X\cdots}.\end{aligned} \tag{B.50}$$

This looks rather cumbersome and it is possible to do better.

B.5.4. Method 3

The Hubbard–Stratonovich transformation is based on the identity

$$\text{const.} \cdot \mathrm{e}^{-J(\bar{\psi}\frac{\boldsymbol{\sigma}}{2}\psi)^2} = \int \mathcal{D}\Phi\, \mathrm{e}^{-\frac{1}{4J}\boldsymbol{\phi}^2 - \mathrm{i}\boldsymbol{\phi}(\bar{\psi}\frac{\boldsymbol{\sigma}}{2}\psi)} \tag{B.51}$$

for Gaussian integrals. A way of introducing an additional parameter in $\mathcal{Z}$ that preserves the general form of (B.51) is to replace $(\boldsymbol{\phi} + 2\mathrm{i}J\bar{\psi}\frac{\sigma}{2}\psi)^2$ by $(\boldsymbol{\phi} + 2\zeta\mathrm{i}J\bar{\psi}\frac{\sigma}{2}\psi)^2$, while keeping the source term fixed. Unless ζ is equal to one at the start of the RG-flow, this corresponds to an incomplete Hubbard–Stratonovich transformation, where the $(\bar{\psi}\frac{\boldsymbol{\sigma}}{2}\psi)^2$-vertex in the action does not vanish completely.

This procedure leads to a partition sum of the form

$$\mathcal{Z}_\zeta(s_B, s_F) = \int \mathcal{D}\Phi \mathrm{e}^{-\int_X \bar{\psi}Q_F\psi + \boldsymbol{\phi}Q_B\boldsymbol{\phi} + \mathrm{i}\zeta\boldsymbol{\phi}(\bar{\psi}\frac{\boldsymbol{\sigma}}{2}\psi) + (1-\zeta^2)J(\bar{\psi}\frac{\boldsymbol{\sigma}}{2}\psi)^2 - \mathrm{A}\boldsymbol{\phi} - \bar{\psi}\eta - \bar{\eta}\psi}, \tag{B.52}$$

so that

$$\partial_{s_B}\mathcal{Z}_\zeta = -\int \mathcal{D}\Phi \int_X \left\{\boldsymbol{\phi}(\partial_{s_B}Q_B)\boldsymbol{\phi} - (\mathrm{i}\boldsymbol{\phi} - 2\zeta J(\bar{\psi}\frac{\boldsymbol{\sigma}}{2}\psi))\bar{\psi}\frac{\boldsymbol{\sigma}}{2}\psi(\partial_{s_B}\zeta)\right\} \mathrm{e}^{-S[\Phi]+\int_X \cdots}. \tag{B.53}$$

A similar expression is obtained for $\partial_{s_B}\mathcal{Z}_\zeta$. Equation (B.53) can once again be cast into a simpler form. Using the reparametrization invariance of (B.52)

- under the transformation $\boldsymbol{\phi} \to \boldsymbol{\phi} + \varepsilon(x)\bar{\psi}\frac{\boldsymbol{\sigma}}{2}\psi$:

$$0 = \int \mathcal{D}\Phi \int_X \left[\left(\boldsymbol{A} - 2Q_B\boldsymbol{\phi} - \mathrm{i}\zeta(\bar{\psi}\frac{\boldsymbol{\sigma}}{2}\psi)\right)(\bar{\psi}\frac{\boldsymbol{\sigma}}{2}\psi)\right] \mathrm{e}^{-S[\Phi]+\int_X \cdots}, \tag{B.54}$$

- under the transformation $\boldsymbol{\phi} \to \boldsymbol{\phi}(1 + \varepsilon(x))$:

$$0 = \int \mathcal{D}\Phi \int_X \left[\delta(0) + \left(\boldsymbol{A} - 2Q_B\boldsymbol{\phi} - \mathrm{i}\zeta(\bar{\psi}\frac{\boldsymbol{\sigma}}{2}\psi)\right)\boldsymbol{\phi}\right] \mathrm{e}^{-S[\Phi]+\int_X \cdots}, \tag{B.55}$$

to eliminate both the $(\bar{\psi}(\boldsymbol{\sigma}/2)\psi)^2$- and the $\boldsymbol{\phi}(\bar{\psi}(\boldsymbol{\sigma}/2)\psi)$-terms, equation (B.53) can be written as

$$\begin{aligned}\partial_{s_B}\mathcal{Z}_\zeta = \int \mathcal{D}\Phi \int_X \Bigg\{ &-\boldsymbol{\phi}\left(\partial_{s_B}Q_B + \frac{2\mathrm{i}}{\zeta}Q_B(1-4JQ_B)\partial_{s_B}\zeta\right)\boldsymbol{\phi} - \frac{\mathrm{i}}{\zeta}(1-4JQ_B)\delta(0)\partial_{s_B}\zeta \\ &- \mathrm{i}(1-4JQ_B)\frac{1}{\zeta}\boldsymbol{A}\boldsymbol{\phi}\partial_{s_B}\zeta + 2J\boldsymbol{A}(\bar{\psi}\frac{\boldsymbol{\sigma}}{2}\psi)\partial_{s_B}\zeta\Bigg\}\mathrm{e}^{-S[\Phi]+\int_X \cdots}.\end{aligned} \tag{B.56}$$

Note that the second part of the first term is zero in the case of a sharp cutoff.

Methods 2 and 3 are closely connected, but not the same, which can be seen by the following consideration. Denoting the respective transformation parameters by ζ_2 and ζ_3, we can compare the coefficients of the field monomials $\boldsymbol{\phi}(\bar{\psi}\frac{\boldsymbol{\sigma}}{2}\psi)$ and $(\bar{\psi}\frac{\boldsymbol{\sigma}}{2}\psi)^2$ in the exponents of (B.46) and (B.52):

$$\mathrm{i}\zeta_3 = \mathrm{i} + 2\zeta_2 Q_B, \tag{B.57}$$

$$J(1-\zeta_3^2) = \mathrm{i}\zeta_2 + \zeta_2^2 Q_B. \tag{B.58}$$

These two conditions can only be fulfilled simultaneously if $4JQ_B = 1$, which is exactly true only at the end of the RG flow.

To conclude, considering the advantages and drawbacks of these approaches, method 3 seems to be most suitable for the model in question.

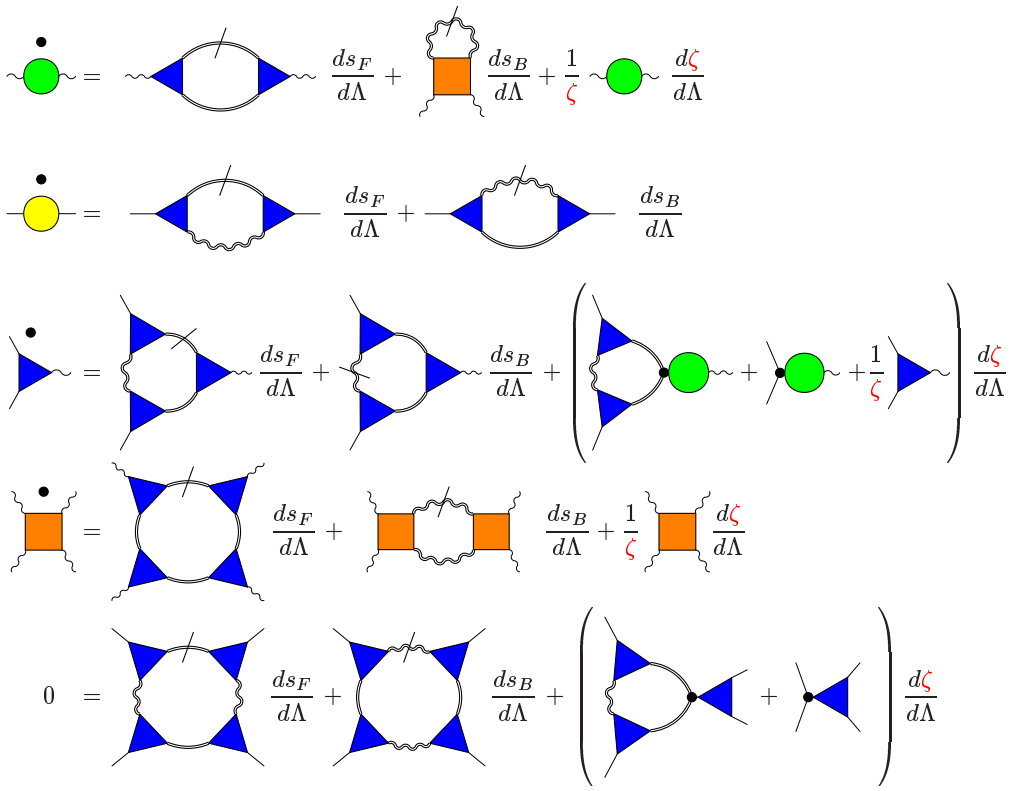

Figure B.4.: Form of the flow equations for a continuous Hubbard-Stratonovich transformation of the form presented in Section B.5.4. The dot in diagrams on the right-hand side of the third and last fRG-equation is a bare fermion-boson vertex.

Bibliography

[1] L. D. Landau, E. M. Lifshitz, and L. P. Pitaevskii, *Elektrodynamik der Kontinua* (Akademie-Verlag, Berlin, 1967), Vol. 8.

[2] P. Bak and M. Høgh, J. Phys. C: Solid St. Phys. **13**, 881 (1980).

[3] Y. Ishikawa, K. Tajima, D. Bloch, and M. Roth, Solid State Commun. **19**, 525 (1976).

[4] K. Kadowaki, K.and Okuda and M. Date, J. Phys. Soc. Jap. **51**, 2433 (1982).

[5] C. P. Pfleiderer, S. R. Julian, and G. Lonzarich, Nature **414**, 427 (2001).

[6] N. Doiron-Leyraud *et al.*, Nature **425**, 595 (2003).

[7] C. Pfleiderer *et al.*, Nature **427**, 227 (2004).

[8] C. Pfleiderer, Journal of the Physics of Condensed Matter **17**, 987 (2005).

[9] L. Pintschovius, D. Reznik, C. Pfleiderer, and H. V. Löhneysen, Pramana J. Phys. **63**, 117 (2004).

[10] W. Yu *et al.*, Physical Review Letters **92**, 086403 (2004).

[11] M. Uchida, Y. Onose, Y. Matsui, and Y. Tokura, Science **311**, 359 (2006).

[12] F. M. Grosche *et al.*, Physica B Condensed Matter **206**, 20 (1995).

[13] S. S. Saxena *et al.*, Nature **406**, 587 (2000).

[14] A. V. Kolomiets *et al.*, Physica B Condensed Matter **259**, 415 (1999).

[15] S. Barakat *et al.*, Physica B Condensed Matter **359**, 1216 (2005).

[16] M. J. Steiner, F. Beckers, P. G. Niklowitz, and G. G. Lonzarich, Physica B Condensed Matter **329**, 1079 (2003).

[17] T. R. Kirkpatrick and D. Belitz, Phys. Rev. B **72**, 180402 (2005).

[18] D. Belitz, T. R. Kirkpatrick, and A. Rosch, Phys. Rev. B **73**, 054431 (2006).

[19] D. Belitz, T. R. Kirkpatrick, and A. Rosch, arXiv:cond-mat/0604427 (2006).

[20] J. Schmalian and M. Turlakov, Phys. Rev. Lett. **93**, 036405 (2004).

[21] S. Tewari, D. Belitz, and T. R. Kirkpatrick, arXiv:cond-mat/0505519 (2005).

[22] T. Vojta and R. Sknepnek, Phys. Rev. B **64**, 052404 (2001).

[23] D. Belitz, T. R. Kirkpatrick, and J. Rollbühler, Physical Review Letters **94**, 247205 (2005).

[24] I. Fischer and A. Rosch, Europhysics Letters **68**, 93 (2004).

[25] O. Nakanishi, A. Yanase, and A. Hasegawa, J. Magn. Magn. Mater. **15-18**, 879 (1980).

[26] L. Taillefer, G. G. Lonzarich, and P. Strange, J. Magn. Magn. Mater. **54-57**, 957 (1986).

[27] P. A. Frigeri, D. F. Agterberg, A. Koga, and M. Sigrist, arXiv:cond-mat/0311354, erratum to Phys. Rev. Lett. **92**, 097001 (2004).

[28] C. Mauz, A. Rosch, and P. Wölfle, Phys. Rev. **B56**, 10953 (1997).

[29] S. Coleman, *Aspects of Symmetry* (Cambridge University Press, Cambridge, 1985).

[30] J. M. Ziman, *Principles of the Theory of Solids* (Cambridge University Press, Cambridge, 1965).

[31] N. W. Ashcroft and N. D. Mermin, *Solid State Physics* (Harcourt Brace College Publishers, Fort Worth, 1976).

[32] M. L. Plumer and M. B. Walker, J. Phys. C: Solid St. Phys. **14**, 4689 (1981).

[33] R. Shankar, Reviews of Modern Physics **66**, 129 (1994).

[34] D. C. Wright and N. D. Mermin, Reviews of Modern Physics **61**, 385 (1989).

[35] P. M. Chaikin and T. C. Lubensky, *Principles of condensed matter physics* (Cambridge University Press, Cambridge, 1995).

[36] R. M. Hornreich, M. Kugler, and S. Shtrikman, Physical Review Letters **48**, 1404 (1982).

[37] S. Meiboom, M. Sammon, and D. W. Berreman, Phys. Rev. A **28**, 3553 (1983).

[38] H.-S. Kitzerow and C. E. Bahr, *Chirality in liquid crystals* (Springer Verlag, Berlin, 2001).

[39] D. K. Yang, P. P. Crooker, and K. Tanimoto, Physical Review Letters **61**, 2685 (1988).

[40] J. A. N. Zasadzinski, S. Meiboom, M. J. Sammon, and D. W. Berreman, Physical Review Letters **57**, 364 (1986).

[41] R. M. Hornreich and S. Shtrikman, Phys. Rev. A **38**, 4843 (1988).

[42] S. Meiboom, M. Sammon, and W. F. Brinkman, Phys. Rev. A **27**, 438 (1983).

[43] J. P. Sethna, Phys. Rev. B **31**, 6278 (1985).

[44] G. L. Squires, *Introduction to the Theory of Thermal Neutron Scattering* (Dover Publications, New York, 1996).

[45] B. Binz, A. Vishwanath, and V. Aji, arXiv:cond-mat/0602529 (2006).

[46] U. K. Roessler, A. N. Bogdanov, and C. Pfleiderer, arXiv:cond-mat/0603103 (2006).

[47] U. K. Roessler, A. N. Bogdanov, and C. Pfleiderer, arXiv:cond-mat/0603104 (2006).

[48] H. Grebel, R. M. Hornreich, and S. Shtrikman, Phys. Rev. A **28**, 1114 (1983).

[49] H. Grebel, R. M. Hornreich, and S. Shtrikman, Phys. Rev. A **30**, 3264 (1984).

[50] J. Englert, L. Longa, H. Stark, and H.-R. Trebin, Physical Review Letters **81**, 1457 (1998).

[51] M. Böhm, *Symmetrien im Festkörper* (Wiley-VCH Verlag, Berlin, 2002).

[52] S. Sachdev, *Quantum Phase Transitions* (Cambridge University Press, Cambridge, 1999).

[53] J. A. Hertz, Phys. Rev. B **14**, 1165 (1976).

[54] M. Vojta, Reports of Progress in Physics **66**, 2069 (2003).

[55] A. J. Millis, Phys. Rev. B **48**, 7183 (1993).

[56] M. Garst, Ph.D. thesis, Universität Karlsruhe, 2003.

[57] A. Rosch, A. Schröder, O. Stockert, and H. V. Löhneysen, Physical Review Letters **79**, 159 (1997).

[58] A. Schröder *et al.*, Nature **407**, 351 (2000).

[59] D. Belitz, T. R. Kirkpatrick, and T. Vojta, Phys. Rev. B **55**, 9452 (1997).

[60] D. Belitz, T. R. Kirkpatrick, M. T. Mercaldo, and S. L. Sessions, Phys. Rev. B **63**, 174428 (2001).

[61] D. Belitz, T. R. Kirkpatrick, and T. Vojta, Phys. Rev. B **65**, 165112 (2002).

[62] A. Abanov and A. V. Chubukov, Phys. Rev. Lett. **84**, 5608 (2000).

[63] A. Abanov, A. V. Chubukov, and J. Schmalian, Advances in Physics **52**, 119 (2003).

[64] A. Rosch, Phys. Rev. B **64**, 174407 (2001).

[65] A. Abanov and A. V. Chubukov, Phys. Rev. Lett. **93**, 255702 (2004).

[66] S. Doniach, Physica B **91**, 213 (1977).

[67] P. Coleman, C. Pépin, and A. M. Tsvelik, Phys. Rev. B **62**, 3852 (2000).

[68] Q. Si, S. Rabello, K. Ingersent, and J. L. Smith, Nature **413**, 804 (2001).

[69] T. Senthil, S. Sachdev, and M. Vojta, Physical Review Letters **90**, 216403 (2003).

[70] P. Coleman and C. Pépin, Acta Physica Polonica B **34**, 691 (2003).

[71] C. Pépin, Physical Review Letters **94**, 066402 (2005).

[72] P. W. Anderson, Materials Research Bulletin **8**, 153 (1973).

[73] T. Senthil, M. Vojta, and S. Sachdev, Phys. Rev. B **69**, 035111 (2004).

[74] M. Oshikawa, Physical Review Letters **84**, 3370 (2000).

[75] P. Coleman, C. Pépin, Q. Si, and R. Ramazashvili, Journal of the Physics of Condensed Matter **13**, 723 (2001).

[76] S. Paschen *et al.*, Nature **432**, 881 (2004).

[77] R. Küchler *et al.*, Physical Review Letters **93**, 096402 (2004).

[78] K. Heuser, E.-W. Scheidt, T. Schreiner, and G. R. Stewart, Phys. Rev. B **58**, 15959 (1998).

[79] H. V. Löhneysen *et al.*, Phys. Rev. B **63**, 134411 (2001).

[80] E. Bauer *et al.*, Physica B Condensed Matter **281**, 319 (2000).

[81] J. Custers *et al.*, Nature **424**, 524 (2003).

[82] J. S. Kim *et al.*, Phys. Rev. B **69**, 024402 (2004).

[83] S. L. Bud'Ko, E. Morosan, and P. C. Canfield, Phys. Rev. B **69**, 014415 (2004).

[84] A. Bianchi *et al.*, Physical Review Letters **91**, 257001 (2003).

[85] J. Paglione *et al.*, Physical Review Letters **91**, 246405 (2003).

[86] S. A. Grigera *et al.*, Science **294**, 329 (2001).

[87] A. Oosawa, M. Ishii, and H. Tanaka, Journal of the Physics of Condensed Matter **11**, 265 (1999).

[88] H. Kageyama *et al.*, Physical Review Letters **82**, 3168 (1999).

[89] M. Jaime *et al.*, Physical Review Letters **93**, 087203 (2004).

[90] G. R. Stewart, Reviews of Modern Physics **73**, 797 (2001).

[91] F. Steglich *et al.*, Journal of Low Temperature Physics **95**, 3 (1994).

[92] K. Maeda *et al.*, Physica B Condensed Matter **259**, 401 (1999).

[93] G. Sparn *et al.*, Rev. High Pressure Sci. Technol. **7**, 431 (1998).

[94] H. V. Löhneysen *et al.*, Physical Review Letters **72**, 3262 (1994).

[95] K. Umeo, H. Kadomatsu, and T. Takabatake, Journal of the Physics of Condensed Matter **8**, 9743 (1996).

[96] T. Moriya, *Spin Fluctuations in Itinerant Electron Magnetism* (Springer Verlag, Berlin, 1985).

[97] F. Ronning *et al.*, arXiv:cond-mat/0602089 (2006).

[98] I. Fischer and A. Rosch, Phys. Rev. B **71**, 184429 (2005).

[99] A. Rosch, Phys. Rev. B **62**, 4945 (2000).

[100] A. Abrikosov, L. Gorkov, and I. Dzyaloshinski, *Methods of Quantum Field Theory in Statistical Physics* (Dover Publications, New York, 1975).

[101] I. Affleck, Phys. Rev. B **43**, 3215 (1991).

[102] T. Nikuni, M. Oshikawa, A. Oosawa, and H. Tanaka, Physical Review Letters **84**, 5868 (2000).

[103] T. Giamarchi and A. M. Tsvelik, Phys. Rev. B **59**, 11398 (1999).

[104] M. Matsumoto, B. Normand, T. M. Rice, and M. Sigrist, Physical Review Letters **89**, 077203 (2002).

[105] O. Nohadani, S. Wessel, and S. Haas, Phys. Rev. B **72**, 024440 (2005).

[106] L. Zhu, M. Garst, A. Rosch, and Q. Si, Physical Review Letters **91**, 066404 (2003).

[107] R. Hlubina and T. M. Rice, Phys. Rev. B **51**, 9253 (1995).

[108] B. L. Altshuler, L. B. Ioffe, and A. J. Millis, Phys. Rev. B **52**, 5563 (1995).

[109] M. Salmhofer and C. Honerkamp, Prog. Theor. Phys. **105**, 1 (2001).

[110] J. Berges, N. Tetradis, and C. Wetterich, Phys. Rept. **363**, 223 (2002).

[111] T. R. Morris, Int. J. Mod. Phys. A **9**, 2411 (1994).

[112] M. Maltseva and P. Coleman, Phys. Rev. B **72**, 174415 (2005).

[113] H. Gies and C. Wetterich, Phys. Rev. D **65**, 065001 (2002).

[114] T. Baier, E. Bick, and C. Wetterich, Phys. Rev. B **70**, 125111 (2004).

Danksagung

Mein besonderer Dank gilt Prof. Dr. Achim Rosch für die Vergabe und Betreuung dieser Arbeit. Seine stete Diskussionsbereitschaft, seine hilfreichen Vorschläge und nicht zuletzt sein unerschöpflicher Enthusiasmus für die Physik haben entscheidend zum Gelingen dieser Arbeit beigetragen.

Bedanken möchte ich mich auch bei Prof. Dr. E. Müller-Hartmann für die Begutachtung dieser Arbeit, sowie bei Prof. Dr. M. Braden für die Übernahme des Prüfungsvorsitzes.

Den Mitgliedern des Instituts für Theorie der Kondensierten Materie der Universität Karlsruhe und des Instituts für Theoretische Physik der Universität zu Köln gilt Dank für das angenehme Arbeitsklima und die vielen interessanten Diskussionen, sowohl über physikalische als auch über nichtphysikalische Dinge. Besonders hervorgehoben seien dabei diejenigen, mit denen ich im Verlauf der Arbeit die wechselnden Büros teilte: T. Ludwig, M. Kircan, R. Narayanan, X. Wan, T. Ulbricht, T. Costi, R. Helmes und P. Jung.

Meiner Familie danke ich für ihre Unterstützung in jeglicher Hinsicht.

Anhänge gemäß Prüfungsordnung

Kurze Zusammenfassung

Die vorliegende Arbeit befasst sich mit zwei Klassen von Systemen, die Nichtfermiflüssigkeitsverhalten zeigen: Wir untersuchten Aspekte von Helimagneten und von antiferromagnetischen Metallen in der Nähe eines quantenkritischen Punktes.

Helimagneten besitzen keine Inversionssymmetrie; in diesen Substanzen tritt daher Spin-Bahn-Kopplung auf, die magnetische Spiral-Ordnung hervorruft. Wir untersuchten die Bewegung von Elektronen in der magnetisch geordneten Phase eines Metalls ohne Inversionssymmetrie. Schon schwache Spin-Bahn-Kopplung verändert die Form der Fermifläche drastisch: Elektronen von einem großen Teil der Fermifläche können sich nicht mehr parallel zur Spiralachse bewegen. Dieser Effekt kann Auswirkungen in Experimenten zur Messung des anomalen Hall-Effektes zeigen.

Der Helimagnet MnSi zeigt in Neutronenstreuexperimenten nicht nur Spiral-Ordnung, sondern auch einen partiell geordneten Zustand, der an die spiral-geordnete Phase angrenzt. Unter der Annahme, dass dieser partiell geordnete Zustand eine separate Phase darstellt, untersuchten wir eine erweiterte Ginzburg-Landau-Theorie für chirale Ferromagneten. In einem gewissen Parameterbereich dieser Theorie konnten wir kristalline Phasen identifizieren, die starke Ähnlichkeit mit den sogenannten "Blauen Phasen" in Flüssigkristallen aufweisen.

Viele antiferromagnetische Schwer-Fermion-Systeme zeigen in einem bestimmten Parameterbereich Nichtfermiflüssigkeitsverhalten z.B. in der Temperaturabhängigkeit von thermodynamischen Größen wie der spezifischen Wärmekapazität. Dieses Verhalten könnte auf einen quantenkritischen Punkt hindeuten. Im Fall von feldinduziertem quantenkritischen Verhalten unterdrückt das externe Magnetfeld nicht nur den Antiferromagnetismus, es induziert auch Präzession und beeinflusst damit die Dynamik des Ordnungsparameters. Wir untersuchten das quantenkritische Verhalten antiferromagnetischer Metalle ohne Unordnung in einem statischen und räumlich homogenen externen Magnetfeld und betrachteten die Auswirkungen des Zusammenspiels von Präzession und Dämpfung auf verschiedene thermodynamische Größen und Transportgrößen. Insbesondere stellten wir fest, dass die Suszeptibilität $\chi = \partial M/\partial B$ die thermodynamische Grösse ist, deren Temperaturhängigkeit die stärksten Änderungen in der Nähe des quantenkritischen Punktes aufweist; dies ermöglicht insbesondere einen experimentellen Zugang zur Spin-Spin-Wechselwirkung.

Schließlich betrachteten wir das quantenkritische Verhalten zweidimensionaler Antiferromagneten. Unter Verwendung der funktionalen Renormierungsgruppe untersuchten wir eine Theorie, die sowohl die elektronischen Quasiteilchen als auch die fluktuierende Magnetisierung berücksichtigt, und gingen damit über eine Ordnungsparametertheorie hinaus. Erste Ergebnisse weisen auf Divergenzen im Renormierungsgruppenfluss schon bei endlichem Abstand vom quantenkritischen Punkt hin und weichen damit stark von den Vorhersagen der Hertz-Millis-Theorie ab.

Abstract

This thesis focusses on two classes of systems that exhibit non-Fermi liquid behaviour in experiments: we investigated aspects of chiral ferromagnets and of antiferromagnetic metals close to a quantum critical point.

In chiral ferromagnets, the absence of inversion symmetry makes spin-orbit coupling possible, which leads to a helical modulation of the ferromagnetically ordered state. We studied the motion of electrons in the magnetically ordered state of a metal without inversion symmetry by calculating their generic band-structure. We found that spin-orbit coupling, although weak, has a profound effect on the shape of the Fermi surface: On a large portion of the Fermi surface the electron motion parallel to the helix practically stops. Signatures of this effect can be expected to show up in measurements of the anomalous Hall effect.

Recent neutron scattering experiments uncovered the existence of a peculiar kind of partial order in a region of the phase diagram adjacent to the ordered state of the chiral ferromagnet MnSi. Starting from the premise that this partially ordered state is a thermodynamically distinct phase, we investigated an extended Ginzburg-Landau theory for chiral ferromagnets. In a certain parameter regime of the Ginzburg-Landau theory we identified crystalline phases that are reminiscent of the so-called blue phases in liquid crystals.

Many antiferromagnetic heavy-fermion systems can be tuned into a regime where they exhibit non-Fermi liquid exponents in the temperature dependence of thermodynamic quantities such as the specific heat capacity; this behaviour could be due to a quantum critical point. If the quantum critical behaviour is field-induced, the external field does not only suppress antiferromagnetism but also induces spin precession and thereby influences the dynamics of the order parameter. We investigated the quantum critical behavior of clean antiferromagnetic metals subject to a static, spatially uniform external magnetic field. We studied how the interplay of precession and damping affects various thermodynamic and transport quantities. We found that the susceptibility $\chi = \partial M/\partial B$ is the thermodynamic quantity which shows the most significant change upon approaching the quantum critical point and which gives experimental access to the (dangerously irrelevant) spin-spin interactions.

Finally, we studied the quantum critical behaviour of two-dimensional antiferromagnetic metals. Going beyond an order parameter theory, we included the electronic quasiparticles as well as the fluctuating magnetization in a functional Renormalization Group calculation. Preliminary results indicate a divergence in the fRG-equations already at a finite distance from the quantum critical point – this is incompatible with the Hertz-Millis picture.

Erklärung

Ich versichere, dass ich die von mir vorgelegte Dissertation selbständig angefertigt, die benutzten Quellen und Hilfmittel vollständig angegeben und die Stellen der Arbeit – einschliesslich Tabellen, Karten, und Abbildungen –, die anderen Werken im Wortlaut oder dem Sinn nach entnommen sind, in jedem Einzelfall als Entlehnung kenntlich gemacht habe; dass diese Dissertation noch keiner anderen Fakultät oder Universität zur Prüfung vorgelegen hat; dass sie – abgesehen von unten angegegebenen Teilpublikationen – noch nicht veröffentlicht worden ist sowie, dass ich eine solche Veröffentlichung vor Abschluss des Promotionsverfahrens nicht vornehmen werde. Die Bestimmungen dieser Promotionsordnung sind mir bekannt. Die von mir vorgelegte Dissertation ist von Herrn Prof. Dr. Rosch betreut worden.

Inga Fischer

Köln, den

Teilpublikationen

Inga Fischer and Achim Rosch
"Weak spin-orbit interactions induce exponentially flat mini-bands in magnetic metals without inversion symmetry"
Europhys. Lett. 68 (1), 93-99 (2004), cond-mat/0406259

Inga Fischer and Achim Rosch
"Field-tuned quantum critical point of antiferromagnetic metals"
Phys. Rev. B 71 (18), 184429 (2005), cond-mat/0412284